University of Sussex

Investigating Exotic Astrophysical Phenomena with The XMM-Newton Cluster Survey:

i) A Weighty Muse on Super Massive Black Holes

ii) Flash! - Rare Behaviour of the Universe

iii) Searching for a Dark Matter Needle in a Ray-Stack

Julian Mayers

Submitted for the degree of Doctor of Philosophy

University of Sussex

September 2017

Declaration

I hereby declare that this thesis has not been and will not be submitted in whole or in part to another University for the award of any other degree.

Signature:

Julian Mayers

UNIVERSITY OF SUSSEX

Julian Mayers, Doctor of Philosophy

Investigating Exotic Astrophysical Phenomena with The XMM-Newton Cluster Survey

i) A Weighty Muse on Super Massive Black Holes

ii) Flash! - Rare Behaviour of the Universe

iii) Searching for a Dark Matter Needle in a Ray-Stack

Summary

In this thesis, we present three projects that describe the use of the XMM-Newton Cluster Survey (XCS) to investigate exotic astrophysical phenomena. Each project widens the scope of XCS beyond the study of cluster cosmology.

In the first project, we derive correlations between X-ray properties of Active Galactic Nuclei (AGN) and mass of its Super Massive Black Hole (SMBH). These properties are the X-ray luminosity ($L_{\rm X}$) and a measure of the variability of the AGN - the normalised excess variance ($\sigma^2_{\rm NXS}$). We confirm previous results indicating an anti-correlation between black hole mass ($M_{\rm BH}$) and $\sigma^2_{\rm NXS}$, as well as anti-correlation between $L_{\rm X}$ and $\sigma^2_{\rm NXS}$, and a positive correlation between $L_{\rm X}$ and $M_{\rm BH}$. We investigate whether there is a redshift evolution in these relations. We then develop methods to estimate $M_{\rm BH}$ from short exposure X-ray observations specific to the eROSITA observatory, to allow us to measure $L_{\rm X}$ of millions of AGN.

The second project describes a new method to detect the rarest of X-ray transient sources, X-ray flashes (XRFs), through a serendipitous search of the XCS catalogue. We categorize the detected XRF candidates and look in more detail at one that is most likely to be an XRF. Based on its properties, we estimate an upper limit to their occurrence.

A third project describes our method to search for an unknown emission line in the stacked spectra of galaxy clusters from the XCS extended source catalogue. This line, if found, may be evidence of a hypothetical particle - the sterile neutrino - which has been postulated as a candidate for dark matter.

We review other research that has led to published work, as well as laying the foundation for future collaborations. This includes work on improving the XCS temperature pipeline in order to estimate the temperatures of galaxy clusters.

Acknowledgements

Many thanks to all those who have helped me with the research that has gone into this thesis. Notably, Arya Farahi for his fitting analysis and plots in Chapter 4, Alberto Bermeo for the cluster sources and temperatures in Chapter 6 and Philip Rooney for his infectious knowledge and help throughout.

Special thanks to Kathy Romer, a brilliant supervisor and friend. I probably would not have completed, and certainly would not have started this thesis without her.

To Joe, Amelie and Lola. Thank you for putting up with my ramblings on the nature of the Universe throughout your childhoods.

Finally to Rebecca. Whichever Universe you find yourself in now, you will always be at the centre of mine. Thank you for making it special.[1]

[1] From here, we revert to the more usual cosmological model of an isotropic and homogeneous Universe.

Contents

List of Tables

List of Figures

Chapter 1

Introduction

1.1 Thesis Introduction and Layout

'The effort to understand the Universe is one of the very few things that lifts human life a little above the level of farce, and gives it some of the grace of tragedy' -Weinberg, S. (1977)

This thesis represents a personal effort to understand the Universe.

Cosmologists ask questions about the structure and evolution of the Universe. Through the projects described herein, we attempt to answer some of these by looking at astrophysical phenomena that reveal their nature through emission of X-ray radiation.

In Chapter 3 we describe how the growth of galaxies interplays with, and can be inferred from, the size of the Super Massive Black Holes (SMBH) at their centre. In Chapter 4, we describe our techniques to estimate the masses of SMBH by measuring the X-rays from their associated Active Galactic Nucleus (AGN) and make predictions about how future X-ray missions will increase our knowledge. This chapter is being prepared as a journal article for submission to MNRAS.

In Chapter 5 we describe a new method to search for and describe detections of one of the most exotic and rare X-ray astrophysical phenomena, X-ray Flashes (XRF).

In Chapter 6 we describe new techniques to search for evidence of an as-yet hypothetical particle - the sterile neutrino. This has been postulated as a candidate for dark matter.

In Chapter 7 we describe some updates that were made to the methodology used by the XCS to estimate the masses of galaxy clusters, and review the papers where this work has been published.

In each of these chapters, we will summarise the aims and results of each project, highlight where the work is new to the field, and suggest how future work may develop the research further. We summarise these in Chapter 8.

All the projects described in this thesis make extensive use of the X-ray sources detected and catalogued by the XMM-Newton Cluster Survey (XCS) Romer et al. (2001). In Chapter 2 we review this thesis-specific project, as well as many software suites and methods used to detect and analyse the X-ray data.

We begin, in this Chapter, with an overview of the current cosmological model and X-ray astronomy which underpins the science that follows. Section 1.2 defines the current cosmological model and distance measurements. Section 1.3 gives an overview on X-ray astronomy and describes some of the astrophysical emission processes relevant to this thesis. Section 1.4 summarises the X-ray sources that are at the heart of the science projects. Section 1.6 is an overview of how X-ray observatories detect those sources. In particular, we introduce and focus on the XMM-Newton observatory in Section 1.8, and mention other X-ray satellites in Section 1.9.

1.2 Cosmological Model

1.2.1 The Current Cosmological Paradigm

Like any traveller, a visitor arriving in the Universe would want to get acquainted with its environs, its history and laws. The current cosmological model is a good place to begin and will be the assumed model throughout this thesis. It is founded on two basic premises. First, that on large enough scale, the Universe is *homogeneous*, it looks the same at each point. Second, it is *isotropic*, it looks the same in all directions. This 20th Century extension of the Copernican principle, that there is nowhere that can be considered as 'special', is the foundation of modern day cosmology upon which we can begin to build its paradigms. In doing so, we look at the expansion, geometry and content of the Universe, which together, allow us to define some equations that are central to any

modern cosmology textbook as well as this thesis.

1.2.2 Expansion

Before Hubble's seminal paper, Hubble (1929), the assumed cosmology was that of a steady state model. Indeed Einstein even built this into his paper on General relativity in 1915 with a cosmological constant Λ, an 'anti-gravity' energy to bring the Universe into static equilibrium. In publishing the correlation between the distance to the galaxies and their recession velocities, Hubble turned this idea on its head. The key point of the observational evidence that he described is that the light from galaxies is redshifted, and the further away the galaxies are, the more pronounced this Doppler effect becomes. Redshift z, is defined as:

$$z = \frac{\lambda_{obs} - \lambda_{em}}{\lambda_{em}} \tag{1.1}$$

where λ_{obs} and λ_{em} are the observed and emitted wavelengths of light. Also if a nearby object is receding with a velocity v, then

$$z = \frac{v}{c} \tag{1.2}$$

where c is the speed of light. From this and Hubble's observations it follow that

$$v = H_0 r \tag{1.3}$$

This is Hubble's law, where H_0 is the Hubble parameter $H(t)$ measured at present and r the actual (or proper) distance to the object. From such a tantalisingly simple relationship, it took until the final years of the 20th Century and the work of Freedman et al. (2001), for a value of $H_0 = 72 \pm 8\,\mathrm{kms}^{-1}\mathrm{Mpc}^{-1}$ to become the accepted value with 95% confidence.

To measure the distance between two points in an expanding universe, we define a co-moving co-ordinate system that is carried along with the expansion. In this, the real distance, between two galaxies is given by

$$r = a(t)\vec{x} \tag{1.4}$$

where $\vec{x}$ is the co-moving distance and $a(t)$ the scale-factor of the Universe which measures the expansion rate. At the present time we set $a_0 = 1$. Hence it follows that at earlier times $a_0 < 1$.

The Hubble parameter can be defined in terms of a as

$$H(t) = \frac{\dot{a}}{a} \tag{1.5}$$

where $\dot{a}$ is the time derivative of a.

1.2.3 Geometry

There is no reason to assume that Universe should have a flat geometry, described in terms of the spatial curvature k, where $k = 0$ in a flat Universe. Other models with open, k=-1, or closed k=+1, geometries are entirely possible. However recent observations, particularly concerning the angular size of features of the cosmic microwave background, together with an inflationary theory which resolves many cosmological problems, have led to a current acceptance that the Universe is indeed flat, or very close to being so. This can be expressed in terms of a density parameter Ω where;

$$\Omega(t) \equiv \frac{\rho}{\rho_c} \tag{1.6}$$

where ρ is the energy density of the universe and ρ_c is a critical density that results in a flat universe i.e. $\Omega_0 = 1$. Each of these three geometries leads to the Universe evolving differently, shown in Figure 1.1.

1.2.4 Content

The Universe is made from of different types of material, each of which has properties that affect the expansion rate. The importance of each to this expansion changes according to the particular epoch. Radiation (photons) and baryons (non-relativistic matter) are the observable everyday building blocks. Relativistic particles, such as neutrinos while difficult to observe are also part of any standard model of particle physics. Evidence for the existence of dark matter has become overwhelming (as reviewed in Section 6.2), although its constitution is at present unknown. The most dominant energy component is the so-called dark energy. This is responsible for the acceleration of the expansion of the Universe. Evidence for dark energy came from results of two competing surveys by Perlmutter et al. (1999) and Schmidt et al. (1998). The goal of these projects was to determine the cosmological parameters of the Universe by using the uniformity of class Ia supernovae as standard candles to measure the distances to nearby galaxies. From their results, it followed that there is a significant dark energy contribution to the total energy

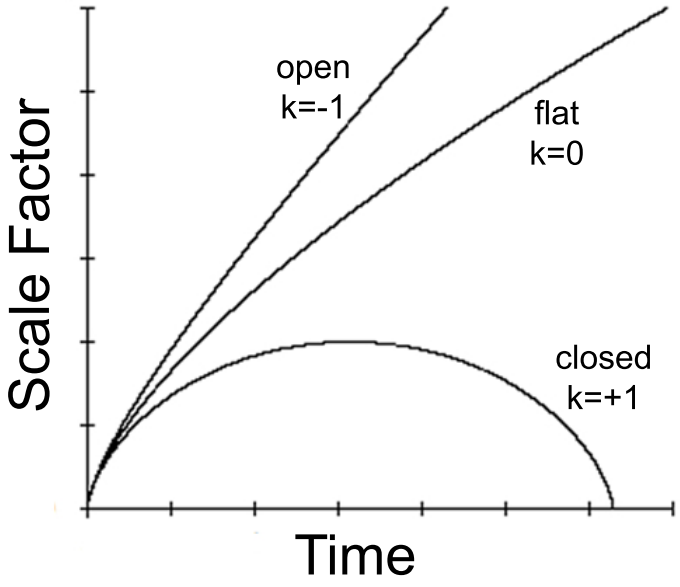

Figure 1.1: The three possible expansions of the Universe within the cosmological model with different geometries; open ($k = -1$), closed, ($k = +1$) and flat ($k = 0$), correspond to a different evolution of the scale factor and hence future fate of the universe. Image made by author.

density of the Universe. One of the proposed forms of dark energy is the cosmological constant Λ, which is thought to permeate through space with constant energy density (e.g. Peebles and Ratra 2003, Carroll et al. 1992).

The relation between the energy density and scale factor of each, can be shown to be:

$$\rho_{\rm rad} \propto \frac{1}{a^4}; \quad \rho_{\rm mat} \propto \frac{1}{a^3}; \quad \rho_{\rm DE} = \text{constant} \tag{1.7}$$

(where $\rho_{\rm mat}$ is the combined energy density of dark matter and baryons).
Figure 1.2 shows how the energy density of the particular content of the Universe evolved with time. At early times when radiation is the dominant factor, the expansion rate of the Universe and the energy density can be shown to evolve with time as;

$$a(t) \propto t^{1/2}; \quad \rho_{\rm rad} \propto \frac{1}{t^{3/2}} \tag{1.8}$$

When matter dominates;

$$a(t) \propto t^{2/3}; \quad \rho_{\rm mat} \propto \frac{1}{t^{8/3}} \tag{1.9}$$

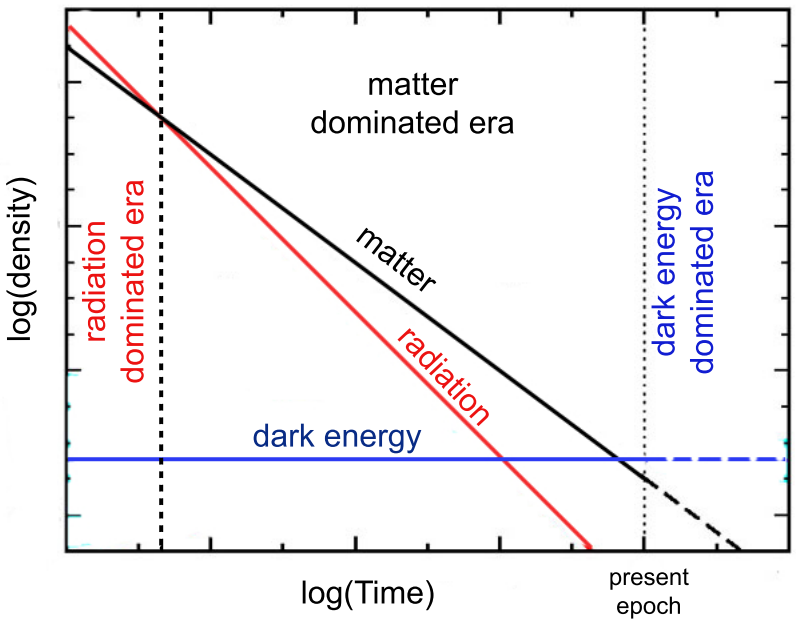

Figure 1.2: A schematic to illustrate the evolution of the energy density of radiation, matter and dark energy. The evolution of the Universe will be due to a combination of all three and the rate of expansion will depend which of the three is the dominant. Figure adapted from Frieman et al. (2008).

and when dark energy dominates;

$$a(t) \propto \exp(Ht); \quad \rho_{\rm DE} = \text{constant} \tag{1.10}$$

If we express the density parameter Ω in terms of the each constituent parts of the Universe, then for a flat Universe where the dark energy is described by the cosmological constant Λ:

$$\Omega_{\rm rel} + \Omega_{\rm baryons} + \Omega_{\rm DM} + \Omega_{\Lambda} \simeq 1 \tag{1.11}$$

where $\Omega_{\rm rel}$ is the total contribution from all relativistic particles: i.e. photons and neutrinos, $\Omega_{\rm DM}$ is the dark matter contribution and Ω_{Λ} the dark energy contribution. Recent results from the all-sky mapping of the Cosmic Microwave Background (CMB) by Planck Collaboration et al. (2016) suggest the important parameters to be;

$$\Omega_{\rm baryons} \simeq 0.0486 \pm 0.0005$$

$$\Omega_{\rm mat} \simeq 0.3089 \pm 0.0062$$

$$\Omega_{\Lambda} \simeq 0.6911 \pm 0.0062$$

$$H_0 = 67.76 \pm 0.46\,{\rm kms}^{-1}{\rm Mpc}^{-1}$$

where $\Omega_{\rm mat}$ is the combined contribution from baryons and dark matter. These are in good agreement with other probes of cosmology such as from weak lensing and the baryon acoustic oscillation (BAO), although the value for H_0 from Planck is in tension with a higher value from other recent surveys (eg. 73.24 ± 1.74 from observations of Cepheid variables and Type 1 supernova Riess et al. 2016, and 69.32 ± 0.8 from CMB observations by the Wilkinson Microwave Anisotropy Probe (WMAP) Bennett et al. 2013).

We can also define the relationship between the mass density and pressure, the **equation of state** for each of the constituent parts in the form

$$p = \omega\rho \tag{1.12}$$

where $\omega = 0$ for matter, $\omega = \frac{1}{3}$ for radiation, $\omega \leqslant -\frac{1}{3}$ for an accelerated expansion (where there are a suite of models of which $\omega = -1$ for a cosmological constant).
One of the central questions of cosmology today is to the nature of this dark energy: whether it is indeed the constant term, Λ, that Einstein wrote into his equation for general relativity (i.e. where $\omega = -1$).

1.2.5 Describing the Universe

Given the observational and theoretical evidence for the expansion, geometry and content of the Universe, we are now able to express the cosmological paradigm in a series of equations. The Friedmann equation is the most important of these as it describes how the expansion of the Universe depends upon its content, geometry and cosmological constant, and can be derived from both Newtonian physics and General Relativity and is defined as:

$$\left(\frac{\dot{a}}{a}\right)^2 = \frac{8\pi G}{3}\rho - \frac{kc^2}{a^2} + \frac{\Lambda c^2}{3} \tag{1.13}$$

where ρ is the overall density of the Universe and where for normalization purposes the speed of light c can be set to equal 1. A second important relation is the **fluid equation** which shows how the density of the material in the Universe, ρ, evolves with time

$$\dot{\rho} + 3\frac{\dot{a}}{a}\left(\rho + \frac{p}{c^2}\right) = 0 \tag{1.14}$$

With these two equations we can derive the **acceleration equation** that describes the acceleration of the scale factor.

$$\frac{\ddot{a}}{a} = \frac{-4\pi G}{3}\left(\rho + \frac{3p}{c^2}\right) \tag{1.15}$$

Since we know that the universe is not only expanding but expanding with a changing rate, we can also define a **deceleration parameter** that describes this.

$$q_0 = \frac{\Omega_{M,0}}{2} - \Omega_\Lambda \tag{1.16}$$

where Ω_M is the overall contribution from baryons and dark matter and where $q_0 < 0$ therefore implies an accelerating universe i.e. $\ddot{a} > 0$. Assuming $k = 0$, and with Ω_M ~0.3 and $\Omega_\Lambda \sim 0.7$, this gives a value of $q_0 \sim 0.55$.

The Hubble parameter H changes with time such that:

$$H(z) = H_0 E(z) \tag{1.17}$$

where H_0 is the value of the Hubble parameter today, and $E(z)$ is dependent on the underlying cosmology. In our model of a flat Universe with a cosmological constant:

$$E(z) = \sqrt{\Omega_M(1+z)^3 + \Omega_\Lambda} \tag{1.18}$$

We can now use this model to describe how distances are measured in such a Universe, as detailed more fully in Appendix A.

1.3 An Overview of X-ray Astronomy

We have been observing the Universe with telescopes for over 400 years in the optical part of the spectrum. However, it is only within in the past half-century that it has been possible to study astronomical X-rays. The Earth's atmosphere completely absorbs extra-terrestrial X-rays, and so the only way we can view them is by launching X-ray observatories into space.

Since the environment of space is hostile, the material that the detector is made from needs to be robust enough to withstand cosmic rays, work in a vacuum, as well as survive the rigours of a rocket launch.

1.3.1 X-ray Emission Processes in Astrophysics

Astronomical X-rays arise from a variety of processes each of which indicate the nature of their source.

Line Emission

In a hot gas, electrons are excited to higher level energy shells further from the nucleus of an atom. When they fall back to the lower state, a photon is emitted with energy that is the difference between the energy states. For X-ray emission, typically in a gas of $T > 10^6$K, the atom has become ionised, and the energy difference when an electron returns to its ground state is sufficient to emit an X-ray photon. The X-ray line emission is given by (e.g. Osterbrock 1974)

$$\int e_\nu^{line} d_\nu = n(X^i) n_e \frac{h^3 \nu \Omega(T_g) B}{4\omega_{gs}(X^i)} \left[\frac{2}{\pi^3 m_e^3 k T_g}\right]^{1/2} e^{-\Delta E/kT} \tag{1.19}$$

where ΔE is the difference in energy between excited and ground state, B is the branching ratio of the line, Ω the collisional strength (rather than the cosmological density parameter), $\omega_{gs}(X^i)$ is the statistical weight of the energy levels of the ion. In galaxy cluster

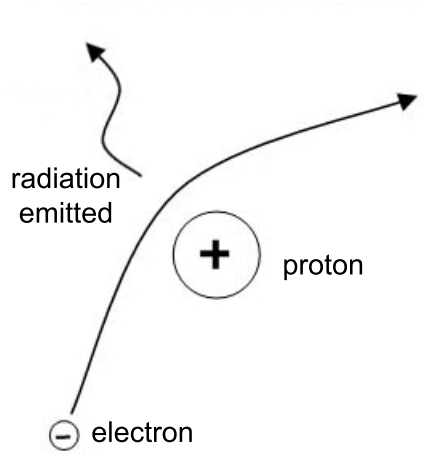

Figure 1.3: Bremsstrahlung radiation occurs when an electron's path is accelerated by an ionised particle.

and AGN astrophysics, an important and prominent line is the iron line Fe K_α line at around 6.7 keV.

Bremsstrahlung

Bremsstrahlung braking radiation occurs when an electron is accelerated in the presence of an ionised atom of a hot gas as shown in Figure 1.3. For example the intra-cluster medium (ICM) of galaxy clusters (Section 1.4.3), where $T > 3 \times 10^7$ keV, bremsstrahlung is the dominant emission process. In the ICM the emission is predominately due to the acceleration of electrons by ions of hydrogen and helium. The energy emitted per unit time, frequency and volume at a frequency ν of an ion of charge Z in a gas of temperature T is given by[1]:

$$\epsilon_\nu^{ff} = \frac{2^5 \pi e^6}{3 m_e c^3} \left(\frac{2\pi}{2 m_e k} \right)^{1/2} n_e T^{1/2} e^{-h\nu/kT} \sum_i Z_i^2 n_i g_{ff}(Z_i, T, \nu) \tag{1.20}$$

where, $g_{ff}(Z_i, T, \nu)$ is the Gaunt factor (which corrects for quantum effects).

Inverse Compton scattering

Inverse Compton scattering of low-energy photons to higher energy X-ray photons by relativistic electrons, Figure 1.4, is a process responsible for X-ray emissions from AGN (Section 1.4.2) and for the power law component of their X-ray spectra. The fractional change of energy of a photon can be shown to be:[2]

[1] from www.astro.utu.fi/~cflynn/astroII/l3.html
[2] from www.astronomy.ohio-state.edu/~ryden/ast822/week10.pdf

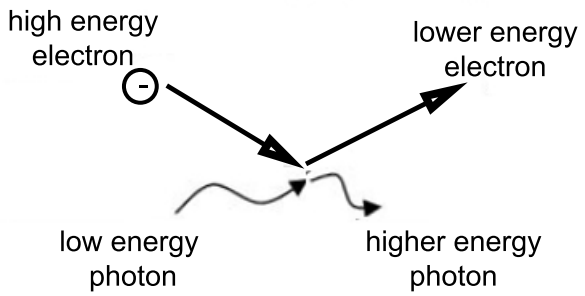

Figure 1.4: Inverse Compton of a low energy photon scattered by high energy electron, results in the increase in energy of the photon. Image by author

$$\frac{X_f - X_i}{X_i} = \frac{(\gamma_i \beta_i - X_i)(1 - \cos\theta)}{\gamma_i(1 + \beta_i \cos\theta) + X_i(1 - \cos\theta)} \tag{1.21}$$

where X_i and X_f are the dimensionless initial and final energy of photon, θ is the angle which the photon has been scattered, $\beta_i = v_i/c$ is the initial speed of the incoming electron (in units of the speed of light) and γ_i is the initial Lorentz factor of the electron. The maximum fractional energy change, therefore, for a low energy photon ($X_i \ll 1$) and relativistic electron ($\gamma_i \sim 1000$) reflected back from the direction it came ($\cos\theta = -1$) can be large enough to increase the photon energy by a factor of 10^6 and hence an ultra-violet photon can be energised in the X-ray part of the spectrum.

$$\frac{X_f - X_i}{X_i} \approx 4\gamma_i^2 \tag{1.22}$$

Synchrotron radiation

In a similar mechanism to thermal bremsstrahlung, X-rays are emitted when relativistic electrons are accelerated around magnetic field lines, Figure 1.5. In some types of AGN (Section 1.4.2) some of the X-ray energy released from the central engine is due to synchrotron emission from particles accelerated by the magnetic field of the accretion disk or associated black hole.

1.4 X-ray Sources

Of the many different types of astronomical X-ray sources, some are not relevant to this thesis. These include; planetary X-rays from within our Solar System, for example due to fluorescence from the atmosphere of Venus and Mars, or due to Jupiter's strong magnetic

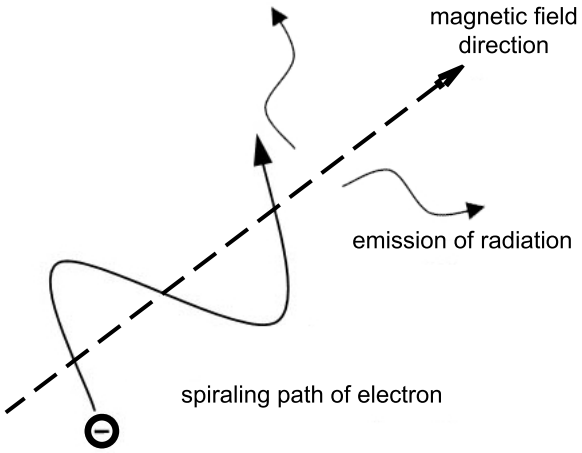

Figure 1.5: Synchrotron radiation produced by electrons spiraling along a magnetic field. Image by author.

field; Solar X-rays from the sun's corona as well as solar flares due to the magnetic field; from supernova remnants and neutron stars where X-rays are produced from the shock waves that heats the debris of the exploded star; and from binary sources where energy of in-falling matter onto an accretion disk is radiated at as X-rays.

Other sources are relevant to the projects described in this thesis and so are expanded upon as follows.

1.4.1 X-ray Background

The term X-ray background has two interpretations. The first is instrumental. This is dependent on the detector and telescope and should be accounted for when extracting image, light-curves and spectra as described in Section 2.3.2 in relation to XMM Newton. The second interpretation is astrophysical. This is the phenomenon known as the cosmic X-ray background (CXB) which is relevant to all X-ray observatories as well as to all the science projects described in this thesis. Here, we describe this second aspect in more detail.

Before the resolution of X-ray point sources was possible, it was thought that an X-ray background bathed the universe in a diffuse glow analogous to the Cosmic Microwave Background (CMB) (though the CXB was discovered two years earlier than the CMB). The original assumption was that this was due to unresolved Active Galactic Nuclei, (AGN) that were too dim to be detected as unique sources in the early X-ray instruments.

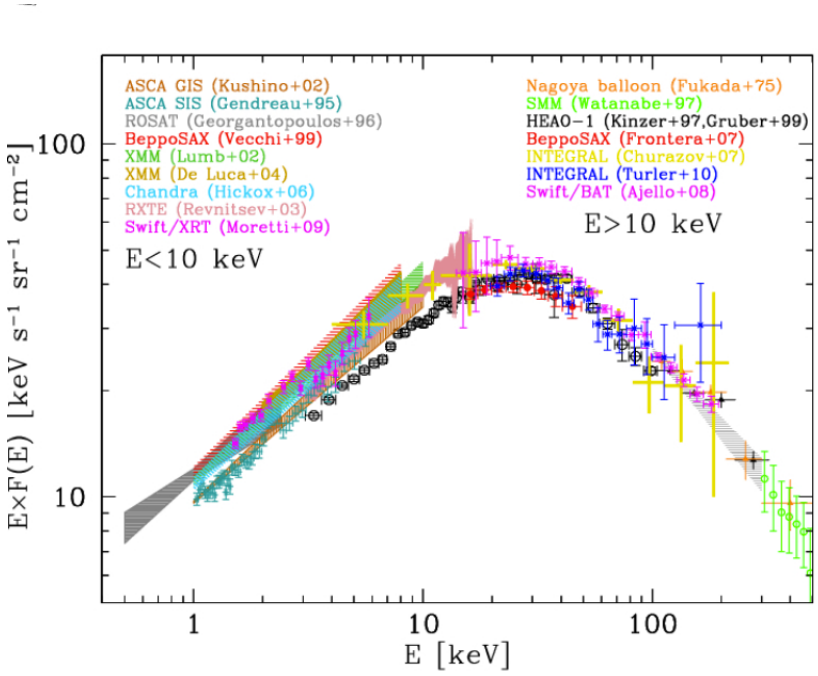

Figure 1.6: The spectrum of the CXB as measured by various X-ray observatories over the past few decades. Image from Gilli (2013).

However, the spectrum above > 1 keV from these diffuse sources did not match those of the major population of AGN. In the last 15 years or so, through deep X-ray surveys e.g. Brandt and Hasinger (2005), the XMM Newton and Chandra observatories have been able to resolve the hard band CXB into individual point sources - around half of which are attributable to galaxies, binary systems and supernovae remnants. The other half are thought to be the various classes of AGN.

In the softer band below 1 keV, the background can be attributed to discrete Galactic sources. These being i) the so-called Local Hot Bubble (LHB), (e.g. Sanders et al. 1977) which is a cavity in the interstellar medium of the Galaxy filled with hot X-ray emitting gas and ii) the Solar Wind Charge eXchange (SWCX) (e.g. Cravens 2000) which is produced when highly charged ions from the solar wind interact with neutral material.

The CXB background spectrum as measured by a variety of missions (shown in Figure 1.6) has a characteristic bell shape peaking at around 30-40 keV. In the 2-10 keV region (the area of interest to the projects described in this thesis) the slope has a power-law of around $\Gamma \simeq 1.4$ e.g Lumb et al. (2002).

1.4.2 Active Galactic Nuclei (AGN)

In this section, we review in more detail X-rays relating to the Active Galactic Nuclei (AGN), as this is central to the project as described in detail in Chapter 4.

In some galaxies, the central region outshines the rest of the combined luminosity of the stars in the galaxy with emission across all wavelengths. This emission varies in intensity on short time-scale periods of less than a day, and from this, we can infer that the cause of the emissions is the accretion of matter onto Super Massive Black Holes (SMBHs).

AGN can be classified as Type 1 and Type 2 Seyfert galaxies, Quasars, BL Lacs or Optically Violent Variables (OOVs) and Radio galaxies (both in 'broad' and 'narrow' line variety). However, all these different classes are powered by the same process of accretion onto supermassive black holes.

Seyfert galaxies are lower-luminosity AGN usually found within spiral galaxies. The type of Seyfert depends on the spectral emission lines. Type 1 Seyfert have broad lines with widths of up to 10^4 km/s as well as narrow lines with widths of several hundred km/s. Type 2 Seyferts have only narrow lines. BL Lacs have no strong emission lines with their related OVV's displaying greater variability in the optical over the shortest (less than a day) timescale. Quasars are the most luminous category of AGN, of which around 5-10% are strong radio emitting sources, and all have spectra similar to Type 1 Seyfert galaxies. Radio galaxy type AGN are all strong radio sources and are associated with giant elliptical galaxies and can also be divided into Type 1 and Type 2 in the same way as Seyferts.

The Unified model (e.g. Antonucci 1993) attempts to explain the different classes of AGN as essentially systems that we observe at different orientations to the line of sight observation. In this model, as shown in Figure 1.7, the central SMBH is surrounded by an accretion gaseous disk of a few light-days across. Further out still, at a distance of ~100 light-days are areas of fast-moving dust clouds - the so-called Broad Line Region (BLR) responsible for the broad emission lines in the spectra. At distances of ~100 light-years, is an optically thick torus of colder gas, which, if obscuring the line-of-sight will be responsible for whether the AGN is classified as Type 1 or II. (AGN types observed at viewing angles in the intersection between Type 1 and II can be labeled 1.3, 1.5, 1.8 etc depending on the angle). Further out still, at distances of ~1000 light-years is an area of

low density slow-moving dust clouds responsible for the narrow emission lines (NLR) in the spectra. However, even though the continuum in Type 2 Seyferts is also obscured at this line-of-sight, it is thought that the continuum radiation is scattered towards us from free electrons within the scattering medium. Similarly Type 1 and Type 2 quasars can be added to this scheme, with blazars defined as sources viewed directly down the jet.

A further unification scheme has been postulated to explain the difference between radio quiet and radio loud AGN as possibly being due to the spin, a, of the black hole. Radio loud AGN are due to high spin black holes, $a \sim 1$, whereas low spin, $a \ll 1$, cause radio quiet AGN.

It is important to determine the orientation and hence the type of AGN, as this is fundamental to some of the physics of the central region. For example, we may be underestimating the intrinsic luminosity of an AGN if we misidentify a Type 2 as Type 1. With a Type 1 AGN, the column density of neutral Hydrogen, $n_{\rm H}$, gas is similar to that of the Galactic value of typically less than 10^{20} cm^{-2}. This value increases to $< 10^{24}$cm^{-2} as the AGN observation angle decreases to shallower, Type 2 AGN range, though X-rays in the 2-10 keV range should have sufficient energy to pass through the torus. At even shallower angles, however, approaching an equatorial view, the $n_{\rm H}$ value of around 10^{24}cm^{-2} allows passage of only the hardest X-ray band 10-100 keV through the so-called 'Compton-thick' (CT) torus and at higher $n_{\rm H}$ values still, the (CT) torus can be invisible to even these hard X-rays, (e.g. Mathur et al. 1998) and thus make the intrinsic luminosity difficult to estimate. Brightman et al. (2017) suggest that the majority of AGN will be obscured, i.e. Type 2, and that between 20-40% will be CT. Marin (2016) review the different observables that indicate the inclination, being; $n_{\rm H}$ column density, Balmer ($H\beta$) line-width from the BLR, optical polarisation and the flux ratio within the infra-red compared to X-rays.

One further issue on classifying AGN type has been raised by the 'receding torus' model, as first noted by Lawrence (1991). This explains how we may be under-counting the number of Type 2 AGN. In this model, the torus has a constant thickness, but the distance from its inner edge to the AGN centre is dependent on the luminosity of the object. At higher luminosity this distance is larger due to the evaporation of dust at the inner radius edge by the increased UV radiation. Hence, if the height of the torus is constant, then the critical angle that the AGN's central region is observed at may be large enough to lead to

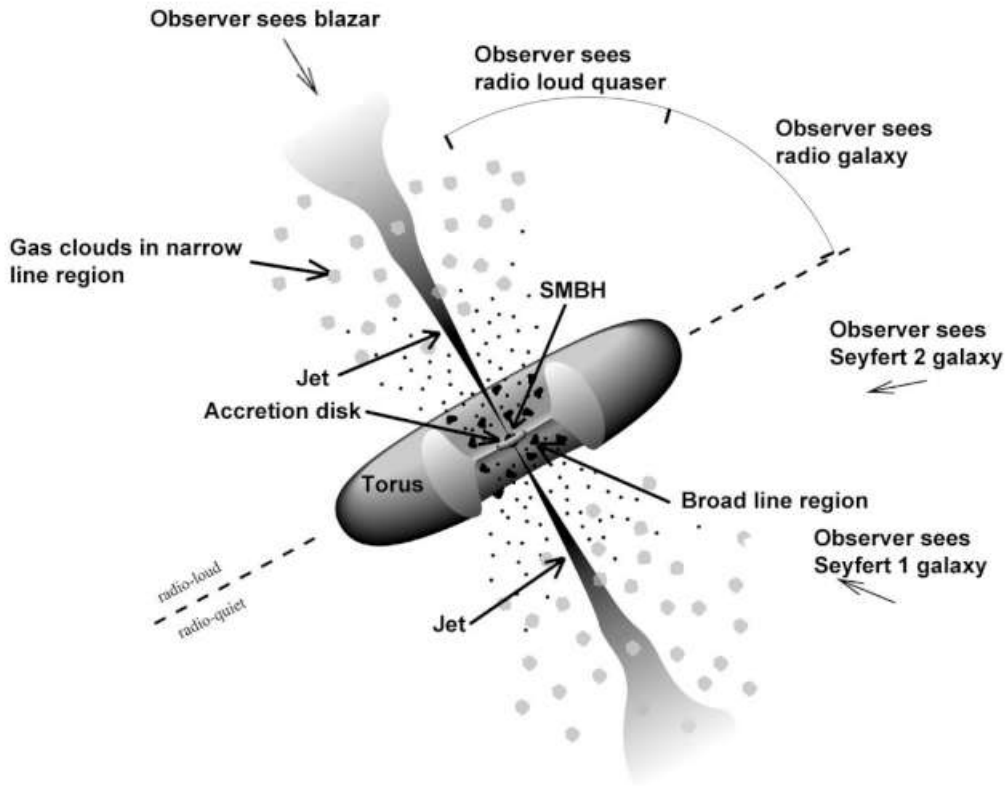

Figure 1.7: Diagram of AGN structure demonstrating Unified Model. The type of AGN depends on the orientation of the accretion disk and torus system with respect to the observer. Image from NASA. https://fermi.gsfc.nasa.gov/science/eteu/agn/

an unobscured view similar to that of a Type 1 AGN.

Since the early days of X-ray astronomy, it has been known that X-ray emissions are by far the most significant contributor to the overall luminosity of AGN, Elvis et al. (1978) and that there is a strong variability observed in X-rays over periods of hours to days. Figure 1.8 shows a typical light-curve of an AGN.

The X-ray emitting region is very compact - since variability is governed by light-crossing time - and located close to the SMBH. The mechanism, as described in Rees (1984) for the emission of the dominant hard X-rays, begins with the accretion of hot gas onto the SMBH. Matter is heated to several thousand Kelvin as it approaches the SMBH, resulting in thermal ultraviolet emission. This radiation is scattered by hot electrons within the accretion disk, thus gaining energy from an inverse-Compton effect process and emerging as hard X-rays. This *Comptonization* produces a power-law emission, with a photon index typically of $\Gamma \approx 1.7$-2.2. e.g. Nandra and Pounds (1994), George et al. (2000) and

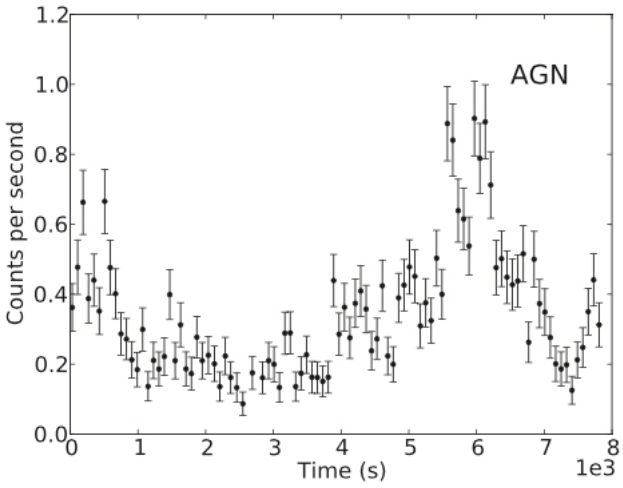

Figure 1.8: Typical light-curve for an AGN from Lo et al. (2014).

Sambruna et al. (1999). Also, X-rays at the soft end of the spectrum are thought to be produced via thermal bremsstrahlung (as described in Section 1.3.1).

1.4.3 Galaxy Clusters

Galaxy clusters are relevant to the projects in Chapter 6 (describing methods of stacking cluster spectra to search for unknown emission lines) as well as Chapter 7 (describing techniques to estimate the temperature of clusters). Here we review some of their properties. Galaxy clusters are the largest gravitationally bound objects in the Universe, consisting of hundreds, sometimes thousands of galaxies with masses ranging from $10^{13} M_{\odot}$ to $10^{15} M_{\odot}$.

Clusters can be thought of being made up of three constituent parts, the most obvious being the galactic stars themselves. Since the work of Zwicky (1933) who first derived cluster masses in 1933, we know that each galaxy exists within its own dark matter halo. Filling the space between the galaxies is a gas cloud of hot intracluster material (ICM). This gas, with temperatures of order 10^7K, is mostly ionised hydrogen and helium, but also contains heavier elements such as iron, nickel, silicon, sulphur, argon, and calcium. The relative contributions to the total mass of the cluster due to each of these components is approximately: ICM (12%), stars (1.3%) and dark matter (87%). We can observe the distribution of the ICM in the X-ray band. The X-ray emission arises mainly from thermal bremsstrahlung or *braking radiation*. This occurs when electrons change course as they speed past the positively charged intracluster ions. This acceleration generates the radiation. Figure 1.9 shows a typical cluster as seen in three wavelengths, from Allen

et al. (2011).

In Chapter 6, we use the X-ray signals from galaxy clusters to search for a hypothesised candidate for dark matter, the 'sterile-neutrino'. If it exists, it would reveal itself through an emission line in the cluster spectrum which isn't due to the known astrophysics of the ICM.

Being the largest gravitationally bound structures in the Universe, clusters are representative of the Universe as a whole. Having reached virial equilibrium if one were to 'scoop' out a sample of cluster material then one should be able to sample a fair representation of that constituent part of the Universe. Thus, clusters are excellent cosmic laboratories for testing theoretical models of content, structure formation and galaxy evolution over cosmological time.

Estimating cluster mass across redshift, for example, allows us to study their evolution and that of large-scale structure and matter in the Universe.

One of the proxies for cluster mass is the temperature of the ICM gas. Vikhlinin et al. (2006), Mantz et al. (2010) and Mantz et al. (2016) for example predict that this scales with the total mass of the cluster as $M \propto T^{3/2}$.
A simplistic yet valid approach to this relationship starts with the assumption that an isolated cluster containing only dark matter particles follows the virial relation:

$$2K + U = 0 \tag{1.23}$$

where K is the kinetic energy and U the potential. Within a spherical radius R_Δ the total mass M_Δ, where Δ is the over density factor as compared to the critical density ρ_c, is

$$M_\Delta = \frac{4}{3}\pi\Delta\rho_c R_\Delta^3 \tag{1.24}$$

The total kinetic energy is simply the sum over all the individual particles within R_Δ

$$K \propto M_\Delta T \tag{1.25}$$

The potential energy is given by,

$$U \propto \frac{GM_\Delta^2}{R_\Delta} \tag{1.26}$$

Figure 1.9: Images of Abell 1835 in X-ray (left), optical (centre), and millimeter (right) wavelengths, demonstrating the multi-wavelength morphology of a massive, dynamically relaxed cluster. Image from Allen et al. (2011).

and so,

$$M_{\Delta}T \propto \frac{GM_{\Delta}^{2}}{R_{\Delta}} \tag{1.27}$$

After combining and re-arranging we find

$$M_{\Delta} \propto T^{\frac{3}{2}}\rho^{-\frac{1}{2}} \tag{1.28}$$

Hence finding the temperature of a cluster is a hugely important tool when estimating cluster mass, and this is something that is central to work described in Section 7.2.

1.5 Overview of Transient Phenomena in Astrophysics

Astronomy in the time-domain arena has experienced a revolution over the past couple of decades. Astronomers are able to detect and monitor transient events with a high cadence across the electromagnetic spectrum, as well as new methods (e.g. that use gravitational waves or neutrinos). New facilities, observing in complementary parts of the waveband, permit new science. This enhances our understanding not just of the astrophysics involved in extreme events, but also, as in the case of Type 1a supernova, of cosmology itself. Observatories that are currently searching for transients include; the Low-Frequency Array for radio astronomy (LOFAR van Haarlem et al. 2013), Gaia (Gaia Collaboration et al. 2016) which has been surveying the whole sky in the optical waveband since 2014, Swift (Gehrels et al. 2004) detecting GRBs since 2004, and, in the X-ray part of the spectrum, the Monitor of All-sky X-ray Image (MAXI Matsuoka et al. 2009) which performs a full-sky survey every 96 minutes.

Figure 1.10 shows the phase-space of typical transient events from X-ray (upper image) and optical (lower image) observations.

A useful definition of a transient event is one where the flux arises above a background and eventually fades away, as opposed to a source whose flux varies periodically (e.g Cepheid variables). The transient duration ranges from fractions of secs, as in the case of gamma-ray bursts (GRB), to weeks in the case of supernovae.

Most catastrophic transient events mark the death of stars, e.g. GRBs from supernova . Other catastrophic events are caused by the merger of discrete compact objects, e.g. merging black holes or neutron-star black hole merger.

Other events include the occasional cataclysmic violent outbursts of stars (usually in a close binary system) caused by thermonuclear processes. Within our Galaxy, flares from M dwarf stars and recurrent novae are also classed as transient.

1.5.1 Recent Developments

New observatories

In the coming few years, new observatories will further add to our knowledge of transient sources and astrophysics. These include; the Square Kilometre Array (SKA Dewdney et al. 2009) which will be the largest radio telescope when operational in 2020, The Large Synoptic Survey Telescope (LSST Tyson 2002) which will photograph the available sky every few nights from 2019, and a new X-ray all sky survey by the extended Roentgen Survey with an Imaging Telescope Array (eROSITA Predehl et al. 2010) from 2018.

Gravitational waves

Recently, the first detections of gravitational waves (GW) have also allowed us to observe transients in the Universe, so heralding a new era in astronomy. The first detection, Abbott et al. (2016), on 14th September 2015, of the merger of stellar-mass binary black holes was confirmed by the advanced Laser Interferometer Gravitational-Wave Observatory (LIGO) located at Livingstone and Hanford. Since then a further six GW signals have been detected, the most recent being the first neutron star merger Abbott et al. (2017).

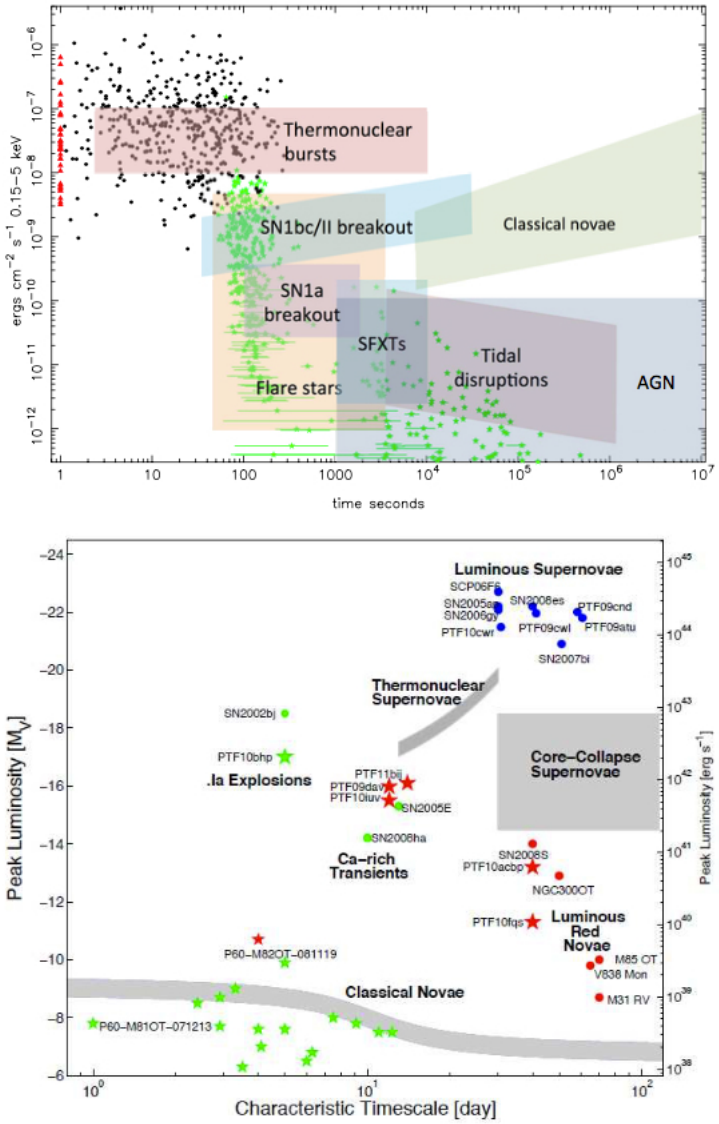

Figure 1.10: Upper: the typical observed X-ray flux plotted against variability timescale for a variety of source types (colour shaded regions) and for the prompt and afterglow fluxes for GRBs detected by the Swift mission (individual points). Black points are Swift BAT GRBs (with the T90 $<$ 1 sec in red), green points are Swift XRT GRB afterglow fluxes. Lower: shows the optical phase space of cosmic explosive events and their characteristic timescales. Image and caption from O'Brien and Smartt (2013).

Neutrino Telescopes

Still very much in its infancy, neutrino telescopes such as IceCube Neutrino Observatory IceCube Collaboration et al. (2006) in Antarctica, and Astronomy with a Neutrino Telescope and Abyss environmental RESearch Ageron et al. (2011) (ANTARES), 40 km offshore France, allow for another new way of detecting transient events.
Interactions of protons with matter will produce mesons and when these decay, neutrinos are yielded. Detection of such a burst of neutrinos, originating from the same direction and occurring withing a defined time period, may therefore be due to an astrophysical process that generates high energy neutrinos in this way (e.g. GRBs, X-ray binaries and supernova). This detection, unlike satellites observing in the electromagnetic spectrum cover the whole celestial hemisphere, so follow-up surveys in the optical, radio, X-ray or gamma-wave band can reveal more about the nature and location of the transient.

Fast Radio Bursts

Fast radio bursts, (FRBs), are radio pulses which last only a few milliseconds and were first discovered in 2007 Lorimer et al. (2007). Of the 26 that have been detected to date, only one (FRB 121102 Spitler et al. 2014) has been observed to repeat. The astrophysical origins are currently unknown, though theories range from them being magnetars Popov and Postnov (2010) (highly magnetized neutron stars) experiencing outbursts related to magnetic field events, to being focused artificial signals suggesting an extraterrestrial intelligence Lingam and Loeb (2017).

1.5.2 X-ray Transients

We summarise transient events that are detected in the X-ray part of the spectrum, as these are most relevant to this thesis.

Most point-like X-ray sources display a degree of periodic variability in flux and changes in their spectrum over a regular period. The nature of this variability gives valuable clues as to the emission physics involved and identification of the source itself.

Sources, where the variability can be considered as aperiodic or inherently stochastic, are dominated by active galactic nuclei (AGNs) which are thought to be associated with 10% of all super-massive black holes (SMBHs), and are central to the project described in Chapter 4.

Large variations in fluctuations can be ascribed to transient sources and include; GRBs, stellar flares, transient X-ray binaries (i.e. black holes, neutron stars and white dwarfs accreting matter from their stellar companion), supernova remnants and X-ray flashes (XRF) - which are central to the project described in Chapter 5. We briefly describe each of these sources below:

X-rays flash (XRF)

If AGN are the most common of extra-galactic point sources, then some of the rarest are transient events labelled X-ray flashes (XRFs). In Chapter 5, where we describe their properties in more detail, we use the XCS source catalogue (see Section 2.3) as a serendipitous search for XRFs and estimate an upper limit on their occurrences.

Gamma-ray bursts (GRB)

Among the most short-lived transient phenomena are gamma-ray bursts, with duration from milliseconds to a few minutes. Shining hundreds of times brighter as a supernova, they are thought to occur when matter collapses onto a black hole. Two classes of GRB have been defined. Short-duration, less than 2 secs, GRBs are caused by merger of either two neutron stars or a black hole and neutron star. Long duration, up to a few minutes, GRBs are associated with supernova. X-ray rich GRBs show an abundance of X-rays and sometimes the X-rays dominate the emission. In Chapter 5 we differentiate between X-ray transients associated with GRBs and those, including XRFs, that are not.

Stellar flares

Closely related to the mechanism that produces solar flares, stellar flares are also a manifestation of a sudden burst of magnetic energy in the star's corona. These, however, have shown more extreme luminosities than solar flares, sometimes by several orders of magnitude with a duration of more than an hour. Although not the focus of any project outlined in this thesis, in Chapter 5 we see that when we trawl the archives for a class of fast variable sources known as X-ray flashes (XRF), we sometimes 'reel in' a stellar flare event into our 'net'.

X-ray binaries

A neutron star can capture matter from a nearby normal companion star which it is close orbit around. This matter will form an accretion disk around the neutron star and as the matter falls towards the neutron star will gain huge amounts of energy. Much of this will be radiated away at X-ray energies. As the neutron star rotates X-ray pulses are produced. A black hole stellar binary system produces X-rays in the same way.

Supernova remnants and neutron stars

Supernova are some of the most violent events in the Universe occurring when a star blows apart. The explosion creates a remnant of multi-million degree gas that shines brightly in X-rays for thousands of years. X-rays are produced by the forward shock wave and reverse shock wave that heats the debris of the exploded star. All that then remains of the original star is a super-compact neutron star, or if the star was particularly massive, a black hole. As well as the supernova remnants, X-rays are also produced due to free electrons moving in the strong magnetic field of the neutron star.

1.6 X-ray Source Detection

When detected, astronomical X-ray photons carry four pieces of information. These are: i) where the photon came from, ii) the time it arrived, iii) the energy of the photon and iv) the polarisation state of the photon.The type and specifications of the detector therefore depends upon which of these factors are relevant to the study.

1.6.1 Proportional Counters

Proportional counter detectors are the most simplistic X-ray detector used on the earliest X-ray satellites (e.g. Uhuru and ROSAT). Working along the same method as a Geiger counter, though operating at a lower voltage, a proportional counter is a box of inert gas with a high voltage wire through the centre and a plastic window that keeps the gas within the box while admitting X-ray photons. The X-ray photon entering the chamber ionises the inert gas producing an ion pair. Any leftover kinetic energy from this interaction will be used by the primary photo-electron to ionize further atoms of the inert gas. Together these primary and secondary electrons accelerate towards the high voltage wire, ionising further gas ions and, in a short time, an avalanche effect is set up. The voltage of the anode

is tuned to make the amplitude of this charge pulse proportional to original incoming X-ray photons. In this way, a proportional counter can be thought of as a basic spectrometer.

A variation is the gas scintillation proportional counter as used for example on EXOSAT (the GSPC) and ASCA (the gas imaging spectrometer GIS) and BeppoSAX HPGSPC. It works similarly to the proportional counter unti the charge collection stage. Instead, atoms of gas, typically xenon, in a scintillation region are excited by the avalanche of primary and secondary electron and emit an ultraviolet photon which is in turn detected by photomultiplier tubes.

The energy resolution of a GSPC is around 7% at 6 keV, twice as good an energy resolution as that of ordinary proportional counters. For energies below 10 keV, charge-coupled devices CCD have now superseded GSPCs.

1.6.2 Microcalorimeters

X-ray microcalorimeters work by measuring the change in the temperature of a material when an X-ray photon is absorbed, with the change in heat proportional to the energy of the photon. Microcalorimeters effectively count individual photons and have an excellent energy resolution of a few eV or better at 6 keV. However because of the high sensitivity these devices need a complex cryogenic system to keep the temperature of the detector cooled to a few tens of mK.

The first space-based calorimeter launched on the Suzaku observatory failed before any observations were made due to the loss of the cryogenic liquid-helium.

1.6.3 Charge Coupled Devise

Charged-coupled devices, CCDs, have revolutionised astronomical detectors over the past 50 years and are now ubiquitous in detectors around the world. Although initially used in optical cameras, it was soon recognised that, with some optimising, CCDs were also sensitive to X-ray radiation. The main advantage of CCDs is their sensitivity and near linear response to brightness. At its simplest, a CCD is an integrated circuit of pixels, each essentially a light-sensitive capacitor, which is printed on a silicon surface. An X-ray photon that hits the silicon substrate releases free electrons through the photo-electric effect and the charge is stored in the adjacent pixel. By linking (or ‘coupling’) each pixel

to the next, this stored charge can be transferred from pixel to neighbouring pixel and eventually to a readout amplifier where it is digitised. The capacitor pixels come as either metal-oxide-semiconductors (`MOS`) or as a p-n (`PN`) junction. In XMM Newton there are both types, one `PN` detector and two `MOS` detectors.

CCD cameras in optical astronomy rely on a much longer frame time to accumulate many thousands of photons, and hence the energy of an individual photon cannot be independently measured. With X-ray detectors, however, the CCDs are mainly operated in a photon-counting mode where the fast frame times and low rate of flux allow the energy and position of individual X-ray photons to be determined. This allows for accurate spectroscopy which is ultimately dependant on the frame time and readout time of the detector.

While it is beyond the scope of this thesis to go too much into the technical details of CCD operation, there are some features and principles that we note now that are useful as to how CCDs perform and the effect they may ultimately have on output data.

Quantum efficiency, (QE), is a function of photon energy and describes the probability of a photo-electron being released by a photon. It is dependent on the properties of the silicon substrate material as well as factors such as whether optical blocking filters are used. QE can be improved by back-illumination as well as adding anti-reflection coating.

Noise Response is a combination of individual sources such as thermally generated 'dark-current' and readout noise. Ideally, we need these to be as low as possible so as not to affect the dynamic range of the CCD.

Pile Up and Out-of-Time events. Pile-up occurs if more than one photon is incident on the same pixel during the frame time resulting in a larger inferred energy for that event. Related to this are out-of-time events, incident photons that are detected during the read-out time phase of the detector as the frame image is being transferred to the readout. These appear as streaks across an image.

Background Effects are detected photons that are not part of the object of interest. They are due to other astrophysical processes (e.g. solar flares) or to emissions of photons as a result of interactions between radiation and the satellites and instruments themselves.

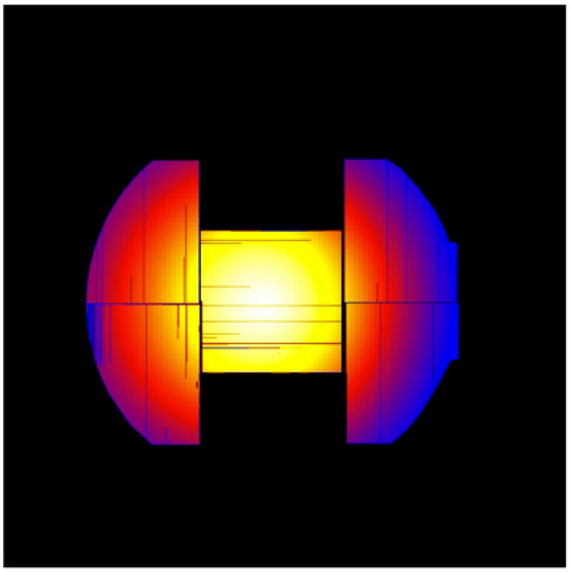

Figure 1.11: Exposure map of the MOS1 detector showing the exposure map after damage to chips 6 and 3. Image from ESA, XMM-Newton. www.cosmos.esa.int/web/xmm-newton/mos1-ccd3

Chip and Pixel damage from micrometre sized particles that impact the CCD will have a varying effect on the detector ranging from defects to individual pixels to long-term damage and failure to whole CCD chips. Such damage occurred to XMM Newton MOS1 in March 2005 and again in December 2012 resulting in failure of chips 6 and 3 respectively, shown in Figure.1.11.

1.7 X-ray Telescope Optics

Having looked at X-ray detectors, we now turn our attention to the optics and specifically the use of grazing incident mirrors that focus the X-ray photons onto the detector. Unlike an optical telescope which focuses the photons by use of either a mirror or lens at near normal incident angle to the radiation, X-ray radiation is much more energetic such that photons would simply pass straight through a mirror.

To overcome this, X-ray telescope mirrors reflect photons that are incident at a very shallow grazing angle as shown in the left of Figure 1.12, typically from $10'$ to 2 degrees. These grazing incident mirrors are commonly known as Wolter Type 1, II and III mirrors depending on the configuration of the mirrors after Hans Wolter who first outlined how

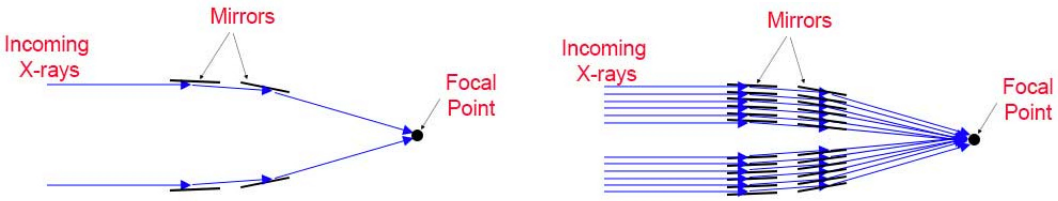

Figure 1.12: Left. Cut-away diagram of an X-ray telescope with one set of mirrors demonstrating how the incoming X-ray photons reflect off the two mirrors with a grazing incidence to be focused at the focal point. Right, By nesting the mirrors, more photons are focused. Image from Imagine the Universe, NASA. https://imagine.gsfc.nasa.gov/science/toolbox/xray_telescopes1.html

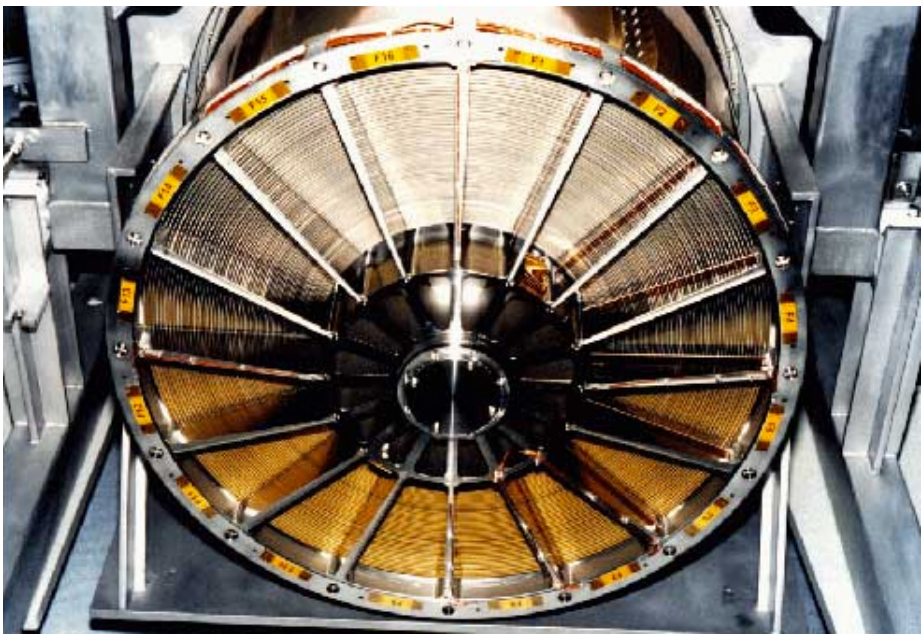

Figure 1.13: Photograph of one of the three Wolter I nested mirrors on the XMM-Newton telescope. Photon from D. de Chambure, XMM Project

X-ray telescopes could work (Wolter 1952).

Nesting many grazing mirrors within each-other, like layers of an onion allows for as many photons as possible to be focused and ultimately detected as shown in Figure 1.12 (right). XMM-Newton (as well as the other current major X-ray observatories, Chandra, Swift and NuStar) use Wolter Type-I X-ray telescopes. Figure 1.13 shows the XMM-Newton nested mirrors in one of the three telescopes.

1.8 The XMM-Newton Observatory

Since the science projects described in this thesis use data taken from XMM-Newton, we describe this satellite and its detectors in more detail here. Weighing 3.8 tonnes and at 10metres long, the X-ray Multi-Mission Newton Satellite is the biggest scientific satellite ever built in Europe, and its telescope mirrors are among the most powerful ever developed in the world. It launched on December 10th 1999 as part of the European Space Agency's Horizon 2000 Science Programme. Its goal has been to make long uninterrupted exposures to provide highly sensitive observations in the X-ray part of the spectrum to study a range of astronomical phenomena from black holes to clusters of galaxies. The spacecraft has a three-axis stabilisation system to deliver an accuracy of one arcsecond in pointing.

1.8.1 Mirrors

There are three nested Wolter I grazing incident mirror telescopes on-board XMM Newton, each with 58 nested mirrors, a focal length of 7.5 metres and diameter of 70 cm. The on-axis effective area for each of the three telescopes is around 1550 cm^2 at 1.5 keV which compares with an effective area of 800cm^2 for NASA's Chandra satellite.

1.8.2 Instruments

XMM Newton has five X-ray imaging cameras and spectrographs, and an optical monitoring telescope.

The European Photon Imaging Camera (EPIC)

European Photon Imaging Camera (EPIC) comprises of three cameras, one at the primary focus of each mirror module and behind a six-position filter wheel. It was designed and constructed by a consortium of ten institutes in four nations. All three detectors are advanced Charge-Coupled Device cameras capable of detecting rapid variations in intensity. One of the cameras uses a p-n semiconductor developed by the Max Planck Institute of Extraterrestrial Physics in Garching and the Astronomical Institute in Tbingen, both in Germany. The other two are MOS based semiconductors developed and built at the University of Leicester's Space Research Centre. They have a superior Point Spread Function (PSF) to the PN detector, though a lesser energy resolution. The radius the EPIC detectors is $16'$.

The PN detector is comprised of four quadrants of three individual CCD units each of 200x64 pixels of 4.1x4.1″ pixel size. The Full Width Half Maximum (FWHM) energy

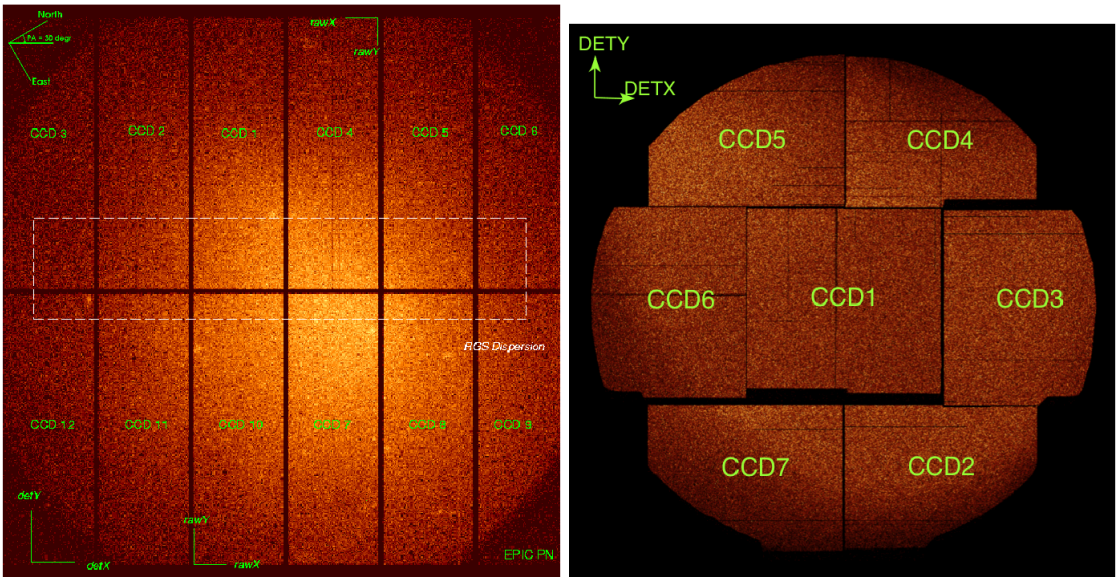

Figure 1.14: Layout of the chips on the EPIC detectors. Left is the PN detector and right, the MOS2 detector (MOS1 follows a similar layout). Images from XMM-Users handbook.
https://xmm-tools.cosmos.esa.int/external/xmm_user_support/documentation/uhb/moschipgeom.html
https://xmm-tools.cosmos.esa.int/external/xmm_user_support/documentation/uhb/pnchipgeom.html

resolution of the PN detector is currently 70 eV at 1 keV and 150 eV at 5 keV, degrading by 2.5eV a year. The MOS detectors are comprised of seven individual CCD units (six arranged around a central CCD) each of 600x600 pixels of 1.1″x1.1″ pixel size. The FWHM energy resolution of the MOS detectors are 100 eV at 1 keV and 170 eV at 5 keV. The chip layout on both types of detector are shown in Figure 1.14

We use data from the EPIC detectors in all the projects described in this thesis.

Pointing Mode

Different pointing modes can be used depending on the particular observation and science being undertaken. These affect the CCD read-out time as well as specifying which part of the detector will be read. For example in full frame modes, all the PN and MOS CCDs are read out and thus the full FOV is covered. In partial window mode, a portion of the central CCD of both MOS cameras that is active can be read out (in small window mode an area of 100 x 100 pixels and in large window mode an area of 300 x 300). In the PN camera, the large window mode selects half the area of all 12 CCDs as active and in small window mode, only the part of CCD0 in quadrant 1 at the focal point is used to collect data. In timing mode, the image is collapsed into one dimension which allows time resolution for

example in the PN detector to as fast as 0.03 ms. We use full window mode for the projects described in this thesis.

Filters

Each of the EPIC cameras has a series of **thick, medium** and **thin** filters that can be used to block optical, UV and near infra-red light. These are important if there is a possibility that the X-ray signal becomes contaminated by these photons that impede the analysis of X-ray photons. The choice of filter depends on the astronomical target being observed e.g. an object with a high optical flux may result in the X-ray photons being contaminated with optical photons - and its use will have an affect at the soft end of the X-ray spectrum.

The Reflection Grating Spectrometer (RGS)

Two of XMM-Newton's three mirror modules are equipped with an RGS grating array that disperses about 40 percent of the light to an RGS detector in a secondary focus. The RGS is not used for the work presented in this thesis.

The Optical Monitor (OM)

An optical/ultraviolet telescope, co-aligned with the main X-ray telescope, gives the XMM-Newton mission a multi-wavelength capacity. The OM is not used for the work presented in this thesis.

1.8.3 XMM Science Archive

Based in Villafranca in Spain since 2002, the XMM-Newton Science Archive (XSA) provides public access to all data from the XMM-Newton mission including including all the raw Observation Data Files (ODF), Slew Data Files (SDF), and Processing Pipeline System (PPS, which produces cleaned event lists, images and exposure maps) as well as all calibration files. The XSA is where we take our input data for all the projects described within this thesis.

1.9 Other X-ray Observatories

Alongside XMM-Newton, three other major observatories are currently in orbit taking data in the X-ray part of the spectrum. These are the latest in a long line of X-ray satellite

Satellite	Mirror PSF	FOV	Energy Range	AE	Energy resolution
	FWHM	diameter		at 1 keV	at 1 keV
	[arcsec]	[arcmin]	[keV]	[cm^2]	[eV]
XMM Newton	6	30	0.15-12	4650	50(EPIC)
Chandra	0.2	30	0.1-10	555(ACIS-S)	∼50
ROSAT	3.5	40 (HRI)	0.1-2.4	400	500
ASCA	73	22	0.5-10	350	100
Suzaku	n.a	17 (XRT)	0.2-600	1760(XIS)	50
RXTE	na	60	2-250	na	na
Swift	8.8	24	0.2-10 (XRT)	133.5	70
NuStar	17	13	3-79	na	na
AstroSat	<4	41.3(SXT)	0.3-8.0	200	na
eROSITA	∼ 28	60	0.3-10	1365	n.a
Athena	∼ 2.5	40(WFI)	0.2-12	15000	2.5
Hitomi	n.a	38(SXI)	0.4-12	160(SXS)	<7(SXS)

Table 1.1: Comparison between performance of XMM Newton and other previous, current and future X-ray observatories as summarised in the text.

that includes EINSTEIN (Nov 1978 to Apr 1981), ROSAT (Jun 1990 to Feb 1999), ASCA (Feb 1993 to Jul 2000) RXTE (December 1995 to January 2012). The performance of XMM-Newton in comparison to some of the more recent, current and future missions is summarised in Table.1.1 and Figure 1.15.

1.9.1 Chandra

When launched in 1999 Chandra was a new generation of X-ray mission (the other being XMM-Newton) which enormously improved the capabilities of earlier X-ray satellites. Chandra operates in a similar energy range to XMM-Newton (0.1-10.0 keV). It has better on-axis spatial resolution than XMM-Newton with a FWHM PSF of 0.6″, but a smaller effective area of around 555 cm^2 for its ACIS-S detector. Originally a five-year mission, Chandra is still on-going and providing outstanding science e.g. Schwartz (2014).

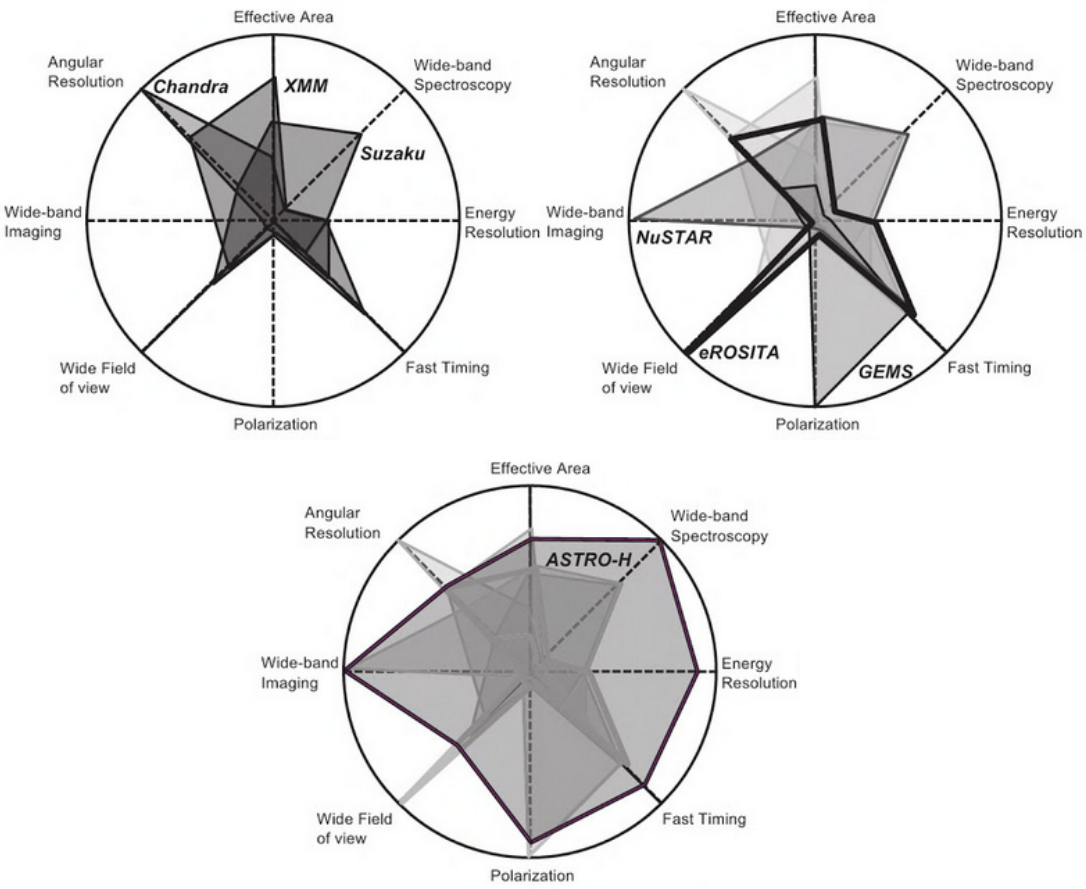

Figure 1.15: Comparison of features between recent and future X-ray observatories. Note that GEMS was a proposed mission canceled by NASA in 2012, ASTRO-H was the original name for the HITOMI mission. Image adapted from Terada and Dotani (2010).

1.9.2 AstroSat

AstroSat was launched in 2015 by the Indian Space Research Organisation (ISRO) and is India's first multi-wavelength observatory. Its goals are the detection and study of new X-ray transients, studies of X-ray binaries, AGN, SNRs, galaxy clusters, and the variability of periodic and non-periodic X-ray sources. Its X-ray detectors include the Soft X-ray Telescope (SXT) operating in the 0.3-8 keV range and the Cadmium Zinc Telluride Imager (CZTI), which detects X-rays in 10-100 keV range.

1.9.3 Swift

Launched in November 2004, Swift is a multi-wavelength observatory whose primary goal is the study of Gamma Ray Bursts (GRBs). Of the three instruments onboard, an X-ray telescope takes images and spectral data of GRB afterglow in the 0.3-10 keV X-ray part of the spectrum. When not detecting and following up observations of GRBs, Swift serves as a general purpose observatory that can be used as a fast response detector of transient events such as supernovae. Originally planned as a two-year mission, Swift detected its 1000th GRB in October 2015 and is still currently operational.

1.9.4 NuStar

The Nuclear Spectroscopic Telescope Array (NuStar) mission was launched in June 2012. Operating in the 3-79 keV range, far beyond the range of XMM-Newton and Chandra, its primary goal is a census of collapsed stars and black holes as well as observing supernova and providing data to understand how stars explode leading to the synthesis of elements. Its mission has recently been extended to 2020.

1.9.5 Recent Observatories

As well as these current missions, the missions of two other X-ray observatories have recently ended.

Suzaku

Suzaku was a joint JAXA and NASA mission launched in July 2005 until August 2015 and operated in a wide energy band (0.2-600 keV).

Hitomi

Hitomi was a short-lived JAXA mission, launched on 17th February 2016 but lost the following month on 26th March after a malfunction of the attitude system. Its goal was to explore large-scale structure and the evolution of the Universe with two telescopes providing high-resolution spectroscopy in an energy range of 0.4-12 keV.

1.9.6 Future Observatories

With XMM-Newton and Chandra outliving their original mission lengths several times over and the failure of Hitomi, there is a pressing need for new generation of X-ray observatories.

eROSITA

The next major detector is eROSITA Predehl et al. (2010). Due for launch in 2018, the extended Roentgen Survey with an Imaging Telescope Array and will be the main instrument on the Russian satellite Spektrum-Roentgen-Gamma (SRG). It will be the first X-ray all-sky survey since ROSAT in the 1990s and will observe at X-ray energies between 0.3-10 keV. Consisting of seven identical Wolter-1 mirror modules, eROSITA is based on the same pn-CCD technology of XMM, but with smaller pixel size (75μm, compared to 150μm), better energy resolution (138 eV at 6 keV, compared to $\sim$ 150 eV at 6 keV) and a larger field of view (1.03° diameter, compared to 0.5°). eROSITA will carry out an all-sky survey (known as eRASS) over 4-years. The survey will be composed of 8 successive passages over the entire celestial sphere. Its goals include the observation of more than 100,000 galaxy clusters that will be used to refine estimates of cosmological parameters and aid our understanding of dark energy, as well as to detect around three million AGN.

ATHENA

Slightly further on the horizon is the Advanced Telescope for High ENergy Astrophysics (ATHENA) Nandra (2011), Barcons et al. (2012) which was selected by ESA as the X-ray observatory mission within its Cosmic Vision 2015-2025 programme and due to be launched in 2028. Operating in the 0.5-12 keV range, it will offer unprecedented spectroscopic and imaging capabilities in its goals to track the growth of large scale structure and a complete census of black hole growth in the Universe.

1.10 Chapter Summary

In this Chapter, we have defined the current cosmological model and definitions of cosmological distances. We have reviewed X-ray astronomy with a focus on the astrophysical processes that are central to the projects in the following chapters, these being AGN (Chapter 4), XRFs (Chapter 5) and galaxy clusters which are used to find evidence of the dark matter candidate, the sterile neutrino (Chapter 6), as well as highlighting other contributed work (Chapter 7).

We have summarised how X-ray satellites detect X-ray photons, what information they can tell us about astrophysical objects and highlighted the XMM-Newton observatory from where we take our raw data.

To turn that data into information and information into knowledge, in the next chapter we introduce the XMM Cluster Survey (XCS). We will summarise its source detection pipelines alongside the software, calibration considerations and methods used throughout the projects.

Throughout the science projects described in this thesis we take the cosmological parameters to be $H_0 = 70\text{km}^{-1}\text{Mpc}^{-1}$, Ω_Λ=0.73 and $\Omega_\text{M} = 0.27$ (following Lloyd-Davies et al. 2011)

Chapter 2

Software and Data Analysis

In this chapter, we describe the software and data analysis techniques used across the projects. In Section 2.1 we summarise the suite of software extensively used throughout and in Section 2.2 we describe XMM-Newton instrument specific calibrations. 2.3 introduces the XMM-Cluster Survey (XCS) and describes in detail how data taken from XMM-Newton is reduced by the pipelines and used in the projects to detect sources and to generate images, spectra and light-curves.

2.1 Software

All of the pipelines and stand-alone routines used to reduce and analyse the data throughout the projects in this thesis make use of the following software:

2.1.1 SAS

The Science Analysis Software (SAS)[1] developed by the XMM-Newton Survey Science Centre (SSC) is a bespoke suite of software designed to reduce and analyse XMM-Newton data. Using SAS, either by the command line or by a GUI, the user can browse the content of the Observation Data Files, `ODF`, as well as find and view XMM-Newton calibration files, generate good time interval (`gti`) files, create `EPIC` detector clean event lists and hence images of observations, light-curves and spectral data files. SAS makes use of many tasks native to the High-Energy Astrophysics (`HEASOFT`) suite of X-ray software which includes `CFITSCIO`, `FTOOLS` and `FV` to manipulate and view `.fits` files. SAS version 14.0.0 is the most up to date version used on the projects described in Chapters 4 and 5 of this thesis with earlier versions used for work described in chapter 7

[1] https://www.cosmos.esa.int/web/xmm-newton/sas

2.1.2 XSPEC

XSPEC[2] is used extensively to analyse spectral data. It takes as input the source spectrum and background data files, along with the auxiliary response file, (`arf` described in Section 2.2.2), and redistribution matrix file (`rmf`, described in 2.2.4). With these it fits an X-ray source to a particular model. It outputs the goodness of the fit, with a choice of χ^2 or Cash statistic as well as the best-fit parameters of the model used with uncertainties on these values. XSPEC can be run from the command line although pipeline scripts are also written in the `TCL` programming language. XSPEC 12.8.2 is the version used on the projects described in Chapters 4, 6 and 5, with earlier versions used for the other work described in Chapter 7.

2.1.3 TOPCAT

TOPCAT[3] is a standalone astronomical tool for manipulating tables of data. It allows the user to read in tables, in a number of formats, from various sources and to inspect and manipulate them. For example, one powerful tool allows the user to query existing catalogues of astronomical data via the online `VizieR` catalogue and quickly cross-match the position of each source with their own table of data. Version 4.3 is used throughout.

2.1.4 SAOIMage DS9

SAOIMage DS9[4] is a stand-alone astronomical imaging and data visualization application. It allows the user to make and manipulate FITS images, as well as creating and layering regions of interest. Version 7.2 is used throughout.

2.1.5 CDS Portal

CDS[5] is the Strasbourg astronomical Data Center and is dedicated to the collection and worldwide distribution of astronomical data and related information. It hosts; the `SIMBAD` astronomical database, for the identification of astronomical objects; `VizieR`, the catalogue service for the CDS reference collection of astronomical catalogues and tables published in academic journals; and the `Aladin` interactive software sky atlas.

[2] https://heasarc.gsfc.nasa.gov/xanadu/xspec/
[3] http://www.star.bris.ac.uk/7Embt/topcat/
[4] http://ds9.si.edu/site/Home
[5] http://cds.u-strasbg.fr/

2.2 Analysing XMM-Newton Data

Each photon event detected by XMM-Newton is written into the event file list associated with the observation. If we wish to make an image, we are interested in the photon's position on the detector. If we wish to make a spectrum, we are interested in the photon's energy and if we wish to make a light-curve, we are interested in the time that the photon arrived. However, to do any of these, we need to be aware of and take account of instrument-specific issues.

2.2.1 Instrument Calibrations

XMM Newton is a satellite that has been in operation for over 16 years. Naturally, over that time, there are changes in the health and hence the performance of the satellite itself, as well as the individual instruments. This ranges from the degradation of the charge transfer in the `EPIC` cameras to the astrometry of the satellite. To account for these, the XMM science team monitor the satellite and instruments and provide updated calibration files. These are important to note, as updates to the `EPIC` detectors as well as to the satellite itself may ultimately give different science results to sets of older data analysed under older calibration files to new data. Our projects use the most recent calibration files as of July 2015. Some of the relevant calibrations that affect projects relevant to this thesis include the following:

2.2.2 Effective Area

Effective area is total area of the mirror capable of focusing photons of a given energy to a particular point on a detector and is measured in cm^2. This is the area that should be used to calculate the flux and other physical properties of sources and takes into account the reflectivity and vignetting of the mirrors, that effectively reduce the geometric area of a telescope. The total on-axis effective area for each telescope is approximately 1550 cm^2 at 1.5 keV giving a combined collecting area of 4650 cm^2. The effective area is encoded in the auxiliary response `ARF` file. This gives the relation between the energy of the photon and effective area. The file is generated by the `arfgen` command in SAS. Figure.2.1 shows the combined effective area of the `EPIC` detectors and illustrates how using blocking filters affects this.

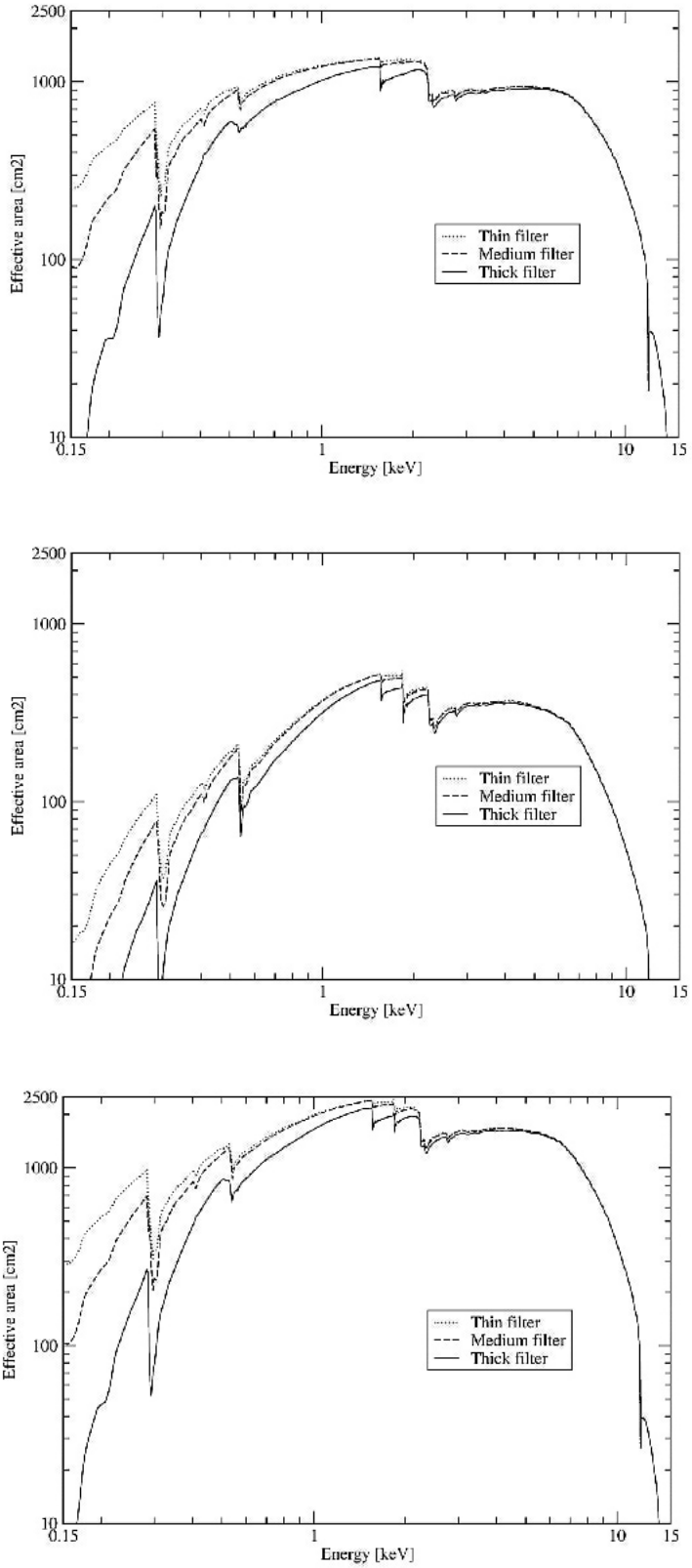

Figure 2.1: The EPIC PN(top) and MOS(middle) and combined (bottom) effective area for each of the optical blocking filters. Image from XMM-Users handbook. https://www.cosmos.esa.int/web/xmm-newton/technical-details-epic

2.2.3 Point Spread Function

The point spread function (PSF) is a description of the response of a point source when focused by the telescope at a particular location on the detector - essentially giving an idea of how a point source is extended or blurred. An object is convolved with the PSF and it is this convolved image that we view. Describing the PSF is no easy task, being dependant on both off-axis angle and photon energy. For example, it varies from its simplest model at the centre of the FOV at low energies where it is effectively circular with FWHM of $4.5''$, to a larger more elliptical bow-tie shape towards the edges of the FOV. The model mostly used in projects described in this thesis is the `ELLBETA` model which is a two-dimensional parameterisation of the three detectors as well as off-axis angle, azimuth angle, energy and star-like spokes due to the mirror support. PSFs are generated by the `psfgen` command in SAS and are shown in Figure 2.2.

2.2.4 Response Files

The response of the detector is defined by the probability that a detected photon with an energy E will be detected in a channel I. It is the product of the redistribution matrix files `RMF` and the ancillary response file `ARF` such that the total spectral response for a photon of energy E is given by:

$$\mathrm{ARF}(E) \cdot \int \mathrm{RMF}(PI, E) \cdot dPI \tag{2.1}$$

where PI is the energy bin associated with the events file.

The `RMF` describes the probability of a photon with a particular energy E being counted in a particular spectral bin PI. Since detectors are not perfect in their spectral mapping, this involves a spreading of the observed counts by the detector's spectral resolution and is described by a matrix. The better the resolution of the detector (e.g. those based on diffraction gratings) the more diagonal this matrix. The spectral response can be thought of as analogous to the PSF spatial response. It is generated by the `rmfgen` command in SAS.

2.3 XMM Cluster Survey Overview

The XMM Newton Cluster Survey (XCS) Romer et al. (2001) is a cluster survey that uses the XMM Newton observation archive to catalogue and measure the physical properties

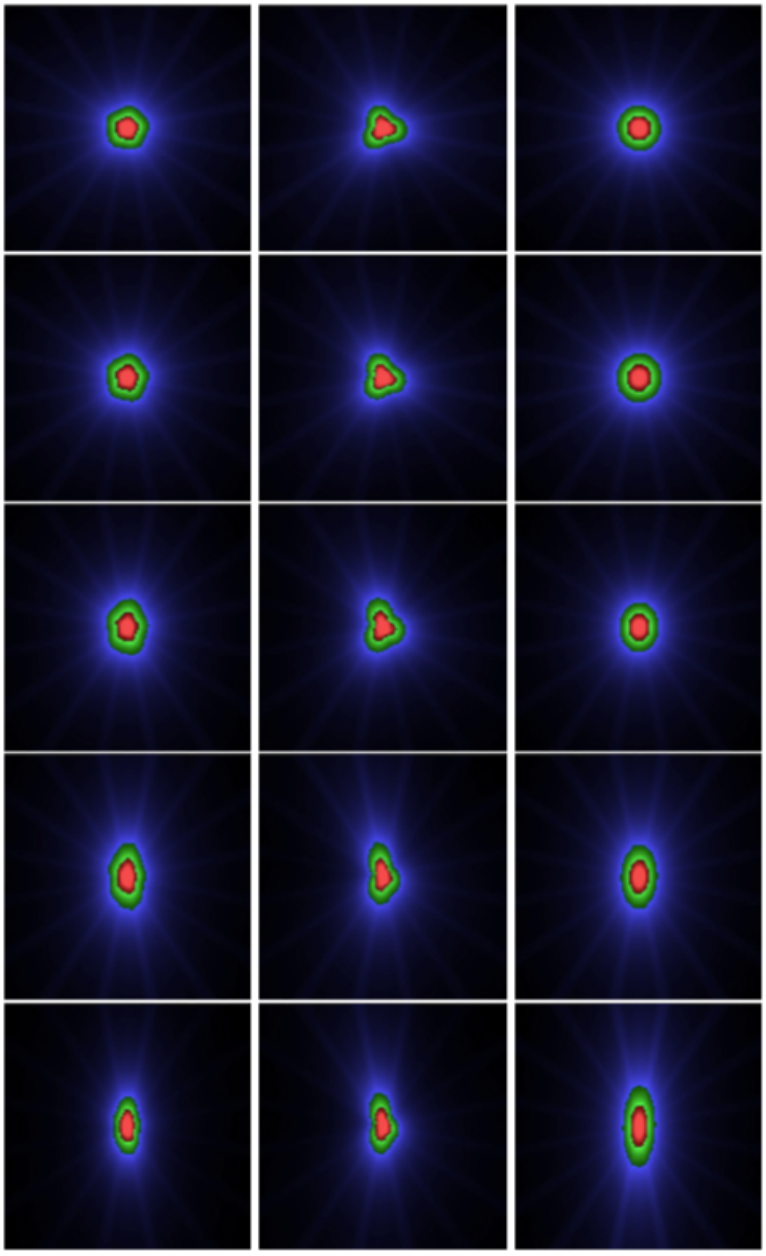

Figure 2.2: PSF for the three XMM `EPIC` cameras from left to right MOS1, `MOS2` and `PN` at off-axis angle from top to bottom 0″, 2.5″, 5″, 7.5″ and 10″ generated using the `sas` task `psfgen` and the `ELLBETA` model. Image from Rooney (2016).

(temperature and luminosity) of both targeted and serendipitous clusters. The goal of the survey is to use the clusters and their properties to constrain cosmological parameters.

2.3.1 Reduction, Flare Cleaning and Generating Clean Events

The acquisition and reduction of the XMM data is done in an automated specially written pipeline named 'The XCS Event List Cleaning and Image Making Pipeline (XIP)'. Under this, the uncalibrated raw observation data files `ODF` that contain the observation specific data are downloaded from the XMM Science Archive `XSA`.

Each XMM observation has its own ObsID, a unique ten-digit identification number, containing information such as the pointing location, timing, camera mode and record of all detected events. These are downloaded, decompressed, reduced and processed in the dedicated XCS pipeline as described in detail in Lloyd-Davies et al. (2011) (referred to from here as LD11) and subsequently updated by Rooney (2016) and Bermeo (2017) , which utilise many of the XMM SAS suite of tools designed to process XMM data, and summarised below:

Each raw ObsID is reduced using SAS software with the command `odfingest`, `cifbuild` (which creates the appropriate calibration files) and `epchain` for `PN` or `emchain` for `MOS`, commands which produce raw events files where only events with patterns 0-4 (which describe the pattern of pixels that have been charged by the photon event) for the `PN` detector and 0-12 for the `MOS` detector were included.

Since XMM does not have a shutter, we need to take account of the fact that the CCDs are taking data all the time, even when data is being read out. Therefore if a photon arrives at the detector during this, so-called out-of-time, readout period it will be assigned to an incorrect position and energy. This affects the `PN` detectors to a greater extent than the `MOS` ones which have a lower readout rate and negligible out-of-time events. An out-of-time events list is thus created for the `PN` detector and then subtracted from the `PN` events list.

The treatment of background flares was achieved by creating lightcurves in 50 sec time bins and a 12-15 keV energy band for `PN` detector and 10-12 keV for MOS, since these high energies are more likely to be particle background rather than source photons. A

Select / All / Invert	TIME D s Modify	RAWX I pixel Modify	RAWY I pixel Modify	DETX I 0.05 arcsec Modify	DETY I 0.05 arcsec Modify	X J 0.05 arcsec Modify	Y J 0.05 arcsec Modify	PHA I channel Modify	PI I eV Modify	PATTERN B Modify
1	1.608795000551E+08	51	100	-6402	7262	18647	22895	1582	8428	0
2	1.608795009315E+08	29	159	-4609	2369	22316	26596	862	4496	0
3	1.608795015371E+08	6	149	-2722	3203	23683	25052	588	5555	3
4	1.608795027465E+08	29	39	-4615	12275	18183	17594	464	3207	1
5	1.608795091588E+08	21	182	-3914	490	23730	28015	103	564	0
6	1.608795096295E+08	55	80	-6775	8859	17642	21599	1768	13822	4
7	1.608795102717E+08	12	149	-3233	3198	23221	25269	1851	9629	0
8	1.608795127567E+08	3	152	-2432	2974	24042	25139	975	7234	1
9	1.608795136872E+08	48	77	-6165	9128	18085	21100	451	2383	0
10	1.608795136493E+08	5	183	-2633	376	24942	27585	40	225	0
11	1.608795141470E+08	39	126	-5417	5114	20437	24438	2458	12870	0
12	1.608795150208E+08	8	27	-2879	13265	19348	15970	188	924	0
13	1.608795157130E+08	4	40	-2553	12226	20077	16779	2345	11879	1
14	1.608795160133E+08	33	30	-4916	12978	17616	17080	523	2592	0
15	1.608795161786E+08	21	128	-3925	4902	21882	24009	831	4321	0
16	1.608795182810E+08	16	55	-3548	10910	19721	18390	146	731	0
17	1.608795192634E+08	35	180	-5092	657	22590	28354	122	1067	3
18	1.608795195548E+08	11	38	-3153	12348	19481	16918	335	1654	0
19	1.608795198876E+08	55	111	-6788	6329	18685	23904	90	793	1

Figure 2.3: An example of clean events file as made by the XIP pipeline. In this case the `PN` detections from observation 0149780101 is shown with the columns indicating the TIME that photon was detected, the position on the particular chip RAWX/Y and detector DETX/Y, the energy channel PHA and associated energy PI. The PATTERN column gives an indication of how the event has affected surrounding pixels and allows for filtering out events other than those due to X-ray photons.

second light-curve is created at the softer photon energy (0.2-1.0 keV) to account for high soft-photon background periods due to instrument noise, solar wind charge exchange and high energy particles interacting with the structure of the instrument itself. In each case, the cleaning procedure involved determining the mean and standard deviation of the light-curve and then removing time bins where the count rate is $\pm 3\sigma$ from the mean. New mean and 3-σ limits are then calculated and the process repeated up to 50 times, so that it is highly likely that all the time periods of high background have been removed. Once this process is complete, a good time interval (`gti`) is defined for the creation of a clean event file which is used to detect sources, make images and spectra. The clean events file is also used as the starting point for the projects outlined in this thesis. These clean events tables are in the form of `.fits` files and include information about each photon event - the time of arrival, the position on the detector and the energy of the photon. An example of a clean events file, in this case, the `PN` detections from observation 0149780101 is shown in Figure 2.3.

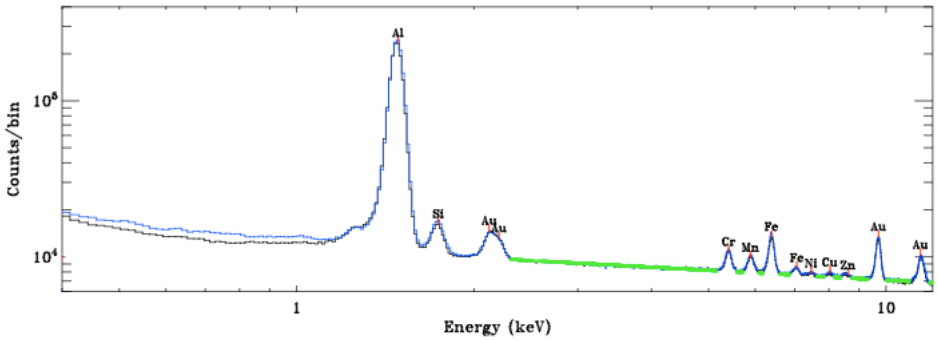

Figure 2.4: The quiescent particle background (QPB) spectra from unexposed data taken from `MOS1` in black and `MOS2` in red. This shows that when the detector filters are fully shut, background photons due to the instrument and telescope are detected. It is this instrument background, in combination with the CXB that we need to account for when creating a background-subtracted spectrum (green line is the fitted power law above 2.4 keV. Image from Kuntz and Snowden 2008.

2.3.2 Accounting for Unwanted Background Signals

Before we can make images, spectra or light-curves, we need to take into account background signals, unwanted noise, cosmic rays which should be subtracted from any source signal of interest. We briefly described, in Section 1.4.1, signals which are from astrophysical sources and how these affect all X-ray surveys. Here, we describe how these are combined with signals which are a by-product of the telescope itself. These include X-rays created by the interaction between high-energy particles and the architecture of the satellite, those by soft protons which have been funnelled onto the detectors by the mirrors and noise from the detectors. Some methods exist to account for this combined background. They include modeling and adding each individual background element to create a background spectrum that is representative of what one would expect at the source position. For example Kuntz and Snowden 2008 characterize and combine each component of the quiescent particle background to model the `MOS` spectra as in Figure 2.4.

Another method, which has the advantage of being computationally quicker (and, therefore, useful for a large survey such as XCS), is to take an annulus background region beyond the source region. The assumption being that all X-ray photons in the annulus are due to these combined background effects and therefore typical of the background likely to be found in the source area. An example is shown in Figure 2.5 which shows the

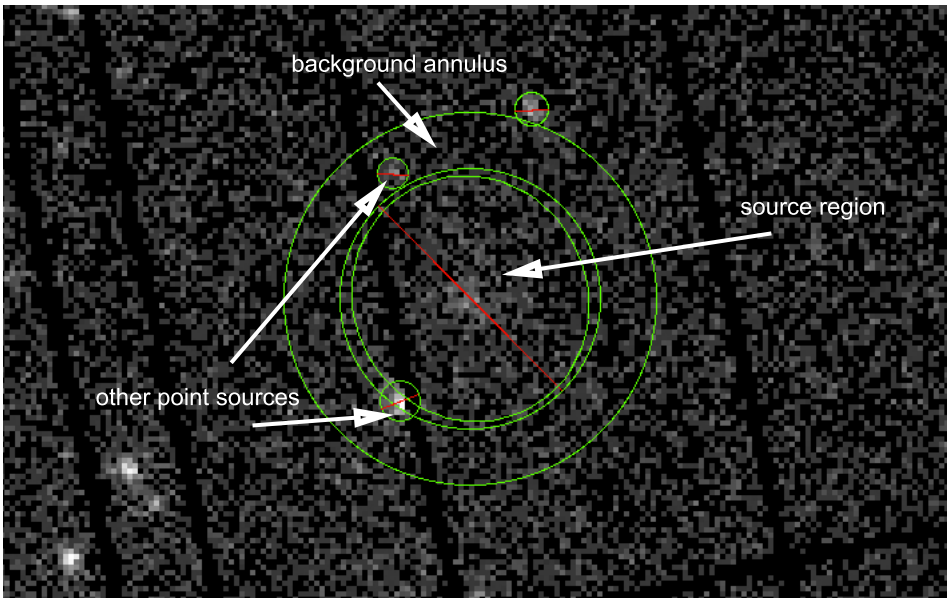

Figure 2.5: X-ray image from PN detector showing source area of a galaxy cluster (XMMXCS J082413.0+300436.9) as detected by XCS with an annulus which we take to be representative of the background X-ray photons. Three point sources are also detected which are excluded before a background spectrum is made.

source area and background annulus for a galaxy cluster detected by XCS, as well as three point sources which are excluded from the background region and spectrum. This second method is how the XCS pipeline treats the X-ray background for spectral and spatial analysis and is used throughout the projects described within this thesis.

2.3.3 Image making

The XIP pipeline automatically makes images from each observation for each detector using the clean events files. Two sets of images, with a pixel size of 4.35″, are made, one in the 0.5-2.0 keV and the other in the 2.0-10.0 keV energy range. Corresponding exposure maps are also made in the same energy bands which give information about chip gaps, bad pixels and vignetting.

2.3.4 Energy Conversion Factors

Energy Conversion Factors (ECF) are useful when we wish to estimate energy fluxes and luminosities from the count-rate. The pipeline automatically calculates ECF point source values for each observation in soft and hard energy bands. The model assumes an absorbed

power-law point-source spectra with power-law index of 1.7 (after Mushotzky et al. 1993) and a photoelectric absorption set to the appropriate n_{H} value from Dickey and Lockman (1990a). Using `XSPEC`, the `ECF` were calculated as the ratio between the flux and count-rate for each detector at the aim point for each ObsID (though these can be scaled by the exposure map to take account of off-axis sources). `ECF` are used in a method to estimate luminosities of AGN using count rates rather than from spectral fitting in part of the project outlined in Chapter 4.

2.3.5 Source Detection

Once the raw observation files have been download and reduced, and image making has been done, a separate package named `XAPA` is used to detect individual sources (as described in LD11). This works by taking merged detector images and exposure maps and by carrying out wavelet transformations at nine different scales outputs. It outputs the detected sources and their properties. These properties include position, elliptical characterisation, background subtracted count-rate, a flux estimated from the `ECF` and whether the source is point-like, extended or `PSF` sized. An example of an image of an observation with detected sources is shown in Figure 2.6.

A final master source list is then generated and contains no duplicates.

2.3.6 Data Release

The first data release of sources, XCS-DR1 Mehrtens et al. (2011), included data of X-ray sources detected from 4,125 XMM observations and contained 503 optically confirmed clusters - 256 being new to literature. Rooney (2016) expanded on this work and as of March 2016, 253,667 unique sources had been found from 8,598 observations. These form an updated internal release database, XCS-DR2 (of these sources, 173,457 are in a region outside of the galactic plane or close to the Magellanic Clouds) in an area of $\sim$688 square degrees. Figure 2.7 shows the area covered as a function of cleaned exposure time. The vast majority, $\simeq$90%, of detected sources are point-like and it is these that we use as our source data for the AGN and XRF projects in Chapters 4 and 5. There are 15,642 extended sources that constitute the cluster candidate list of which 8,306 are either firm (1,117) or preliminary (7,129) cluster identifications - all of which have redshift information. Not all of these 8,306 clusters have temperature luminosity information due to them having insufficient signal-to-noise to yield acceptable fits. T_{x} and L_x values are available for 4,987. We make use of the XCS cluster catalogue in the projects described in Chapters 6 and 7.

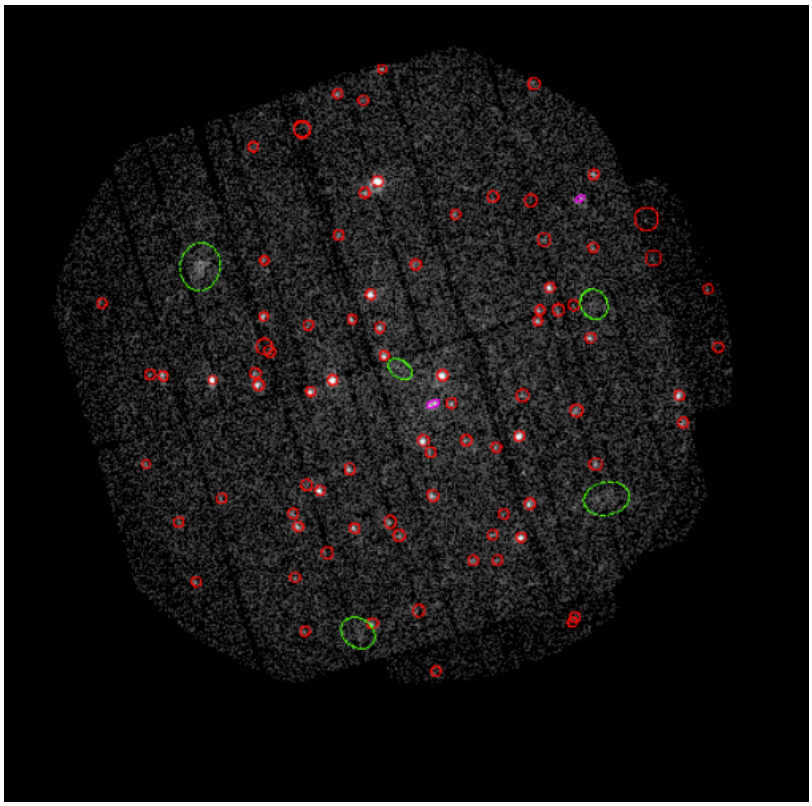

Figure 2.6: An example of an image and detected sources from the `XAPA` pipeline. In this case for ObsID 0057560301 in 2.0-10.0 keV. The three `EPIC` detector images have been merged. Detected point sources are shown as red ellipses, extended sources in green and psf sized in purple.

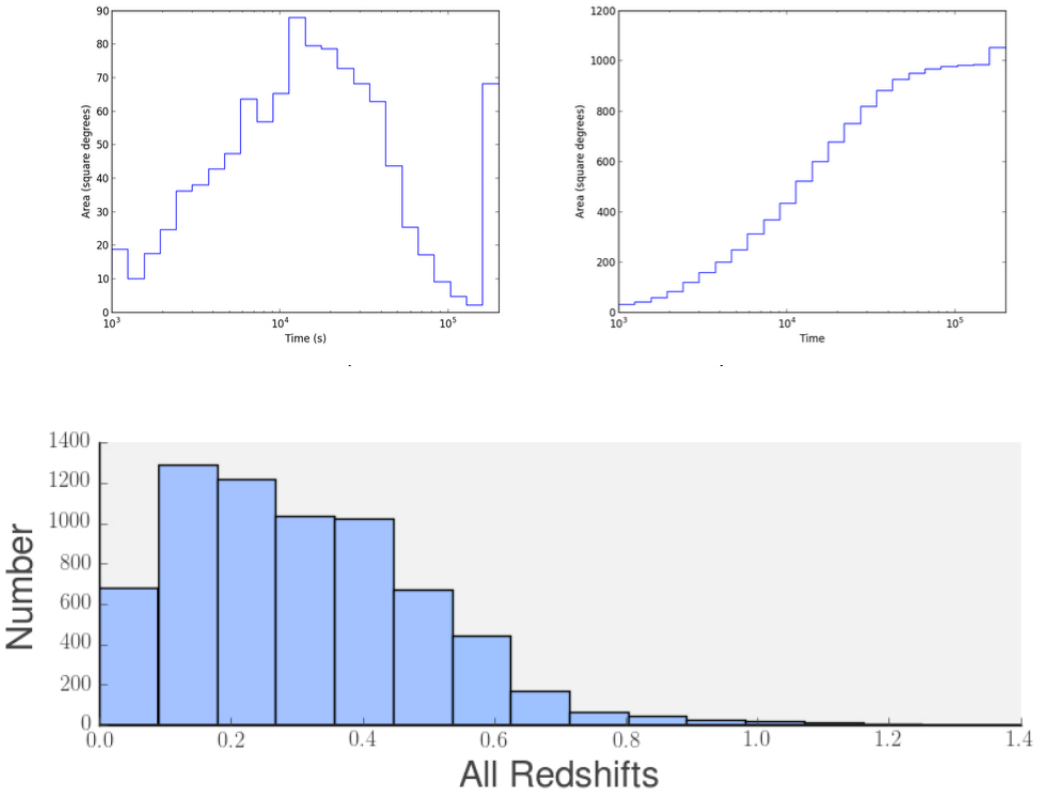

Figure 2.7: XCS-DR2 catalogue, Top (left) area of sky covered as a function of cleaned exposure time and (right) cumulative plot of the same. Bottom, redshift distribution of confirmed clusters. Images from Rooney (2016).

2.3.7 Spectral analysis

Spectra are generated using the SAS software. They are made automatically by taking the clean events file, the source and background region, selecting a minimum spectral bin size and filtering within an energy range. For example:

```
evselect table=PNclean.fits withspectrumset=yes spectrumset=PNsource.fits
energycolumn=PI spectralbinsize=5 withspecranges=yes specchannelmin=0
specchannelmax=20479 expression='(FLAG==0) && (PATTERN<=4) && PI in [300:10000]
&& ((X,Y) IN circle(DETX,DETY,400))'
```

will produce a source spectrum centred around the DETX/Y co-ordinates within a radius of 20″ (each pixel being 0.05″) and within an energy range of 0.3 to 10 keV.

For both the point sources and cluster sources analysed in the projects described, the background is taken using an in-field method, (as described in Section 2.3.2) usually a circular annulus around a point source. For clusters, the source elliptical region is given by the XAPA region parameters, and the outer region of the background annulus is 1.5 times the XAPA defined major axis of the cluster candidate. The inner radius of the annulus is no less than 1.05 times the major axis. For point sources, a source region is usually 20″ and background annulus 50-60″ around the source. In both cases, any area within the background region that have been defined as other point sources are excluded from the background spectrum.

rmf and arf files are generated for each spectrum using the rmfgen and arfgen commands. Spectral fitting is then carried out using XSPEC by running scripts written in the tcl programming language. The spectral generation and fitting pipeline for galaxy clusters was developed for XCS by LD11 specifically to estimate the temperature of galaxy clusters. It was further adapted by us, with the modifications described in Chapter 7. The pipeline to create and analyse spectra of AGN was written specifically for the project described in Chapter 4.

Clusters. The XSPEC model used to analyse galaxy clusters convolved a photoelectric absorption component, wabs (which simulates the n_{H} absorption), with a hot plasma component, MEKAL, to simulate the X-ray emission from the ICM.

AGNs. AGN analysis uses a model that is defined by a photon absorption (phabs) multiplied by a powerlaw and soft-energy blackbody components (po + bb).

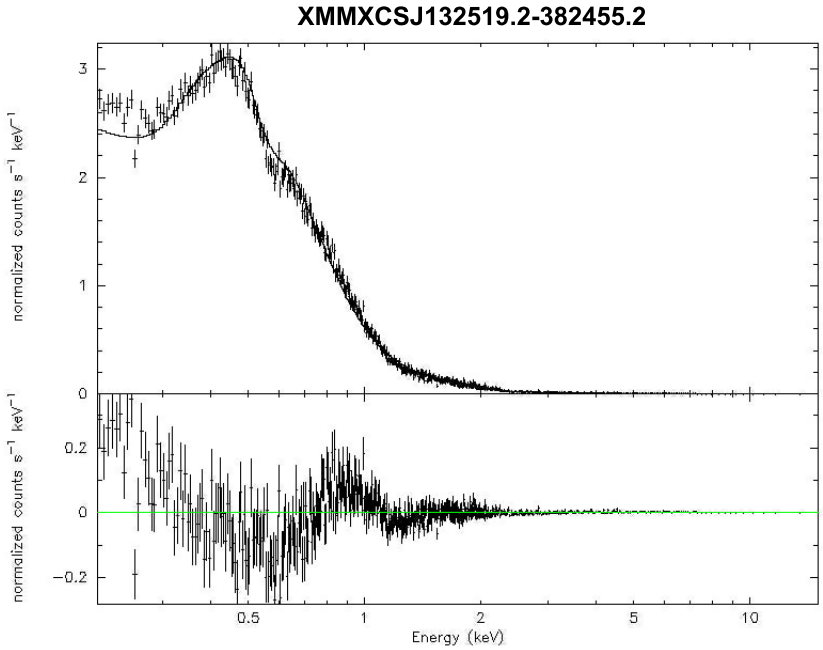

Figure 2.8: Example of a spectrum produced using `XSPEC`. In this case of an AGN candidate XMMXCSJ132519.2-382455.2 where a powerlaw and black-body model has been folded to the data in the top plot (the solid line is the best fit model). The residuals from the best fit shown in the bottom.

The fitting process estimates the 68% uncertainty bounds on the parameters of interest - i.e. $T_{\rm x}$ and L_x for clusters and the power-law index Γ and L_x for AGN - given the model. Figure 2.8 shows an example of an `XSPEC` plot, in this case an AGN. The data and best-fit model is shown in the upper window and the residuals from the best fit in the lower.

2.3.8 Light-curve Analysis

Light-curves are created to produce a good-time-interval (`gti`) in the preparation of clean events. However, they are also used in the AGN and XRF projects described in the Chapters 4 and 5. Light-curves are made automatically by taking the clean events file, the source and background region (as for spectral analysis), selecting a bin-size in seconds and by filtering for a particular photon energy range. For example:

```
evselect table=PNevt.fits energycolumn=PI expression='XMMEA_EP(PATTERN<=4)
&& ((X,Y) IN circle(DETX,DETY,400))&&(PI in [300:10000]) 'withrateset=yes
rateset='PNlightcurve.lc' timebinsize=250  maketimecolumn=yes
makeratecolumn=yes
```

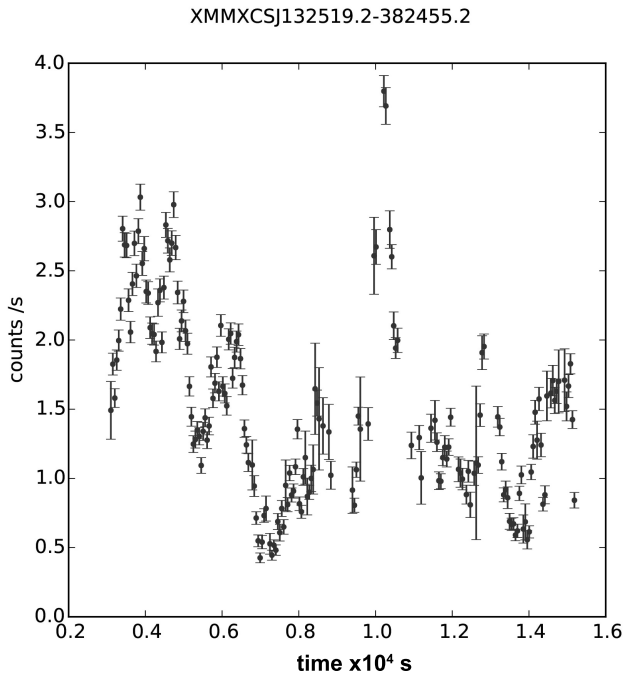

Figure 2.9: Example of a background corrected light-curve produced for AGN candidate XMMXCSJ132519.2-382455.2 from the `PN` detector using the SAS task `EPICLCCORR`.

will produce a light-curve from the `PN` detector in 250 sec bins, of a source at location given by the `DETX/Y` position with a radius 20″ (each pixel being 0.05″) in the energy range 0.3-10 keV. A background-subtracted light-curve is produced with the SAS task `EPICLCCORR` which automatically corrects for photon energy dependent inefficiencies of the mirror system such as vignetting, bad pixels, chip gaps, PSF and quantum efficiency and therefore gives the count-rate that would have been detected by the camera if it had been observed on-axis. It also takes into account time-varying corrections such as dead time. Figure 2.9 shows an example of a light-curve that has been produced by this in this way for the same AGN candidate XMMXCSJ132519.2-382455.2 as in Figure.2.8. Neither `XAPA` nor `XIP` create source light curves automatically in this way - the method was something we wrote for the projects in Chapters 4 and 5.

2.4 Chapter Summary

In this chapter we have summarised the methods whereby XMM-Newton observation data is reduced by our XCS pipelines and how, with other software and scripts, we can detect X-ray sources, make images, spectra and light-curves. These are used extensively in the science projects described in Chapters 4, 5, 6 and 7.

The next chapter lays some of the background and motivation to the first of these projects. It is a review of the methods of estimating the masses of Super Massive Black Holes (SMBH) as well as the relationship between SMBH mass and the growth of the host galaxy.

Chapter 3

Super Massive Black Holes (SMBH)

One of the central tasks of modern cosmology is to describe and explain the growth of large-scale structure in the Universe. The estimation of the masses and growth of Super Massive Black Holes is one of the clues that reveal some insight into this. Where the SMBH has an associated AGN, the mass may be estimated from X-ray associated parameters. In this section, we review the science and methods related to this, as it is central to the project described in Chapter 4.

Section 3.1 is a short historical overview of black holes. Section 3.3 describes some of the accretion disk physics that leads to the production of X-rays. Section 3.4 reviews techniques to measure the masses of SMBHs, with an emphasis on reverberation mapping in Section 3.4.2 and scaling relations from AGN variability in Section 3.4.7. Section 3.5 reviews the relationship between black hole mass ($M_{\rm BH}$) and properties of the host galaxy. These are used to predict the co-evolution of SMBH and galaxy, as described in Section 3.6.

3.1 A Historical Overview

The existence of Black Holes goes back to the 18th Century with the ideas of the British natural philosopher, Reverend John Mitchell, who pursued the idea of how light is affected by gravity. Mitchell reasoned that if the radius of a star were to increase, then the escape velocity would be larger, eventually exceeding the velocity of light itself. Mitchell called this phenomena 'dark stars'. However, it was not until 1916 that Karl Schwarzchild Schwarzschild (1916) solved Einstein's field equation for a non-rotating spherical body,

thus enabling him to put a theoretical critical radius at which such a star would have this effect on light. Pioneering theoretical work continued by Chandrasekhar (1935) on the stellar dynamics of white dwarfs and by Oppenheimer and Serber (1938) on neutron stars. These provided solutions for how a heavy star would collapse once all the sources of thermonuclear energy had been exhausted and showed that this contraction would continue indefinitely, leaving only its gravitational field as evidence for its existence. The term 'Black Hole' was coined by John Wheeler in 1960.

Observational work by Seyfert (1943) hinted tantalizingly at evidence for black holes. In investigating emission lines from 12 galaxies, Seyfert's results showed Doppler broadened hydrogen lines in NGC3516 and NGC7469 by up to 8500 kms^{-1}, a velocity of which was associated only with supernova explosions in our Galaxy. It was only when new radio sources were discovered a decade later, notably from M87 in the Virgo cluster (Baade and Minkowski 1954), that together with Seyfert's work, it was apparent that extraordinary physical processes were at the heart of the nuclei of galaxies. Appropriately, it was also in M87 where the first firm evidence of a black hole was confirmed by the Hubble Space Telescope in 1994, Harms et al. (1994) and Ford et al. (1994).
The project described in Chapter 4 describes work to estimate the mass of the largest type of black hole, the super-massive black holes (SMBH), thought to reside the centre of all galaxies with masses of order of $10^5 - 10^9 M_\odot$.

3.2 SMBH Formation

Quasars have been observed at $z \sim 6$. This implies that the earliest SMBHs were formed at a very early time in the history of the Universe. For example, a quasar at this redshift with luminosity in excess of $10^{47}\mathrm{erg\,s}^{-1}$ implies a SMBH of $M \sim 10^9 M_\odot$. For this to have been formed by this epoch we can estimate, from the increase in mass growing at the Eddington rate over time, when the 'seed' black hole must have existed as derived from Equation 3.1 (taken from Volonteri 2010) :

$$M(t) = M(0)\,\exp\left(\frac{t}{t_{\mathrm{Edd}}}\frac{1-\epsilon}{\epsilon}\right) \tag{3.1}$$

where t_{Edd}=0.45 Gyr and ϵ is the radiative efficiency. If we take $\epsilon \sim 0.1$ then a seed black hole with mass $M(0) \sim 100 M_\odot$ will take at quickest ~0.35 Gyr to grow to its supermassive size - i.e. the seed must have existed in an era when galaxies were in their infancy.

Whilst there is no agreed mechanism for the formation of SMBHs, several possible scenarios have been presented for the initial formation process as well as the nature of seed. These are summarised briefly below:

3.2.1 Population III remnants

The first of these, (e.g. Volonteri et al. 2003), suggests that massive first generation population III stars which have collapsed at z ∼20-50 become black holes with masses of the order of 10 to 100s $M_{\odot}$. These combine through a series of mergers into a larger entities which accrete gas from the remnants of the merger and become supermassive forming a binary systems, which finally coalesce.

3.2.2 Gas dynamics

Another family of models suggests that SMBH were formed directly from the collapse of a large dense gas cloud in the era before the first stars were formed (e.g. Haehnelt and Rees 1993, Begelman et al. 2006). Bromm and Loeb (2003) suggest that this only occurs in metal-free halos where the virial temperature $\gtrsim 10^4$ K. In this scenario, a mechanism is required that transports angular momentum away, in order for the gas to form a central core object which eventually collapses (different mechanism have also been suggested by Umemura et al. 1993, Colgate et al. 2003 and by Shlosman et al. 1989). The proto-black holes formed in this way have a mass of $\sim 20 M_{\odot}$ from which they rapidly grow to massive and supermassive size.

3.2.3 Stellar dynamics

Dynamical interactions within globular clusters provide a further possible model for SMBH formation (e.g. Begelman and Rees 1978, Miller and Hamilton 2002). In this scenario the core of a dense star cluster contracts as it tries to reach thermal equilibrium. The density of the central region therefore increases and the velocity dispersion in the core is driven to relativistic speeds and the core collapse speeds up.

3.2.4 Primordial black holes

Evidence that SMBHs formed before and evolved together with the bulges of their galaxies (Silk and Rees 1998) is in some tension with the detection of quasars at $z \gtrsim 6$, since the

above theories rely on the SMBH seed being from galactic stars or gas. Düchting (2004) suggest that at such redshifts SMBHs would have needed have been seeded and growing from a very early epoch, ($z \gtrsim 15$). They suggest an alternative scenario in which primordial black holes, i.e. those that formed early in the Universe, are the seeds of SMBHs.

3.3 Accretion Disk Physics

Although the physics and the exact processes of accretion of material on the SMBH is beyond the scope of this thesis, we review some of the salient points relevant to the production of X-rays.

Accretion material is thought to come from gas which has been expelled from stars (via stellar winds and supernova), from intergalactic clouds captured by a galaxy, or debris from a galaxy's central region. The in-falling material is prevented from falling directly onto the black hole due to its angular momentum but instead forms an accretion disk. Viscous processes within the disk allows for both the gravitational energy and angular momentum of the material to be released outwards. This results in a flattening of the structure as matter falls further toward the gravitational centre. However, there is a limit to how far the material can be accreted due to the effects of the radiation pressure that is felt by the in-falling matter.

This critical limit, as suggested by Arthur Eddington, is defined by the Eddington luminosity ($L_{\rm Edd}$) which sets an upper limit to the AGN luminosity. This is found by equating the pressure gradient due to the gravitational well of the SMBH;

$$\frac{dP}{dr} = \frac{-GM_{\rm BH}\rho}{r^2} \tag{3.2}$$

to the pressure gradient due to radiation produced from within the disk by the gravitational and viscous processes;

$$\frac{dP}{dr} = \frac{L}{4\pi r^2}\frac{-\sigma_\tau \rho}{m_p c} \tag{3.3}$$

where ρ is density of the in-falling matter which we take to be ionised Hydrogen, m_p, the proton mass and σ_τ the electron scattering cross-section and hence;

$$L_{\rm Edd} = \frac{4\pi G M m_p c}{\sigma_\tau} \simeq 1.3 \times 10^{38} \frac{M}{M_\odot}\,{\rm erg\,s^{-1}} \tag{3.4}$$

In terms of the bolometric luminosity of the AGN, the Eddington rate is given by:

$$\lambda_{\rm Edd} = L_{\rm bol}/L_{\rm Edd} \tag{3.5}$$

and the Eddington limit is reached when this is equal to 1. Using $L_{\rm Edd}$, we can define an Eddington accretion rate;

$$\dot{M}_{\rm Edd} = \frac{L_{\rm Edd}}{\epsilon c^2} \tag{3.6}$$

where ϵ is the efficiency of the radiation of the gravitational energy. It has been shown that if the accretion disc is physically thin and optically thick, the black body temperature at distance r of the AGN can be derived by;

$$T(r) = \left(\frac{3G\dot{M}M}{8\pi r^3\sigma}\right)^{1/4} \tag{3.7}$$

The maximum temperature for such a disk for a SMBH of the order of $10^6 M_\odot$ is less than 1 keV. Therefore another process is needed to account for the radiation of X-rays. These are thought to be produced when low energy photons are up-scattered to higher energies by relativistic electrons (which reside in the corona above the disk) through the inverse Compton effect (e.g. Haardt and Maraschi 1993). The final energy of the photon E_f is related to its initial energy E_i by;

$$E_f = e^{\gamma} E_i \tag{3.8}$$

where γ is the Compton parameter dependent on the optical thickness of the electron gas as well as its temperature. In this way, low energy photons from the accretion disk are emitted within the X-ray range of spectral energy up to a few hundred keV with a power-law index $\Gamma \sim 1.8 - 2$. Figure 3.1 shows a schematic representation of a Type 1 AGN spectrum with various features, including a soft-excess at the low energy end, the prominent Iron Kα emission line and a reflection hump at > 10 keV. It is at energies between 0.2 and 10 keV, where XMM-Newton operates, an energy range which is particularly relevant to the projects described in Chapters 4, 5, 6 and 7.

3.4 Black Hole Mass Estimation Techniques

We can divide the techniques to measure the mass of a SMBH into direct and indirect methods. Direct methods include the dynamics of stellar and gas accretion onto the black hole, as well as reverberation mapping. Indirect methods include those where the mass of

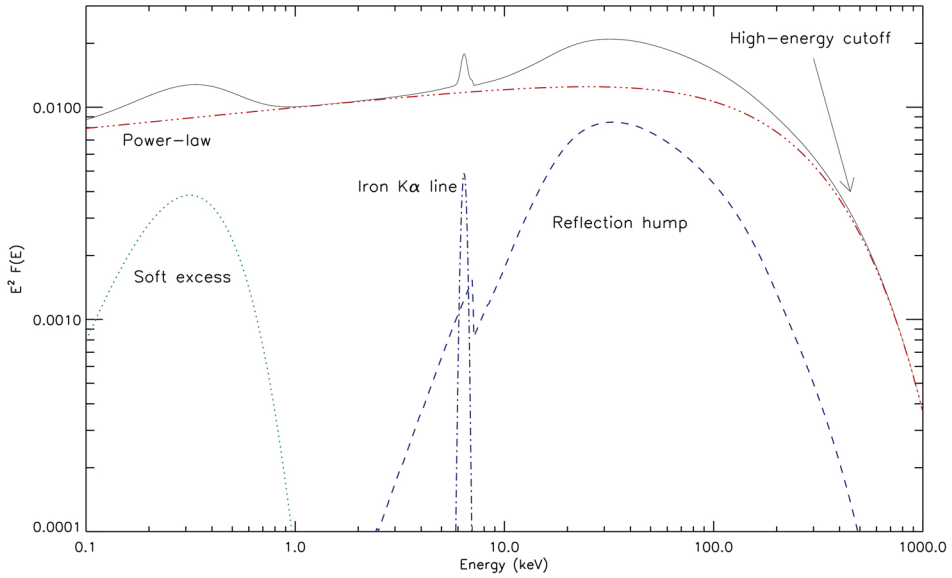

Figure 3.1: A schematic 0.1-1000 keV spectrum of a Type 1 AGN with prominent features. Image from Ricci (2011).

the black hole is inferred from scaling relations associated with $M_{\rm BH}$. These include host galaxy properties such as the velocity dispersion of bulge stars $M_{\rm BH}$-σ_* relation, as well as the luminosity of bulge stars $M_{\rm BH}$ -$L_{\rm bulge}$. Also included are relations based on the broad line region emissions and X-ray variability. We shall look at each of these in turn with a focus on the techniques of reverberation mapping and estimation of X-ray variability from the normalised excess variance. Both these techniques are central to the work described in Chapter 4.

3.4.1 Mass from Stellar and Water Megamaser Dynamics

The most accurate method to measure the $M_{\rm BH}$ is through the dynamics of individual or collective sources, i.e. the radial motions of gas or individual stars. In mapping this velocity field due to the SMBH, stars are a better tracer than gas since they are affected only by the gravitational field and not by any magnetic or frictional force. In this way, for example, Ghez et al. (2003) estimated a mass of SGR A* at the Galactic centre of $4 \times 10^6 \pm 0.3 M_{\odot}$.

To date, just over 70 SMBH have masses estimated from stellar or dust dynamics (McConnell and Ma 2013) as there is the need to resolve radius of the SMBH, which is difficult to do except in the most local region (and not possible currently beyond the Virgo cluster at a redshift of $z \sim 0.0038$). Therefore, it is likely that we have reached a limit of $M_{\rm BH}$ that

have been estimated in this way and so we require other methods at higher cosmological distances.

Similar to gas dynamics, it has recently become possible to estimate $M_{\rm BH}$ by using radio interferometry to measure the dynamics of water megamaser orbiting the SMBH, e.g. Kuo et al. (2011). We go into no further detail of the methods of SMBH mass estimation from stellar and gas dynamics as the black hole sample we use in Chapter 4 have not been measured in this way.

3.4.2 Mass from Reverberation Mapping

Three methods rely on using broad emission lines and estimating the radius of the Broad Line Region (BLR) as a virial estimator of $M_{\rm BH}$. The first is reverberation mapping (Blandford and McKee 1982).

Using the virial theorem, we assume that the gas in the BLR of the AGN is gravitationally bound to the SMBH at a distance $R_{\rm BLR}$, and is virialised. Its velocity dispersion, $V_{\rm BLR}$, can be expressed as $f\times$ FWHM, where f is a factor of order unity dependent on the particular kinematics and geometry and FWHM is the full width half maximum value of the emission line of the BLR gas spectrum (e.g. Hβ or Hα at low redshift and MgII and CIV at intermediate redshift). The $M_{\rm BH}$ is then given by Equation 3.9:

$$M_{\rm BH} = \frac{R_{\rm BLR}(f \times {\rm FWHM})^2}{G} \tag{3.9}$$

In reality, all the terms on the right-hand side are difficult to measure accurately. The factor f is poorly understood with uncertainties from different AGN dynamics and orientation effects, and the appropriateness of FWHM of the line broadening depends on which line is chosen (some authors claim that the line dispersion, σ, is a better choice than FWHM, e.g. Peterson et al. 2004). Further, the radius $R_{\rm BLR}$ is uncertain since the BLR and continuum emission regions are not spatially resolved. It is this distance, $R_{\rm BLR}$, that the reverberation mapping technique aims to estimate.

Figure 3.2 shows a simplistic system of a BLR cloud orbiting a black hole continuum source at radius $R_{\rm BLR}$. We imagine a delta function light-pulse from the continuum which is then reprocessed in the BLR cloud as an emission line. At the continuum centre, an observer would measure a time delay $\tau = 2R/c$ between the pulse and the emission line. However,

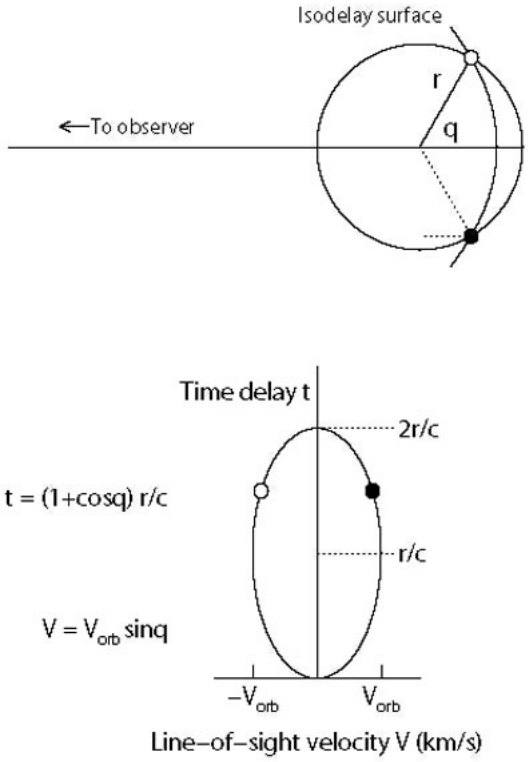

Figure 3.2: A notional BLR of clouds orbiting at distance R in a circular orbit around a black hole. Top. The dotted line is a path taken by an ionizing photon to the cloud at coordinate $(R, -\theta)$ plus the path of an emission line photon until it is the same distance from the observer as a photon from the continuum source. The light time travel along this dotted line is the time lag that the observer sees between the continuum outburst and the emission line from the BLR and is given by $\tau = (1 + \cos\theta)R/c$. All the points on the isodelay surface have this same delay. Bottom, the same system projected into the observable Doppler velocity and time delay. Image from Peterson (2003).

for an observer at any large distance, this delay τ, depends on where on the circumference of the orbit of the BLR the emission photon originates. Relative to the continuum source, the emission line is delayed by the time the continuum photons take to reach the BLR region plus the time that the emission photons from the BLR region take to reach the equivalent of the continuum distance from the observer, i.e. the sum of the dotted lines. This is given by the Equation 3.10:

$$\tau = (1 + \cos\theta)R_{\rm BLR}/c \tag{3.10}$$

If the radius can be derived in this way and the FWHM can be measured from the Hβ line, then $M_{\rm BH}$ can be estimated from Equation 3.9. Although the measurements on mass

derived in this way are the most accurate, this relies on certain assumptions including: (1) the BLR region is much larger than the continuum emitting region; (2) the emission lines are isotropic; (3) no contamination from other emission lines; and (4) that the BLR doesn't dynamically change over time.

Thus far, due to reverberation mapping requiring many spectra across long time intervals of typically several years, only around 60 AGN at low redshift have been observed (e.g. Bentz et al. 2009b). Only three reverberation mapped AGN are close enough to have allowed an independent measurement of $M_{\rm BH}$ by stellar dynamics. The results from NGC 4151 (Onken et al. 2007) and NGC 3227 (Davies et al. 2006) show good agreement between the two methods. The third is NGC 6814 where the reverberation mapped $M_{\rm BH}$ has been estimated by Bentz et al. (2009b) though the stellar dynamics results by Manne-Nicholas et al. (2016) are yet unpublished.

3.4.3 Mass from Scaling Relationships

Although the reverberation mapping method is unlikely to deliver SMBH masses for large (>100) samples of AGN, it can be used to calibrate indirect methods that are less costly in terms of telescope time. For example, Kaspi et al. (2000) and Wandel et al. (1999) estimate relations from reverberation mapping studies to derive a relation between the BLR size ($R_{\rm BLR}$)and monochromatic luminosity (λL_λ) from the continuum at 5100Å, as shown for example in Figure 3.3. From this, a single epoch spectral method can be used to infer the mass of many more SMBHs than can be studied using reverberation mapping. Kaspi et al. (2000) derive this relation to be:

$$R_{\rm BLR} = (32.0^{+2.0}_{-1.9}) \left[\frac{\lambda L_\lambda (5100\text{Å})}{10^{44}\,{\rm erg\,s^{-1}}} \right]^{0.7\pm0.333} {\rm light-days} \tag{3.11}$$

Therefore from Equations 3.9 and 3.11 we can estimate values for $M_{\rm BH}$ from a single-epoch AGN spectrum by measuring the Hβ emission line and luminosity at λL_λ(5100Å). At higher redshifts > 0.7, where the Hβ would be redshifted into the infra-red region and thus not observable to ground based optical telescopes, other scaling relations based on C IV (1549Å) and Mg II (2789Å) lines have been used (e.g. Wang et al. 2009).

3.4.4 Mass Estimation from Photonisation Methods

Before the use of reverberation mapping techniques and the associated scaling relations - e.g. between the luminosity of Hβ emission line and monochromatic luminosity at

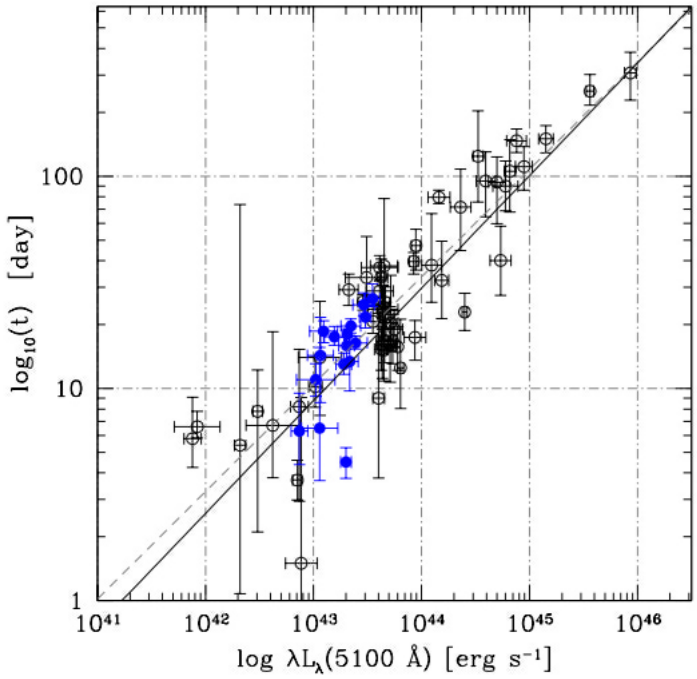

Figure 3.3: Correlation between continuum luminosity at 5100Å and time delay from reverberation mapping. Individual points represent separate determinations for the same object. Blue circles relate to NGC5548. Solid line is weighted best fit. The dotted line is unweighted best-fit. Image from Marziani and Sulentic (2012) based on data from Bentz et al. (2009a).

$\lambda L_\lambda(5700\text{Å})$ - studying the BLR was done by photoionisation equilibrium modelling methods. It was through this technique that a predicted relation between BLR radius and continuum luminosity was first suggested. U is defined as an ionisation parameter that describes the ratio of the ionising photon density to the particle density in the BLR cloud and is expressed as,

$$U = \frac{Q(H)}{4\pi R^2 n_e c} \tag{3.12}$$

where n_e is the particle density, $Q(H)$ is the rate at which ionising photons are produced in the continuum, and R is the BLR radius. Using the R_{BLR} results derived from reverberation mapping studies where the number of ionising photons could also be measured, Padovani (1989) found the mean of $U \times n_e \sim 10^{9.8}$. From this Padovani and Rafanelli (1988) estimated the masses of a large sample of black holes, which correlated well to M_{BH} found through reverberation mapping.

3.4.5 Mass Estimation from X-ray Variability

A leading *indirect* method to estimate M_{BH} uses the variability of AGN emissions in the X-ray part of the spectrum. When SMBHs of known mass are correlated against this variability, a scaling relation can be used estimate M_{BH} of other SMBHs. Several studies (Ponti et al. 2012, Zhou et al. 2010, Kelly et al. 2011) have suggested that, in this way, X-ray variability provides as good an estimate of M_{BH} (with intrinsic dispersion of ∼0.2 - 0.3 dex precision) as M_{BH} derived from the $M_{\text{BH}} - \sigma_*$ relations associated with stellar velocity dispersion (e.g. Tremaine et al. 2002). A further advantage of using X-ray variability is that it is not dependent on the orientation of the AGN (whereas reverberation mapping is applicable solely to Type 1).

Figure 3.4 from Zhou et al. (2010) shows the tight correlation between M_{BH} estimated through the technique of reverberation mapping and that of using X-ray variability and this is relevant to our work as described in Chapter 4.

In the next two subsections, we describe two approaches to quantifying this X-ray variability, with an emphasis on the so-called 'normalised excess variance method', which we use in our project outlined in Chapter 4.

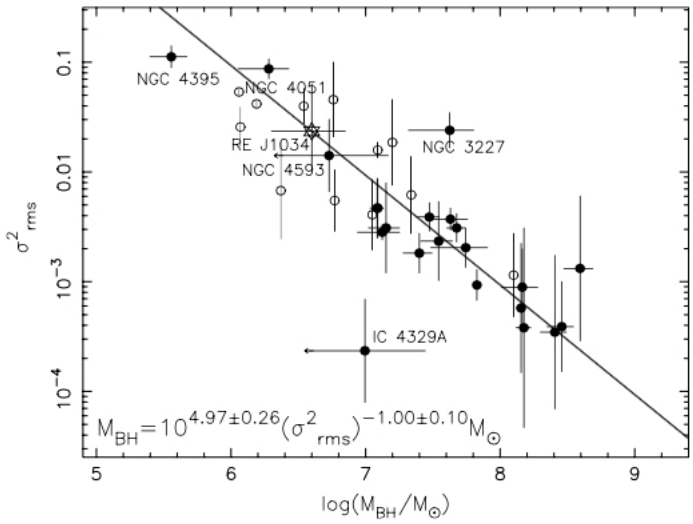

Figure 3.4: Correlation between X-ray variability amplitude $\sigma^2_{\rm NXS}$ and $M_{\rm BH}$ derived from reverberation mapping (black circles) The solid line is the best fit relation for these AGN. The open circles are $M_{\rm BH}$ from virial estimates which follow the relation well. Figure from Zhou et al. 2010.

3.4.6 PSD

The most accurate method to quantify the X-ray variability of an AGN is to analyse its power spectral density function (PSD). Analysis from *EXOSAT* e.g. Lawrence and Papadakis (1993) and later *RTXE*, e.g. Uttley et al. (2002) showed that the PSD could be fit by a power-law with slopes of around -2, flattening at some break frequency to around -1, as shown in Figure 3.5.

In a sample of six Type 1 AGN, Markowitz et al. (2003) find a significant correlation between the break timescale (the reciprocal of break frequency) and $M_{\rm BH}$ as shown in Figure 3.6. This was similarly found by McHardy et al. (2006) and Körding et al. (2007) who showed that $M_{\rm BH}$ and break timescale (or the break frequency) are intimately related.

González-Martín and Vaughan (2012) showed a strong correlation between $M_{\rm BH}$ and timescale where a bending power-law model is a better fit to the PSD than a simple power-law. Figure 3.7 shows 17 AGN from their survey and others from literature. (The 104 AGNs - identified in Veron-Cetty and Veron (2010) - in this study were selected from all observations in the XMM Newton pubic archive and include all sources within the 2XMMi DR3 catalogue Watson et al. 2009. The $M_{\rm BH}$ were derived by several different methods, with a preference for reverberation mapping where available).

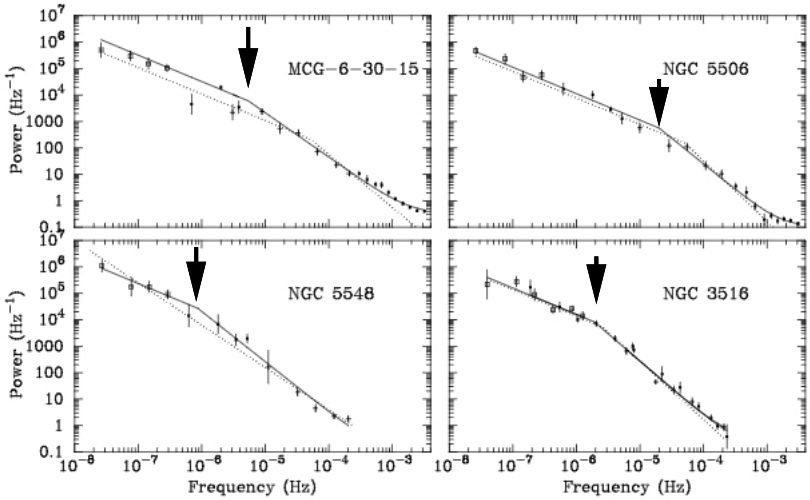

Figure 3.5: Power spectra (points with error bars) of four AGN with the best-fitting high-frequency models shown in solid lines with the break frequency indicated with arrow. The dotted lines are the best-fitting model obtained from Monte Carlo fits with broken power-law model (except NGC 5548 which is single power law). Figure adapted from Uttley et al. (2002).

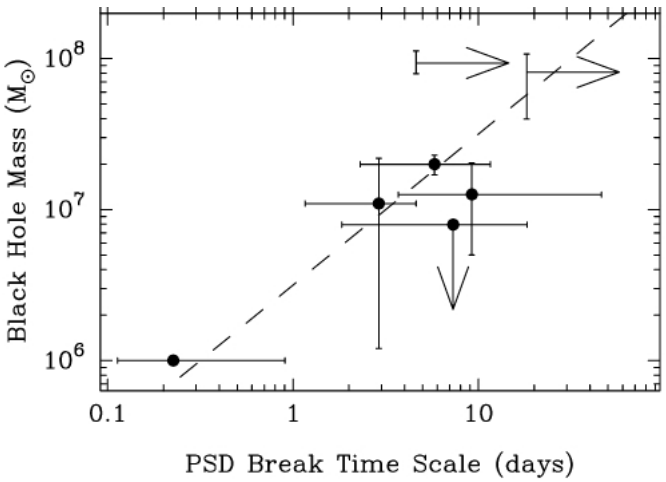

Figure 3.6: Relationship between $M_{\rm BH}$ and power spectrum break time-scale for six AGN. The masses have been estimated from reverberation mapping studies. The dashed line is the best fit linear relation between mass and timescale, $T_{\rm days} = M_{\rm BH}/10^{6.5} M_\odot$. Figure adapted from Markowitz et al. (2003).

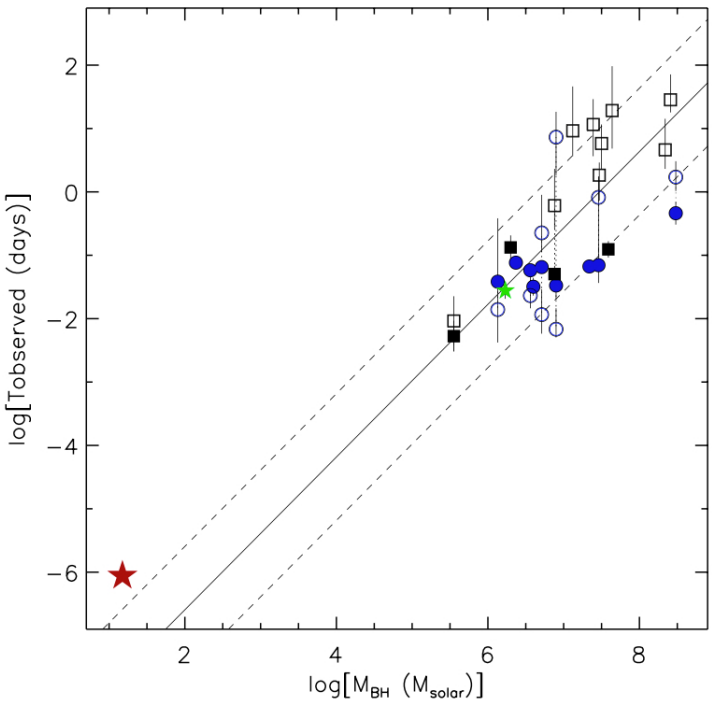

Figure 3.7: Relation between observed bend timescale and $M_{\rm BH}$. The solid line is the best fit and the dashed lines are ± 1 dex region. Circles represent Narrow Line Seyfert Type 1s, squares are Seyfert Type 1, and the green star is a Seyfert Type 2. Cygnus X-1 is the red star. The open symbols are data taken from literature. The filled symbols are data taken from the survey. Figure and caption from González-Martín and Vaughan (2012).

Simm et al. (2016) demonstrated a correlation between $L_{\rm X}$ and PSD amplitude. They show this in a study of 72 AGN for which they derived a PSD and compared to bolometric luminosity as shown in Figure 3.8.

3.4.7 Normalised Excess Variance, $\sigma^2_{\rm NXS}$

The PSD method necessitates long X-ray observations of individual AGN and is therefore not suited for very large samples. For this reason, Nandra et al. (1997) developed an alternative method to define X-ray variability that is less costly in terms of X-ray telescope time. This method uses the normalised excess variance, $\sigma^2_{\rm NXS}$ of a light-curve (Turner et al. 1999, Vaughan et al. 2003b). It is the integral of the PSD of a light-curve over a frequency interval set by the length of the time bins and total observation duration, e.g. van der Klis (1989), i.e.

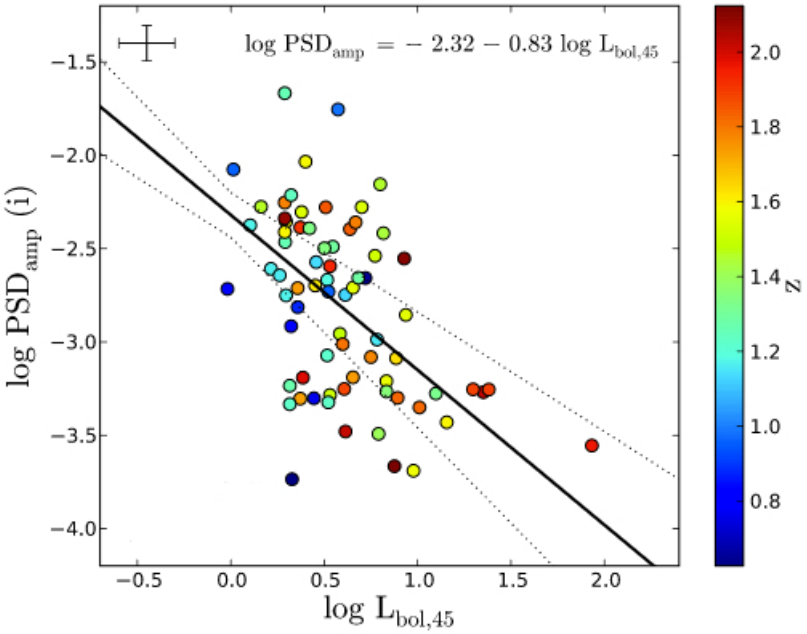

Figure 3.8: PSD amplitude plotted against bolometric luminosity with best fit power-law relations, from a sample of 72 AGN. The redshift is shown as a colour-bar. Figure from Simm et al. (2016).

$$\sigma^2_{\rm NXS} = \int_{\nu_{min}}^{\nu_{max}} P(\nu) d\nu \tag{3.13}$$

$P(\nu)$ is the power at frequency ν, $\nu_{min} = 1/T$, $\nu_{max} = 1/2\Delta T$, where T and ΔT are the time duration and binsize of the light-curve respectively.

$\sigma^2_{\rm NXS}$ is much easier-to-calculate than PSD analysis and is a measure of the variability after taking into account measurement error (i.e. Poisson noise) and defined by the equation:

$$\sigma^2_{\rm NXS} = \frac{1}{\bar{x}^2}\left[\frac{1}{N-1}\sum_{i=1}^{N}(x_i - \bar{x})^2 - \frac{1}{N}\sum_{i=1}^{N}\sigma_i^2\right] \tag{3.14}$$

where N is the number of good time bins, $\bar{x}$ is the mean count rate, x_i is the count-rate in bin i and σ_i^2 the error in count rate in bin i. A positive value of $\sigma^2_{\rm NXS}$ therefore implies that the intrinsic variability of the source dominates the measurement uncertainty. Whereas a negative value implies the reverse.

The derived $\sigma^2_{\rm NXS}$ value should then be scaled to take account for two effects. First the cosmological time dilation of the detected photons. Secondly, as Kelly et al. (2013) discuss,

the $\sigma^2_{\rm NXS}$ value will be dependent on the length and sampling of the individual AGN light-curve. Since the observation time of each source differs one should normalise individual values. According to Middei et al. (2016) these two factors can be accounted for by the scaling relation:

$$^{*}\sigma^2_{\rm NXS} = \sigma^2_{\rm NXS}\left(\frac{\Delta t^{\star}}{\Delta t_{obs}}\right)^{2\beta}(1+z)^{2\beta} \tag{3.15}$$

(where z is the redshift of the AGN, $\Delta t^{\star}$ is a fixed time interval, Δt_{obs} is the time interval over the observation and β estimated to be 0.10 ± 0.01 in Antonucci et al. 2014 equal to the value found in Vagnetti et al. 2011).

$\sigma^2_{\rm NXS}$ analysis of 168 radio-quiet and targeted AGN, observed by XMM-Newton, is described in Ponti et al. (2012): the *Catalogue of AGN In the XMM Archive* (CAIXA). Of these, 32 have $M_{\rm BH}$ taken from the results of reverberation mapping analysis only, and the rest by indirect methods, including stellar velocity dispersion and emission lines in the BLR and optical luminosity. Figure 3.9 from Ponti et al. (2012), top, shows the relation between $M_{\rm BH}$ (taken only from reverberation mapping) and $\sigma^2_{\rm NXS}$ (in light-curve 20 ks segments), where a strong anti-correlation between the $M_{\rm BH}$ and $\sigma^2_{\rm NXS}$ can be seen. This has been also found by other studies (e.g. O'Neill et al. 2005, Papadakis 2004, Zhou et al. 2010).

There is also a strong anti-correlation between X-ray luminosity and variability as shown in the bottom of Figure 3.9. This is in agreement with studies that take the PSD as the variability parameter. e.g. Kelly et al. (2013), Simm et al. (2016) i.e. the more luminous the AGN, the less it varies.

3.4.8 Considerations Using $\sigma^2_{\rm NXS}$

Although the $\sigma^2_{\rm NXS}$ is relatively straightforward to measure compared with the PSD, Kelly et al. (2013) remind us that for the linear relation suggested in Equation 3.13 to hold, the light-curve length must not be significantly longer than the break time scale τ, which is an unknown at the outset. This is important since it is only at frequencies above τ where the strong $\sigma^2_{\rm NXS}$ to $M_{\rm BH}$ anti-correlation relation holds. Since $M_{\rm BH}$ is also correlated with τ, (i.e. the lower the mass, the higher the break frequency), as Figure 3.10 shows, at the lower $M_{\rm BH}$ regime we may be estimating $M_{\rm BH}$ erroneously if we use the same correlation as in the higher mass regime.

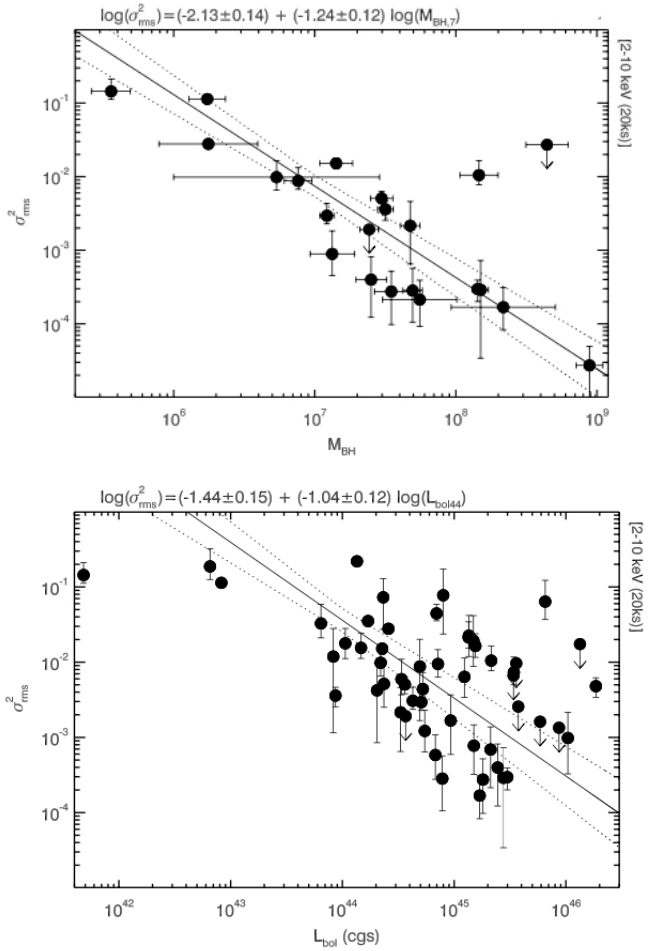

Figure 3.9: Top. Relationship between $M_{\rm BH}$ and $\sigma^2_{\rm NXS}$ in 20 ks segments of observation duration (referred to as $\sigma_{\rm rms}$ by the authors) for the CAIXA sample of AGN (black dots with error bars) where masses are taken from reverberation mapping. Bottom, relationship between bolometric luminosity and $\sigma^2_{\rm NXS}$ for same sample. In each case the black solid lines are the best fit relationship and the dotted line is the 1-σ error on the slope. Figures from Ponti et al. (2012).

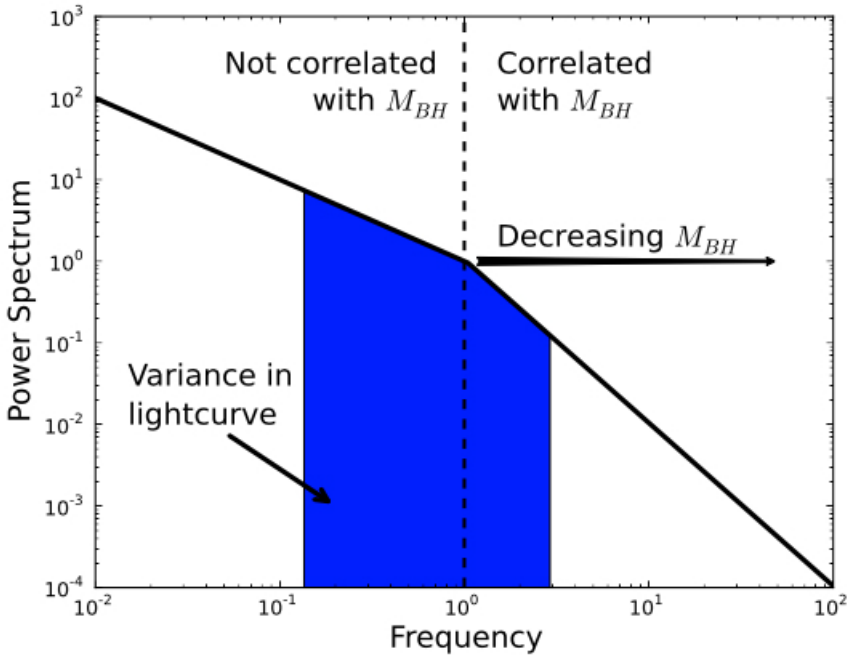

Figure 3.10: Illustration showing how the $\sigma^2_{\rm NXS}$ is related to the PSD of an AGN. Both the break frequency and PSD amplitude above the break depend on the mass $M_{\rm BH}$. Above the break frequency, the $\sigma^2_{\rm NXS}$ is correlated with $M_{\rm BH}$. However below this break frequency this relation weakens. Figure from Kelly et al. (2013).

In their study of 15 AGN in the low mass range 10^5 to 10^6 $M_\odot$, with masses estimated from the luminosity and the width of the broad Hα line, Pan et al. (2016) confirm this effect. They show that the inverse correlation between $\sigma^2_{\rm NXS}$ and $M_{\rm BH}$ flattens below $10^6 M_\odot$, as shown in Figure 3.11. They conclude that in this low-mass regime $\sigma^2_{\rm NXS}$ does not provide an accurate estimate of $M_{\rm BH}$.

3.5 Relationships Between Black Hole Mass and Host Galaxy

We wish to measure $M_{\rm BH}$ to understand how galaxies form and evolve since it seems apparent that there is a very close relationship between the mass of a SMBH and properties of the host galaxy, e.g. Kormendy and Ho (2013). This allows us to link the growth of the SMBH with that of its galactic host and vice-versa. We, therefore, summarise three of these scaling relationships.

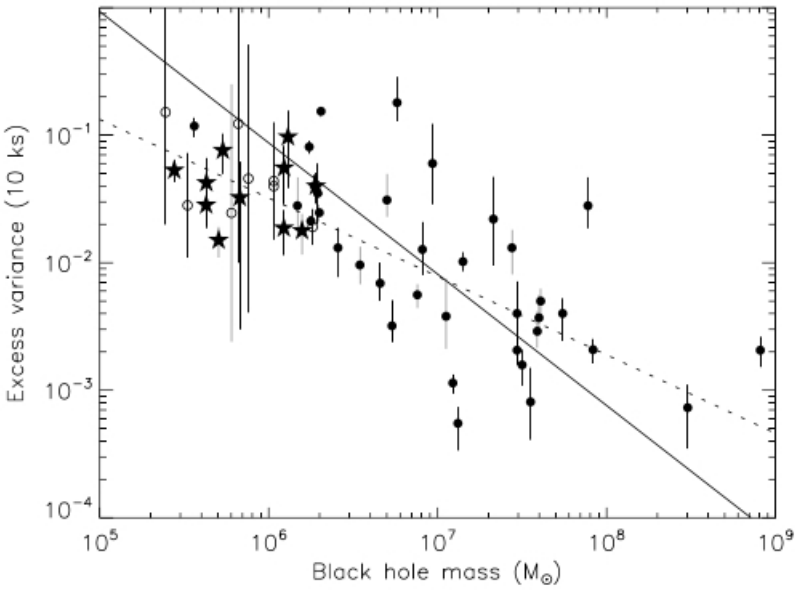

Figure 3.11: The relationship between $M_{\rm BH}$ and $\sigma^2_{\rm NXS}$ over 10 ks bins for a sample of low mass regime AGN shown as stars from Pan et al. (2016) and open circles from Ludlam et al. (2015) and sample from Ponti et al. (2012) black dots. The solid line is the best fit given for the Ponti et al. (2012) sample which shows a significant difference to the best fit (dashed line) when all the low mass SMBHs are also included. Figures from Pan et al. (2016).

3.5.1 Bulge Stellar Mass

Using a sample of 36 local galaxies observed by the Hubble Space Telescope (HST), Magorrian et al. (1998) show a relationship between the galaxy bulge (defined as the mass of the hot stellar component) and the mass of the central black hole, with a correlation $M_{\rm BH} \simeq 0.005 M_{\rm bulge}$ (though with a large scatter). The masses of the SMBH were derived from modelling of kinematics (velocity dispersion together with rotational speed) of the galaxy.

Later studies improved this relation after determining that the masses modelled by Magorrian et al. (1998) were overestimated, sometimes by as much as a factor of ten. Häring and Rix (2004), for example, use a sample of 30 local galaxies. 20 of the bulge masses were from literature with a further 10 from solving the Jean equation:

$$\frac{d(\rho_* \sigma_r^2)}{dr} + 2\frac{\beta \rho_* \sigma_r^2}{r} = -\rho_* \frac{d\Phi_*}{dr} \tag{3.16}$$

where r is the radius, ρ_* is the stellar mass density of the bulge, σ_r is the stellar velocity dispersion, β is the anisotropy in the velocity (set to zero as assumes the galaxies are isotropic) and Φ_* is the total potential due to the stars and is derived from an assumed constant mass-to-light ratio Υ.

They find a relation of $M_{\rm BH} \simeq 0.0014 M_{\rm bulge}$. Figure 3.12 shows this relationship together with a comparison of 27 galaxies (with 20 in common) from Marconi and Hunt (2003) who related literature values of $M_{\rm BH}$ to bulge mass from an estimation from velocity dispersion and who find a relation in statistical agreement of $\simeq 0.002\, M_{\rm bulge}$.

3.5.2 Stellar Velocity Dispersion

Another scaling relation comes from the correlation between $M_{\rm BH}$ and velocity dispersion σ. Gebhardt et al. (2000) use the masses of a sample of 26 galaxies to describe a tight correlation between $M_{\rm BH}$ and the luminosity-weighted line-of-sight velocity dispersion. The $M_{\rm BH}$ are taken from literature, 18 derived from stellar dynamics, six from gas dynamics and two from maser dynamics. The velocity dispersion σ_e values are estimated from a region at R_e, the effective half-light radius rather than from a central region, since the variation in the dispersion profile tends to be small between $0.5R_e$ and $2R_e$. Figure 3.13 shows the relation between the $M_{\rm BH}$ and bulge luminosity (left) and between $M_{\rm BH}$ and σ_e (right) with a best fit line:

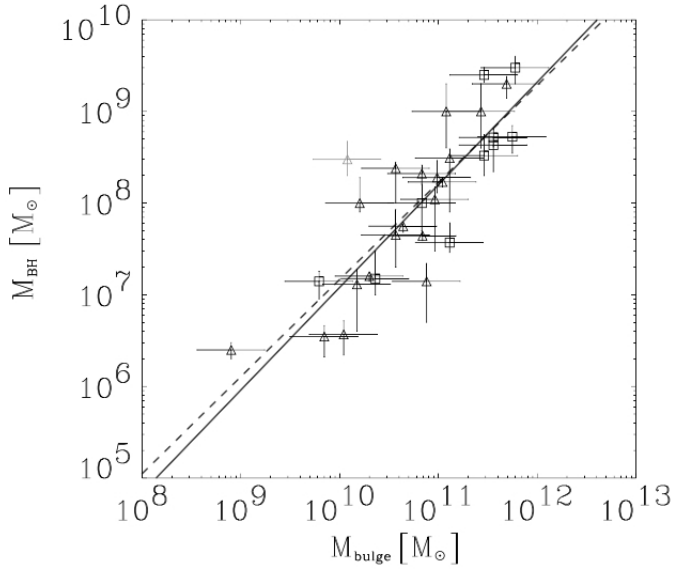

Figure 3.12: $M_{\rm BH}$ plotted against bulge mass for 30 galaxies. The solid line is the line of best fit relation from Häring and Rix (2004). Squares are galaxies where bulge mass is determined by solving Eq. 3.16, triangles where bulge mass is from literature. The dotted line is the relation from Marconi and Hunt (2003).

$$M_{\rm BH} = 1.2 \times 10^8 M_\odot \left(\frac{\sigma_e}{200\,{\rm km\,s^{-1}}} \right)^{3.75\pm0.3} \tag{3.17}$$

This tight correlation between $M_{\rm BH}$ and σ_e is further reflected in subsequent studies by Ferarrase and Merritt, though with steeper slope, 4.8 ± 0.5 in Ferrarese and Merritt (2000), 4.72 ± 0.36 in Merritt and Ferrarese (2001) and 4.58 ± 0.52 in Ferrarese (2002). Tremaine et al. (2002) report a slope of 4.02 ± 0.32 and suggest that these discrepancies can be accounted for by the systematic differences in the estimation of the velocity dispersion of the same galaxy by the different groups. However, Kormendy and Ho (2013) have suggested that only elliptical and classic bulges follow a $M_{\rm BH} - \sigma$ relation and that it is not valid for disk galaxies and pseudobulges.

3.5.3 Bulge Light Concentration Parameter

A final scaling relation can be derived by estimating a parameter, $C_{r_e}(1/3)$ (Trujillo et al. 2001) based on the concentration of bulge light of the galaxy, rather than simply the absolute luminosity (for which the scaling relation with SMBH results in a large scatter McLure and Dunlop 2002). Using data from 23 galaxies, Graham et al. (2001) find a tight

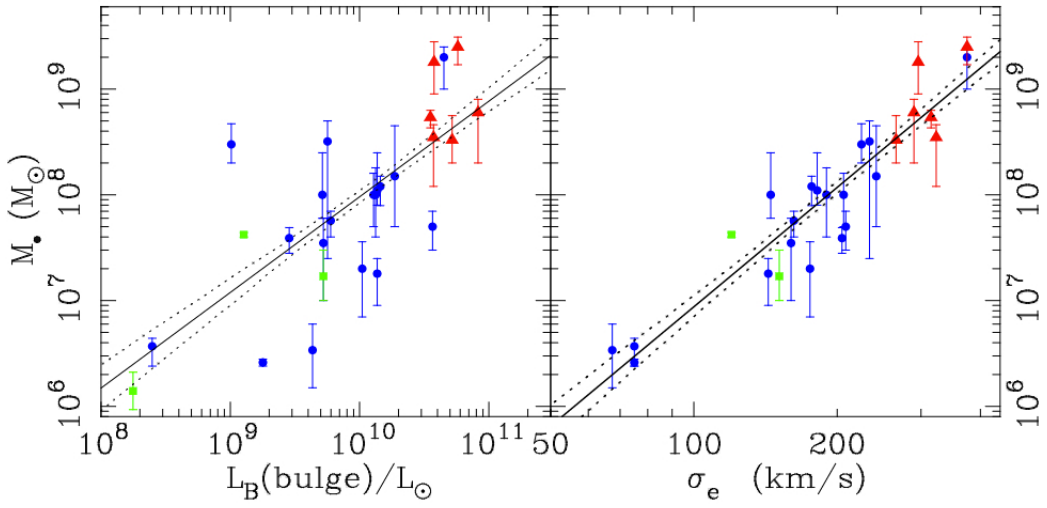

Figure 3.13: $M_{\rm BH}$ plotted against bulge luminosity (right) and luminosity-weighted aperture dispersion for 26 galaxies. Green squares are for $M_{\rm BH}$s from maser detections, red triangles from gas kinematics and blue circles from stellar kinematics. Solid line is the best fit with 68% confidence dotted line. Image from Gebhardt et al. (2000)

correlation between this parameter and the associated $M_{\rm BH}$ as shown in Fig. 3.14 with a best fit of:

$$\log(M_{\rm BH}) = (6.81 \pm 0.95)C_{r_e} + (5.03 \pm 0.41) \tag{3.18}$$

3.6 Evolution of Growth of SMBH and Host Galaxy

An important area to consider is the co-evolution of SMBH and host galaxy and to what extent they regulate each others growth.

From hydrodynamic simulations of the ΛCDM cosmological model that incorporate the growth of black holes and associated AGN, Di Matteo et al. (2008) find a strong correlation between $M_{\rm BH}$ and stellar velocity dispersion and between $M_{\rm BH}$ and stellar mass. Their results agree with observations in the local Universe, and thus a reflect a good representation of the underlying physics. They also find a weak evolution with redshift in the normalisation and slopes for each relation.

Other more recent simulation work by DeGraf et al. (2012), investigating the growth rate of SMBHs in the early Universe has found that SMBHs grow more quickly at higher redshifts. They also found that the growth-rate (λ) scales as $(1 + z)^3$, with more massive

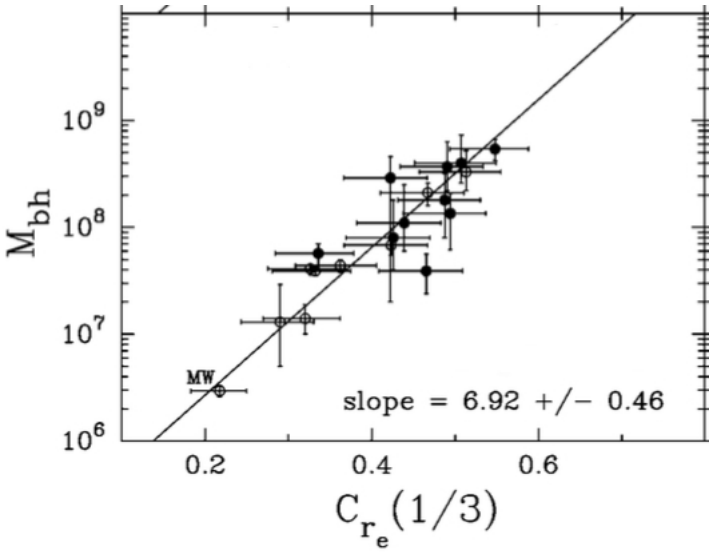

Figure 3.14: $M_{\rm BH}$ plotted against the bulge concentration parameter $C_{r_e}(1/3)$ for 23 galaxies. Image from Graham et al. (2001).

black holes growing faster than lower mass ones up to a maximum rate reached between 4-8 x$10^7 M_{\odot}$. They attribute this to the interplay between SMBH and host galaxy regulating the growth of the SMBH. In this scenario, in its early life, the SMBH grows quickly until a point when AGN feedback begins to affect the growth of the local gas density in the surrounding environment and hence the SMBH itself. Figure 3.15 shows the relation between black hole growth rate and $M_{\rm BH}$ across a range of redshifts and also shows that for $z > 4.75$ this relation is independent of mass.

In reviewing the co-evolution of SMBH and host galaxy from observational studies, however, Kormendy and Ho (2013) suggest that recent results show that applying this strong co-evolution of SMBH with host galaxy is too simplistic. They suggest that SMBHs correlate differently depending on the galaxy environment and its components with non-AGN physics being the dominating factor.

Therefore, to investigate the extent of co-evolution between SMBH and host galaxy, it would be hugely advantageous to estimate the $M_{\rm BH}$ of as many SMBH as possible at a range of redshifts, and this is where the work described in Chapter 4 of this thesis may be of particular use.

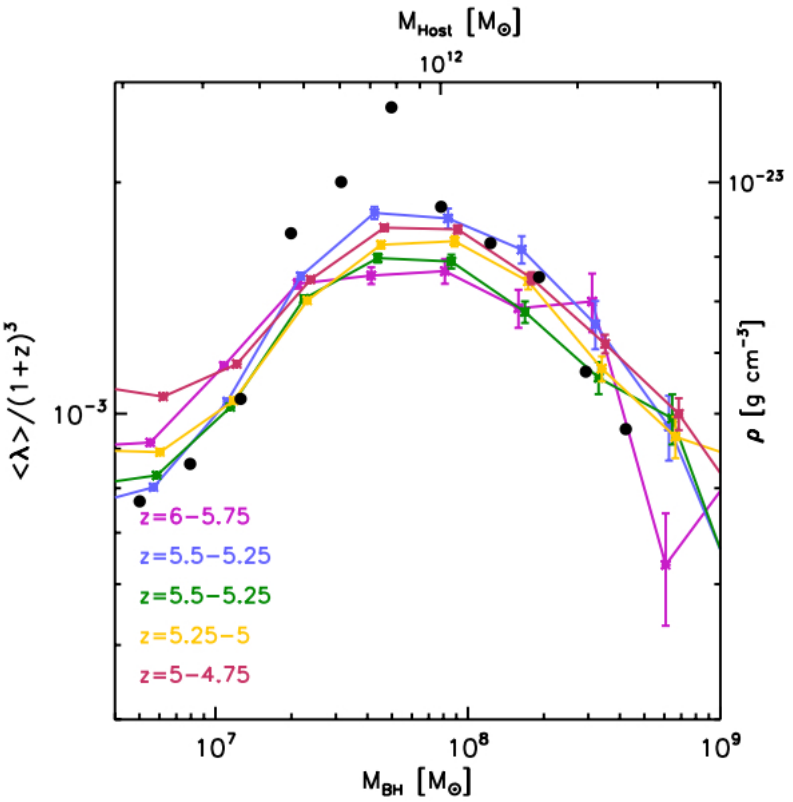

Figure 3.15: SMBH growth rate, λ, scaled by $1/(1+z)^3$ as a function of $M_{\rm BH}$ for a range of redshifts as shown in the different colours. The typical host galaxy mass is shown on the top-axis. Filled circles are average gas density, shown on the right axis, at the position of the SMBH. Image from DeGraf et al. (2012).

3.7 Chapter Summary

In this chapter we have summarised the methods of estimating the masses of SMBHs. This is central to deriving scaling relations with that of its host galaxy. We have shown that, while in the local Universe the best estimates of $M_{\rm BH}$ come from stellar, gas and megamaser dynamics, at higher redshifts estimates from reverberation mapping of AGN are the only direct method available. We have summarised studies that have indicated a high correlation between $M_{\rm BH}$ from reverberation mapping and X-ray variability of AGN and that this variability can be expressed as the normalised excess variance, $\sigma^2_{\rm NXS}$, of a light-curve. We aim to derive relations between $\sigma^2_{\rm NXS}$, $L_{\rm X}$ and $M_{\rm BH}$ to use as an indirect mass estimates where reverberation mapping is not possible and to probe to higher redshift. In the next chapter, we do just that.

Chapter 4

Correlations Between X-ray Properties and Black Hole Mass in AGN: Towards New Methods to Estimate Black Hole Mass from Short Exposure X-ray Observations of AGN

4.1 Introduction

The work presented in this chapter has been submitted as a journal article to MNRAS Mayers et al. (2018).

In the previous chapter, we summarised methods of estimating the masses of SMBH from the X-ray parameters, $\sigma^2_{\rm NXS}$ and $L_{\rm X}$, associated with AGN and how they scale with $M_{\rm BH}$ (from reverberation mapping). We highlighted previous studies that have shown the $\sigma^2_{\rm NXS}$ can be used to provide a quick and good estimate of $M_{\rm BH}$ (§3.4.7) and that it is anti-correlated with both $M_{\rm BH}$ and $L_{\rm X}$, and is independent of AGN orientation.

In this study, we re-examine these correlations and, for the first time in the literature, we attempt to test for potential redshift evolution in the correlations.

Thus far $\sigma^2_{\rm NXS}$ has been measured for less than a few hundred AGN, mostly at low redshift, due for a need for long (> 10 ks) observation exposure. So its use as a method to estimate $M_{\rm BH}$ for much higher samples of AGN is limited.

Our goal is to determine the reliability of $M_{\rm BH}$ estimates derived from $L_{\rm X}$ measurements alone - in the case where X-ray variability information is not available. We explore the specific case of the eROSITA mission, which will measure hundreds of thousands of $L_{\rm X}$ values for AGN, but very few – if any – values of $\sigma^2_{\rm NXS}$. This, in turn, may allow us to investigate the relationships between $M_{\rm BH}$, $L_{\rm X}$ and $\sigma^2_{\rm NXS}$ as a function of redshift and apply the results to the study of galaxy growth.

Section 4.2 describes how sources were identified, cross-matched with literature and how we determined our survey sources. Section 4.3 describes methods used to measure $\sigma^2_{\rm NXS}$ and $L_{\rm X}$ (as well as spectral index Γ). Section 4.4 presents the measured correlations between the X-ray observables and $M_{\rm BH}$. Evolution in these correlations is tested, as are various aspects of the methodology. Section 4.7 looks ahead to the launch of eROSITA and forecasts the potential to derive $M_{\rm BH}$ estimates from eROSITA luminosity measurements. Section 4.8 presents discussions and future directions.

4.2 Data

4.2.1 A New Sample of X-ray Detected AGN

Our X-ray sample is drawn from latest XCS catalogue of X-ray sources as described in Section 2.3. In addition to collating detections of extended X-ray sources, i.e. cluster candidates, XCS also identifies serendipitous and targeted point-like X-ray sources. The XCS source catalogue grows with the size of the XMM public archive. At the time of writing, it contained over 250,000 point sources.

For our study, we limit ourselves only to point-like sources detected by the XCS Automated Pipeline Algorithm (`XAPA`) with more than 300 (background subtracted) soft-band photons. LD11 showed that, above that threshold, the XCS morphological classification (point-like versus extended) is robust. There are 12,532 such sources in the current version of the XCS point source catalogue. Using TOPCAT, their positions have been compared to those of known AGN in the 13th edition of Veron-Cetty and Veron (2010) (VC13)

Sample	Description	No.
(1)	(2)	(3)
Initial	XCS sources in VC13 and/or SDSS-DR12Q	2039[1] (46)
S0	AGN $> 1^\circ$ outside of Galactic plane	1316 (38)
S1	S0 and L_X value where $\frac{\Delta L_X}{L_X} < 1$	1091 (31)
S10	S1 and $\geqslant$5 10 ks light-curve segments	88 (12)
S20	S1 and $\geqslant$5 20 ks light-curve segments	53 (11)
S40	S1 and $\geqslant$5 40 ks light-curve segments	25 (7)

Table 4.1: Table defining samples of AGN used in the analysis. (1) sample name, (2) defines how the sample was filtered, (3) the number of AGN in the sample and in brackets the number with masses from reverberation mapping. [1]1689 from VC13, 513 from DSDSS-DR12Q with 163 common to both.

catalogue (168,940 quasars and AGN), and the SDSS-DR12Q Quasar Catalog (297,301 quasars) Kozłowski (2016).

The matching radius was set to a conservative value of 5 arcsec (LD11 find 95 per cent of matches fall within within 6.6 arcsec with a 1 per cent chance of false identification within 10 arcsec). We find 2039 matches to XCS point sources ($>$ 300 counts): 1,689 sources in VC13 and 513 in SDSS DR12Q, with 163 in common[1]. Figure 4.1 shows the distribution of separation between XCS point sources and AGN positions in both catalogues. The darker bars are where the separation is $<$5 arcsec. After removing sources within 10° of the Galactic plane, 1,316 remained sources in our sample (Sample-S0 hereafter, see Table 4.1).

[1]Including XCS point sources with fewer than 300 counts, the number of matches increases to 6,505 sources in VC13 and 6,339 in SDSS DR12, with 890 sources in common.

Survey	Type	No.	10 ks	20 ks	40 ks	z
(1)	(2)	(3)	(4)	(5)	(6)	(7)
XCS	Targeted and serendipitous (XMM)	1316	446(63)	292(41)	148(20)	0.001-4.9
Ponti et al. (2012)	Radio quiet targeted (XMM)	161	51	58	45	0.001-4.52
O'Neill et al. (2005)	Radio quiet targeted (ASCA)	68			46	0.001-0.234
Zhou et al. (2010)	Reverb. mapped AGN (ASCA/XMM)	21			21	0.001-0.14

Table 4.2: Comparison between our survey sample and previous similar studies. (1) survey name, (2) detector (3) type of AGN analysed (4) total number of AGN in survey (5) Number of AGN with at least one good 10 ks light-curve segment and in brackets number of these with five or more segments as used in our analysis. (6),(7) as (5) for 20 ks and 40 ks light-curve segments. (8) redshift range.

Redshifts for the AGN in Sample-S0 are taken from VC13 or from SDSS-DR12Q - if the AGN appears in both catalogues, the VC13 value was used (there is minimal difference in redshift for AGN appearing in both catalogues). Many of the AGN were detected in multiple XMM observations. A total of 2,649 XMM observations have been included in the analyses of Sample-S0 presented herein. The distributions of redshift for each AGN, off-axis angle and the full observation duration (i.e. before flare correction) of the 2,649 individual observations are shown in Figure 4.2.

4.3 Data Reduction

4.3.1 Extracting Light-curves and Estimating Variability

For each[2] PN observation of the 1,316 AGN in Sample-S0, we generate a clean event list which takes into account flare cleaning according to the methodology of LD11. We note that, for this study, we use only PN detector data, because the other two EPIC camera detectors (MOS1 and MOS2) are less sensitive, especially in the soft, $0.5-2.0\,\mathrm{keV}$ energy band.

We extract the source light-curve from a circular region $20''$ in radius centred on the XAPA defined coordinate for the AGN. We extract a background light-curve from a circular annulus centred on the same coordinate, with inner and outer radii of $50''$ and $60''$ respectively. If other X-ray sources overlap with the source or background apertures, they are 'cheesed out' using $20''$ radius circles. We then generate rest frame $0.3-10.0\,\mathrm{keV}$ source and background light-curves in the PN detector in 250 sectime bins using the XMM Science Analysis System (SAS) script, for example:

evselect table = PN_evt.fits energycolumn = PI
expression =′ XMMEA_EP(PATTERN <= 4)&&
((X, Y) IN circle(DETX, DETY, 400))&&(PI in[300 : 10000])′
withrateset = yes rateset = 'PN source_lightcurve.lc′
timebinsize = 250 maketimecolumn = yesmakeratecolumn = yes

(This is a similar method to Kamizasa et al. 2012 with the exception that they choose a rectangular background).

[2]Many of the AGN were observed by the XMM-Newton EPIC-PN camera several times.

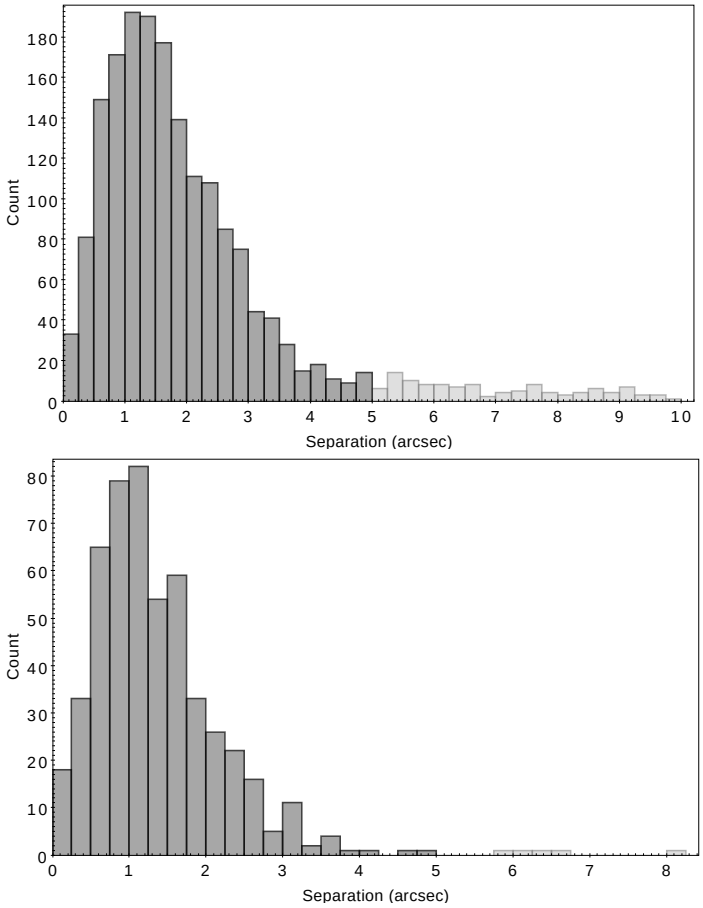

Figure 4.1: Angular offset (in arcsecs) between the locations of XCS point sources (with more than 300 background subtracted soft counts) and positions of AGN in the V13 (top) or SDSS-DR12Q (bottom) catalogues. Only those 1,316 AGN within 5″ (dark shaded) of an XCS point source are included in the analyses herein (Sample-S0 in Table 4.1).

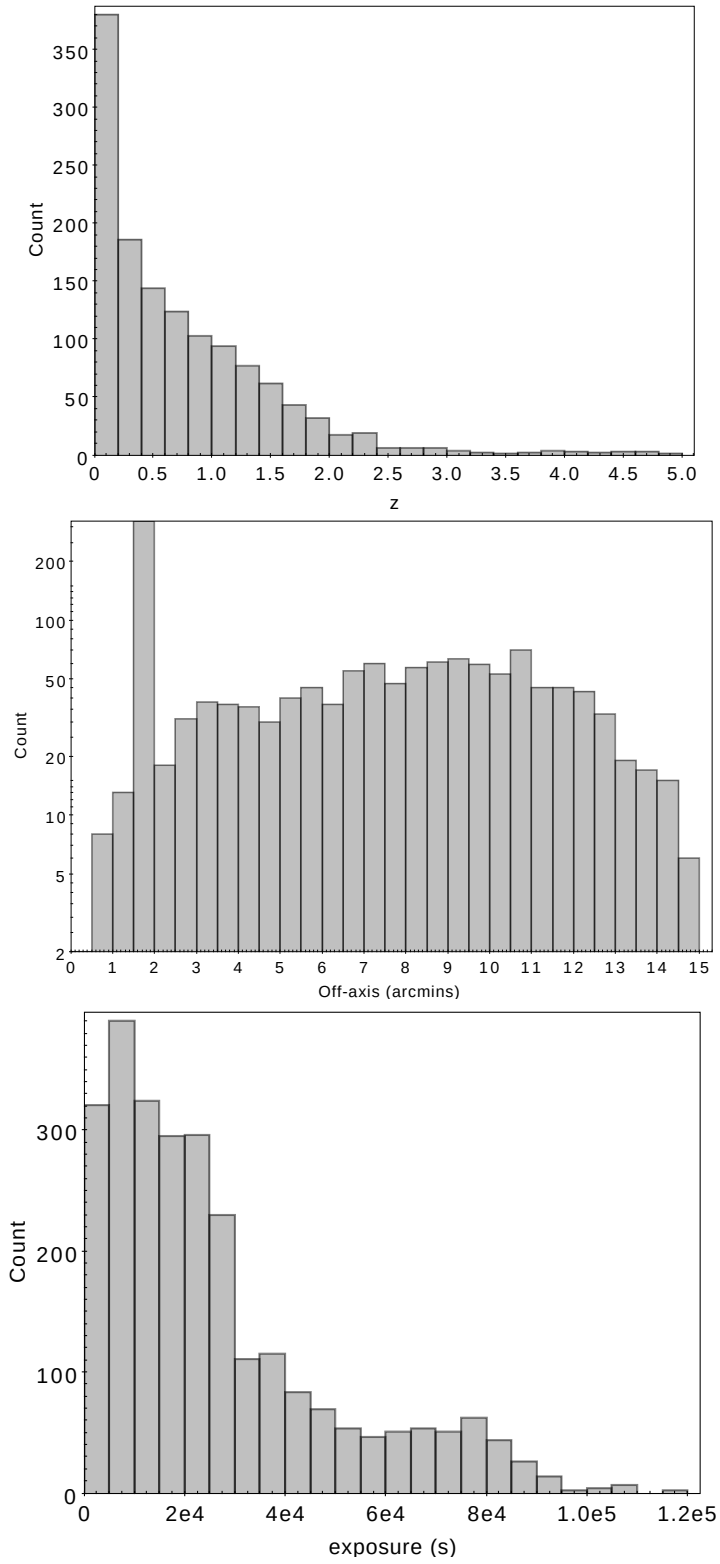

Figure 4.2: Properties of the 1,316 AGN in Sample-S0 (see Table 4.1). Top: Redshift distribution. Middle: Angular offset (arc minutes) between the AGN location and the aim point of the respective XMM observation. Bottom: Full, i.e. before flare correction, XMM `PN` camera exposure time of the respective XMM observation.

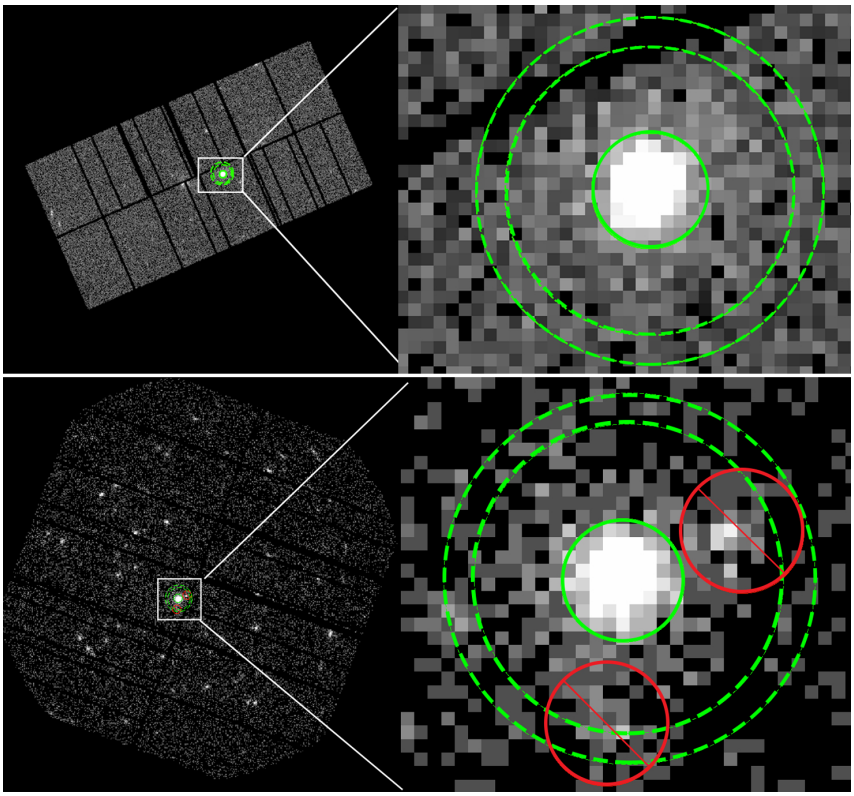

Figure 4.3: Top. X-ray full and 16x zoomed image from PN detector of ObsID 0673580301 showing 20″ radius source and 50 − 60″ extraction regions of AGN candidate XMMXCSJ132519.2-382455.2 (IRAS 13224-3809 in VC13), redshift 0.65, Bottom. X-ray full and 16x zoomed image from PN detector of AGN candidate XMMXCSJ152553.9+513649.3 in ObsID 0011830201 with two nearby point sources masked. In each case, pixel size 4.52″ in energy range 2 − 10 keV.

Figure 4.3 shows typical EPIC-PN images of AGN in our sample. The source extraction regions are defined by the solid green circles, and the background regions by the dashed green circles. The bottom image shows an AGN with two nearby point sources (red circles). Areas that overlap between the red circles and the green dashed annulus are excluded from the light-curves.

The background subtracted light-curve is produced using the SAS task EPICLCCORR. From this we derive an initial $\sigma^2_{\rm NXS}$ value from Equation 3.14. Figure 4.4 shows the background corrected light curves for the AGNs featured in Figure 4.3.

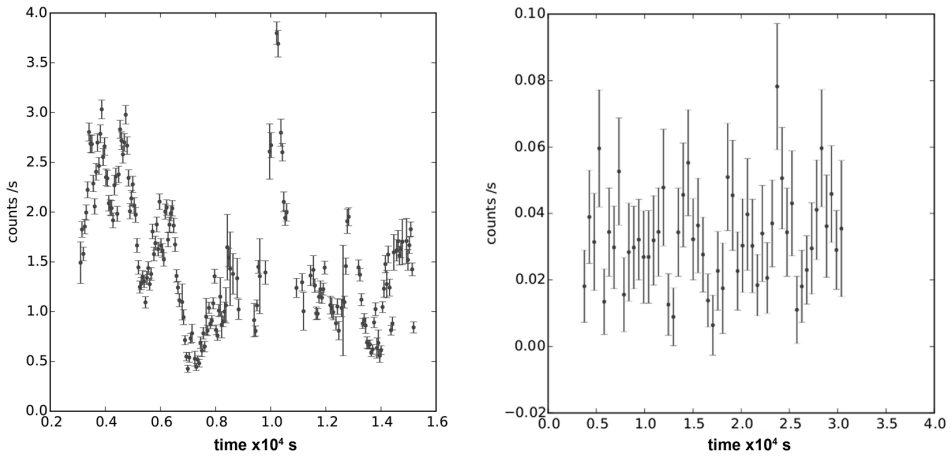

Figure 4.4: Background corrected light curves for AGN point-sources XMMXCSJ132519.2-382455.2 (left) and XMMXCSJ152553.9+513649.3 (right) taken from ObsID 0673580301 and 0011830201 respectively, with source and background regions extracted as Figure 4.3, in 250 secs and the energy range $0.3 - 10$ keV.

4.3.2 Spectral Fitting and Luminosity Estimates

For each `PN` observation of the 1,316 AGN in Sample-S0, we extract spectra. The spectra are generated using the same same source, background and clean event lists used to generate the light-curves (see Section 4.3.1).

The `arfgen` and `rmfgen` commands in `SAS` were used to generate the associated ancillary response files and detector matrices. The spectra were grouped such that there are a minimum of 20 counts in each channel. We fit spectra in the $0.2 - 10.0$ keV energy range to a typical AGN model (e.g. Kamizasa et al. 2012) using `XSPEC` v12.8.2:

```
phabs*cflux(powerlaw + bbody)
```

The free parameters in the fit were the powerlaw index (Γ) and black body temperature and normalisation. All other parameters in the model are fixed (where $n_{\rm H}$ is taken from Dickey and Lockman 1990b). From the best fit model, we estimated the hard-band ($2.0 - 10.0$keV) luminosity ($L_{\rm X}$), and 68.3% confidence level upper and lower limits.

If the difference between the upper and lower limit on the luminosity ($\Delta L_{\rm X}$) was larger than the best fit value, i.e. $\frac{\Delta L_{\rm X}}{L_{\rm X}} > 1$ then the respective AGN was excluded from further analyses. The remaining sample contained 1,091 AGN (making this the largest study of the X-ray spectral properties of AGNs) and is referred to as Sample-S1 hereafter (see

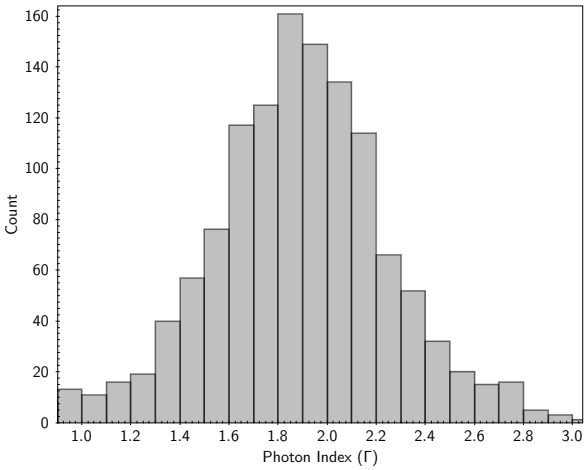

Figure 4.5: Histogram of hard-band photon index Γ, in Sample-S1 (1091 AGN).

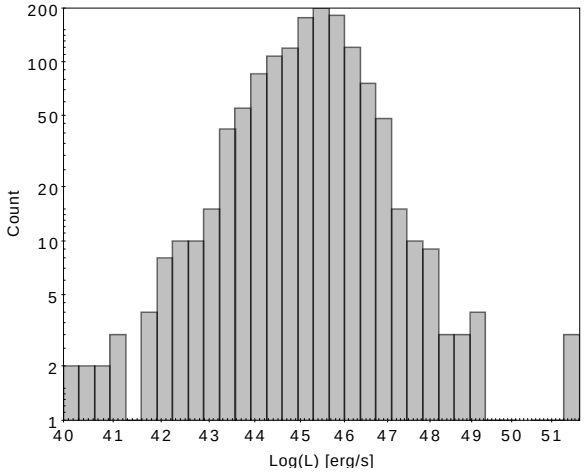

Figure 4.6: Histogram of hard-band luminosity in Sample-S1 (1091 AGN).

Table 4.1). The median $\frac{\Delta L_{\rm X}}{L_{\rm X}}$ of this sample is 0.16.

Figures 4.5 and 4.6 show the distribution of power law index (Γ) and hard-band luminosity for Sample-S1. Where there are multiple observations of the same source we use the value derived from the observation with the longest exposure time. Figure 4.7 shows the redshift distribution versus hard-band-luminosity for Sample-S1.

The average hard-band spectral index was measured to be $\bar{\Gamma} = 1.81 \pm 0.34$. This compares well with previous determinations: Nandra and Pounds 1994 measured $1.9 < \Gamma < 2.0$ using Ginga Large Area proportional Counter observations of 27 AGN. Corral et al. (2011) found $\bar{\Gamma} = 2.05 \pm 0.03$ using XMM observations of 305 AGN. Unlike previous studies, e.g. Connolly et al. (2016) and Corral et al. (2011), we find no evidence for an anti-correlation

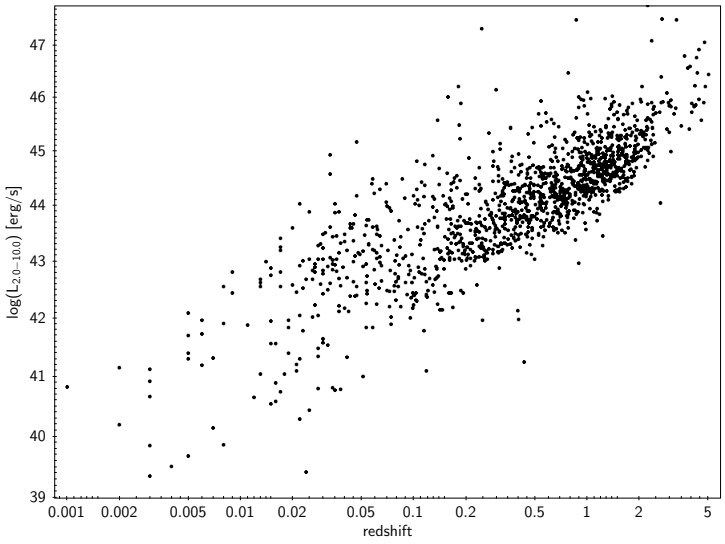

Figure 4.7: Redshift distribution of hard-band luminosity in Sample-S1 (1091 AGN).

between power law and luminosity.

4.3.3 Determining Normalised Excess Variance

In this project we use the $\sigma^2_{\rm NXS}$ (as defined in Section 3.4.7) to measure the variability of our AGN sample as it is a very quick parameter to estimate across a large sample of AGN. We begin by generating light-curves as described in Section 4.3.1.

The light-curves were divided into equal segments of 10 ks (then again into segments of 20 ks and 40 ks). As we used Gaussian statistics to derive a value of variability, we required a minimum of twenty time bins (of 250 secduration) per light-curve segment. Each time bin was required to have a minimum of 20 counts after correction for the effective fractional exposure (EFE). The EFE corrects for effects such as chip gaps and vignetting. Its value is stored in the `FRACEXP` parameter in the header of the background subtracted light-curve *.fits* file. Following the method of O'Neill et al. (2005), any bin with `FRACEXP` $<$ `0.35` is rejected, even if the corrected counts is $\geqslant 20$. Again following O'Neill et al. (2005), segments are rejected if they contain one or more bins with $\leqslant 20$ where the fractional exposure is high (`FRACEXP` $>$ `0.9`).

We also tested whether each of the light-curve segments for an individual AGN are in themselves *variable* by performing the chi-squared probability of constancy test included within the `SAS` task `EKSTEST`. Following Ponti et al. (2012), we rejected any segment where the probability that the segment is not variable is > 0.01.

The uncertainty on an individual measurement of $\sigma^2_{\rm NXS}$ has been been estimated by Vaughan et al. (2003b). This method takes into account both the uncertainty in measurement in each time bin as well as the stochastic variability of the light-curve itself:

$$\Delta(\sigma^2_{\rm NXS}) = \sqrt{\left(\sqrt{\frac{2}{N}}.\frac{\overline{\sigma^2_{err}}}{\bar{x}^2}\right)^2 + \left(\sqrt{\frac{\overline{\sigma^2_{err}}}{N}}.\frac{2\sigma_{nxs}}{\bar{x}}\right)} \tag{4.1}$$

where $\overline{\sigma^2_{err}}$ is the mean square error.

Using this equation, we reject segments where $\Delta\sigma^2_{\rm NXS}/\sigma^2_{\rm NXS} > 1$. All remaining segments are labelled as *good*.

4.3.4 Mitigation of red-noise

AGN exhibit a-periodic *red-noise*, whereby there is an inherent uncertainty in the long-term variability due to the stochastic nature of AGN emission. As a result, an AGN light-curve generated at a given epoch is just one of many manifestations of the light-curve that the AGN will exhibit over its lifetime (see Vaughan et al., 2003a). Estimating *red-noise* is difficult, as it depends on the steepness the of the PSD of the AGN. Thus, uncertainty regarding *red-noise* would persist even if the measurement errors on a given $\sigma^2_{\rm NXS}$ could be reduced to zero. This is demonstrated in Figure 4.8, which shows light curves for an AGN that was observed by XMM at multiple epochs, the offset in the normalization between the six curves demonstrates the underlying stochastic variability. Figure 4.9 shows the respective $\sigma^2_{\rm NXS}$ value (across the duration of the observation rather than in 10, 20 or 40 ks segments) measured from these observations, with the x-axis showing the start of observation in XMM mission time. The dark and light grey shaded areas represent the 1 and 2σ scatter regions relative to the best fit $L_{\rm X}$-$\sigma^2_{\rm NXS}$ [20ks] relation (as defined in Figure 4.11) at the mean LX of this AGN (i.e. all the $\sigma^2_{\rm NXS}$ measurements are within 2σ of the derived $L_{\rm X}$-$\sigma^2_{\rm NXS}$ relation.)

We also note that since each segment is of a fixed time interval, Equation 3.15 reduces to:

$${}^*\sigma^2_{\rm NXS} = \sigma^2_{\rm NXS}(1+z)^{2\beta} \tag{4.2}$$

(This correction makes only a small difference at low redshift, and although we use ${}^*\sigma^2_{\rm NXS}$ throughout, we will continue to refer to this parameter as $\sigma^2_{\rm NXS}$ hereafter).

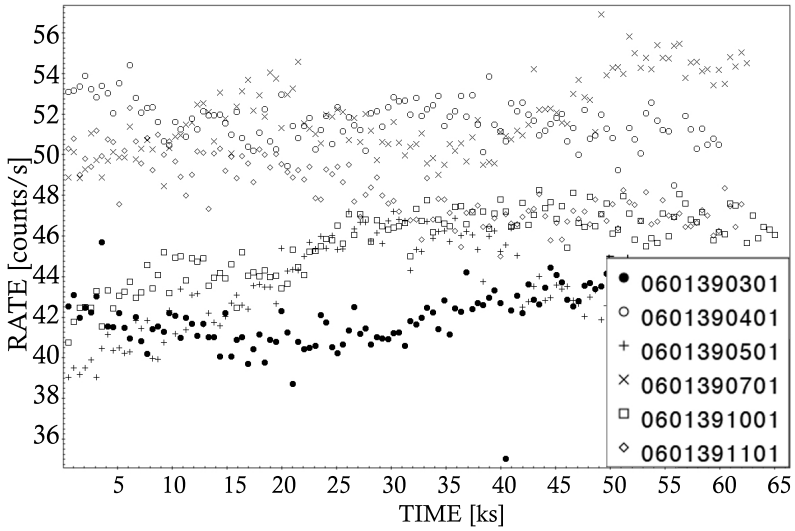

Figure 4.8: The PN detector light-curves in 250 sec bins of the AGN XMMXCSJ204409.7-104325.8 in ObsIDs 0601390301, 0601390401, 0601390501, 0601390701, 0601391001 and 0601391101 (0.5-10 keV).

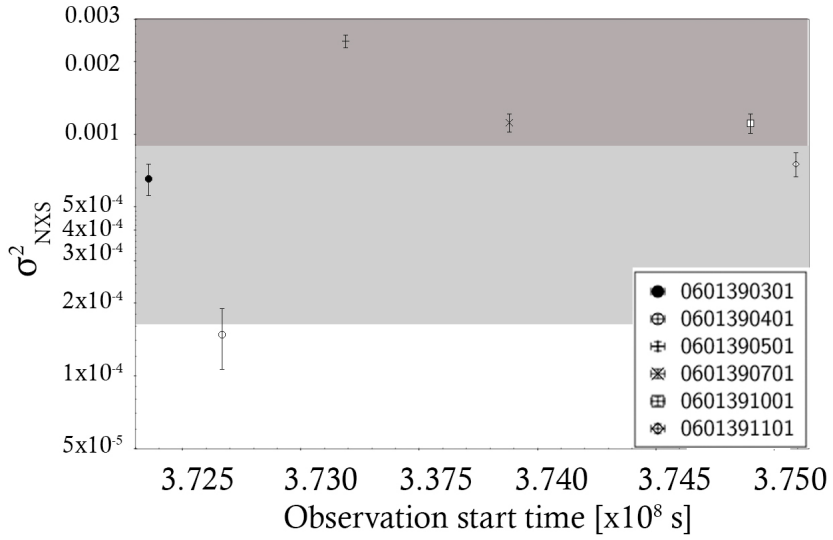

Figure 4.9: The measured $\sigma^2_{\rm NXS}$ value for the AGN XMMXCSJ204409.7-104325.8 using the lightcurves shown in Figure 4.8. The respective observation start time is indicated on the x-axis. For reference, we show the 1 and 2σ (dark and light grey respectively) confidence regions relative to the best fit $L_{\rm X}$-$\sigma^2_{\rm NXS}$ [20ks] relation at the mean $L_{\rm X}$ for this AGN (see Figure 4.11).

For each AGN we derive an unweighted mean value for $\sigma^2_{\rm NXS}$ from all *good* 10 ks (20 ks, 40 ks) light-curve segments. We calculate the 1σ uncertainty on this mean value as:

$$\Delta\sigma^2_{\rm NXS} = \frac{\sigma^2_{\rm NXSmax} - \sigma^2_{\rm NXSmin}}{2\sqrt{N_{\rm segs}}} \tag{4.3}$$

where $\sigma^2_{\rm NXSmax}$ and $\sigma^2_{\rm NXSmin}$ are the maximum and minimum variability values, and $N_{\rm segs}$ is the number of *good* 10 ks (20 ks, 40 ks) segments.

For our correlation analysis, we have only included AGN with five or more good segments and where the mean value of $\sigma^2_{\rm NXS} > 0$, shown as dark bars in Figure 4.10, (see Section 4.6.3 for a discussion). Figure 4.10 shows number of AGN with *good* 10 ks, 20 ks and 40 ks segments available from the AGNs in Sample-S1.

4.3.5 S10, S20, S40 sub-samples

From this approach we defined three different sub-samples as S10, S20 and S40. These contain 63, 41 and 20 AGN respectively. All $L_{\rm X}$, $\sigma^2_{\rm NXS}$ and Γ values derived for the AGN in these samples as well as $M_{\rm BH}$ from reverberation mapping studies and AGN type are combined in Table B.1 in Appendix B. These sub-samples were used to investigate the correlations between X-ray properties and $M_{\rm BH}$.

With regard to $M_{\rm BH}$, these values were taken from Bentz and Katz (2015), using a cross match radius of 5 arcsec. The number of Bentz and Katz (2015) masses for each of the respective sub-samples are listed in Table 4.1. With regard to AGN type, these were taken primarily from VC13 (where AGN type is based of the appearance of the Balmer lines) and in the case of two not given in VC13, supplemented by information in the SIMBAD database of astronomical objects (Wenger et al., 2000). Accordingly; 52 of the 89 AGN in the table are classed solely as Type 1, six as Type 1.2, fifteen as 1.5, four as 1.8, one as 1.9 and one as Type 2. The rest are classified as BL (Blazars) and Q (Quasars i.e. a high luminosity and redshift AGN), see § 4.8.1 for a discussion.

4.4 Correlations Between X-ray properties and Black Hole Mass

We use the regression method of Kelly (2007) to derive relationships between: i) AGN hard-band luminosity $L_{\rm X}$ and normalised excess variance $\sigma^2_{\rm NXS}$, ii) $\sigma^2_{\rm NXS}$ and $M_{\rm BH}$, and iii) $L_{\rm X}$ and $M_{\rm BH}$. The $M_{\rm BH}$ are taken from the Bentz and Katz (2015) database of rever-

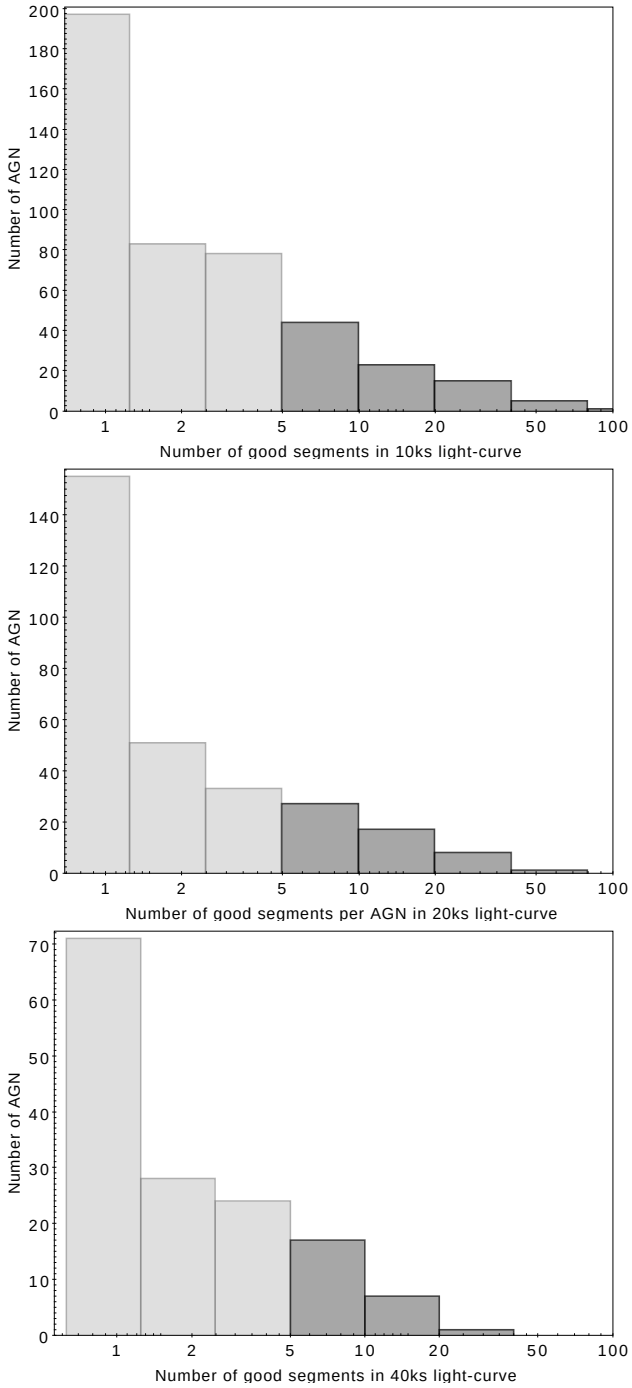

Figure 4.10: Histogram of number of AGN with *good* 10 ks (top), 20 ks (middle) and 40 ks (bottom) segments from our Sample-S1. The dark bars are for AGN with five or more segments.

Seg. dur.	Norm	Slope	Scatter	Correlation	Correlation
[ks]	π	α	σ	unweighted	weighted
(1)	(2)	(3)	(4)	(5)	(6)
10	0.0026±0.001	-1.13±0.20	1.09±0.38	-0.91	-0.92
20	0.0036±0.0013	-1.07±0.18	1.01±0.4	-0.93	-0.95
40	0.075±0.054	-1.31±0.5	1.53±1.11	-0.91	-0.91

Table 4.3: Correlations between black hole mass from Bentz and Katz (2015) and $\sigma^2_{\rm NXS}$ of the form $\log(\sigma^2_{\rm NXS}) = \pi \log(\rm M/M_{piv})^{\alpha}$ where there are five or more good light curve segments for each of the segment duration length in column (1). (2) normalisation, (3) slope, (4) σ scatter, (5) Pearson's product moment correlation coefficient, (6) as (5) weighted on $\sigma^2_{\rm NXS}$ error. $\rm M_{piv} = 2x10^7 M_{\odot}$

beration mapped black holes, using a cross match radius of 5″. The number of Bentz and Katz (2015) masses for each of the respective subsamples are listed in Table 4.1.

The relationship between $\sigma^2_{\rm NXS}$ and $L_{\rm X}$ is shown in Figure 4.11 and Table 4.5. The relationship between $M_{\rm BH}$ and $\sigma^2_{\rm NXS}$ is shown in Figure 4.12 and Table 4.3. The relationship between $M_{\rm BH}$ and $L_{\rm X}$ is shown in Figure 4.13 and Table 4.4. Significant correlations can be seen in all cases. There is a negative correlation between $\sigma^2_{\rm NXS}$ and $L_{\rm X}$, i.e. brighter AGN are less variable. There is also a negative correlation between $\sigma^2_{\rm NXS}$ and $M_{\rm BH}$, i.e. more massive black holes are surrounded by less variable AGN. Not surprisingly, therefore, there is a positive correlation between $L_{\rm X}$ and $M_{\rm BH}$, i.e. brighter AGN contain more massive black holes.

Our results are consistent with previous studies that have demonstrated an anti-correlation between luminosity and variability, e.g. Ponti et al. (2012), O'Neill et al. (2005), Barr and Mushotzky (1986), Lawrence and Papadakis (1993). We cannot compare slopes, scatter and normalisation directly that we measure to those in other studies because of our differing approach to fitting. Therefore, we have applied our fitting method to the variability and $L_{\rm X}$ data in Ponti et al. (2012), see Figure 4.14. We note that what we call $\sigma^2_{\rm NXS}$[20ks], they define as `s20`, albeit with a different approach to error estimation. The fitting results are compared in Table 4.5 and show an excellent agreement (comparing rows labeled 20 and 20^{CAIXA}).

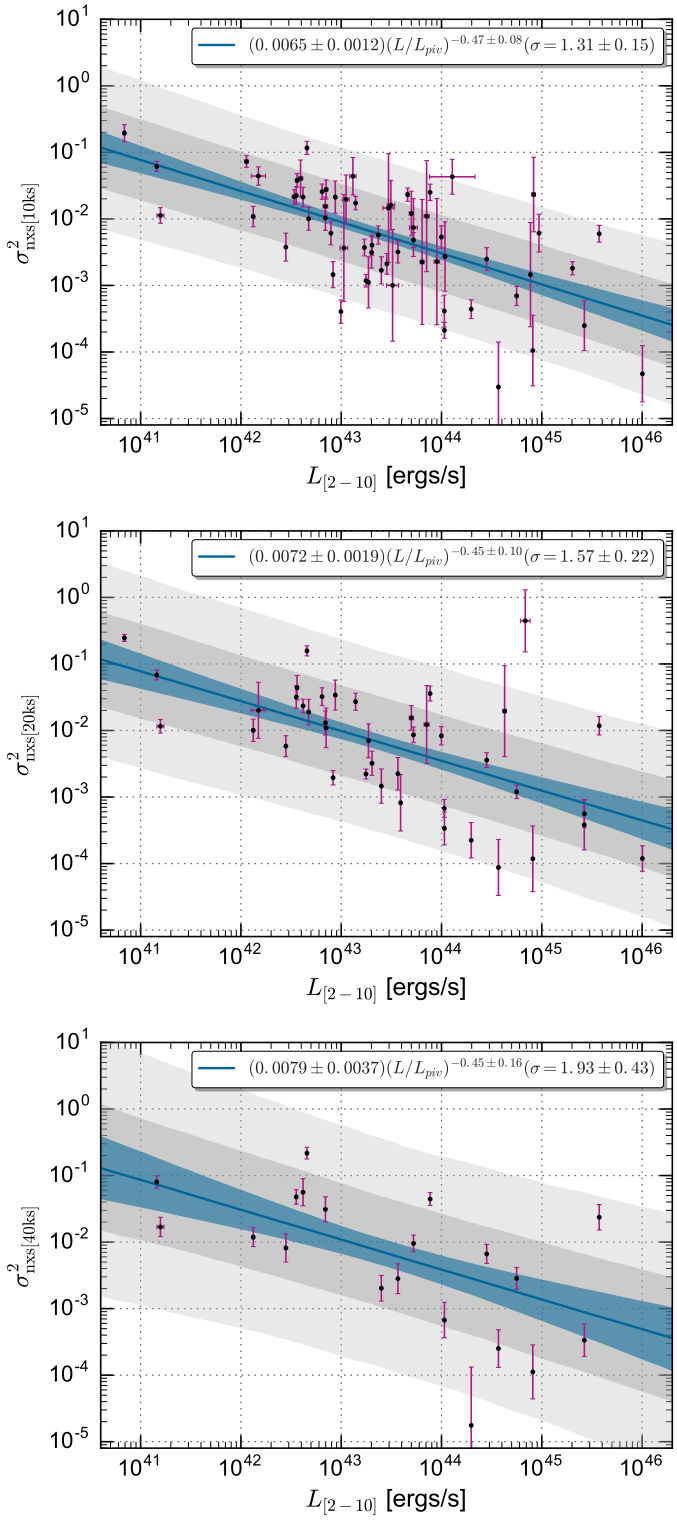

Figure 4.11: Hard-band luminosity plotted against $\sigma^2_{\rm NXS}$ where there are five or more *good* 10 ks (top), 20 ks (middle), 40 ks (bottom) light-curve segments for each AGN in our sample ($L_{\rm piv=2\times10^{43}erg/s}$). Plots and correlations by Arya Farahi, University of Michigan.

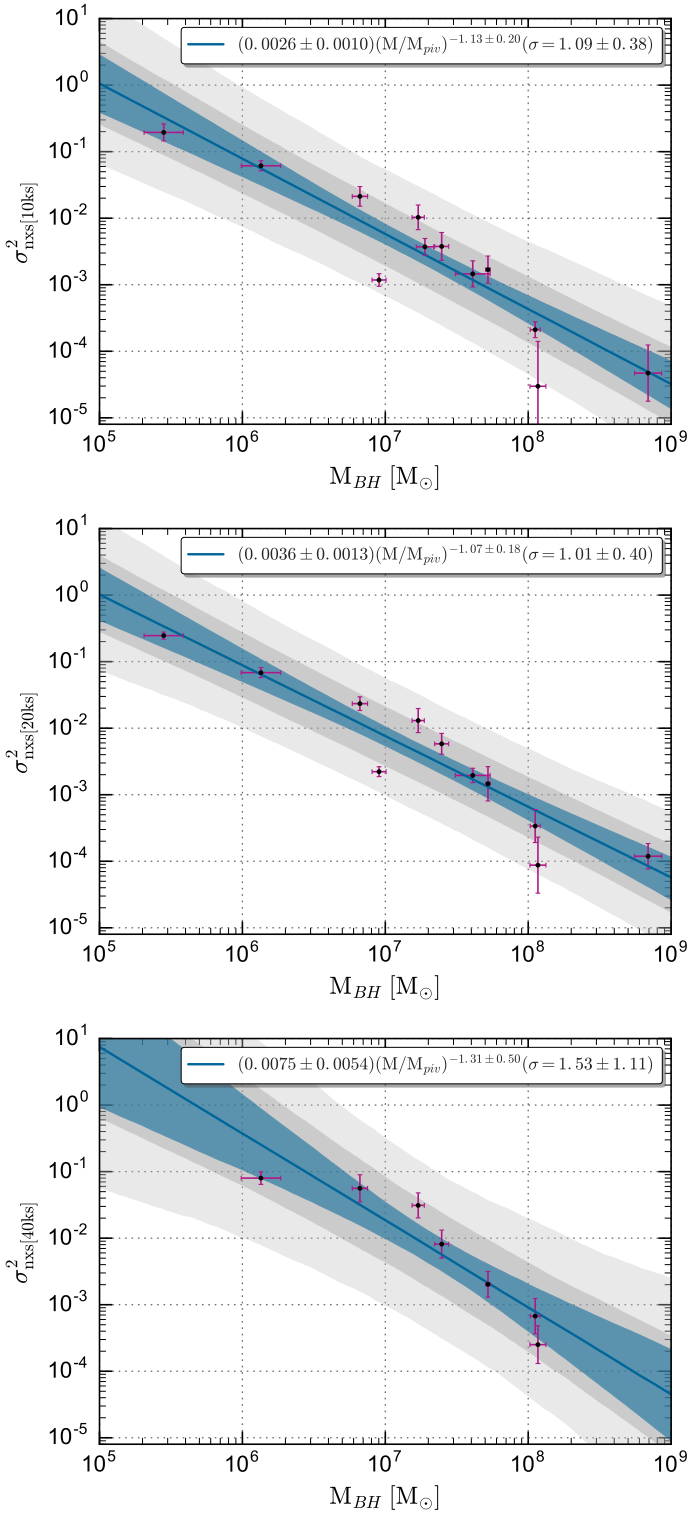

Figure 4.12: Black hole masses from reverberation mapping studies as catalogued in Bentz and Katz (2015) mass plotted against σ^2_{NXS}10 ks (top), 20 ks (middle) and 40 ks (bottom) segment light-curves. ($M_{\mathrm{piv}} = 2 \times 10^7 \mathrm{M}_\odot$). Plots and correlations by Arya Farahi, University of Michigan.

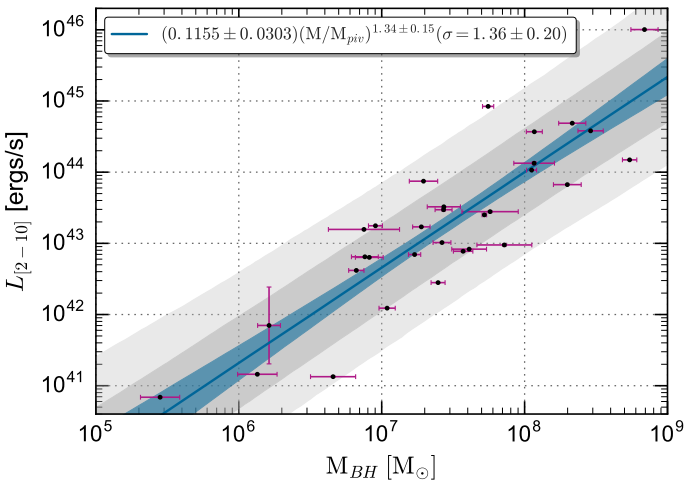

Figure 4.13: Black Hole masses from reverberation mapping studies as catalogued in Bentz and Katz (2015) mass plotted against hard-band luminosity. ($M_{\rm piv} = 2 \times 10^7 \mathrm{M}_\odot$). Plot and correlation by Arya Farahi, University of Michigan.

$L_{\rm X}$ method	Norm	Slope	Scatter	Cor	Cor
	π	α	σ	unweighted	weighted
(1)	(2)	(3)	(4)	(5)	(6)
Full spectral	0.115±0.030	1.34±0.15	1.36±0.20	0.87	0.94
eROSITA CR	0.1076±0.037	1.38±0.19	1.28±0.35	0.87	0.91

Table 4.4: Correlations between black hole mass from Bentz and Katz (2015) and estimated $L_{\rm X}$ of the form $\log(\mathrm{L_X}) = \pi \log(\mathrm{M}/\mathrm{M_{piv}})^{\alpha}$.(1) Method to determine $L_{\rm X}$: Top is from full spectral fitting, bottom is from eROSITA count-rate method as described in §4.7.3 and Figure 4.24. (2) normalisation, (3) slope, (4) σ scatter, (5) Pearson's product moment correlation coefficient, (6) as (5) weighted on $L_{\rm X}$ error. $\mathrm{M_{piv}} = 2\mathrm{x}10^7 \mathrm{M}_\odot$

Seg. dur.	Norm.	Slope	Scatter	Correlation	Correlation
[ks]	π	α	σ	unweighted	weighted
(1)	(2)	(3)	(4)	(5)	(6)
10	0.0065±0.0012	-0.47±0.08	1.31±0.15	-0.63	-0.66
20	0.0072±0.0019	-0.45±0.10	1.57±0.22	-0.58	-0.69
20^{CAIXA}	0.0070±0.0018	-0.60±0.21	1.53±0.21	-0.60	-0.60
40	0.0079±0.0037	-0.45±0.16	1.93±0.43	-0.59	-0.56

Table 4.5: Correlations between hard-band $L_{\rm X}$ and $\sigma^2_{\rm NXS}$ of the form $\log(\sigma^2_{\rm NXS}) = \pi\log(L/L_{piv})^{\alpha}$ where there are five or more good light-curve segments for each of the segment duration length in column (1). (2) normalisation, (3) slope, (4) σ scatter, (5) Pearson's product moment correlation coefficient, (6) as (5) weighted on $\sigma^2_{\rm NXS}$ error. $\rm L_{piv} = 2x10^{43}$ erg $\rm s^{-1}$. ^{CAIXA} Results from Bianchi et al. (2009b) survey with our fitting methodology.

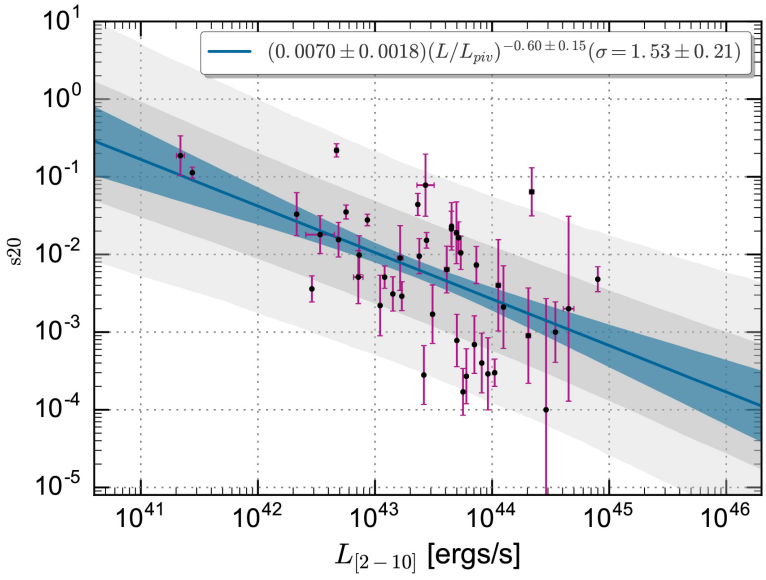

Figure 4.14: Hard-band Luminosity from Bianchi et al. (2009a) plotted against `s20` (equivalent to our $\sigma^2_{\rm NXS[20ks]}$ term) for 45 AGN in the CAIXA survey Ponti et al. (2012) ($L_{\rm piv} = 2 \times 10^{43}$ erg/s). Plot and correlation by Arya Farahi, University of Michigan.

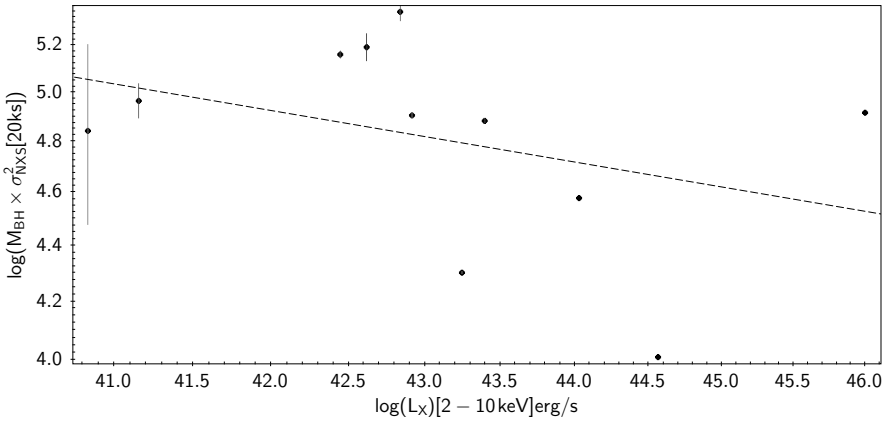

Figure 4.15: Log of the product of $M_{\rm BH}$ and $\sigma^2_{\rm NXS}$[20ks] plotted against the 2-10 keV $L_{\rm X}$. The best-fit line is shown.

4.4.1 Testing for the primary correlation

Our results confirm previous studies showing that there is a strong anti-correlation between $L_{\rm X}$ and $\sigma^2_{\rm NXS}$, and between $M_{\rm BH}$ and $\sigma^2_{\rm NXS}$, and positive correlation between $M_{\rm BH}$ and $L_{\rm X}$. It is interesting to test which of these relations is the primary correlation and which are bi-products. Following the method of O'Neill et al. (2005) we plot the quantity log ($M_{\rm BH} \times \sigma^2_{\rm NXS}$[20ks]) against $L_{\rm X}$, as shown in Figure 4.15. This quantity removes the dependence of $\sigma^2_{\rm NXS}$ on mass. We find that the strong correlation between $L_{\rm X}$ and $\sigma^2_{\rm NXS}$ disappears when we plot our results in this way.

Similarly, after O'Neill et al. (2005), we plot log($\sigma^2_{\rm NXS}$) and log ($M_{\rm BH} \times \sigma^2_{\rm NXS}$[20ks]) against the log of the $L_{\rm X}$ normalised by $M_{\rm BH}$ as shown in Figure 4.16.

The best-fit correlation coefficients from our analysis are shown in Table 4.6 and compared with those of O'Neill et al. (2005). Although there is some tension between the two sets of results, they both show a reduction in correlation between $L_{\rm X}$ and $\sigma^2_{\rm NXS}$ once the dependency of $M_{\rm BH}$ on $\sigma^2_{\rm NXS}$ is accounted for, whereas there is still a significant correlation when the $L_{\rm X}$ is normalised by $M_{\rm BH}$. The correlations derived between log ($M_{\rm BH} \times \sigma^2_{\rm NXS}$[20ks]) and log($L_{\rm X}$ normalised by $M_{\rm BH}$) agree well. These results hint towards the primary correlation being between $M_{\rm BH}$ and $\sigma^2_{\rm NXS}$ and that the correlation between $L_{\rm X}$ and $\sigma^2_{\rm NXS}$ is a secondary one. That said, the two data sets are different (coming from ASCA and XMM Newton), and whereas the coefficients from O'Neill et al. (2005) are Spearmans and Kendall, ours are Pearsons (for consistency with our other analysis). Therefore the conclusions should be treated with caution.

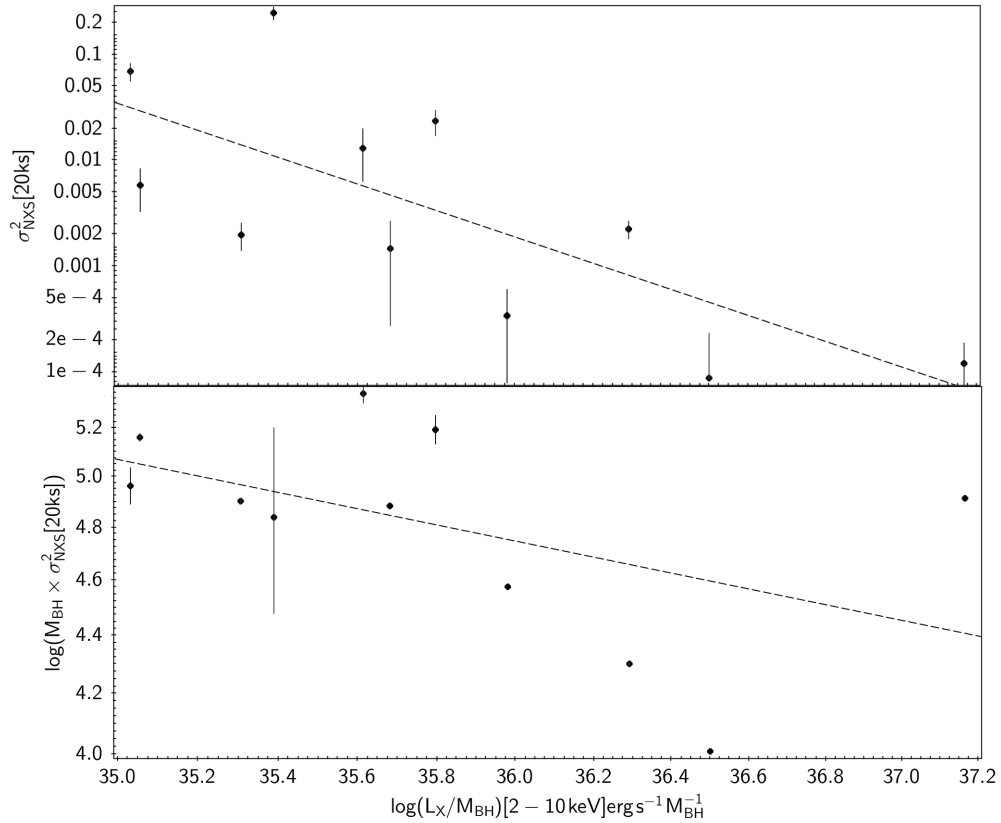

Figure 4.16: Log $\sigma^2_{\rm NXS}$[20ks](top) and Log of the product of $M_{\rm BH}$ and $\sigma^2_{\rm NXS}$[20ks](bottom) plotted against the 2-10 keV $L_{\rm X}$ normalised by $M_{\rm BH}$. The best-fit line is shown in each case.

Observable relation	Our Res. Pearson.	O'Neill Spearman	O'Neill Kendall
(1)	(2)	(3)	(4)
$\log(L_{\rm X})$ and $\log(\sigma^2_{\rm NXS}[20{\rm ks}])$	-0.69	-0.61	-0.43
$\log(L_{\rm X})$ and $\log(M_{\rm BH} \times \sigma^2_{\rm NXS}[20{\rm ks}])$	-0.26	0.13	0.10
$\log(L_{\rm X}/M_{\rm BH})$ and $\log\ \sigma^2_{\rm NXS}[20{\rm ks}]$	-0.77	0.29	0.19
$\log(L_{\rm X}/M_{\rm BH})$ and $\log(M_{\rm BH} \times \sigma^2_{\rm NXS}[20{\rm ks}])$	-0.5	-0.5	-0.31

Table 4.6: C

4.5 Test for Redshift Evolution

We have also tested for evidence of redshift evolution in the scaling relations shown in Figure 4.17.

The method assumes a null hypothesis that there is no redshift evolution. We then add an evolution factor, $E(z)^{\alpha}$ term - where $E(z)$ is defined from Equation 1.18 - and look for model where gives us the smallest intrinsic scatter. For each value of α we run an MCMC fitting. Then we compare it with our null hypothesis to see if the intrinsic scatter has decreased with the addition of the extra term.

The analysis, fitting and plots (by our XCS collaborator Arya Farahi at the University of Michigan) in Figure 4.17, allow us to visualise this. On the x-axis we have the evolution factor $E(z)^{\alpha}$ and on the y-axis we can have the posterior distribution of intrinsic scatter. We identify where on the x-axis the intrinsic scatter is minimized and compare it with the null assumption ($\alpha = 0$). If there is a statistically significant change at that minimum, then we can say that we have evidence for the redshift evolution.

In none of the correlations tested, i.e. between $L_{\rm X}$ and $\sigma^2_{\rm NXS}$ (in samples S10, S20 and S40), between $M_{\rm BH}$ and $\sigma^2_{\rm NXS}$ (in samples S10, S20 and S40) and between $M_{\rm BH}$ and $L_{\rm X}$ (sample S1), do we find statistically significant evidence for decreasing scatter. We conclude that our data are consistent with a no evolution. It is worth noting two things. First that our null hypothesis (i.e. no redshift evolution) is an arbitrary choice. Second that we are limited by the statistical power of the sample. Hence if we have a larger sample size we may find evidence of an evolutionary trend. Reducing our choice of minimum light-curve segments may provide this, with the trade off being greater uncertainty on $\sigma^2_{\rm NXS}$ error (see §4.6.3). Further, we are using $E(z)$ as the redshift-evolution parameter and it may be of interest to compare our results by using $(1 + z)$.
As this is the first attempt to look at evolution in the $L_{\rm X}$, $\sigma^2_{\rm NXS}$ and $M_{\rm BH}$ relations in this way, we cannot compare our findings against previous results.

4.6 Methodology Tests

We have carried out several tests to explore the robustness of the results presented in Section 4.4.

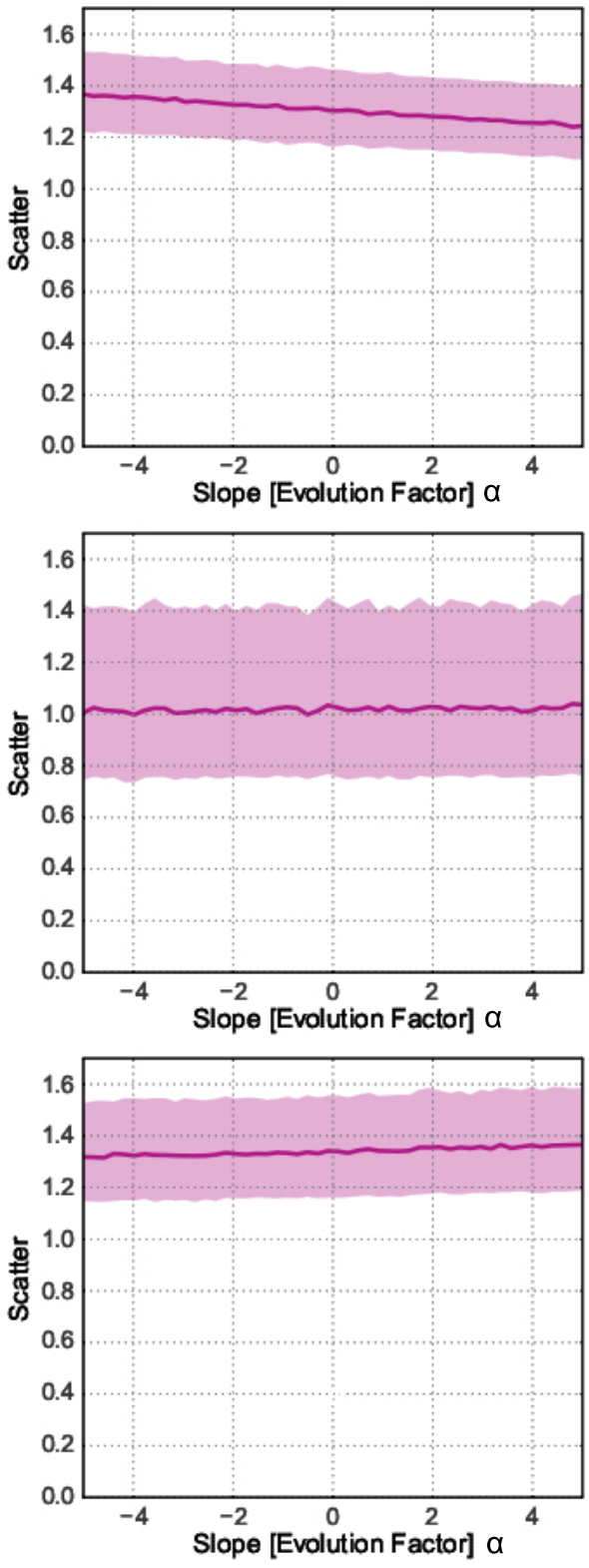

Figure 4.17: Redshift evolution plots showing the how the scatter of each of the best-fit relationships changes when a redshift-evolution factor $E(z)^{\alpha}$ is added. In each case the red line is the scatter at each value of α and the pink region is the $1-\sigma$ uncertainty. Hard-band L_{X} and σ^2_{NXS} from sample S10 (top). Mass and σ^2_{NXS} from sample S10 (middle). Black Hole mass and hard-band L_{X} from sample S1 (bottom). Plots and correlations by Arya Farahi, University of Michigan.

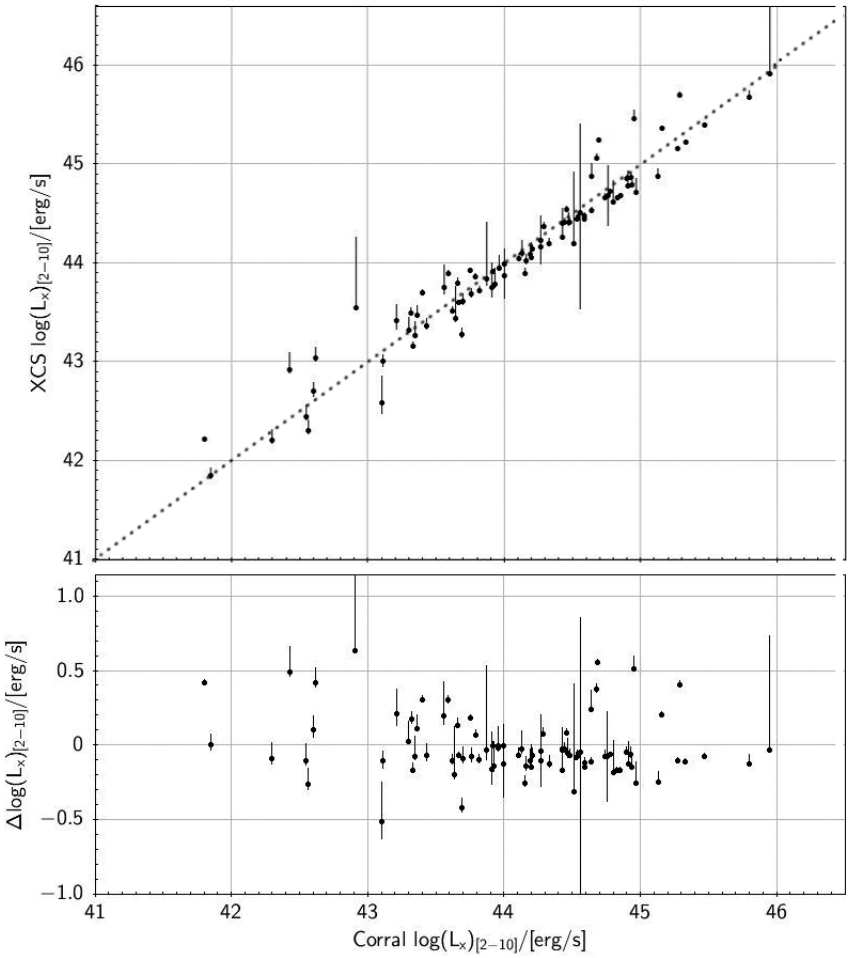

Figure 4.18: Hard-band (2.0-10 keV) luminosity of 78 AGN in Sample-S1 common with Corral et al. (2011). The dashed line shows the one-to-one relation.

4.6.1 Luminosity

We have compared our hard-band luminosity results with those estimated by Corral et al. (2011), a X-ray spectral analysis of over 300 AGN belonging to the XMM-Newton bright survey (XBS) up to redshift ∼2.4. There are 78 AGN in common between Corral et al. (2011) and our S1 sample. We find good agreement between the two sets of $L_{\rm X}$ measurements, see Figure 4.18.

4.6.2 Normalised excess variance

We have compared our values for $\sigma^2_{\rm NXS}$ with those of the Ponti et al. (2012) CAIXA survey. There are 98 AGN in common between Ponti et al. (2012) and our S1 sample. Of these, there are 19 AGN in the S20 samples (i.e. with five or more good 20 ks light-curve segments). We find a good agreement between our $\sigma^2_{\rm NXS}$[20ks] results and the equivalent

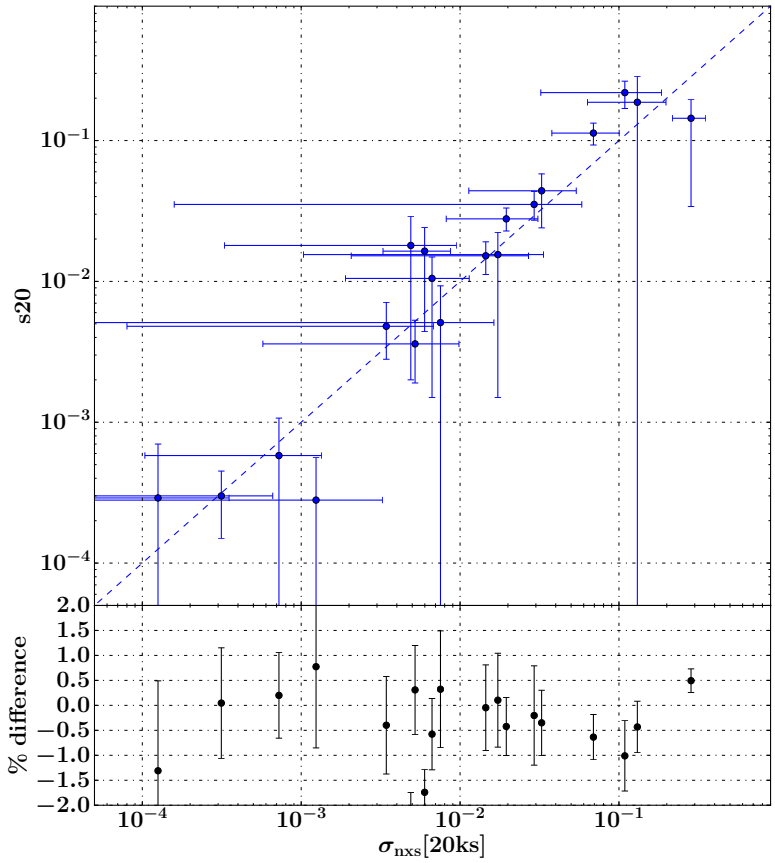

Figure 4.19: Comparison between CAIXA `s20` and our $\sigma^2_{\rm NXS}$ over 20 ks with five or more good light-curve segments (Sample-S20). Dashed line is a one-to-one relation. Bottom plot shows difference.

`s20` values from Ponti et al. (2012), see Figure 4.19.

4.6.3 Choice of minimum number of light-curve segments

The results presented in Table 4.5 were based on setting the minimum number of *good* light-curve segments at five. This is a somewhat arbitrary choice. Setting a lower minimum would have allowed us to include more AGN in the fits. Setting a higher minimum would have increased the precision on the individual measurements. Setting the minimum to 2, 3 or 4 segments for the 20ks $\sigma^2_{\rm NXS}$ results, would increase the sample to 90, 53 and 50 AGN respectively (compared to our sample of 41 for a minimum of 5 segments). Therefore, we have investigated how the fit to the $L_{\rm X}$ to $\sigma^2_{\rm NXS}$ relation changes with the minimum number of light-curve segments (from 2 to 10) for both $\sigma^2_{\rm NXS}$[10ks] and $\sigma^2_{\rm NXS}$[20ks]. No

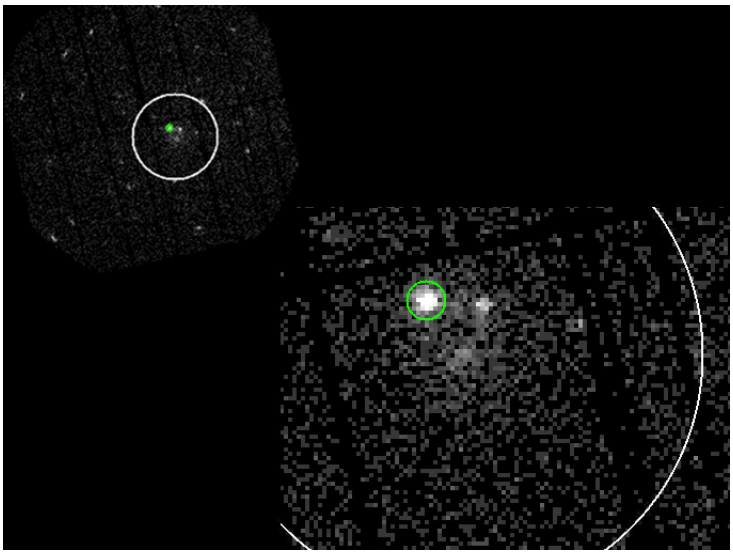

Figure 4.20: PN image and zoomed image of AGN candidate XMMXCSJ143450.6+033842.5 (green circle) in Observation 0305920401. This AGN is within the 250 kpc core radius (white circle) of nearby cluster. Pixel size 4.52″ in energy range $0.5 - 2.0$ keV.

significant effect was found, see Figure 4.21.

4.6.4 Luminosity contamination by line-of-sight clusters

We also check whether any AGN lies within the line-of-sight of the core radius (∼250 kpc) of a galaxy cluster. If this is the case, emission from the cluster may be boosting the $L_{\rm X}$ of the AGN. We cross match the all AGN positions in our S0-Sample with that of all extended sources in XCS-DR2 which have also been identified as a cluster in the redMaPPer SDSS DR8 cluster catalogue Rykoff et al. (2014). We find 12 such AGN, thoguh none were included in any of the scaling relations we subsequently derive. Figure 4.20 shows an example where an AGN, in green, is found in the line-of-sight of a cluster core, circled in white.

4.7 Implications for eROSITA

As mentioned in Section 3.6, we need large samples of AGN with estimated $M_{\rm BH}$, over a wide redshift range, to be able to determine how galaxies and black holes co-evolve.

eRASS (desribed in Section 1.9.6) is expected to detect up to 3 million AGN out to $z \sim 6$.

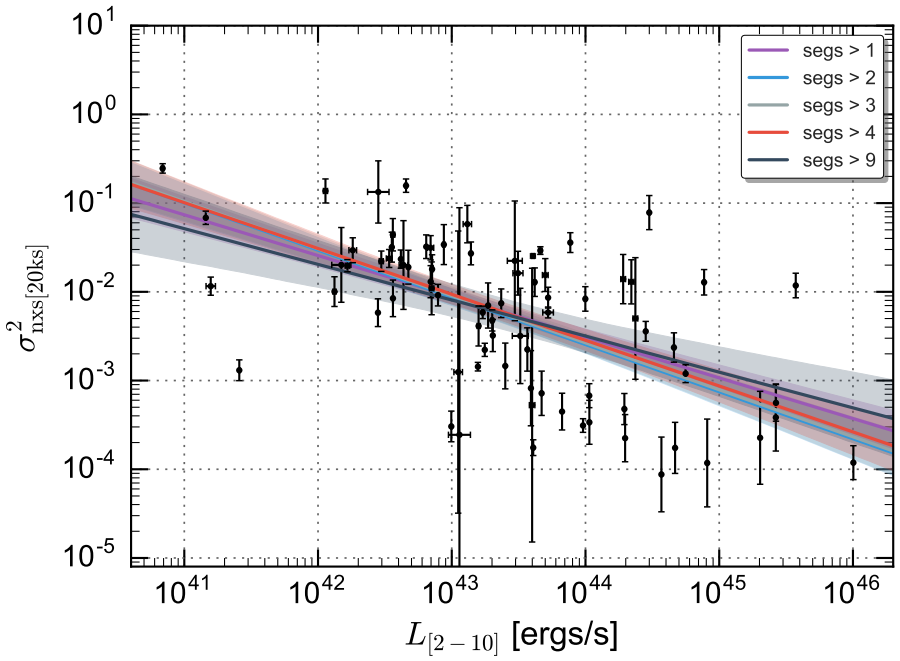

Figure 4.21: $L_{\rm X}$ plotted against 20 ks $\sigma^2_{\rm NXS}$ showing how the best fit relation changes when we change the number of good 20 ks segments to include in our sample. (For clarity, only the data points for > 2 segments, and only the 1-σ errors for the fit for > 5 segments are plotted). Uncertainties on $\sigma^2_{\rm NXS}$ were calculated using Equation. 4.3. Plots by Arya Farahi, University of Michigan.

The science potential of the eRASS AGN sample is enormous. However, to fully exploit this potential it will be necessary to estimate the $M_{\rm BH}$ from eRASS observations of the AGN. As shown in Figure 4.13 there is a significant correlation between AGN $L_{\rm X}$ and $M_{\rm BH}$. In the following we explore whether the $L_{\rm X}$ measurements expected from eRASS will be sufficient for this correlation to be useful in $M_{\rm BH}$ estimation.

4.7.1 Expectations for eROSITA Luminosity Measurements

The eRASS exposure time is dependent on ecliptic latitude (lat). According to Merloni et al. (2012) the approximate exposure time $T_{\rm EXP}$ is given by $T_{\rm EXP} \sim 1627/\cos(lat)$ secs for -84° <lat< 84° and $T_{\rm EXP} \sim 17,500$ secs within 6° of the each ecliptic pole. This assumes 100% observing efficiency. A more realistic efficiency is 80%. These predictions refer to the full four year survey. The exposure time for each of the eight all-sky surveys, will be 8 times lower, so only $\simeq 100$ secs on average. Therefore, it will be impossible to measure $\sigma^2_{\rm NXS}$ values using our method, from eRASS data. However, it will still be possible to estimate $L_{\rm X}$ values. We forecast the accuracy of the eRASS derived $L_{\rm X}$ values below.

4.7.2 eRASS $L_{\rm X}$ from spectral fitting

If the AGN flux is sufficiently high, it will be possible to estimate $L_{\rm X}$ from the eRASS data using spectral fitting. To predict the accuracy of such fits, we have used the existing XMM observations of AGN in Sample-S1 and selected 2-10 keV light-curve segments at random, with a duration of the likely eROSITA exposure time in one of the eight All Sky Surveys. The exposure time was adjusted respective to the AGN latitude. For this exercise we continued to use XMM calibration files, but scaled the exposure time by the ratio of the XMM:eRASS sensitivity (from a comparison of respective effective area in the 2-10 keV energy range, the combined effective area of the seven eROSITA detectors is a factor of about 3.2 less than the XMM `PN` detector, Merloni et al., 2012). We extracted source and background spectra for these light-curve segments, and then fit the absorbed powerlaw models as described in Section 4.3.2. From these fits we extracted $L_{\rm X}$ and $\Delta L_{\rm X}$ values.

Of the 1091 AGN from 1753 XMM observations tested, successful spectral fits were derived in only 172 cases, corresponding to 98 unique AGN. Of these, there were 80 fits (44 unique AGN) where $\frac{\Delta L_{\rm X}}{L_{\rm X}} < 1$. The results from these 80 fits are compared to those derived from

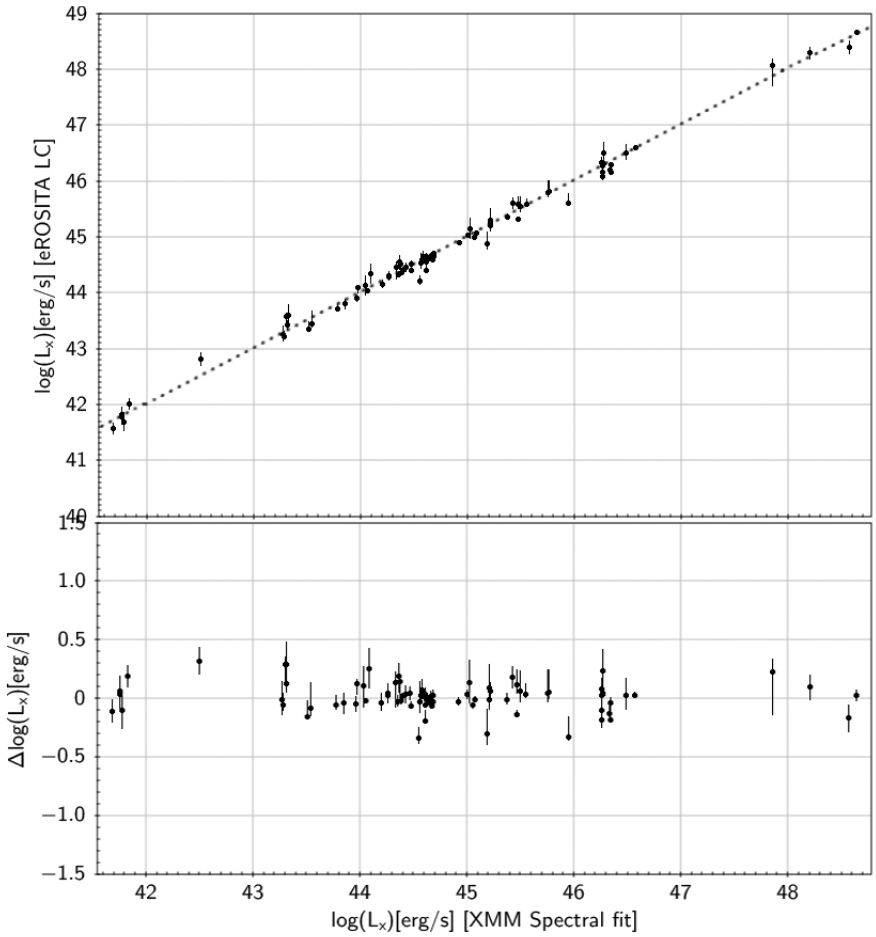

Figure 4.22: Comparison of the 2-10 keV luminosity derived from spectral fitting to the XMM full exposure time observations to the luminosities fit to an estimated eROSITA observation time for 80 observations of 44 AGN. The dotted line shows the one-to-one relation

the full XMM exposure time in Figure 4.22. There is excellent agreement albeit only for the $\simeq 4\%$ highest flux AGN.

4.7.3 eRASS $L_{\rm X}$ from count-rates

Where the AGN flux is not high enough to yield a meaningful spectral fit, then it is still possible to estimate $L_{\rm X}$ from the source count-rate using an assumed spectral model. For this exercise, we used an absorbed powerlaw (with $\Gamma = 1.7$), with an $n_{\rm H}$ value appropriate for the respective AGN galactic latitude. The conversion factors between count-rate and luminosity were generated using XSPEC. For this test we used 254 on-axis observations of 154 AGN.

To predict an $L_{\rm X}$ value for a typical eRASS observation duration, we chose a random

start time in the respective observations and set the light-curve duration to be the typical eROSITA observation time at that latitude with a scaling to account for the difference in the XMM:eROSITA sensitivity as used above (Section 4.7.2). A background subtracted light-curve was extracted in the 2-10 keV range and the count-rate recorded. This is converted into a flux by dividing by hard-band ECFs. Hard-band $L_{\rm X}$ is then calculated from Equation 4.4.

$$L_{\rm X} = F \times 4\pi \times D_L^2 \tag{4.4}$$

where F is the flux, and D_L^2 is the luminosity distance which has the redshift folded in. We repeated eight times (to mimic the eight eRASS passes) and calculated the mean and error on the mean. (We note that the error on the mean is likely to be an underestimate since the eight light curves came from the same observation rather than eight different epoch observations as would be the case with eRASS). All 254 observations provided an estimate for $L_{\rm X}$.

Figure 4.23 shows a comparison between $L_{\rm X}$ derived from the full-observation spectral method and from this count-rate method (where there were two or more observations of the same AGN, we took the most recent for the count-rate $L_{\rm X}$ comparison).

We plot the $M_{\rm BH}$ to $L_{\rm X}$ relation for luminosity derived this way and find that the relation is statistically similar to the relation of $M_{\rm BH}$-$L_{\rm X}$ from a spectroscopic analysis of full XMM observations, albeit with larger uncertainty. This is shown in Figure 4.24 with correlation shown in Table 4.4.

4.8 Discussion

4.8.1 AGN Type

Our calculations of $L_{\rm X}$ assumed that the emission from the AGN is isotropic. This is valid if the emission is not beamed but should be taken into account otherwise. Viewing angle will also have an effect on the line-of-sight hydrogen column density, with Type 2 having higher intrinsic values than Type 1. Therefore, an estimate of the absorption at the location of the AGN itself should be combined with the $n_{\rm H}$ value (e.g. from Dickey and Lockman 1990b) when the fitting the model.

However, the relationship derived between $L_{\rm X}$ and $M_{\rm BH}$ shown in Figure 4.13 and Table 4.4 is based only on Type 1 AGN (these are the only ones for which reverberation mapping mass estimates can be made). Therefore, AGN type should not be an issue. That said,

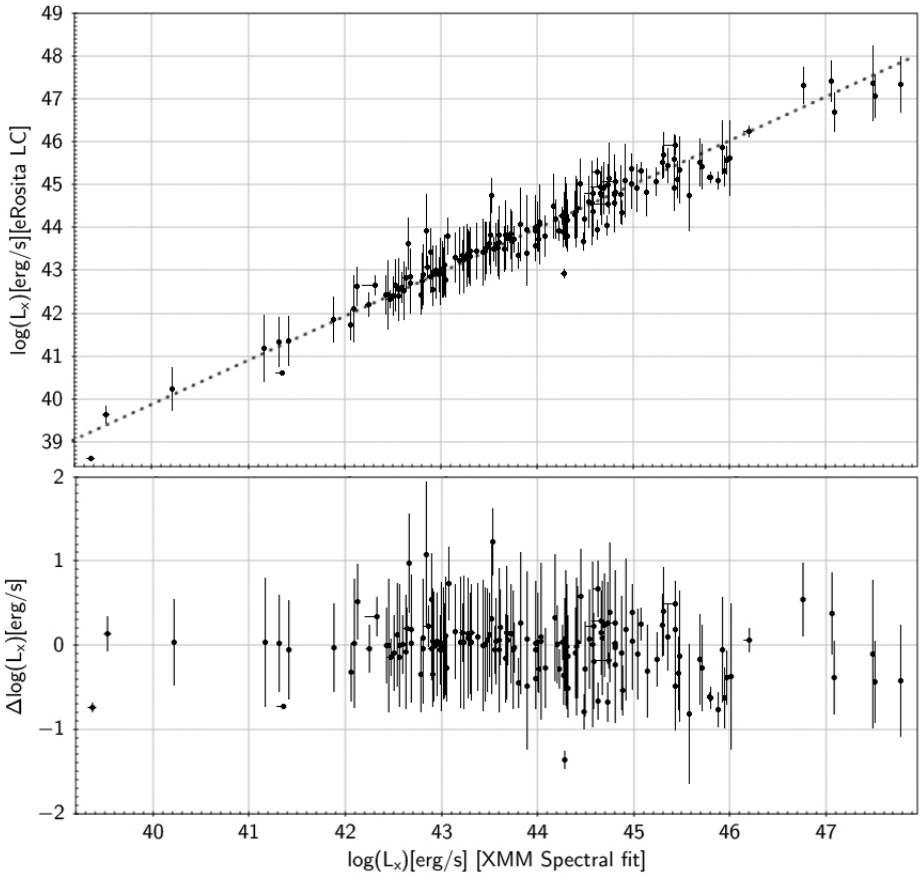

Figure 4.23: Comparison of the 2-10 keV luminosity derived from spectral fitting from actual XMM full observation time with fitting from the light-curve method 154 AGN. The dotted line shows the one-to-one relation

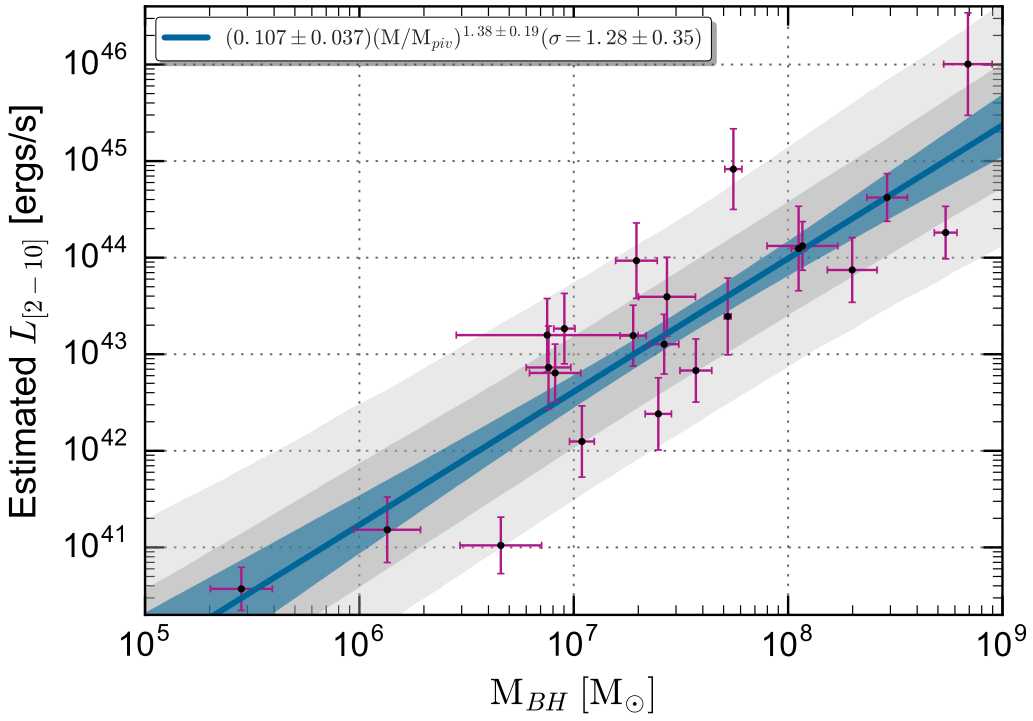

Figure 4.24: Black Hole masses from reverberation mapping studies as catalogued in Bentz and Katz (2015) plotted against hard-band luminosity estimated from the count-rate of eight passes of typical eROSITA exposure duration ($\mathrm{M_{piv}} = 2\mathrm{x}10^7\mathrm{M}_\odot$). Blue line is the best fit relation with 1-σ uncertainty. Grey regions are 1 and 2-σ scatter. Plots and correlations by Arya Farahi, University of Michigan.

when using eRASS L_X as a proxy for M_{BH}, one would need to take into account the impact of mixing AGN types. This should not be a problem because spectra will be needed to secure redshifts, and those same spectra can be used to determine AGN type. (A large fraction of the eRASS AGN are planned to be observed by the 4MOST[3] spectrograph.)

4.8.2 Selection effect at high redshift

We see from Figure 4.7 that there is a clear trend of increasing L_X with redshift in sample S1 due to the flux limited nature of the observations. Therefore there may be selection effects that have not so far been taken into account within our correlations involving L_X. Further selection effects may also be involved for relations involving M_{BH}, as the reverberation-mapped masses are available only for the brightest AGN at relatively low-z ($z < 0.24$ in our study).

4.8.3 Expanding the sample size

We have based our M_{BH} to σ^2_{NXS} and M_{BH} to L_X relationship on only ~ 30 Type 1 AGN at $z < 0.24$, because these were the only AGN available to us that had M_{BH} measurements from reverberation mapping. In future work, we will extend our analysis by including other types of M_{BH} measurements e.g. from the luminosity and the width of the broad Hα line. For example, there are a $\sim$220 AGN in our S1 sample where M_{BH} has been estimated in Shen et al. (2008) based on Hβ, Mg II, and C IV emission lines.

We can also extend our sample by drawing on new compilations of reverberation mapping M_{BH} measurements. In particular, we look forward to measurements from the OzDES project Tie et al. (2016). This project is targeting AGN in the Dark Energy Survey deep fields. It aims to derive reverberation mapped M_{BH} for ~ 500 AGN over a redshift range of $0 < z < 4$, with 3 per cent uncertainty. Cross-matching the OzDES target list with Sample S1, we found 35 AGN in common. Of these, fifteen were not already included in Figure 4.13. In Table 4.7, we present L_X values for these 15 derived by following the same spectral fitting methodology as before and these are shown in Table 4.7.

4.9 Chapter Summary

In this chapter we have used AGN associated with XCS point sources to confirm the existence of scaling relations between M_{BH}, L_X and with σ^2_{NXS}. With our sample, we have found no significant redshift evolution of these scaling relations, thus improving the

[3] www.4most.eu

XCS Source	z	$\log(L_{\rm X})$ erg/s
XMMXCSJ021557.6-045010.3	0.884	$44.03\pm^{0.12}_{0.02}$
XMMXCSJ021628.3-040146.8	0.830	$44.46\pm^{0.14}_{0.02}$
XMMXCSJ021659.7-053204.0	2.81	$45.80\pm^{0.09}_{0.01}$
XMMXCSJ021910.5-055114.0	0.558	$44.22\pm^{0.09}_{0.01}$
XMMXCSJ022024.9-061732.1	0.139	$43.12\pm^{0.16}_{0.02}$
XMMXCSJ022249.5-051453.7	0.314	$44.08\pm^{0.09}_{0.02}$
XMMXCSJ022258.8-045854.8	0.466	$43.69\pm^{0.30}_{0.04}$
XMMXCSJ022415.7-041418.4	1.653	$44.47\pm^{0.10}_{0.01}$
XMMXCSJ022452.1-040519.7	0.695	$43.89\pm^{0.23}_{0.03}$
XMMXCSJ022711.8-045037.4	0.961	$44.49\pm^{0.06}_{0.02}$
XMMXCSJ022716.1-044537.6	0.721	$44.53\pm^{0.10}_{0.02}$
XMMXCSJ022845.6-043350.7	1.865	$45.50\pm^{0.07}_{0.01}$
XMMXCSJ022851.4-051224.4	0.316	$44.13\pm^{0.05}_{0.03}$
XMMXCSJ033208.9-274732.1	0.544	$43.91\pm^{0.03}_{0.02}$
XMMXCSJ033211.5-273727.8	1.570	$44.48\pm^{0.25}_{0.00}$

Table 4.7: Estimated hard-band $L_{\rm X}$ from spectral fitting of AGN within OzDES reverberation mapping survey for AGN point sources not already in included in our $L_{\rm X}$-$M_{\rm BH}$ relation in Figure 4.13.

accuracy of the $L_{\rm X}$-$M_{\rm BH}$ relation.

We have estimated that our sample of AGN with both XCS derived $L_{\rm X}$ values, and $M_{\rm BH}$ estimates, can be doubled once the OzDES survey starts providing new reverberation mapped data of AGN.

We have also described a method to estimate the $L_{\rm X}$ of an AGN from count-rates of short duration observations where the $\sigma^2_{\rm NXS}$ cannot be measured. We have shown that though the uncertainties on the count-rate derived $L_{\rm X}$ are larger than spectrally derived $L_{\rm X}$, the scaling relation with $M_{\rm BH}$ is the statistically similar. This will be particularly relevant to future X-ray missions such as eROSITA where short observations allow us to estimate potentially millions of $M_{\rm BH}$ from this scaling relation.

The work in presented in this chapter has been submitted to MNRAS.

Chapter 5

A Serendipitous Search for X-ray Flashes (XRF) in the XCS Point Source Catalogue

5.1 Introduction

In this project, we describe a new method that searches for a class of random, fast transient X-ray event, the X-ray flash (XRFs). We aim to use this method to detect XRFs that are new to literature using the XCS point source catalogue and to estimate an upper limit on their occurrence.

We describe XRFs further in Section 5.2. Section 5.3 describes our source selection from the XCS catalogue and Section 5.4 our method for detecting XRFs within this. We describe tests of our method in Section 5.4.1 and a reanalysis of XRFs detected by XMM in literature in Section 5.5. We present our results of potential XRF candidates in Section 5.6 and we describe how we categorize these into those most likely to be genuine XRFs in Section 5.7. The most likely XRF candidate is analysed in more detail in Section 5.8 and we derive an all sky upper-limit from this event in Section 5.9.
This chapter is being prepared for submission to MNRAS.

5.2 Background

XRFs were first discovered in 2001 using the Wide Field Cameras (WFC) on board the Italian-Dutch X-ray satellite BeppoSAX by Heise et al. (2001). They are defined as a fast

transient X-ray source with duration less than 1000 sec, and where the t_{90} time (the period where the count-rate is above 90% peak) ranges from 10 to 200 sec (Heise et al. 2001). To further distinguish them from flaring stars, which have a longer duration, XRFs have no strong optical or infra-red counterpart.

The closest counterpart in terms of light-curve duration is that of Type 1 X-ray bursts which Lewin et al. (1995) attribute to thermonuclear flashes from neutron stars in an X-ray binary system. Type 1 X-ray bursts have light-curves with rise-time $\approx$1 sec and exponential decay of 10-100 sec. They have spectra which are thermal in nature and can be fitted by a black body model. In contrast, the spectra of XRFs are modeled by a single power law and their light-curves have a rise-time/decay which is non-exponential in nature.

XRFs show little or no detection in the gamma-ray energy range 40-700 keV. Barraud et al. (2005) suggest that they can be thought of as extending the population of the classic Gamma Ray Burst (GRB) into the range of lower energy. Further, they define the division between XRFs and GRBs by using the ratio $R_{x/\gamma}$ of the 2-30 keV to the 30-400 keV fluences, where XRFs are considered to be $R_{x/\gamma} \geqslant 1$. Therefore, they represent separate class of fast X-ray transient events which are not triggered by a GRB. Fast X-ray transient events that are triggered by a GRB are referred to hereafter as GRB-counterparts.

Figure 5.1 shows an example of an X-ray flash clearly seen in the BeppoSAX Wide Field Camera (WFC) lower energy bands, and not in the gamma ray bands. Figure 5.2 shows the light-curve for a different XRF detected by the WFC. On the left the event XRF 97019 does not produce any signal in the Gamma-Ray Burst Monitor (GRBM) which compares to the light-curve for GRB 980329 on the right which does. This is a GRB-counterpart.

As well as 17[1] XRFs discovered by Beppo Sax (Heise et al. 2001, Amati et al. 2004), seven have also been detected by the Wide Field X-ray Monitor onboard the High Energy Transient Explorer 2 (HETE-2) (Butler et al. 2004 Sakamoto et al. 2004). Bauer et al. (2017) find a fast transient X-ray source which they detect in the Chandra Deep Field-South. Although not referred to as an XRF, the event with a rise time of $\sim$ 100s, is not observed in any other Chandra or XMM observations at the same location. Nor do they find any other sources of this nature in the Chandra source catalogue.

[1]Seven if we take the definition of XRF from Barraud et al. 2005

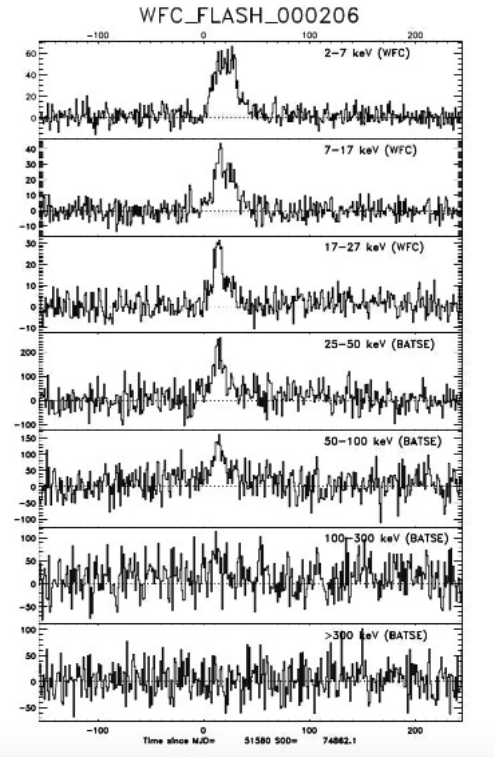

Figure 5.1: Light-curves in different energy bands of the Wide Field Cameras on-board BeppoSAX, showing an XRF detected in the lower energy band X-ray region but not in higher gamma ray regions. Image from Heise et al. (2001).

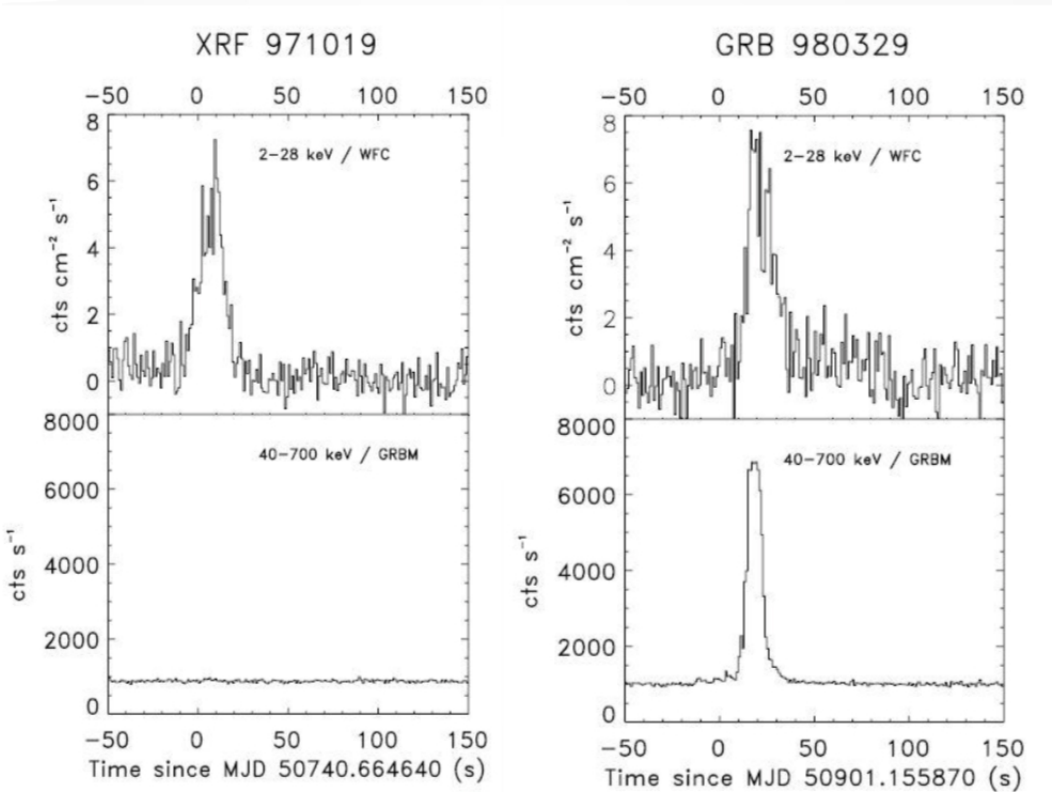

Figure 5.2: The lightcurves on the same scale of a typical gamma-ray burst GRB 980329 (right) and a prototypical X-ray flash 971019 (left) as recorded by the Wide Field Camera (WFC) and the Gamma-Ray Burst Monitor (GRBM), aboard the ItalianDutch satellite BeppoSAX. GRB 980329 produces a strong signal in the GRBM (40 to 700 keV) as is expected of a gamma-ray burst. In contrast, the event of 971019 does not produce any signal in the GRBM. Image from Heise et al. (2001).

Law et al. (2004) performed a serendipitous search for XRFs in observations with exposure > 50ks in XMM-Newton using the publicly available data as of June 2002. Although they find two candidate events in the PN detector, both of these were not confirmed with a simultaneous detection in either MOS detector suggesting that these events may be due to detector effects. Law et al. (2004) put a full-sky upper limit on the XRF event rate combining their results with XRF detections from the Burst and Transient Source Experiment (BATSE) and BeppoSAX as shown in Figure 5.3 which shows the two detected XRFs labeled XMM (a) and XMM (b) and an upper limit from Vikhlinin (1998).

XRFs are rare compared to other transient X-ray sources and at first, were associated with high redshift, $z > 5$, GRBs, where the gamma rays had been redshifted into the X-ray range (i.e not a true GRB-counterpart but an actual redshifted GRB itself). This hypothesis was rejected by Barraud et al. (2003), who, through generating and analysing large samples of synthetic GRBs, concluded that the similar distributions of duration of both GRB and XRFs discount this. This is because at a high redshifts, cosmological time dilation of gamma-rays would result in a longer duration of the X-ray detected flash and this is not seen when comparing XRFs with the GRB-counterpart (as shown in Figure 5.4). Further, estimates of redshift of XRFs including that of XRF040701 by Soderberg et al. 2004 at $z \sim 0.215$, has provided more evidence against this hypothesis.

Other explanations of XRFs include that they may be associated with a third type of manifestation of an exploding star (along with supernova and GRBs) in star-forming galaxies Bloom et al. (2003). Or that they are associated with merging black holes or neutron stars e.g. Chincarini (2005). Heise et al. (2001) suggest that XRFs may be a lower energy extension of the circumstance that lead to GRBs that are formed by a process called 'cosmic ray fireball scenario'

Bauer et al. (2017) suggest further possible interpretations that may help us to explain the origin of XRFs. These include i) a manifestation of a classic GRB viewed away from the axis of the beamed radiation, ii) they are a representation of a Shock Breakout (SBO) from a core-collapsed supernova, iii) a Tidal Disruption Event (TDE) occurring as a star is 'shredded' as it passes close by to a black hole.

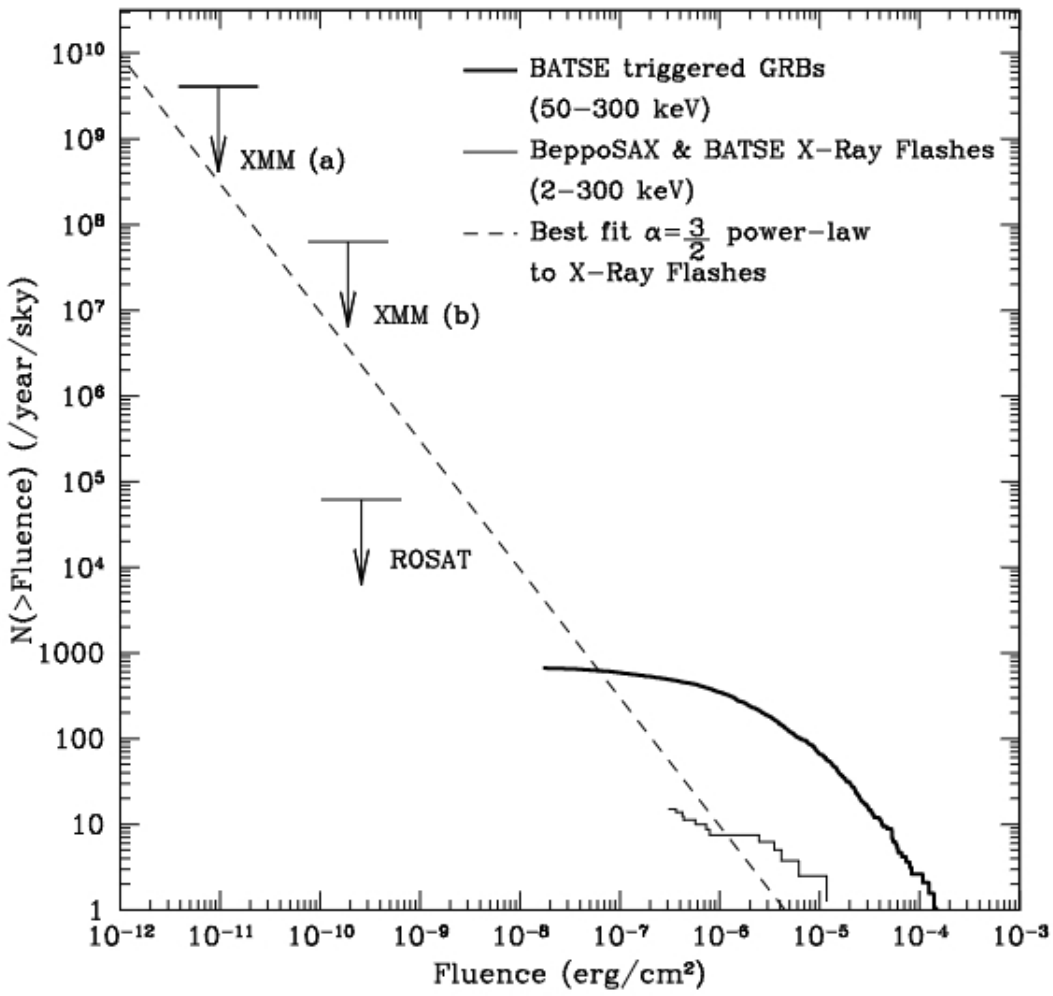

Figure 5.3: Figure from Law et al. (2004). XMM (a) is 90 per cent upper limit at 10 counts per XRF, XMM (b) is 90 per cent upper limit at 200 counts per XRF, both limits are derived with an energy passband of 1.4 to 15 keV from Law et al. (2004). The 90 per cent ROSAT upper limit with an energy passband of 0.5 to 2.0 keV from Vikhlinin (1998) is also shown, as is The Burst and Transient Source Experiment (BATSE) and BeppoSAX GRBs and XRFs results. The best fit power-law α is shown to XRFs where $\alpha = -\frac{3}{2}$.

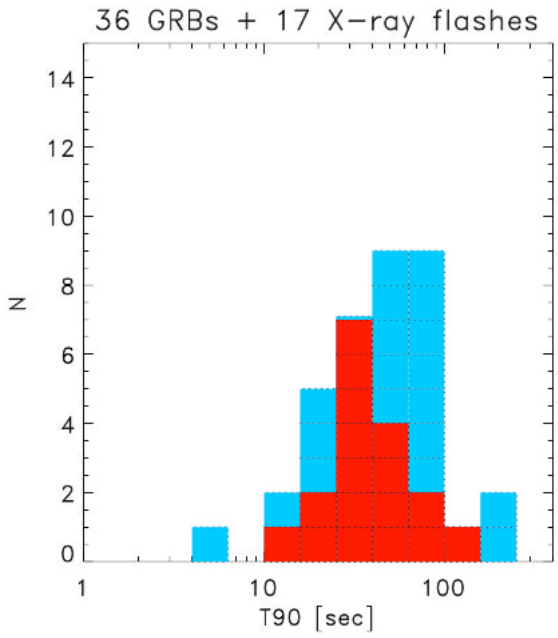

Figure 5.4: Histogram of T90 duration for X-ray counterpart of GRBs (blue) and X-ray flashes (red) where T90 is the duration of the interval above 90% of the peak flux. Image from Heise et al. (2001).

Whichever of these origins is correct, and it may be more than one, finding XRFs may allow us to put a estimate on the number of events of this nature that are likely to occur each year.

5.3 Source Selection

For our study, we start with all XCS point sources detected and catalogued in XCS-DR2, as described in Section 2.3.6, with an exposure time greater than 15 ks (a duration we justify in Section 5.4.1). There are 149,721 of these. We filter out sources within 15° of the Galactic plane to reduce the number of Galactic sources of a variable nature (flaring stars for example). We are left with a total of 107,412 sources from 2355 observations.

5.4 Method

We first take the clean event file of the `PN` detector (being more sensitive that then `MOS`), selecting events with `FLAG`==0, PATTERN<=4 and XMMEA_EP and select a source region of 20″ in radius centred on each point source and a background annulus region 50″ - 60″ from the source (as per our XCS infield background subtraction method as detailed

in Section 2.3.2).

We make light-curves in 512 second bins for the source and background regions in the $0.2 - 10.0$ keV band. We combine these into a background-subtracted light-curve using the `epiclccorr` command. This command accounts for *absolute* corrections such as bad pixels, vignetting, chip gaps, quantum efficiency as well as *timing* corrections including dead time and the good time interval for the event list.

We choose 512 secs as the time bin duration as it is long enough such that a typical XRF duration (as in Figure 5.4) occurs in one bin (or across the boundary of two), yet short enough so that there are at least 20 bins in the light-curve. As we are dealing with Poisson statistics, any source where there are less than 20 time bins is excluded from our results.

We test each light-curve to check if the bin with the highest count-rate, $\mathrm{CR_{MAX}}$, is more than 5σ higher than that of the mean count-rate $\mathrm{CR_{MEAN}}$ of the complete light-curve. We ensure that $\mathrm{CR_{MAX}} - \mathrm{error}(\mathrm{CR_{MAX}}) > \mathrm{CR_{MEAN}}$ by the same 5σ margin.

There is of course a possibility that the XRF event occurs across the boundary of two light-curve bins resulting in a non-detection of 5σ in either bin. Therefore, we repeat the process but shift the start time by 128 secs and again check the maximum count-rate level for a 5σ detection. Where the candidate meets this criteria, in either of the two light-curves, it is flagged as an XRF candidate.

At the 5σ level we would expect one bin in every 3.5 million to be detected purely from statistical fluctuations for an individual detector. When we add together all sources that successfully resulted in an output through our pipeline (whether detected as potential XRF or not) we find 2.26million `PN` light-curve time bins. We therefore expect less than one XRF candidate detected by chance alone. Should the `MOS` detectors for the same source also result in a potential XRF being flagged, then this would make it highly improbably that this was due to statistical fluctuations.

5.4.1 Testing the Method

In order to test our XRF detection pipeline, we insert a 20 photon count (and then 40, 80, 160) fake XRF into 1000 random `PN` observations and test how many of these are detected

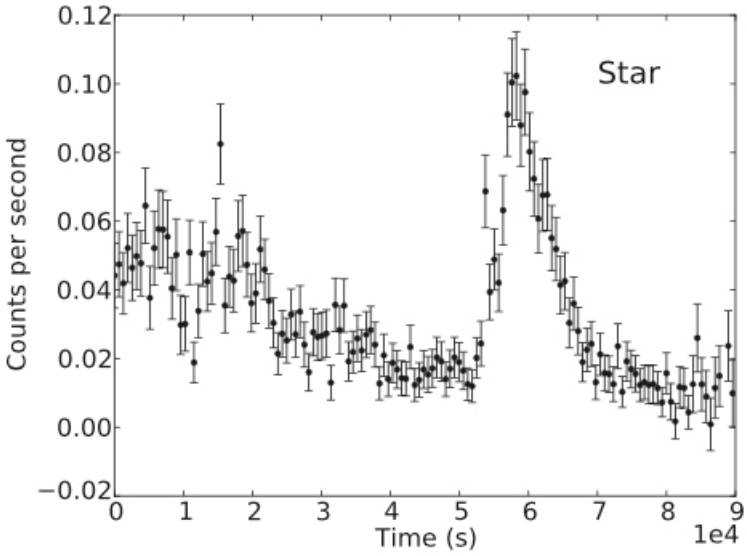

Figure 5.5: Typical light-curve of a flaring star from Lo et al. (2014) showing that the peak rate in light-curve at the flare falls away exponentially over a longer period than an XRF (compare with Figure 5.4).

as per our method described in Section 5.4 above.

For each ObsID, we select a random position on the detector within $14'$ from the centre of the observation pointing to be our dummy XRF detection position. We check whether this falls on or near a chip gap by taking the exposure map of the ObsID. These are made automatically for all ObsIDs during the image making stage of the XCS pipeline as summarised in Section 2.3.3. We check whether the value of the exposure map (at the dummy XRF centre) is <20% of the maximum value on the observation. If so, we reject the dummy XRF.

We wish to position the individual photons of the XRF as realistically as possible taking into account the PSF of the detector (as summarised in Section 2.2.3 and shown in Figure 2.2). We use the SAS software script psfgen to create a PSF matrix, i.e.

psfgen region = (DETX, DETY) IN circle (DETX, DETY, 400) instrument = EPN
output = psf.fits level = ELLBETA energy = 2000

This creates a 38x38 PSF matrix around the XRF centre on the detector (as defined by the

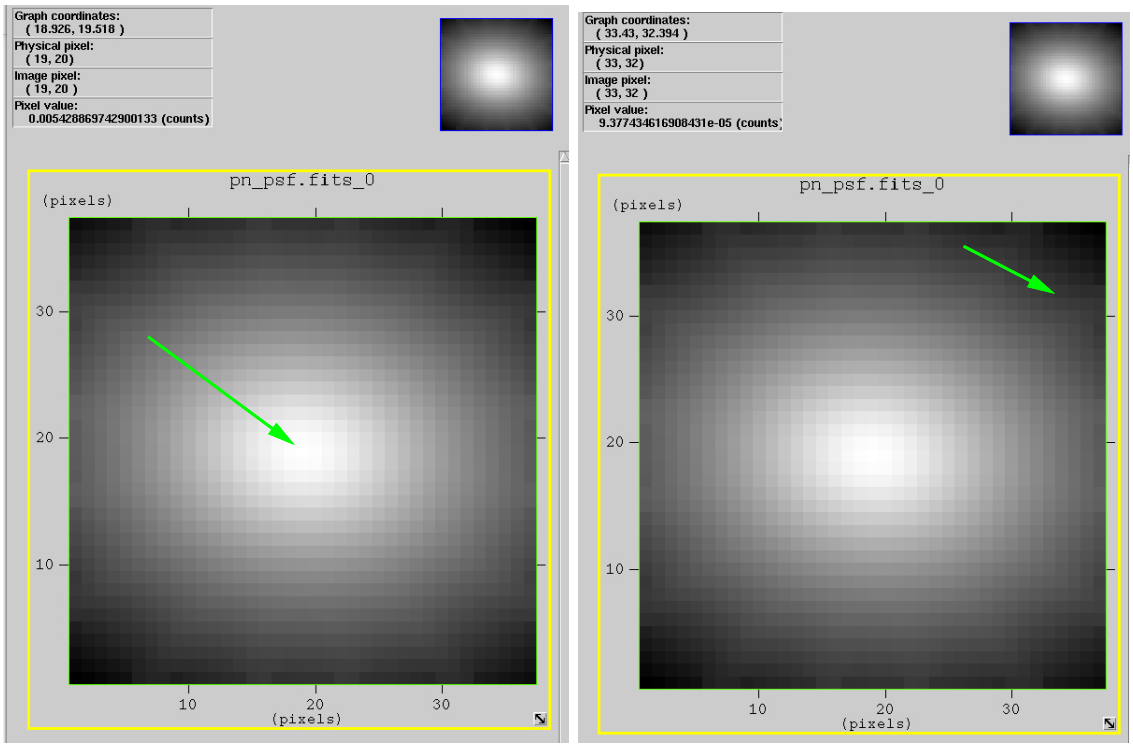

Figure 5.6: A PSF generated from the **psfgen** script as described above in Section 5.4.1. Right, a pixel near the centre has a greater value, (in this case 0.0054) than one at the outskirts shown on the left ($9.38\text{x}10^{-5}$).

DETX/Y co-ordinates) where each element in the matrix represents a probability that the photon is detected by that pixel (i.e by the effect of the PSF). This is shown in Figure 5.6 which compares two pixels in the PSF. The value of the central pixel, shown on the left is greater than one on the edge of the PSF, shown on the right. We use the matrix pixel values as a weighted probability to randomly position the each of the 20 individual XRF photons within the PSF region onto the detector, centred on the fake XRF.

We now write into the clean events file 20 dummy new events. We assign the position (DETX DETY) co-ordinates of each event as just described. We assign a start time and duration to the fake XRF by choosing a random time from within the period of the ObsID with duration between 20 and 200 sec. From this period each photon is assigned a random detection energy,PI. (Each photon event PI is set with an random energy between 0.4 and 2 keV).

After completing this exercise with 20 count fake XRFs, we repeat the process creating 40, 80 and 160 count dummy photons. An example is shown in Figure 5.7 where the top

image shows the entire observation where an 160 photon XRF event is shown in green. The bottom three images show, the 500 second period directly before, during and after the event.

We input our known position of the dummy XRF into our XRF detection pipeline to determine how many have been detected. Figure 5.8 shows histograms of the number of observations in binned exposure times where we detected fake XRFs (dark grey bars) as well as all observations where XRFs were inserted (light-grey). Figure 5.9 shows how the percentage of detection changes by exposure time and by the number of counts in the fake XRF.

There are two reasons for non detection of our fake XRF. One which is statistical, in that the observation exposure time is too short to allow sufficient bins of 512 sec. In this case a detection of 5σ is not possible. Another reason is astrophysical where that the dummy flash event has been inserted into an area of already high X-ray activity. Here the XRF photons are swamped by photons from other astrophysical objects. In the real world both of these may also result in a non-detection.

The results in Figure 5.9 show, for example, that for exposure times $\geqslant$40 ks, the detected fraction of 40 photons XRFs (green points) is $\geqslant$0.75. For shorter exposure times and for XRFs with fewer counts, this detection rate reduces accordingly. For exposure times $\leqslant$10 ks the detection rate is below 0.03 even for XRFs with 160 photons. Hence this justifies our decision to analyse XCS point sources with a minimum observation exposure time of 15 ks.

5.4.2 Methodology advantages and disadvantages

The method that we use to detect potential XRFs has both advantages and disadvantages which are worth considering.

Pipeline

The major advantage was that much of the code to generate and analyse the light-curves from clean-event files had already been written (or were developed in tandem) for use in the AGN project described in Chapter 4. Therefore, the pipeline software for these two projects progressed in parallel - with relevant error corrections in the code being quickly

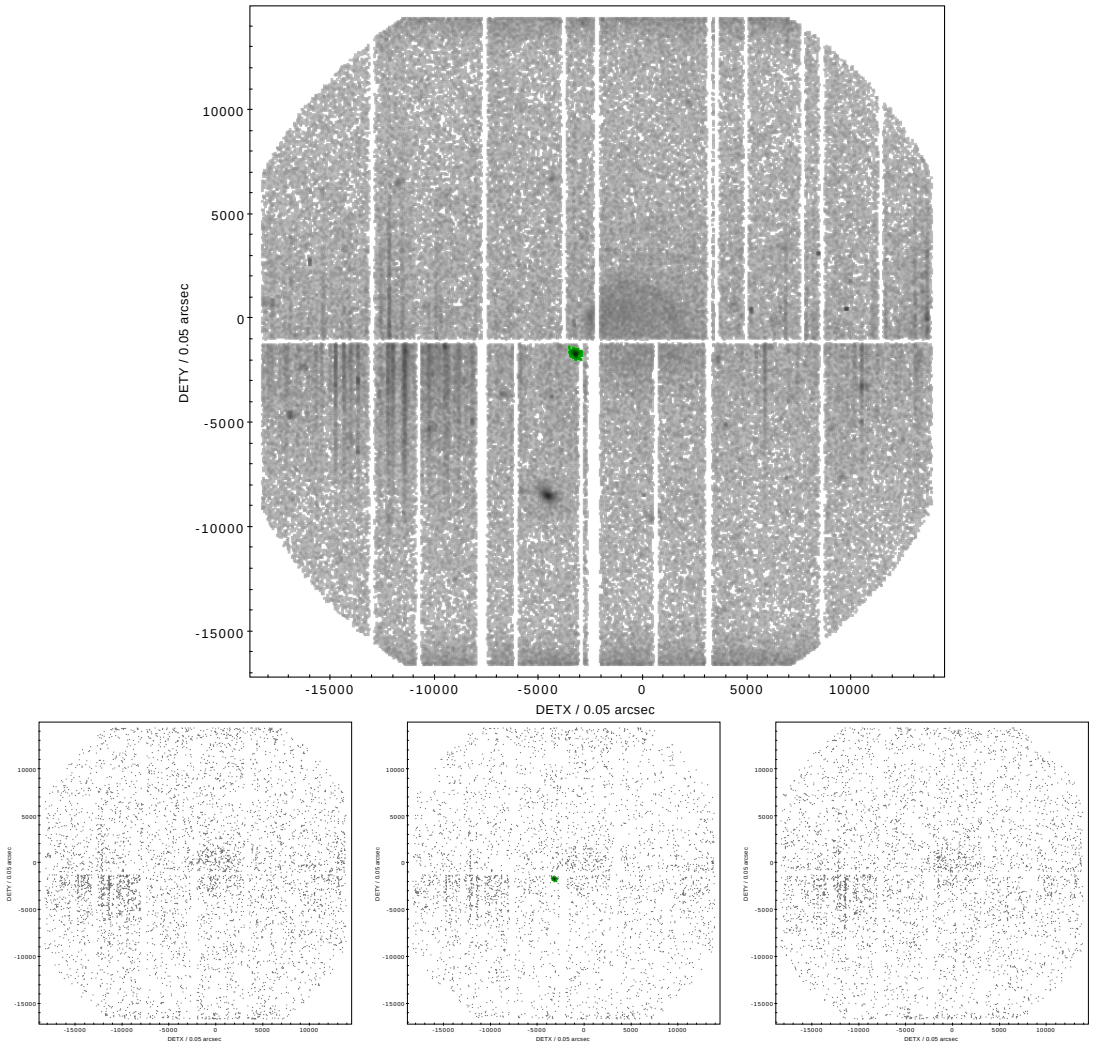

Figure 5.7: PN ObsID 012590101, shown in DETX, DETY chip coordinates with a fake 160 count XRF Top, Full 47 ks exposure time with XRF shown in green, and all other photons in grey. Bottom, left 500 sec time bin before the dummy XRF, middle 500 sec during flash, right 500 sec time bin after the dummy XRF.

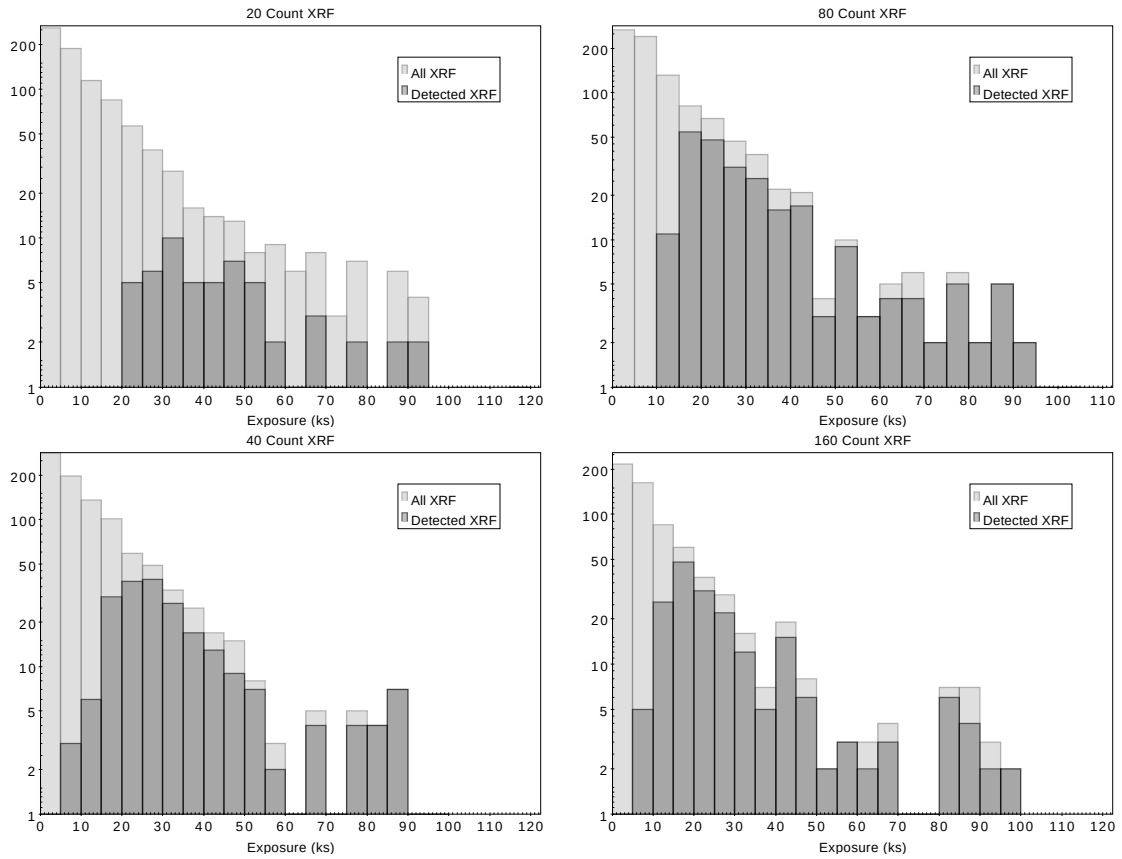

Figure 5.8: Histograms showing exposure time of detected dummy XRFs (dark grey bars) with 20 (left top), 40 (left bottom), 80(right top) and 160 photons (right bottom) and all ObsIDS where dummy flashes were inserted (light grey).

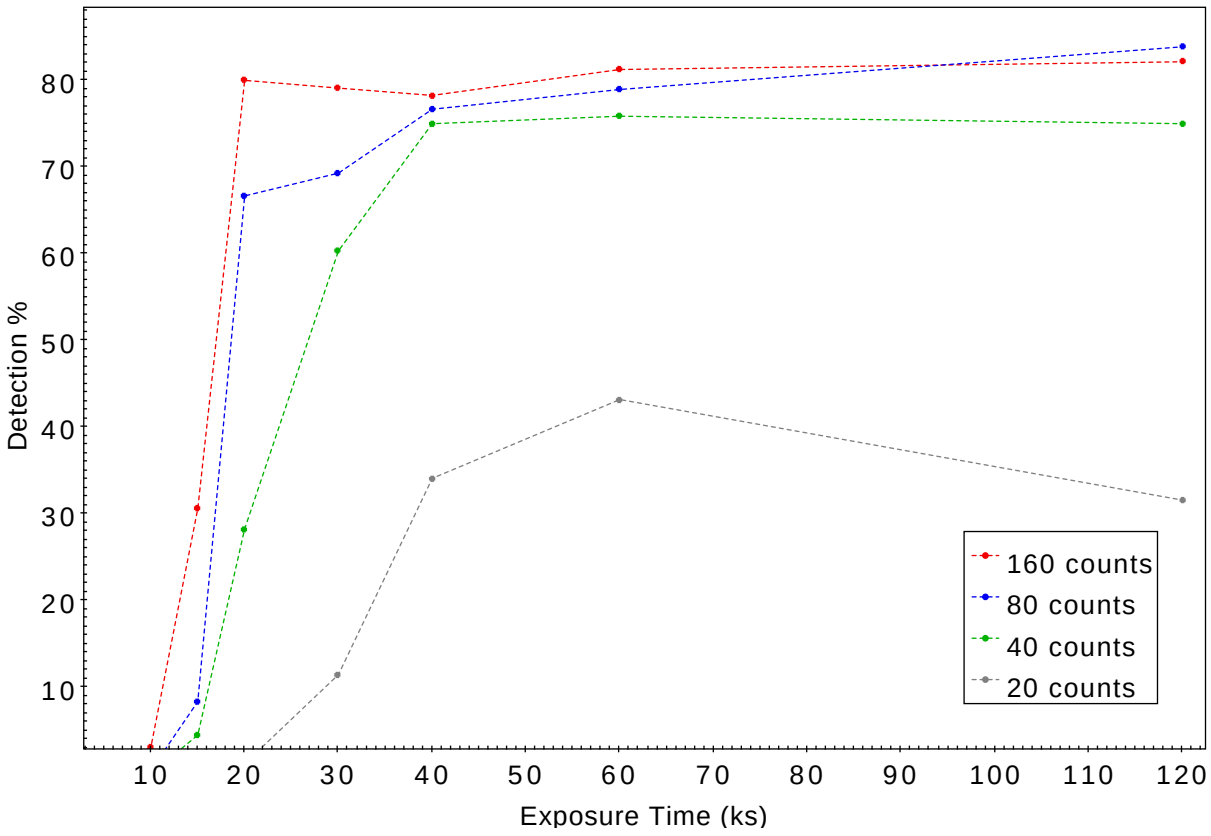

Figure 5.9: Percentage of dummy XFRs with 20 (grey) 40 green), 80 (blue) and 160 (red) photons that are detected by our method when inserted into 1000 random ObsIDs as a function of ObsID exposure time.

written across from one to the other. It was a very fast method to analyse our source data, with results from all 107,412 point sources output within a week.

Completeness of source catalogue

The detection of XRF candidates, using our methodology, naturally depends on the size and the quality of the source catalogue. These were taken from XCS-DR2 (as of March 2016) which is not a public access catalogue and as such therefore information about the point sources was available only to the XCS collaboration. That said, there is naturally the question of how complete the catalogue is: how many extra point sources were not detected by XCS which would increase the input to the pipeline. An alternative, more up-to-date, catalogue such as XMM DR7 Webb and XMM-Newton Survey Science Centre (2017) would have provided us with a larger source catalogue. (In comparison with XCS-DR2's 253,667 total unique sources, 3XMM claim 499,266 as of June 2017). It would be a straight-forward task to re-run the analysis based on the larger, 3MM DR7, catalogue.

Detection of low-count XRFs

Related to the completeness is the issue of whether a low count XRF is detected as a point source in XCS. We see that in Figure 5.9, for example, when we search for fake XRFs with 20 photons, even with exposure times greater than 50 ks, less than half of them are detected using our pipeline. However, this assumes that these sources would have been detected by `XAPA` in the first place, which may not be the case. Therefore the percentage detection of is likely to be less. Whilst it would be a useful exercise to test this by inserting many thousand dummy XRFs into random observations to determine how many are detected by `XAPA`, this would be a hugely time consuming process (many weeks if not months). This is because combined images would need to be made for all three `EPIC` detectors and then analysed through `XAPA` to test whether the dummy sources are detected.

Blind search

If we were to proceed down this path, then it would feasible to do a blind search across all XMM observations rather than relying on the completeness of the input catalogue. In this case, rather than analysing in the time-domain, it may be more insightful to make full-map images for each 512 second time-slice of an XMM observation, checking where a point source is detected in only a single image of these (or in consecutive images if an

XRF occurs across the two time-slices). This method may have the advantage of being able to detect XRFs in observations of less than the 15 ks minimum cut-off, as well as in observations where a low count event is unaccompanied by lower levels of emission at other periods within the observation (and therefore not detected as a source by `XAPA`). However as with the issues above, it would be hugely time consuming to write a dedicated pipeline to generate multi time-slice images across all observations and cross match these to search for XRFs, as well as the processing time involved. For those reasons it wasn't considered as appropriate to this project. We note that a blind search was carried out by Law et al. (2004) using all observations (as of June 2002) with exposure time > 50 ks to reduce the file handling and data collection.

Alternative method

We note that an alternate method to detect fast transients is descibed by Irwin et al. (2016) in their search for flaring sources to nearby elliptical galaxies. This is based on the probability of the arrival time of a photon rather than the level at which maximum count-rate in the light curve is above the mean. Taking all point sources from 70 Chandra observations, clean event files are created. These are scanned by looking at the arrival time of each photon and the one which is three photons forward in time (i.e. a 4-photon burst) and determining the probability of this detection given the overall count-rate of the observation. This is then repeated for a 5, 6, 7 up to 20 photon burst. This might be an interesting method to test ours against though much more time consuming due to the repetition of the burst detection process.

5.5 Re-analyzing XRFs in Literature

Given the random and transitory nature of XRFs we can analyse only those sources described in literature from XMM-Newton observations since they would not have been in the FOV of other missions at the same time.

We re-analyse the two candidate events in Law et al. (2004) taking the XMM position and the two ObsIDs (0055140101 and 0125300101). No point source is detected by `XAPA` for either, as shown in Figure 5.10. We note the in the case of ObsID 0055140101 the exact time that the `PN` candidate source was detected by the authors falls outside the 'good time interval' (gti) of our detection. Their methodology is slightly different to ours as well as using an earlier version of `SAS` software and associated calibration files. The authors

themselves concluded that the two events they detected were probably not XRFs, so our non-detection is not a surprise.

5.6 XRF Candiate list

From our method to detect XRFs described in Section 5.4, we find 77 potential candidates in the light-curves of the PN detector at $> 5\sigma$ level. In this section we describe the following tests on these candidates in order to classify the likelihood that they are genuine XRFs. These tests are run in the following order:

5.6.1 Checking MOS Detectors

To discount the possibility that the detection is due to an anomaly in the PN detector, we make the background subtracted light-curves to check that the event is also detected in both of the two MOS detectors at $\geqslant 3.9\sigma$ levels (or at the MOS2 detector if the MOS1 detector chip at the flash location is not functioning) . There are 21 of these. Table 5.1 summarizes these 21 sources, the detection level in each of the three EPIC detectors. To these 21 we now apply the following further tests:

5.6.2 Checking for Flares

We also check the light-curve to look for signs of an exponential decay after the peak, over a period longer than a few hundred secs which suggests a flaring star. It is possible that an XRF candidate is a source where the peak of the flare is at our 5σ level. Such a light-curve would look like that in Figure 5.5. We perform a quick check by running the flare test which is included with the EKSTEST script. This searches for the highest peak in the lightcurve, which is over a threshold value with a number of consecutive bins over the same threshold. We choose the threshold to be 3σ and the number of consecutive bins to be three. Seven of the 21 sources were found to be flares of this nature and included in Table 5.1.

5.6.3 Checking for Gamma Ray Bursts

We cross check our detections with Grupe et al. (2013), a ten year catalogue of 754 GRBs detected by SWIFT, to see if there is a GRB within $5^{'}$ (the pointing accuracy of the satellite is $3^{'}$). This is to discount transient X-ray events which have been triggered by, and detected as GRBs (as the example shown in the right panel of Figure 5.2). We find none.

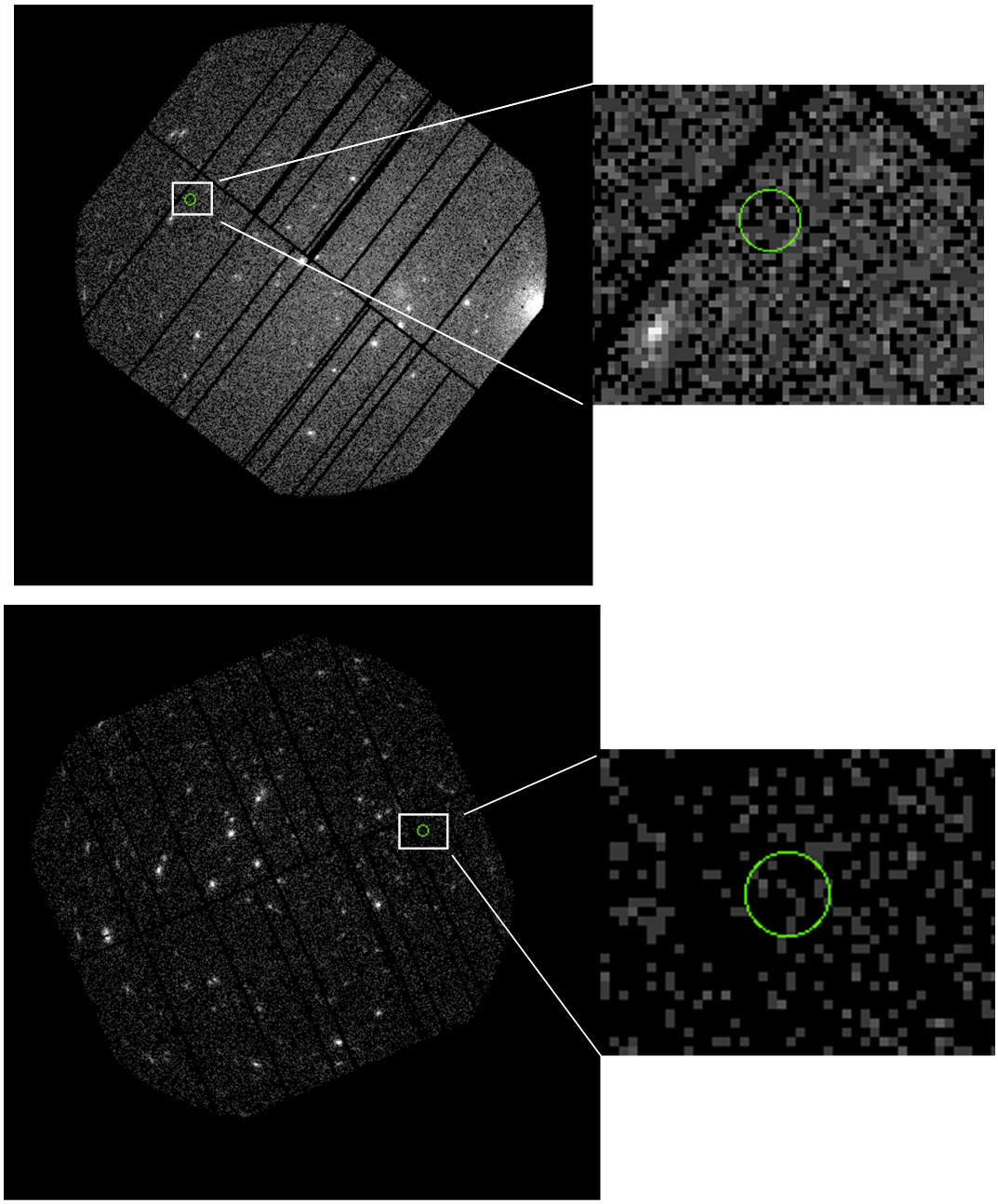

Figure 5.10: Top. Image from PN detector of ObsID 0055140101 with 20″ green region around position of the candidate XRF detected by Law et al. (2004). Bottom. Image from PN detector of ObsID 0125300101 with 20″ green region detected by Law et al. (2004). No point source is detected by XAPA at either position.

5.6.4 Checking Other Observations where the Source Position Falls in the FOV

We check other XMM observations where the XRF candidate falls within the FOV to see whether `XAPA` has identified a point source (within a 20″ radius). A match means that an X-ray point source is present in more than one XMM observation (e.g a flare star), which is therefore not an XRF. There are 12 such cases in our list of 21. Where a source does appear in other ObsIDs, we confirm that the transient XRF-like event occurs in only one unique observation. If it occurs in more than one, then the source is variable, rather than transient.

5.6.5 Checking Chandra Observations

We cross-check with positions of the candidate XRFs with the Chandra Source Catalogue Evans et al. (2010) within a 30″ radius for point sources. Since these would have been observed at a different epoch, any match is not an XRF. We find five of these matches from our 21.

5.6.6 Checking for an Optical Counterpart

We check the astronomical archives looking in NASA/IPAC Extragalactic Database (NED) Helou et al. (1991), SIMBAD Wenger et al. (2000) and The Two Micron All Sky Survey (2MASS) Skrutskie et al. (2006) to check if there is a known optical or infra-red source within 30″ which could be associated with the detected event. We note the source, separation and catalogue. We find 15 optical sources of confirmed stars and 5 infra-red sources and one source, XMMXCSJ001527.9-390508.8, without a counterpart.

5.6.7 Checking for Optical/IR Source in X-ray Image

Using our XCS image making pipeline we make X-ray images of these 21 candidate from the `PN` observation (or `MOS` camera where the `PN` detections falls on a chip-gap) indicating the source region on the full observation as well as zoomed in image of the source itself. We make optical / IR images at the source position using, in preferential order i) optical image from the Dark Energy Survey (DES) The Dark Energy Survey Collaboration (2005), ii) optical image from The Sloan Digital Sky Survey (SDSS) Abolfathi et al. (2017) iii) optical image from Digital Sky Survey (DSS) Djorgovski et al. (1998), iv) infra-red image from 2MASS. The images with respective light-curves are shown in Figures. D.1 to D.17.

5.7 Categorizing Candidates

Using the tests as described above we divide of our candidates into three categories which we sumamrise in Table 5.2 where category C) is a confirmed star, category B) is not-confirmed but likely star from an infra-red source and A) is a likely XRF.

XCS Name	ObsID	Exposure	PN	MOS1	MOS2
		s	σ	σ	σ
(1)	(2)	(3)	(4)	(5)	(6)
XMMXCSJ001445.7-391440.9	0655050101	91012	6.28	5.48	5.53
XMMXCSJ001527.9-390508.8	0149780101	91380	5.62	*	5.68
XMMXCSJ004336.3+405336.1	0672130101	72079	8.08	7.01	3.87
XMMXCSJ011057.3-730515.2	0601212201	18395	5.27	4.76	3.43
XMMXCSJ015708.9+373739.8	0149780101	30829	6.49	5.42	7.21
XMMXCSJ025412.5+414303.0	0605540101	95584	5.61	*	5.1
XMMXCSJ033241.9-275704.0	0604960801	68694	7.56	*	7.25
XMMXCSJ042815.1+155410.6	0101440501	36456	5.78	5.21	5.97
XMMXCSJ050749.0-373823.9	0110980801	29347	5.42	4.07	4.81
XMMXCSJ053547.0-062911.8	0089940301	34986	5.25	5.34	4.78
XMMXCSJ061606.4-211801.4	0300800101	27469	5.63	*	5.9
XMMXCSJ065423.9-240056.5	0652250701	91464	6.19	5.23	5.16
XMMXCSJ074410.3+393507.2	0551851201	59163	6.28	3.91	5.75
XMMXCSJ083841.2+195946.2	0721620101	49335	8.50	5.69	7.60
XMMXCSJ095802.0+685710.3	0200980101	59439	5.62	6.12	6.76
XMMXCSJ102809.3-434628.7	0300430101	85509	7.74	*	5.43
XMMXCSJ191527.4-241826.5	0605580901	47106	6.01	*	7.59
XMMXCSJ205958.4-425647.8	0691670101	42973	5.81	*	6.93
XMMXCSJ215906.1-201602.3	0555220101	43529	5.31	*	4.54
XMMXCSJ220310.7-344406.5	0722360301	87628	6.73	*	6.32
XMMXCSJ235138.2-261304.0	0148990101	19288	5.12	5.31	4.64

Table 5.1: Sources detected as possible XRFs. (1) XCS name. (2) XMM Observation ID. (3)PN Live time of CCDs in extraction region,i.e.the time that the CCD is taking data. (4),(5),(6) Lower limit of number of σ maximum count rate from mean count rate in each camera. (7) results from flare test σ of peak above median level and across three or more consecutive time bins. *no MOS1 light-curve made due to event falling on area of dead CCD chip.

XCS Name	Other source det.	Other FOV	Chandra det.	Nearest source $< 30''$	Sep $''$	Fig.	Flare σ	Cat.
(1)	(2)	(3)	(4)	(5)	(6)	(7)	(8)	(9)
XMMXCSJ001445.7-391440.9	2	2	yes	variable star[1]	5	D.1		C
XMMXCSJ001527.9-390508.8	2	2	yes	star[2]	1.6	D.2	5.42	C
XMMXCSJ004336.3+405336.1	0	2	no	IR source[3]	0.6	D.3	2.72	C
XMMXCSJ011057.3-730515.2	1	2	no	star[2]	2.5	D.4		C
XMMXCSJ015708.9+373739.8	0	0	no	none		5.11		A
XMMXCSJ025412.5+414303.0	0	1	no	star[2]	0.6	D.5	4.32	C
XMMXCSJ033241.9-275704.0	3	7	no	star[1]	1.6	D.6	5.27	C
XMMXCSJ042815.1+155410.6	0	0	no	star[2]	8.3	D.7		C
XMMXCSJ050749.0-373823.9	0	0	yes	star[1]	3	D.8		C
XMMXCSJ053547.0-062911.8	0	0	yes	flare star[2]	2.7	D.9		C
XMMXCSJ061606.4-211801.4	0	0	no	IR source[3]	0.7	C.1		B
XMMXCSJ065423.9-240056.5	2	3	no	IR source[3]	0.6	D.10	4.55	C
XMMXCSJ074410.3+393507.2	0	1	no	star[3]	1.7	D.11		C
XMMXCSJ083841.2+195946.2	0	0	no	star[2]	1.6	D.12		C
XMMXCSJ095802.0+685710.3	9	9	no	star[1]	1.8	D.13	4.44	C
XMMXCSJ102809.3-434628.7	0	1	no	IR source[3]	0.7	C.2		B
XMMXCSJ191527.4-241826.5	6	6	yes	IR source[3]	1.5	D.14		C
XMMXCSJ205958.4-425647.8	0	1	no	IR source[3]	2.1	C.3		B
XMMXCSJ215906.1-201602.3	0	0	no	IR source[3]	2.1	D.15		C
XMMXCSJ220310.7-344406.5	0	0	no	IR source[3]	2.8	D.16		C
XMMXCSJ235138.2-261304.0	0	0	no	IR source[3]	0.4	D.17	2.42	C

Table 5.2: XRFs.candidates (1) XCS name. (2) Number of other ObsID where a source is detected by XAPA at the location. (3) Number of other XMM ObsIDs where the candidate position is in the FOV (4) Whether a source detected in Chandra within $30''$. (5) Nearest optical or IR source in catalogue ([1]NED, [2]SIMBAD, [3]2MASS), (6) Separation between XRF candidate and source (7) Figure reference, (8) Flare test result from `PN` detector using `EKSTEST` routine with number of σ the peak count-rate is above medium for minimum of three consecutive bins(9) Category as defined in the text, A) most likely XRF, B) non-confirmed likely star C) star.

5.7.1 Category C - Star

We reject a candidate that has been catalogued as a star in SIMBAD or where the light curve suggests an exponential decay typical of a star. Also where the candidate is detected as a source in other XMM observations. These are classified as category C candidates. XMMXCSJ001445.7-391440.9 is an example of this. X-ray and optical images and light-

curves for the XMMXCSJ001445.7-391440.9 are shown in Figure D.1. A flare event was detected at 5.65σ above the median level and the optical SDSS image shows a star at 0.5″ separation. The source position is also in the FOV in two other observations (0028740101 and 0028740201) where is it detected as a point source by XAPA. It is also detected in an observation by Chandra at 5″ separation. SIMBAD defines this source as a flaring star. Other candidates, which are clearly starts, in this category are described in Appendix D.

5.7.2 Category B - non-confirmed star or IR/Optical source

Where a candidate has not been identified as a star, but where an infra-red or optical source has been detected nearby, we categorise as category B. These may be genuine XRFs associated with an extra-galactic origin and would require further investigation to determine the nature of the nearby source. XMMXCSJ061606.4-211801.4 is an example of a candidate which is an infra-red source not confirmed as a star. X-ray and optical images and light-curves for the candidate XMMXCSJ061606.4-211801.4 are shown in Figure C.1. The source falls in the FOV of only one observation. A source 2MASS 06160644-2118014 is at 0.7″ separation in SIMBAD. Others candidates which are non-confirmed stars or other IR sources are described in Appendix C.

5.8 Category A - Likely XRF

Having categorized each of our XRF candidates, we can see from Table 5.2 that we discounted 17 of the 21 sources as stars (category C) and are left with three IR/Optical sources not confirmed as stars (B) and one final candidate without a nearby confirmed source (A). In this section we investigate further the nature of this candidate. Figure 5.11 shows the X-ray image of the full ObsID and source image (with 16x zoom) from the `PN` detection as well as the three light curves from each detector and an optical image from DSS.

We make a background subtracted spectrum - taking the same source and background regions as for generation of the light curves. The spectra are binned so that there are at least 25 counts in each spectral bin. Associated `rmf` and `arf` files are make using the commands `rmfgen` and `arfgen` and the spectrum made in `XSPEC` where we note the total background subtracted counts and flux.

The upper image in Figure 5.12 shows the three `EPIC` combined images in the 0.5-2.0 keV band together with 16x zoomed into source region. The middle image shows three 1500 secs

image frames (with the full ∼30 ks duration such that 20 were made across the observation) from the PN exposure at the source region, clearly showing the transient event in only one frame, the bottom shows the PN light-curve in 50 second time bins centred around the flash event showing a duration of around 400 secs (with a t_{90} time of around 200 secs) and PN spectrum.

We fit the PN spectrum with a simple absorbed powerlaw model (after Heise et al. 2001) phabs(po), with the absorption column n_H value from the Dickey and Lockman derived value. With the best fit parameters we find a flux of between 8.17×10^{-13} and 1.06×10^{-12}erg/cm^2/s (relating to a fluence of between 3.27×10^{-10} and 4.24×10^{-10}erg/cm^2) from 142 background subtracted photons.

We suggest alternatives to it being a genuine XRF.

Random nature of statistics. Given that this transient event was seen at greater than 5σ in all three EPIC detectors, its is almost certain that this is not due to statistical fluctuations.

Cosmic ray. We rule out a cosmic ray, since in making our clean events file, we choose photon event grades PATTERN <= 4. This rules out non X-ray events e.g. cosmic rays.

False detection of source by XAPA. We rule this out since the source is also detected in the 3XMM DR-5 X-ray catalogue Rosen et al. (2016).

Faint optical source. It is possible that there is an optical or IR source at the position which is too faint to have been detected by previous observations. This can only be discounted with a follow-up targeted deeper observation.

Type 1 X-ray burst from neutron star.

We compare the spectral fit of XMMXCSJ015708.9+373739.8 with two models. An absorbed powerlaw, typical of a genuine XRF, and an absorbed black-body, typical of a Type 1 X-ray burst. Figure 5.13 shows the spectra points with best fit model lines and residuals in the low panel for each model. For the powerlaw model, the reduced χ^2 value is 0.827 for 4 degrees of freedom and a null hypothesis probability of 0.51. The power law index

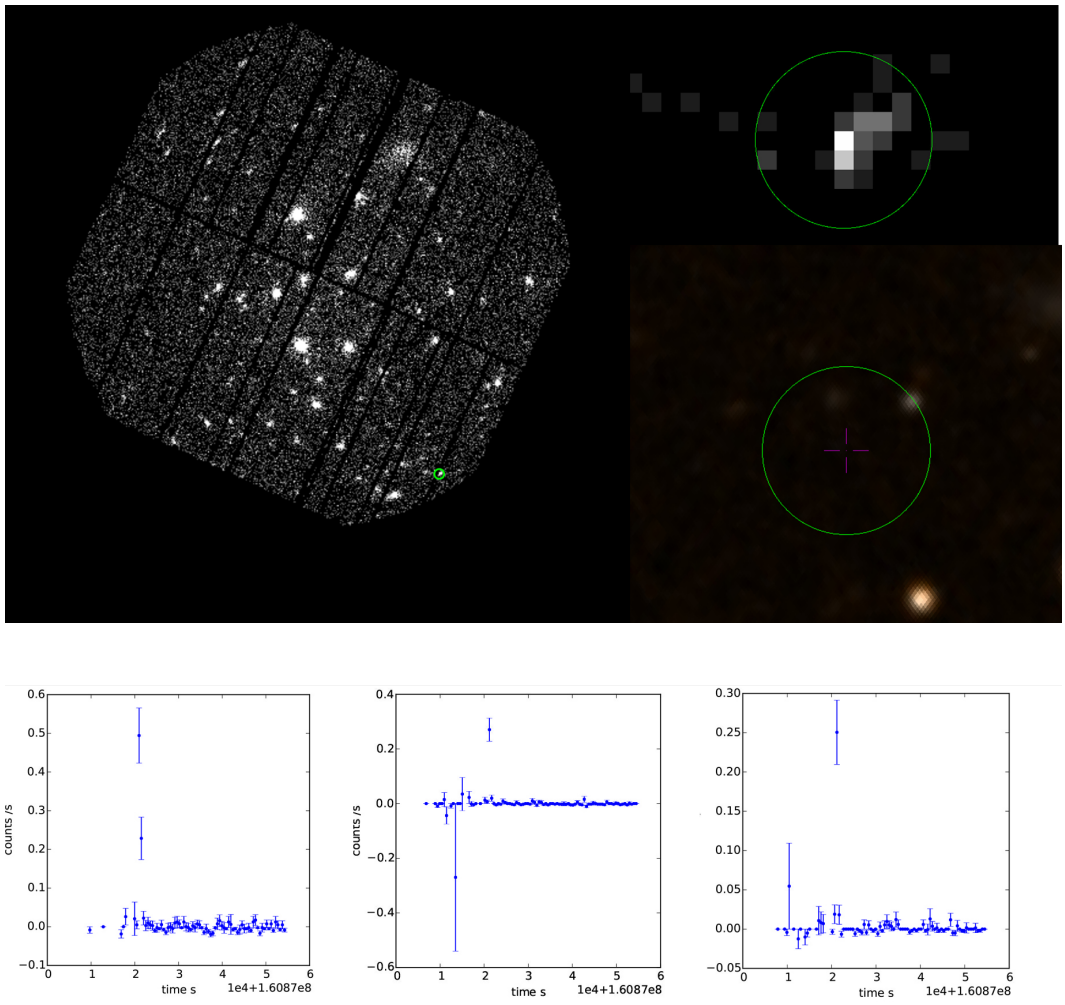

Figure 5.11: XMMXCSJ015708.9+373739.8. Top. X-ray image in PN observation 0149780101 in 0.5-2.0 keV with 16× zoom and optical DSS image, each with green 20″ region. Bottom. PN, MOS1 and MOS2 light curves.

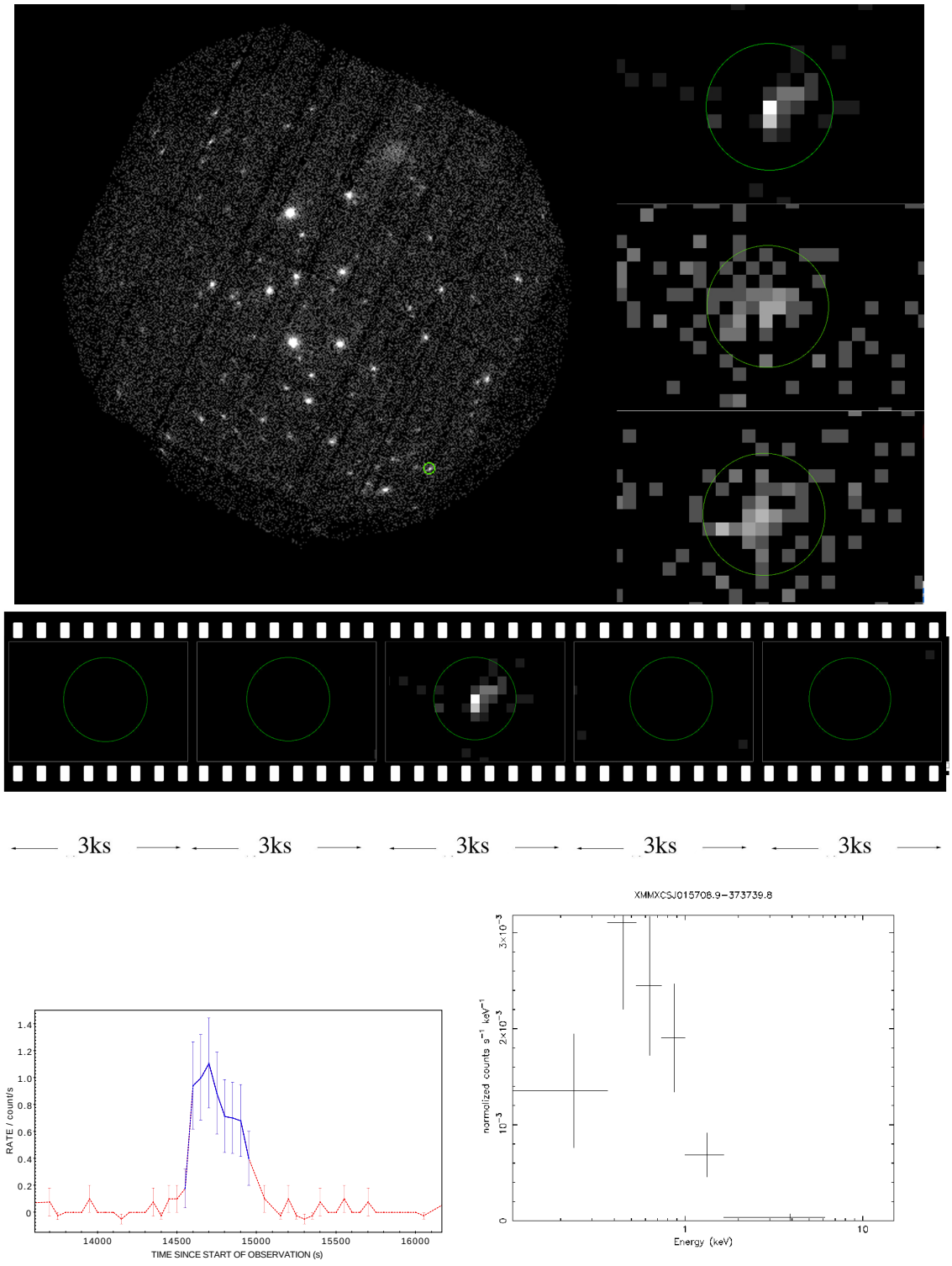

Figure 5.12: XMMXCSJ015708.9+373739.8. Top Combined PN, MOS1 and MOS2 images of ObsID 0148990101 in 0.5-2.0 keV band together with 32xzoom of source region in PN, MOS1 and MOS2. Middle, 'Film strip' of PN images around the source region in 1500 sec frames, showing frames 3-7 (of 20) from total exposure. Bottom. Left - PN detector Light-curve in 50 sec time-bins centred around the flash event. Right, source spectrum from PN detector.

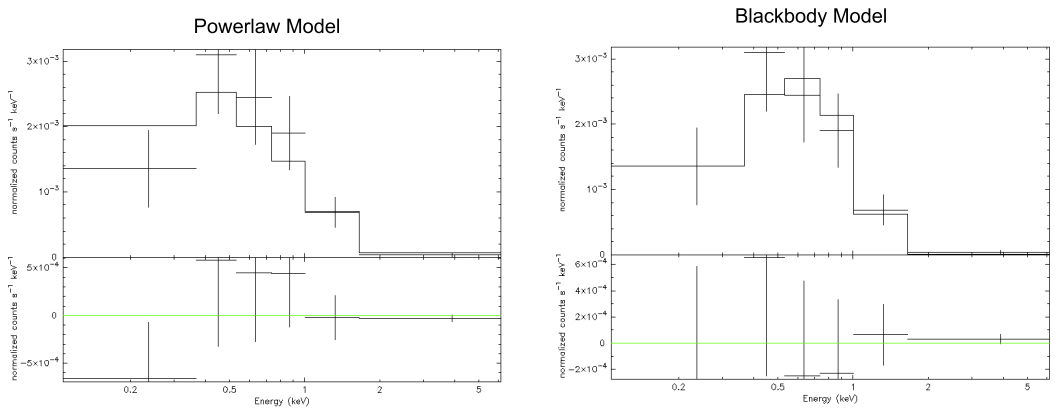

Figure 5.13: Comparison between the best fit models for the PN detector spectrum of XRF candidate XMMXCSJ015708.9+373739.8. Left is the spectrum fit to an absorbed powerlaw (typical of an XRF), and right when fit with an absorbed blackbody model (typical of a Type 1 X-ray burst). The lower panel in each case are the residuals from the best fit.

for this model is 2.55±0.27. For the black body model the reduced χ^2 value is 0.394 for 4 degrees of freedom and a null hypothesis probability of 0.81. Given these results, and the low number of counts, we cannot rule out that XMMXCSJ015708.9+373739.8 is a Type 1 X-ray burst rather than an XRF. However, we remake the light-curve now in 5 second time bins as shown in Figure 5.14. This shows a rise time and decay more consistent with that of an XRF than a Type 1 X-ray burst (which would show a faster rise time ∼1 sec and exponential decay).

5.9 Deriving an Upper Limit on the Full-Sky Event Rate

We now attempt to estimate a full sky yearly rate of XRFs typical of XMMXCSJ015708.9+373739.8 by first assuming an upper limit for this event of 1. The live exposure time for the observation (i.e. the time over which the CCD was taking data) of this event is 30829 secs over a FOV of 0.19 square degrees. (We note that at this stage we don't take into account the chip gaps, nor vignetting, nor effect of n_H column which would reduce this FOV.) In order to estimate a full-sky rate we need to derive a detection fraction factor. This is the fraction of likely detection of a 142 count flash as a function of exposure live-time. We have seen from Section 5.4.1 that the longer the exposure, the more likely we are to have observed such a flash.

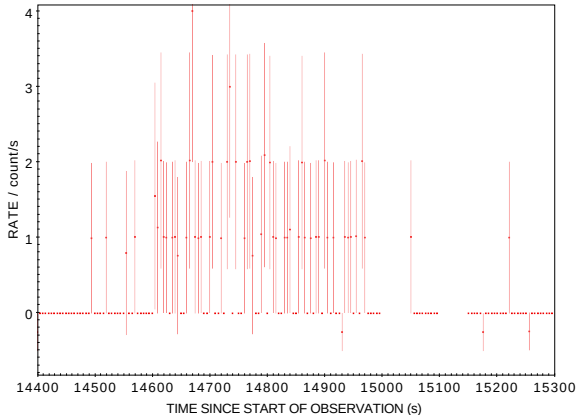

Figure 5.14: Light-curve for XMMXCSJ015708.9+373739.8 now in 5 second time bins showing the period of the flash event. The rise time and decay is consistant with being an XRF rather than that of a Type 1 X-ray burst which would show a fast rise time and exponential decay.

Following the method outlined in Section 5.4.1, we add a fake 142-count XRF into 1000 random observations and use our pipeline to determine whether they are detected as a flash or not.

Figure 5.15 Top shows a histogram of detections (dark grey) and all observations (light grey) by binned exposure time. Bottom shows the detection fraction in time bins.

Since we detect one 142 count flash XRF in the 2355 individual observations (as outlined in Section 5.3) our total exposure coverage, the product of exposure and FOV coverage, is given by;

$$\Sigma_i(FOV \times T_{\rm exposure} \times D_{\rm frac}) \tag{5.1}$$

where i is the individual observation, FOV is the field of view in square degrees and depends on the on science mode used for that observation (i.e. 0.19 for `FULL FRAME`, 0.095 for `LARGE WINDOW` and 0.0054 for `SMALL WINDOW`), $T_{\rm exposure}$ is the live exposure time for each of the observations and $D_{\rm frac}$ is the detection fraction appropriate to the exposure. From Equation 5.1 this exposure coverage comes to 9.7x10^6 sec deg^2.

The full-sky area total exposure coverage is 1.30 x 10^{12} sec deg^2 (an area of 41253 deg^2 and time of 31556736 secs in a year). We therefore estimate an upper limit of 1.3x10^5 events at a fluence of between 3.27x10^{-10} to 4.24x10^{-10} erg cm^{-2} which agrees well when plotted

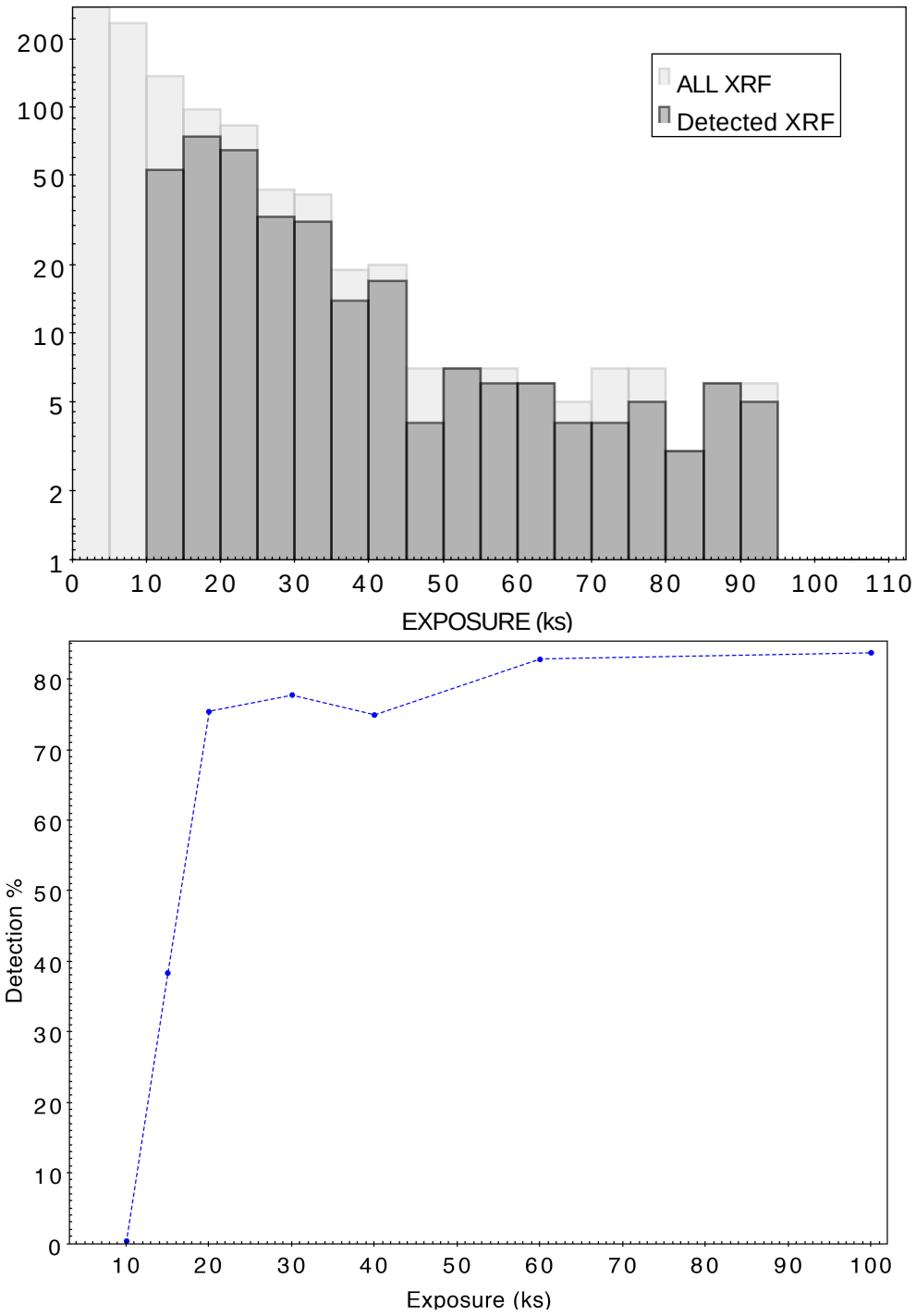

Figure 5.15: Top. Histogram of exposure live times for 1023 observations where a dummy XRF with 142 counts has been inserted at random with blue bars showing number of flashes detected using our method described in Section 5.4.1. Bottom shows the detection fraction by exposure live time.

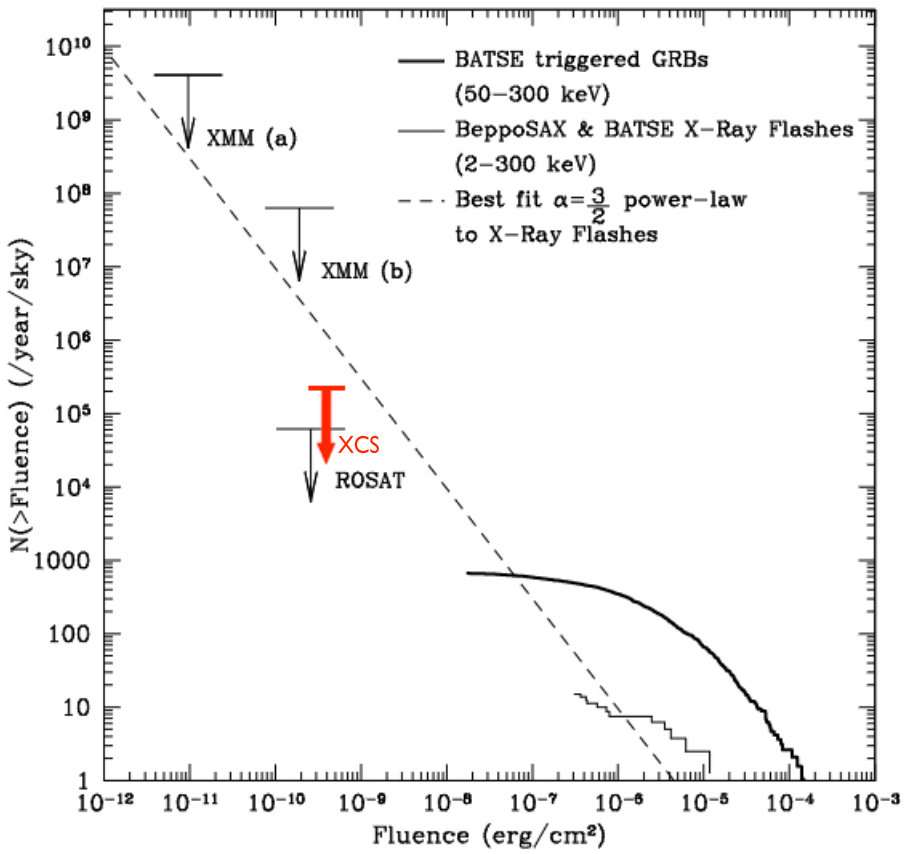

Figure 5.16: Figure adapted from Law et al. (2004). As Figure 5.3 but now including our 68% upper limit result in the energy passband 0.5 to 2.0 keV shown in red.

against the 90 per cent ROSAT upper limit of Vikhlinin (1998) and results from Law et al. (2004) (who assume an upper limit of 1 for their detections) as shown in Figure 5.16.

5.10 Chapter Summary

In this chapter we have described a new method to detect XRFs, some of the rarest X-ray transient events, by a serendipitous search through the XCS point source catalogue. From the 21 candidates we have detected to $> 5\sigma$ level in the PN and $> 3.9\sigma$ in the MOS cameras we categorized them into confirmed (presumably flaring) stars, non-confirmed IR sources, and one strong XRF candidate. We looked in detail at this candidate and speculated on its nature by comparing its spectrum and light-curve with that a Type-I X-ray burst. We cannot be certain that this candidate is an XRF rather than a Type 1 X-ray burst (or other source). For future work we would like to obtain a deep optical/IR image of this source to ascertain if there is a faint external galaxy or Milky Way star at that location.

It would also be useful to obtain another targeted XMM or Chandra observation of this location, as it only appears in the FOV of one unique ObsID to date. The second XMM or Chandra observation would demonstrate if there is a faint X-ray source at that location.

We defined a method to derive a selection function of percentage of XRF detection to observation exposure time which we made by injecting dummy XRF events in to existing XMM observations. We used this to estimate an upper-limit of number of XRFs of a fluence per sky per year based on our best candidate XRF.

Looking forward, for this work to be suitable for journal publication, more work would need to be done on the selection function used to estimate the fluence. For example, by taking into account vignetting, chip gaps, and n_H column as well as scaling the dummy counts to take account of the exposure map. Further, we assumed that all our fake XRF sources would have been detected as point sources by our `XAPA` detection pipeline. We should like to test whether this is a fair assumption. This is a non-trivial and time consuming effort, as it involves re-running thousands of ObsIDS in each of the three `EPIC` camera through the XCS source detection pipeline.

Using our pipeline we would also like to investigate variable X-ray sources candidates within Galactic Plane (our current analysis is restricted to $|b| > 15^\circ$). The methodology we have developed can be adapted to uncover *all* flaring and transient sources in the XMM archive. We would then be able to predict the expected detection rate of such sources in eRASS.

Chapter 6

A Search for Dark Matter Emission Lines in the X-rays of XCS Clusters

6.1 Introduction

One of the most fundamental questions in current cosmology concerns the nature of dark matter. Although the evidence for its existence is overwhelming, it is not incontrovertible (other theories such as those invoking modifications of Newtonian gravity exist) and its nature is still unknown. In this chapter we describe preliminary work using the XCS cluster catalogue in order to search for evidence of one possible dark matter candidate, the so-called 'sterile neutrino'. We aim to test whether any detection is dependant on cluster temperature, something which would be new to literature.

Section 6.2 is an overview for the evidence of dark matter and the various candidates summarised in Section 6.3 with a focus on the sterile neutrino in Section 6.4. Section 6.5 reviews recent attempts that claim to have found evidence of an unknown emission line in galaxy clusters that might be due to the sterile neutrino, along with other authors disputing these claims. We describe our cluster sample and methodology in Section 6.6 with Section 6.7 charting how we test this methodology. We present application of our method to sample of stacked clusters in Section 6.9 and suggest how further work can take this research forward in Section **??**.

6.2 Dark Matter Evidence

Ever since Zwicky (1933), in his famous paper studying the rotational motion of the outlying galaxies in the Coma cluster, postulated the existence of dark matter, there has been speculation as to the exact nature of what this unseen matter actually is. Since then, other independent evidence that points towards including dark matter in our current cosmological model makes this even more compelling. Here, starting with Zwicky's findings, we summarise some of them.

6.2.1 Mass-to-Light Ratio of the Coma Cluster

Using the virial theorem, Zwicky inferred the mass of the Coma cluster and compared this to the luminous content. His mass-to-light ratio of around $400M_{\odot}$ per solar luminosity far exceeded by two orders of magnitude what was expected given the luminous content alone. In fact, the total luminous mass would not be enough to keep the galaxies bound to the cluster and hence he postulated a *dunkle kalte Materie* or dark cold matter (though probably not *cold* in the sense that we understand it today).

6.2.2 Galactic Star Rotation Curves

Further direct evidence of the existence of a dark matter comes from studying the rotation curves of stars, i.e. their rotational velocity as a function of distance from the centre of the galaxy. Using Newtonian dynamics, we should expect the velocity to fall further from the centre of mass by:

$$v(r) = \sqrt{\frac{GM(r)}{r}} \tag{6.1}$$

where $M(r) = 4\pi \int \rho(r) r^2 dr$, and $\rho(r)$ is the mass density profile and would be expected to fall as $\propto \frac{1}{\sqrt{r}}$. However, for example, as shown in Figure 6.1 from Begeman et al. (1991), the velocity of stars remain fairly constant and independent of how far from the centre they are. This implies that the $M(r) \propto r$ and points to the existence of a dark matter halo.

6.2.3 Gravitational Lensing - The Bullet Cluster

Figure 6.2 shows a composite X-ray, optical and gravitational lensing map image of the 'Bullet Cluster' (1E 0657-56) Markevitch et al. (2006). There are, in fact, two clusters which have undergone a merger. The red traces out the X-ray of the hot intra-cluster gas

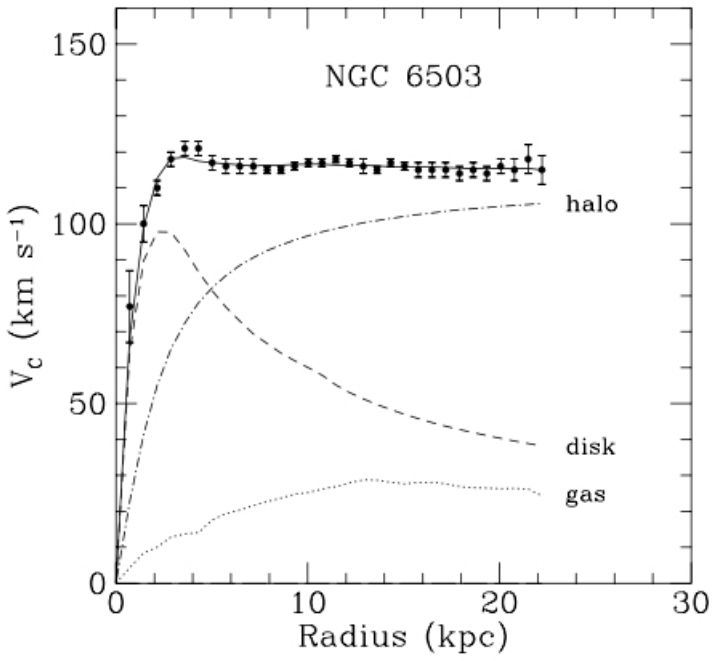

Figure 6.1: Rotation curve of NGC 6503. The black dots are the estimated rotational velocity of stars from observations, the dotted, dashed and dash-dotted lines are the contributions of gas, disk and dark matter, respectively. Image and caption from Begeman et al. (1991).

Figure 6.2: Composite image of The Bullet Cluster. The red traces the hot intra-cluster gas, the blue traces the dark matter component through gravitational lensing and the white is the optical content. Image composite credit: X-ray: NASA / CXC / CfA / M.Markevitch et al.; Optical: NASA / STScI; Magellan / U.Arizona / D.Clowe et al.; Lensing Map: NASA / STScI; ESO WFI; Magellan / U.Arizona / D.Clowe et al.

of the two clusters as it interacts, slows down and heats up in the heart of the system. The blue traces out the centre of mass of the system through lensing techniques, hence the dark matter. This shows that rather than one centre of mass in the heart of the luminous material, there are two either side. Therefore, it can be concluded that the normal matter, i.e. the gas, has become disconnected from the dark matter which has slipped through the system with little interaction. Although some recent authors have suggested alternate modified gravity hypotheses that might have resulted in the gravitational lensed signals e.g. Milgrom (2008), the Bullet Cluster is still one of the most important current evidence for the existence of dark matter (e.g. Clowe et al. 2006).

6.2.4 Cosmic Microwave Background

A futher clue pointing towards the existence of dark matter comes from the cosmic microwave background. Before recombination at around z ~1100, gravity compressed the baryon dark matter photon fluid into potential wells with a resisting photon pressure which

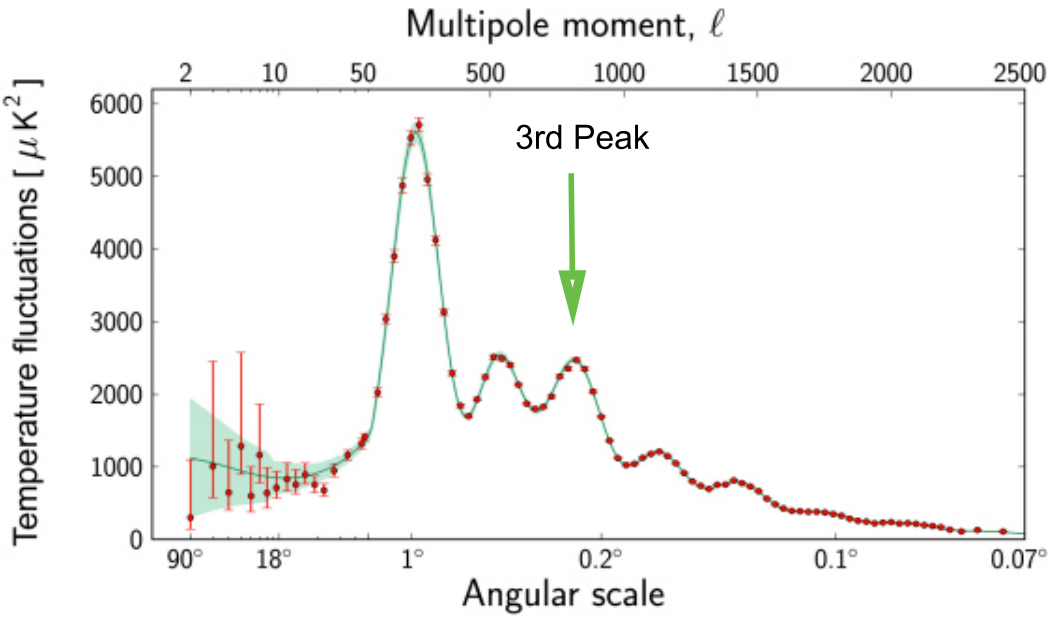

Figure 6.3: Power spectrum of the temperature fluctuations in the Cosmic Microwave Background. The height of the third peak indicates the amount of dark matter present in the Universe. Image from ESA and the Planck Collaboration.

sets up acoustic oscillations. Although the dark matter particles coalesce through gravity, in the same way as regular matter, they interact very weakly with photons. Therefore whilst normal matter experiences a repulsive force from pressure of the photons, dark matter does not. These different modes of the acoustic oscillations are frozen at recombination into the snapshot of the CMB we detect today. Looking at the power spectrum of the CMB, specifically the height of the third peak in relation to the second peak as shown for example in Figure 6.3 gives us an estimate of the dark matter content of the Universe, which has been measured most recently by Planck Collaboration et al. (2014) at a value of 26.8% of the energy density of the Universe.

6.2.5 Large scale structure

If studying the CMB shows us the density distribution in the Universe at z∼1100, then mapping the distribution of galaxies and clusters with observation from the Sloan Digital Sky Survey for example, gives us a snapshot of large scale structure, as shown in 6.4. Here, we see patterns in the distribution of large scale objects. Using N-body simulations, Lemson and Virgo Consortium (2006) suggest that this structure could not have occurred

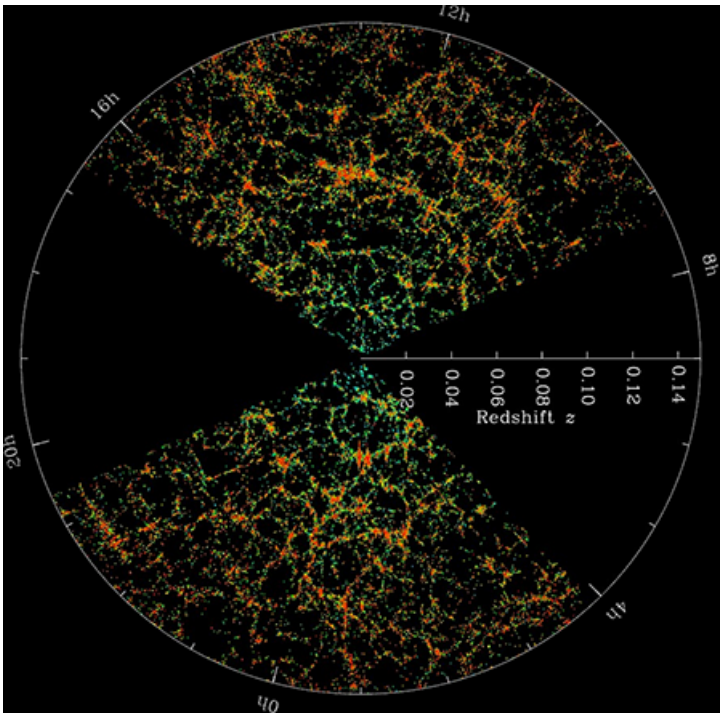

Figure 6.4: Large scale structure as shown in Sloan Digital Sky Survey 1.25 Declination Slice 2013. Image from by M. Blanton and the Sloan Digital Sky Survey.

through the gravitational effect of normal matter alone given the time available. They resolve this problem by adding in a dark matter content.

6.3 Dark Matter Candidates

Although many different candidates have been postulated - ranging from relativistic *hot* (HDM) to non-relativistic weakly interactive *cold* (CDM), and those in-between dubbed *warm* (WDM) - each of these must pass the following tests; i) they are stable on a cosmological timescale, ii) they have the correct density, iii) they can accurately describe the formation of structure and iv) they interact very weakly, or not at all, with observable matter.

This still leaves a large range of candidates from axions, e.g. Blumenthal et al. (1984), to black holes, e.g. Frampton et al. (2010) covering a mass range of tens of orders of magnitude as shown in Figure 6.5.

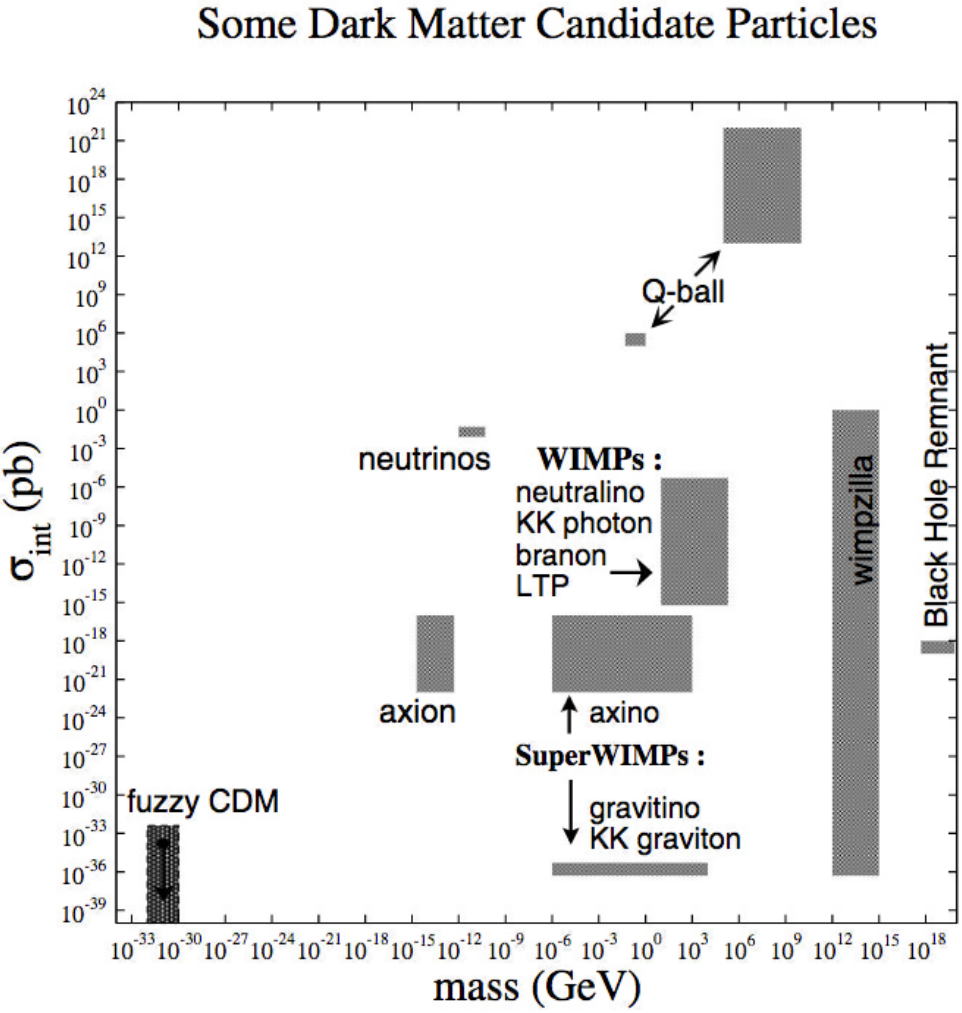

Figure 6.5: Estimated loci of select dark-matter models in the space of candidate mass in GeV versus dark-matter-candidatenucleon interaction cross section, Figure by EK Park from Report on the Direct Detection and Study of Dark Matter. https://science.energy.gov/~/media/hep/pdf/files/pdfs/dmsagreportjuly18_2007.pdf

6.3.1 Problems with HDM

In the recent years, the HDM model has become less popular as the fast-moving relativistic particles, neutrinos, present in the early universe, would not have resulted in the initial perturbations in density to clump together in the structure we see today. In the Standard Model of particle physics there are three types of neutrinos ν_e, ν_μ and ν_τ. These, alone, have been ruled out as candidates for dark matter, for although they are chargeless, collisionless and almost massless, they could only make up the entire dark matter if the total of the mass of the three flavours added up to 44eV. From analyses of cosmological data, such as the cosmic microwave background radiation, galaxy surveys, and the Lyman-alpha forest, results indicate that the summed masses of the three neutrinos must be less than 0.3eV, e.g. Goobar et al. (2006).

6.3.2 Problems with CDM

There are also problems associated with CDM. N-body simulations combined with data from studies of the CMB and large scale structure, predict more satellite galaxies than we observe e.g Klypin et al. (1999). Similarly there is a lack of substructure seen in dwarf galaxies observations but not predicted in simulations. Strigari (2013)

6.4 The Sterile Neutrino as a Candidate

The introduction of warm dark matter candidate with a rest-mass energy >1 keV (e.g. Strigari 2013) may resolve the inconsistencies associated with both HDM and CDM. The existence of a fourth kind of neutrino, the so-called sterile neutrino, is one such candidate. Unlike the three known neutrinos which are left-handed (their spin is in the opposite direction to the momentum vector), sterile neutrinos are thought to be right-handed and to spontaneously decay with the rate (e.g Boehm, F. and P. 1987),

$$\Gamma_\gamma(m_s, \theta) = 8.7 \times 10^{-31} s^{-1} \left(\frac{sin^2 2\theta}{10^{-10}}\right) \left(\frac{m_s}{1\,\mathrm{keV}}\right)^5 \tag{6.2}$$

where m_s is the particle mass and θ is the so-called mixing angle. By nature, sterile neutrinos that are both stable on cosmological scale and which do not interact with ordinary matter can only be detected by the way they interact with the other neutrinos. They do this via oscillations, transforming continually as they travel with one of the three active flavour neutrinos, producing an active neutrino and photon of energy $E = \frac{m_s}{2}$. Within the three known neutrinos for example an electron neutrino will become some quantum

superposition of the three states ν_e, ν_μ and ν_τ, after propagating a distance. This oscillation is represented by the mixing matrix U defined by:

$$U = \begin{bmatrix} c_{12}c_{13} & s_{12}c_{13} & s_{13}e^{-i\delta} \\ -s_{12}c_{23} - c_{12}s_{13}s_{23}e^{-i\delta} & c_{12}c_{13} - s_{12}s_{13}s_{23}e^{-i\delta} & c_{13}s_{23} \\ s_{12}s_{23} - c_{12}s_{13}c_{23}e^{-i\delta} & -c_{12}s_{23} - s_{12}s_{13}c_{23}e^{-i\delta} & c_{13}c_{23} \end{bmatrix} \begin{bmatrix} e^{-i\alpha_1} & 0 & 0 \\ 0 & e^{-i\alpha_2} & 0 \\ 0 & 0 & e^{-i\alpha_3} \end{bmatrix} \tag{6.3}$$

where c_{ij} and s_{ij} is the cosine and sine respectively of the three mass states and α_i is the neutrino flavour.

Among others, Dolgov and Hansen (2002) show that the mass of sterile neutrinos should fall in the range 1 to 40 keV with corresponding mixing angles $sin^2 2\theta > 10^{11}$ for mixing with ν_μ or ν_τ (although mixing with ν_e is also marginally allowed at a mass of 30 keV and mixing and angle 10^{11}).

This energy falls within the X-ray part of the spectrum and therefore, if they existence, the photons should be detectable to telescopes studying high-mass clusters and nearby dwarf galaxies with high mass-to-light ratio.

6.5 Previous Attempts to Find Evidence of the Sterile Neutrino in X-ray Spectra of Clusters

An X-ray emission line resulting from the interactions of sterile neutrinos would be a faint signal in a single spectrum of even the brightest cluster. However, stacking many clusters after blueshifting to the local frame has the potential to increase the signal to noise ratio. It is this technique that has been used recently. Bulbul et al. (2014) who, by stacking X-ray blueshifted spectra (to the local frame) from 73 galaxy clusters observed by XMM Newton, claim evidence of a previously unknown emission line at 3.57 keV (as shown in Figure 6.6). If this were due to the sterile neutrino decay, it would correspond to a mass of 7.04 keV. Boyarsky et al. (2014) also by stacking spectra from XMM-Newton observations of the Andromeda galaxy and Perseus galaxy cluster also claim evidence of an unknown line at 3.52 ± 0.02 keV.

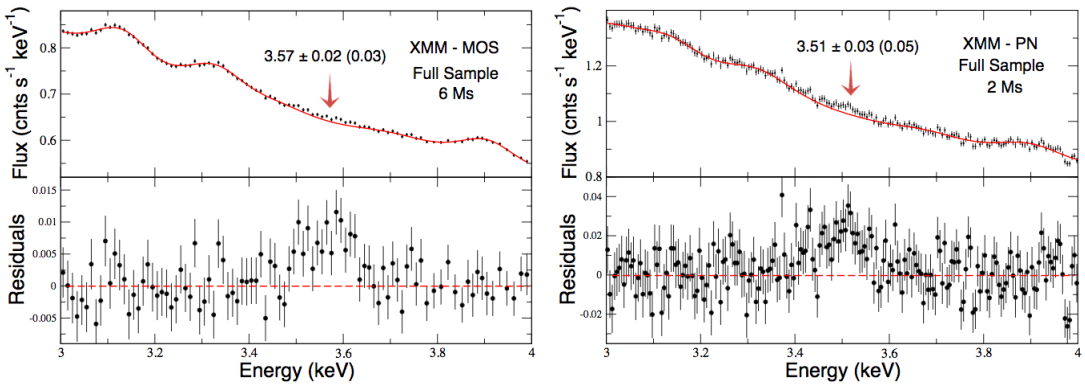

Figure 6.6: `MOS` (left) and `PN` stacked spectra from XMM observations of 73 clusters as analyzed by Bulbul et al. (2014). The red line is the best fit `APEC` model. The residuals at ∼3.57 keV are apparent in the bottom panels. Image from Bulbul et al. (2014).

Urban et al. (2015), using Suzaku X-ray data of the Perseus cluster seem to back up these claims. Modeling the stacked spectra, within 3.2-5.4 keV, with a baseline plasma with only the strongest emission lines (S, Ar Ca) as free parameters, they too find evidence of an additional emission at between 3.51 and 3.59 keV (in the core region and at larger radii respectively). This is shown in Figure 6.7. Using this result, however, they do not detect this line emission in three other clusters, Coma, Virgo and Ophiuchus. They conclude that refining their Perseus spectral fitting with a more complex plasma model with further emission lines (Cl, K, Ti and V) would remove the necessity to include the unknown line feature at 3.5 keV.

Other authors also do not find significant evidence for an unknown emission line at this energy. In an analysis of the Galactic center and a reanalysis of the data on M31 and clusters, Jeltema and Profumo (2015) suggest that known plasma lines, particularly K XVIII provide a satisfactory fit to a 3.5 keV feature they detect. Further, Malyshev et al. (2014) find no evidence of a decay line at 3.55 keV in the analysis of dwarf spherical galaxies from XMM observations.

Cline and Frey (2014) look at how the possible positive results from some of the cluster surveys might still be consistent with a negative result from dwarf galaxies. They suggest that the potential decay line is due to inelastic scattering of dark matter to a higher state that then subsequently decays, dubbed an excited Dark matter (XDM) and that this is seen in higher velocity dispersion systems such as clusters.

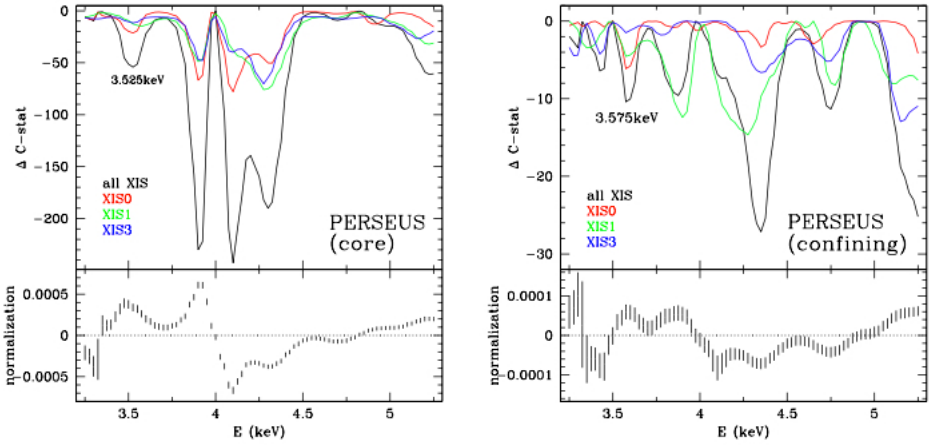

Figure 6.7: Improvement of the fit when adding a Gaussian emission line into the fitting model of the Perseus cluster as observed by Suzaku. Different colours are from individual detectors and the black line from the combined detectors. Left image is from the core region, right image is from stacked observations of regions away from the core. Bottom panel of each is the best fit normalisation. Image from Urban et al. (2015) who highlight the two unknown lines of interest at 3.525 keV and 3.575 keV in the images.

Using Chandra observations of 33 high mass clusters and stacking the blueshifted spectra Hofmann et al. (2016) find no evidence of an unidentified emission line at 3.55 keV. Furthermore, due to its superior spectral energy resolution (<7eV), the most notable study, by the short-lived Hitomi satellite, is of the Perseus cluster Aharonian et al. (2017). They too concluded that no unknown emission line at ∼3.55 keV was found in their spectrum (shown in Figure 6.8) and attribute the positive result of Bulbul et al. (2014) to systematic error.

In trying to resolve the inconsistency in Perseus results, Conlon et al. (2016) suggest that whilst the spectral data from XMM and Chandra observations were of diffuse cluster emissions only, the Hitomi observation included emission from an AGN. By modeling the spectrum of the AGN (from Chandra data) they find a Gaussian dip at around 3.54 ±0.2 keV. This is the identical energy of the emission line excess seen in the Chandra and XMM observations. They posit that when the cluster excess and AGN dip are combined, as for the Hitomi observation, the result would be no overall excess at 3.54 keV and they conclude that the disparity between the results therefore disappear. Figure 6.9 shows the modeling of the AGN before and after a negative Gaussian parameter is added to the

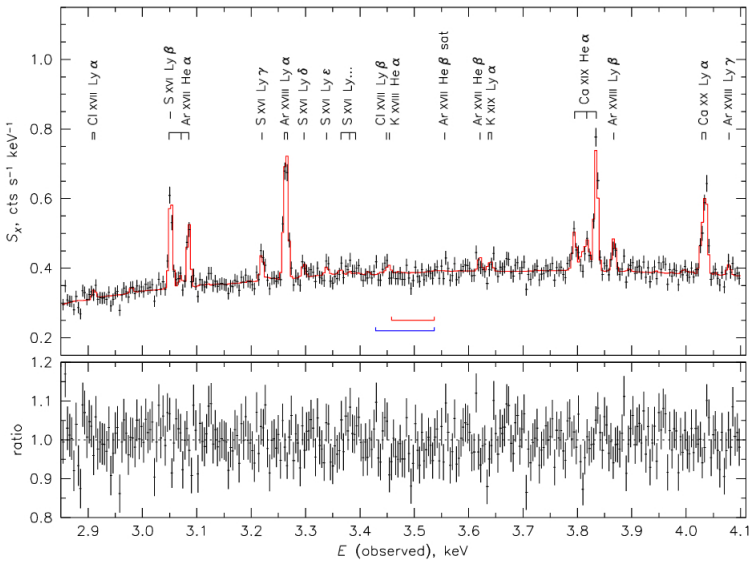

Figure 6.8: Spectrum from Hitomi SXS detector of the Perseus cluster. The energy is in the observer frame and energy bins in 4eV. The red line is the best-fit `BAPEC` model with thermal plasma temperature at 3.5 keV and $Z_{\odot}$ at 0.54. Image from Aharonian et al. (2017).

model.

Most recently Cappelluti et al. (2017) report a detection $> 3\sigma$ level of an emission line at $3.54\pm^{+0.2}_{-0.2}$ keV by examining the spectra of the cosmic X-ray background data of Chandra observations towards the COSMOS Legacy and CDFS survey fields. Fitting the spectra with an absorbed power-law model and adding a Gaussian line at around 3.5 keV, shown in Figure 6.10. They conclude that the emission at ∼3.54 keV has no known instrument line nor can be accounted by a charge exchange between neutral Hydrogen and Sulphur ions but can be interpreted as a signal of dark matter decay along the line-of-sight in the Milky Way halo. This claim is back up by Neronov et al. (2016), who detect a line at ∼3.51 keV at a level of 11σ in the NuStar observations of the same COSMOS and extended CDFS (ECDFS) fields.

From all these studies it is apparent that there is no consensus as to the physical nature of emission line at ∼3.55 keV, with some authors doubting that it exists at all.

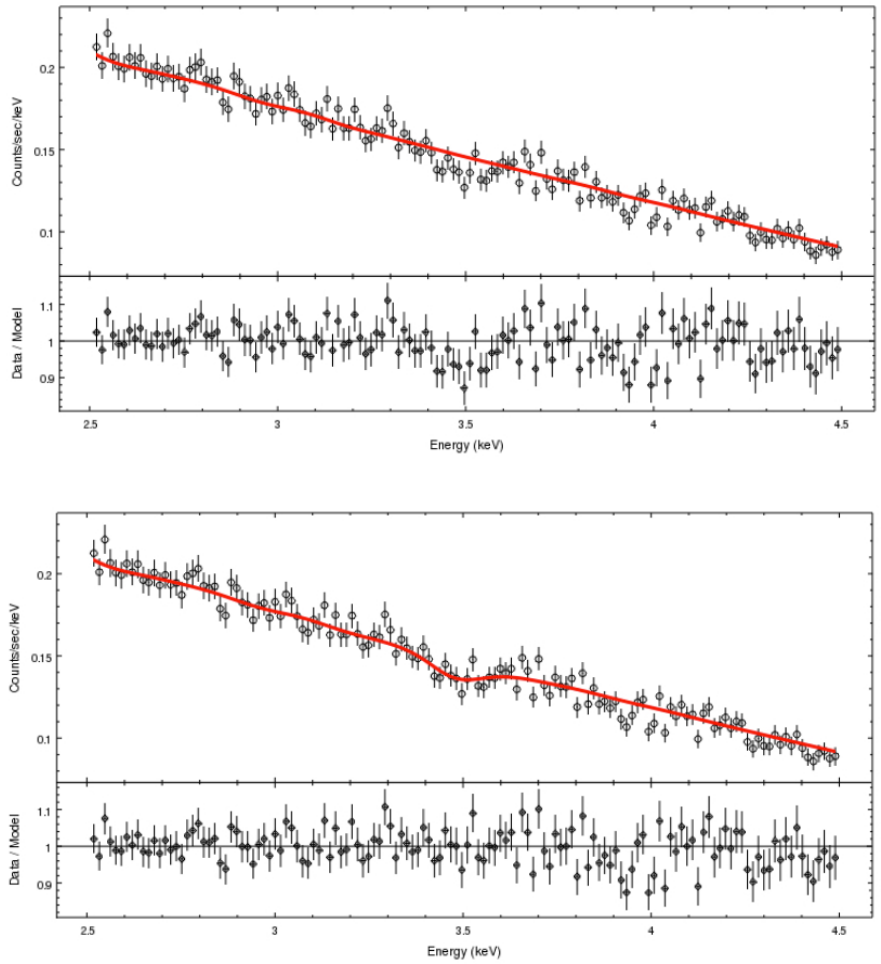

Figure 6.9: Top. Stacked spectrum taken from four Chandra observations of the AGN in galaxy NGC1275 which is within the Perseus cluster. The spectrum is fit with an `xswabs` × (`powlaw1d` + `xsbapec`) model where the red line is the best fit model and the bottom panel is the residuals from the fit. This shows a deficit at around 3.5 keV. Bottom is the same data but where a negative Gaussian `szgauss` parameter in the range 3.3 to 3.7 keV has been added to model. This shows a better fit at around 3.5 keV. Images from Conlon et al. (2016).

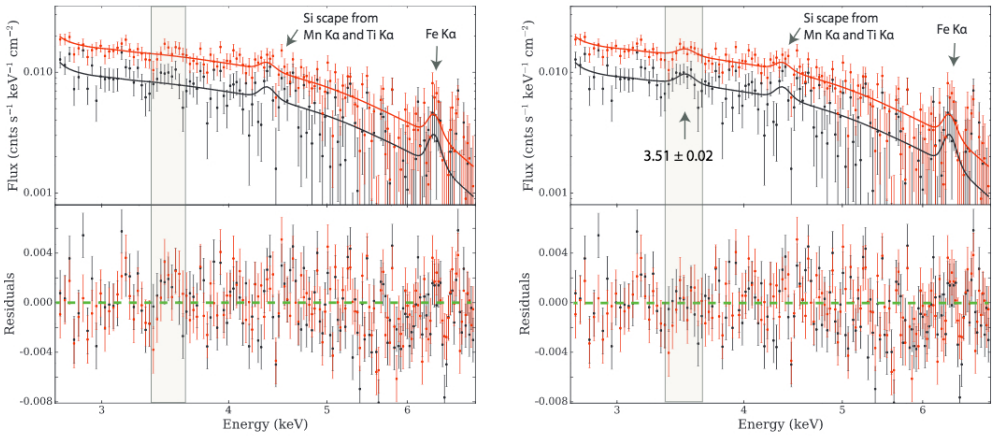

Figure 6.10: (Left) CXB spectra from COSMOS Legacy (red) and CDFS (black) survey fields fitted with an absorbed power-law model (solid lines) with resdiduals in the bottom panel. (Right) as before but with a Gaussian line added to the fit at ∼3.5 keV Image from Cappelluti et al. (2017).

6.6 Developing a Test for the detection of Dark Matter lines in XCS cluster spectra.

In this project, we use the XCS cluster catalogue to investigate whether a line at around 3.55 keV (or other energy) is detectable. In order to replicate the recent works of observations of the Perseus cluster (e.g. Urban et al. 2015 and Bulbul et al. 2014), we stack XCS observations of the Perseus cluster from both the core region and the combined core and outer regions. We then stack a sample of other clusters detected by XCS within temperature bins. Our aim is to investigate whether a detection of an unknown emission line is dependent on the temperature of the cluster, since the cluster temperature is closely related to the cluster mass. This temperature dependence work is genuinely new to the field.

6.6.1 Cluster Sample

We take clusters identified and analysed by the XMM Cluster Survey, Romer et al. (2001), as detailed in Section 2.3. We choose our clusters so that they are above $z > 0.05$ so that the source region does not extended too far across the field of view as we wish to subtract a background annulus from around the cluster region. Since we shall be blueshifting the spectra from each cluster back to the local frame, it is important to have a robust redshift for each candidate, consistently estimated from the same method. We choose to take these

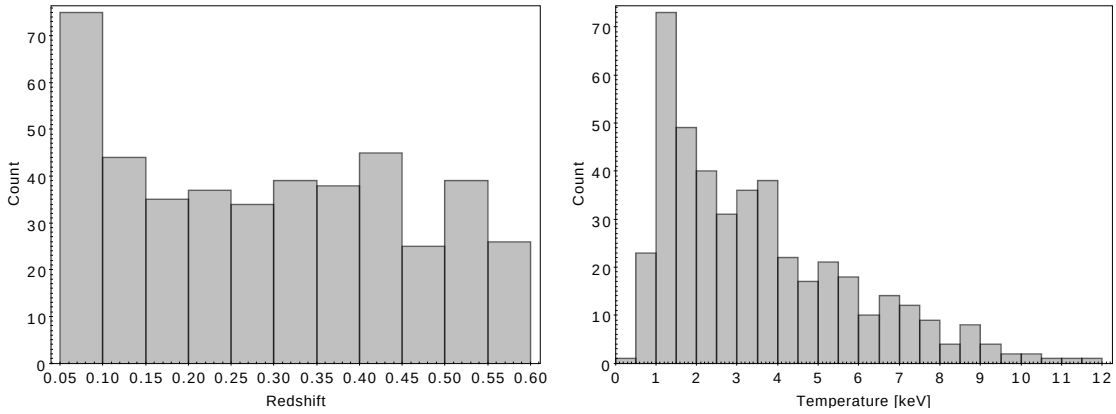

Figure 6.11: Our sample of 437 clusters where the redshift is taken from Rykoff et al. (2014) and where the where $\frac{\Delta T}{T}$ <0.15, before further filtering for observation times >5000 sec and >500 source counts.

redshift values from the `redMaPPer` catalogue, described in Rykoff et al. (2014) which is a red-sequence cluster finder. The photometric redshifts have a scatter $\sigma_z \approx 0.006$ at $z \approx 0.10$, increasing to $\sigma_z \approx 0.02$ at $z \approx 0.5$ due to increased photometric noise near the survey limit. The median value for $|\Delta z| /(1+z)$ for the full sample is 0.006. Therefore, the 1-σ error in energy in blueshifting a 3.55 keV line to the local frame ranges from ≈ 20 eV for a cluster at $z \approx 0.1$ to ≈ 30 eV at $z \approx 0.5$, which is below the spectral energy resolution of the `PN` detector.

We cross match the entire `redMaPPer` catalogue within the SDSS region with the most recent XCS master source list for extended sources i.e. likely clusters within the redshift range and choose XCS clusters within $3^{'}$ of a `redMaPPer` centre. These have been previously confirmed as clusters by Bermeo 2017. We find 1247 matches. As we wish to make separate cluster samples within five temperature bins, we now estimate the temperature of the cluster.

At the redshifts we have chosen for our sample, XCS clusters do not have large angular sizes ($< 3-4^{'}$). Therefore the background spectra were taken from a circular annulus around the source. The outer radius of the background annulus is 1.5 times the `XAPA` defined major axis of the respective cluster. The inner edge varies depending on the exposure, but is no less than 1.05 times the major axis. Any pixels within the background region that overlap with other `XAPA` sources are excluded from the background spectrum.

T_x[keV]	no. of spectra	Exposure [Msecs]	Source counts [10^6]
<2.0	216	4.9	1.68
2.0-3.0	129	6.82	2.97
3.0-4.0	108	4.48	2.55
4.0-6.0	62	1.10	5.27
>6.0	108	1.91	7.72

Table 6.1: Table showing the number of spectra, combined exposure time and combined counts in each of the five temperature bins.

Following methodology described in Section 2.3 we make the group source and background spectra as well as the `rmf` and the `arf` files corresponding to each cluster.

The spectral fitting to determine the temperature of each cluster was carried out using `XSPEC` using the maximum likelihood Cash statistic. Within each spectrum, photons are grouped into bins of a minimum of five counts before fitting. The model used to fit for temperature was a `wabs`(`mekal`) model with the hydrogen column, n_H, frozen at the Dickey and Lockman (1990a) value and the metalicity, Z, frozen at $0.3Z\odot$. The 68% uncertainty bounds on the best-fit temperature values are provided as part of the standard `XSPEC` fitting process.

We filter for clusters where the uncertainty on the temperature $\frac{\Delta T}{T}$ <0.15. Our sample reduces to 437 clusters from 823 observations, the distribution of redshift and temperature are shown in Figure 6.11. We further filter out observations of duration less than 5000 secs or where the cluster has less than 500 source counts in order to include only the highest signal to noise observations.

At the end of this process we have a total of 623 `PN` spectra from clusters which we divide into five temperature bins as shown in Table 6.1.

6.6.2 Method

If an unknown emission line exists, then this would potentially show up in the spectrum of the cluster when fitting with an `APEC` model[1] as this model includes features of the cluster

[1]The closely related `VAPEC` model is also used in Section 6.8 which allows for variations in metalicity of individual elements

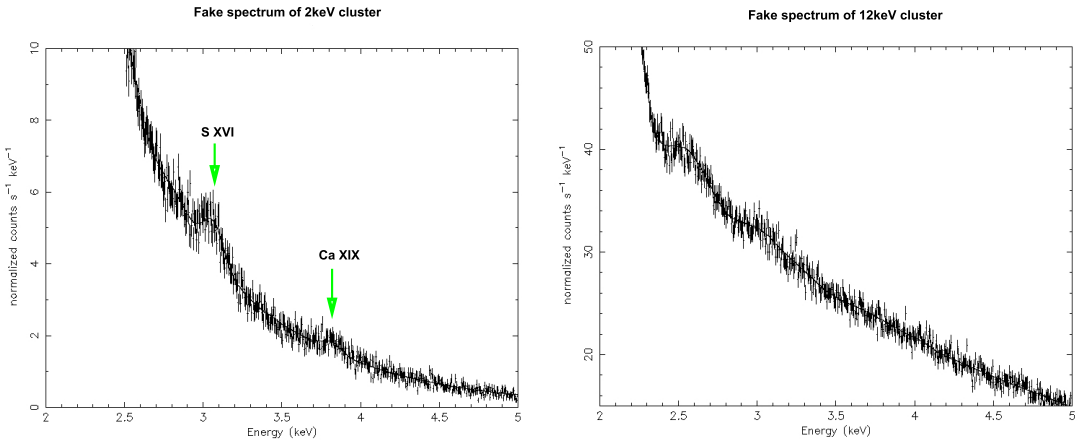

Figure 6.12: Spectra created using the `fakeit` command in `XSPEC` with `wabs`(`apec`) cluster model. Left the temperature is fixed at 2 keV and show prominent S XVI and Ca XIX emission lines which are much less observable in the right spectrum, where the cluster temperature is fixed to 12 keV.

plasma and known emission lines. Therefore adding a Gaussian line to the model at the energy of any unknown dark matter line emission should improve the fit. However, if such a line is weak, and therefore unlikely to show up to any significance in any one observation, we need to stack many high signal-to-noise spectra together. The size of the cluster is dependent on the dark matter content, we would thus expect that in more massive clusters the strength of such an unknown 'dark matter' emission line would become greater (i.e. a line not due to the ICM). Conversely more massive clusters are hotter, and hotter clusters have weaker known emission lines.

This second point is demonstrated in Figure 6.12 showing two spectra of a cluster generated using the `fakeit` routine in `xspec` based on a `wabs`(`apec`) model, where the temperature is fixed to 2 keV in the left spectrum and 12 keV in the right. The emission lines shown in the cooler spectrum are more prominent than in the spectrum of the hotter cluster (the `apec` model database used within `XSPEC` suggests that the emissivity of these two lines at 2 keV are an order of magnitude greater than than at 12 keV).

Therefore, we hypothesize that we are more likely to detect unknown emission lines in stacked clusters of hotter (i.e. more massive) clusters than cooler ones, if they have a dark matter origin.

Since the our methodology depends on **stacking** mulitple spectra together, **blueshifting**

spectra to the rest frame and **fitting** the stacked spectrum to a cluster model with added emission line, we now describe each of these techniques.

6.6.3 Stacking Spectra

Stacked `PN` spectra are made by using the `FTOOLS` `mathpha` routine and summing over the spectra that we want to include in each stack.

In order to generate the stacked `rmf` and `arf` files we use `FTOOLS` `addrmf` and `addarf` adding over each weighted `rmf` or `arf` associated for each `PN` observation. The weight having been calculated from total source spectrum counts from the individual observations as a percentage of the total stacked counts.

A stacked `PN` spectrum made from 19 observations of the Perseus cluster is shown in Figure 6.13 in black, and a single of these observations in red, showing the improvement of the signal-to-noise and clarity of emission lines when clusters are stacked. The prominent iron line Fe XXV at 6.58 keV is indicated which at its rest frame of 6.7 keV agrees with a literature redshift of $\sim$0.0179.

6.6.4 Blueshifting Spectra

When stacking different clusters, we require that all the spectra are blueshifted to the local frame so that any astrophysical emission lines effectively line up. Since the spectra are taken from clusters at different redshift, the instrument lines (which are in the detector frame) will be smeared out once they are blueshifted and combined together. We do not need to stack spectra if all are from of the same cluster (e.g. Perseus). We require that the source and background spectra are blueshifted to the rest frame, but we must keep `rmf` and `arf` files in the observer frame.

A script was written which counts all the photons in each individual `PI` channel in the source spectrum. The upper and lower energy bounds for each of those channels are taken from the associated `rmf` file. These are labeled `E_MIN` and `E_MAX`. We randomise an energy for that number of counts in each `PI` channel with a value between `E_MIN` and `E_MAX`. We then scale that photon energy by $(1+z)$ and store the resulting energies in a list. Once we have done this for all photons in the original spectrum, we remake the spectral histogram from the new list, re-binning to the corresponding energy bins of the spectrum. This is

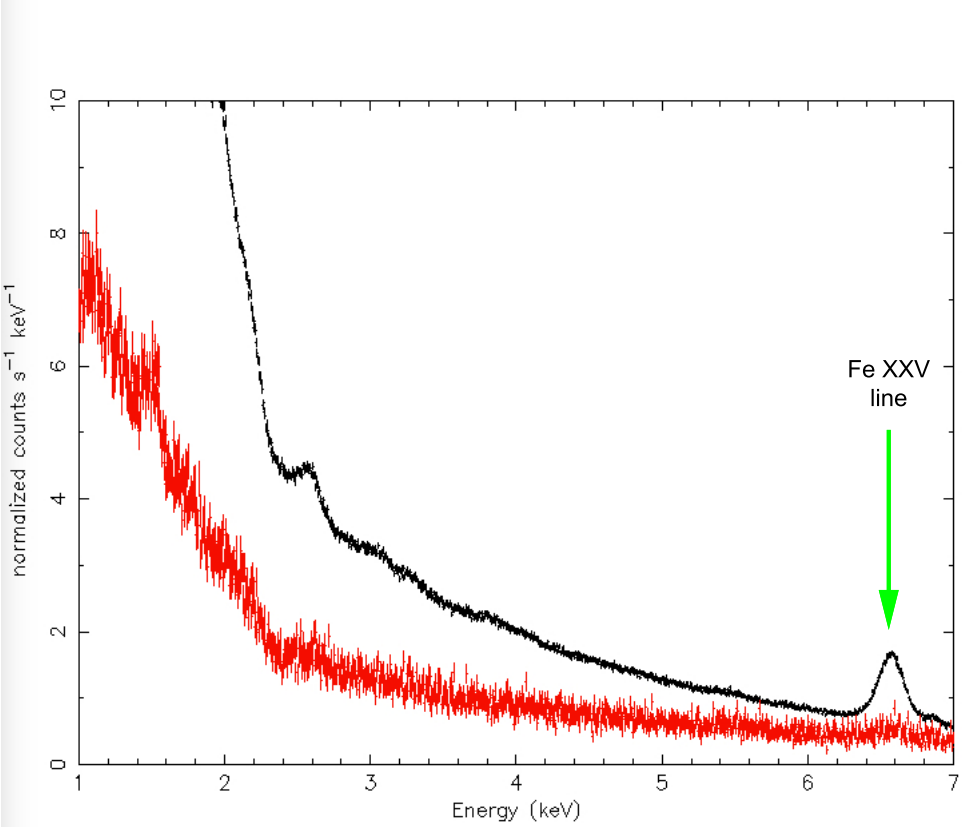

Figure 6.13: A stacked PN spectrum (black) made from 19 individual spectra of the Perseus cluster showing an improvement on the signal-to-noise over a spectrum from an individual observation (red). The Fe XXV line is shown in the observer frame at 6.58 keV (rest frame energy 6.7 keV).

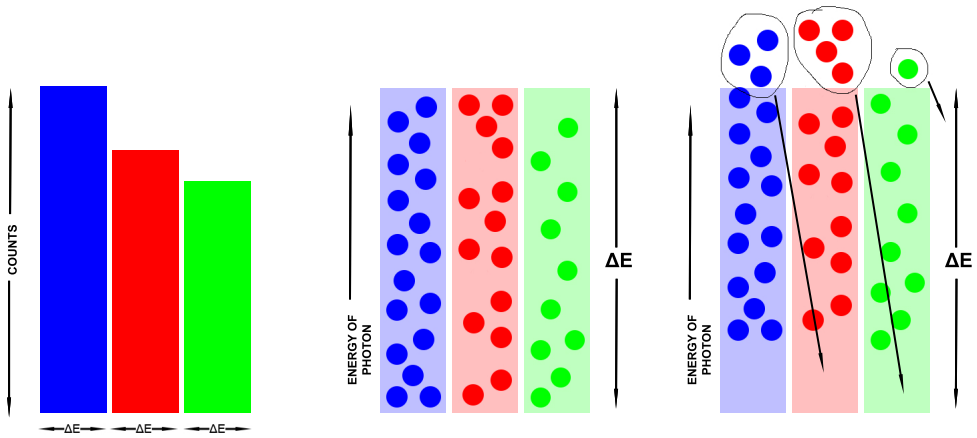

Figure 6.14: Schematic diagram demonstrating our spectral blueshifing method. Left. A histogram of three consecutive energy bins of the spectrum are represented by the three coloured bars, each with a energy range of ΔE and with a height depending on a number of photons within the energy range of the bin. Centre. We assign a random energy for each photon within the energy range of the bin. The higher the energy of the photon, the higher up the bin they sit, to a maximum energy of the bin. Right. When blueshifting, the photon energy is increased by a factor $(1+z)$, represented as the photons being higher within the bin. Where photons are now above the maximum energy for the bin, they transfer to a higher energy bin. We make a new spectrum from this new distribution.

demonstrated schematically in Figure 6.14. We now have **counts vs pha channel** in the rest frame and we now do the same for the background spectrum.

We use the `FTOOLS mathpha` routine to generate each background subtracted spectrum for each observation, by subtracting the blueshifted background spectrum from its associated blueshifted source spectrum, having first scaled by its `BACKSCAL` value which is defined by (`area from which spectrum is extracted`)/(`total detector area`). This is done automatically in `XSPEC` when background subtracted spectra are made but must be done outside of `XSPEC` if we are to stack background subtracted spectra together before fitting. The scaled weight, w, of an individual background spectrum is defined as:

$$w = (\texttt{BACKSCAL}_\texttt{s}/\texttt{BACKSCAL}_\texttt{b}) \times (\texttt{exposure}_\texttt{s}/\texttt{exposure}_\texttt{b}) \tag{6.4}$$

where the `BACKSCAL` value is for the individual source (`s`) or background (`b`) spectrum and `exposure` is the corresponding exposure time.

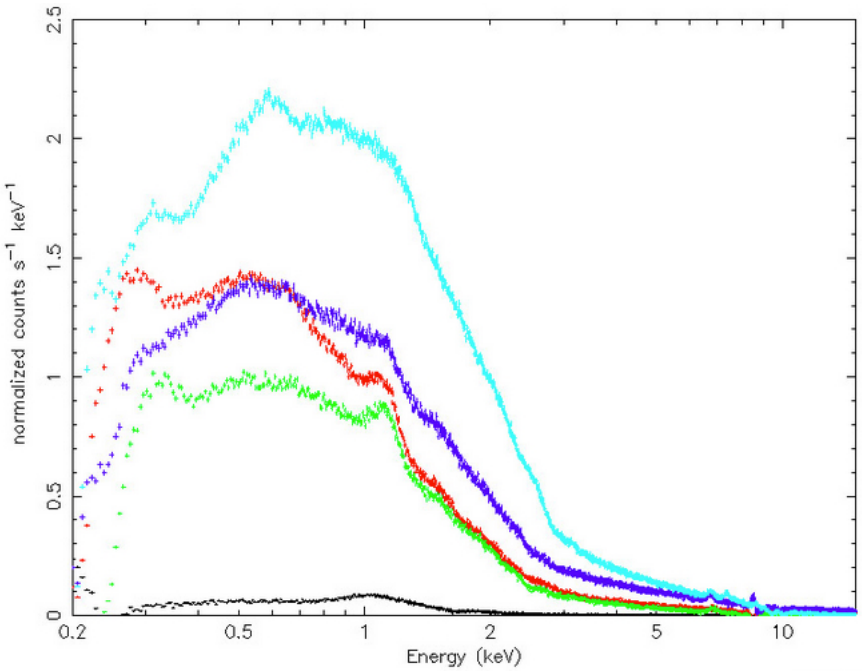

Figure 6.15: Stacked background subtracted spectra from each of the five combined blue-shifted temperature bins. cyan >6.0 keV, blue 4.0-6.0 keV, red 3.0-4.0 keV, green 2.0-3.0 keV and black <2.0 keV.

For each temperature bin in our sample, we stack the blueshifted spectra (and associated stacked `rmf` and `arf` files) as described in Section 6.6.3. Figure 6.15 shows the background subtracted spectra in each of the blushifted-stacked temperature bins.
We note that at low photon energy (< 0.3) keV the red spectrum 3.0-4.0 keV bin spectrum is strangely higher than that of blue 4.0-6.0 keV spectrum. We suggest that this may be due to spectra from observations of lower temperature clusters being erroneously included in the stacked 4.0-6.0 keV bin, and/or higher temperature spectra included in the 3.0-4.0 keV bin. Hence, this may be an issue of poorly selected source data, rather than an error in the stacking or blueshifting routines. We discuss this issue further in Section 6.10.

6.6.5 Fitting the Stacked Spectra

Using `XSPEC`, we fit the stacked spectra with an absorbed `apec` (or `vapec`) model. This models a cluster's hot plasma together with the known emission lines. We then run an iterative fitting loop which adds a Gaussian emission line at energies between 3 and 5 keV, this being the energy range of interest, in steps of 25 eV, (which is about half the energy resolution of the detector). We set the line width to zero so that it effectively takes on the spectral resolution of the detector and the normalization of the line is set free. We note

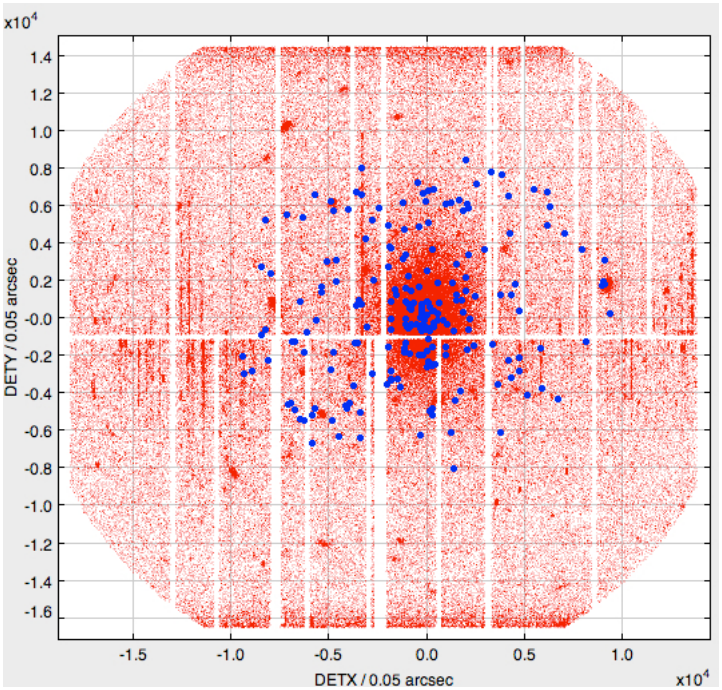

Figure 6.16: PN observation 0201900101 of cluster XMMXCSJ000349.3-020404.8 showing blue dummy photons added into the clean events file.

how the Cash statistic (C-stat) and the normalization of Gaussian line change at each 25 eV energy step when adding the Gaussian line to the model. The more negative the change in C-stat, the better the fit.The higher the normalisation, the stronger the line.

6.7 Testing our Methodology

6.7.1 Testing our methodology with a fake emission line

In order to test that our method can detect unknown emission line at around 3.55 keV, we inject dummy photons into a high S/N observation 0201900101 of cluster XMMXCSJ000349.3-020404.8 at redshift 0.1. We do this by manipulating the original clean events file by adding one dummy photon for every 100 real source photons into the source region of data. The energy of this dummy photon is from a randomized Gaussian distribution with mean energy set at $3.55\,\mathrm{keV}/(1+z)$ (i.e. 3.23 keV) with σ set to 50 eV. Figure 6.16 shows the image of the clean events on the detector in `DETX DETY` co-ordinates where the blue dots represent a dummy photon.

We make a background subtracted spectra from both, the original and new observations with the dummy photons. We blueshift both using the method described in Section 6.6.4.

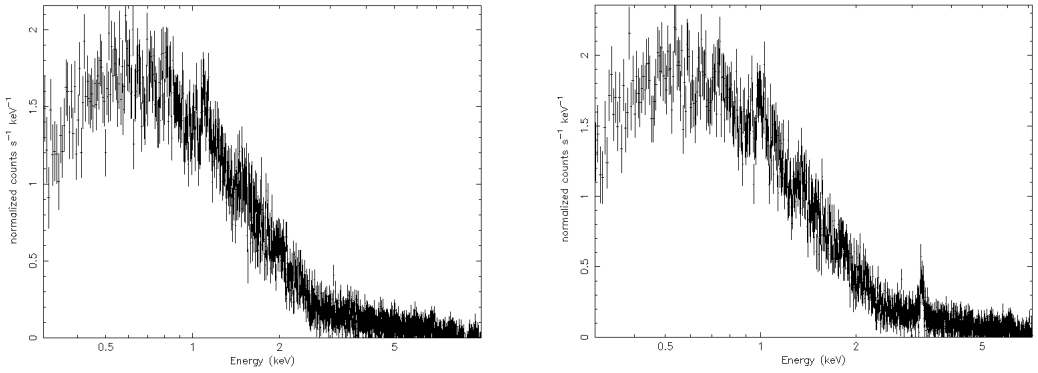

Figure 6.17: Comparisons of spectra from the PN detector of observation 0201900101. The left image is the spectrum of the original detection. The right image is the blueshifted to the local frame spectrum with one fake photon added into the clean events file at ∼3.55 keV for every 100 source photons.

We compare these spectra in Figure 6.17. Clearly we can see the fake emission line in the right image which has been blueshifted to the expected 3.55 keV energy.

We analyze both the original and the dummy injected spectra by our fitting method described in Section 6.6.5. We keep the redshift fixed to 0.1, the abundance fixed to 0.3 $Z_{\odot}$, the $\mathtt{n_H}$ column to the value given by Dickey and Lockman (1990a) and the temperature and normalisations are both free. We see in Figure 6.18, that in the original spectrum there is no improvement in the C-statistic in the 3.0-4.0 keV energy range, but when an extra Gaussian emission line component is added there is an improvement in the fitting at around 3.55 keV with positive normalisation - i.e our fake 3.55 keV emission line has been detected.

6.8 Application of our Method to the Perseus Cluster

The search for an unknown emission line in the Perseus cluster has been carried out by Bulbul et al. (2014), Boyarsky et al. (2014) and Urban et al. (2015) so this seems a natural place to test our method.

We select 19 XMM-Newton ObIDs where the observation centre is $< 50^{'}$ from the Perseus cluster centre (Perseus has a diameter of $\sim 863^{'}$ Helou et al. 1991) and which have been previously reduced in the XCS pipeline as described in Section 2.3. From each we extract a spectrum from the PN detector from a $12^{'}$ radius around the observation centre. We stack

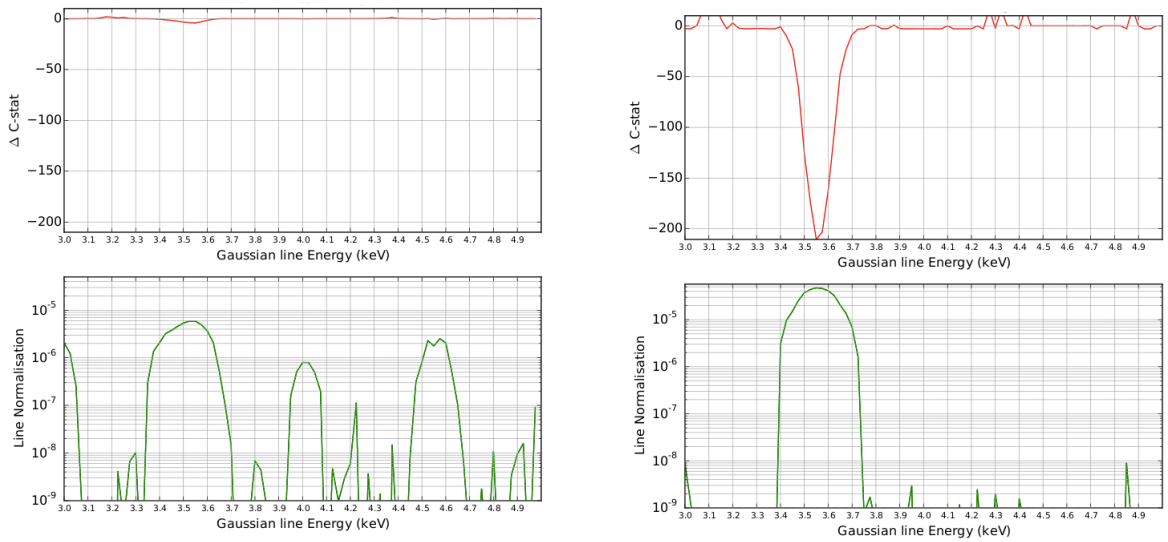

Figure 6.18: Comparisons of change in Cash statistic (top panel) of fitting the background subtracted spectrum from observation 0201900101 when an emission line is added into the model at the energy on the x-axis, and with normalistion of the emission line in the lower panel. Left is the original observation and right when a fake photon is added into the clean events file at $\sim$3.55 keV for every 100 source photons, and blueshift the spectrum to the local frame. Clearly, comparing left with right, it shows that adding an emission line at 3.55 keV results in a better fit and positive normalisation.

Region / detector	no. of spectra	Exposure [Msecs]	Source counts [10^6]
core PN	2	0.08	14
All	19	0.35	16.6

Table 6.2: Table showing the number of spectra, combined exposure time and combined counts from our Perseus sample.

these 19 spectra together (as described in Section 6.6.3). Together these have combined exposure time of 3.52x10^5 s and total of 1.66x10^7 counts. The spectra are not background subtracted since Perseus takes up the field of view, and our standard XCS method relies on the background being taken from an annulus surrounding the cluster. Nor are the spectra blueshifted since they are all at the same redshift ~ 0.0179.

We also take a sub-sample of the two of the observations (0085110101 and 0305780101) which are targeted at the cluster's central core. Spectra are extracted from a $6'$ radius around the cluster centre with combined exposure time of 8.03x10^4s with 1.41x10^7 and as shown in Table 6.2.

We fit the stacked spectrum, using the method as described in Section 6.6.5, though in this case we use an absorbed `vapec` model after Urban et al. (2015) rather than `apec`. Again following their method, three of the prominent emission lines (S, Ar and Ca) included in this model are free to vary, the others frozen at $0.5Z_{\odot}$. We freeze the redshift at 0.0179, and the powerlaw component at 1.52 (taken from Urban et al. 2015), the Galactic $\mathtt{n_H}$ absorption column frozen at $1.5 \times 10^{21}\,\mathrm{cm}^{-2}$ (from Dickey and Lockman 1990b) and allow the temperature T_{x} to vary. We then run the iterative fitting loop adding a Gaussian emission line at energies between 3 and 5 keV in steps of 25 eV.

6.8.1 Results

Our results are shown in Figure 6.19. The stacked spectrum from all 19 observations is shown on the left hand side and the two (of the 19) observations made of the Perseus core-region on the right. The green bar highlights the 3.55 keV rest frame position of the line claimed to be detected in previous studies. We see no such evidence of such a line in either of the stacks: the clear dip in the relative Cash value seen in Figure 6.17 (where a dummy line has been added) is not seen in the Perseus data.

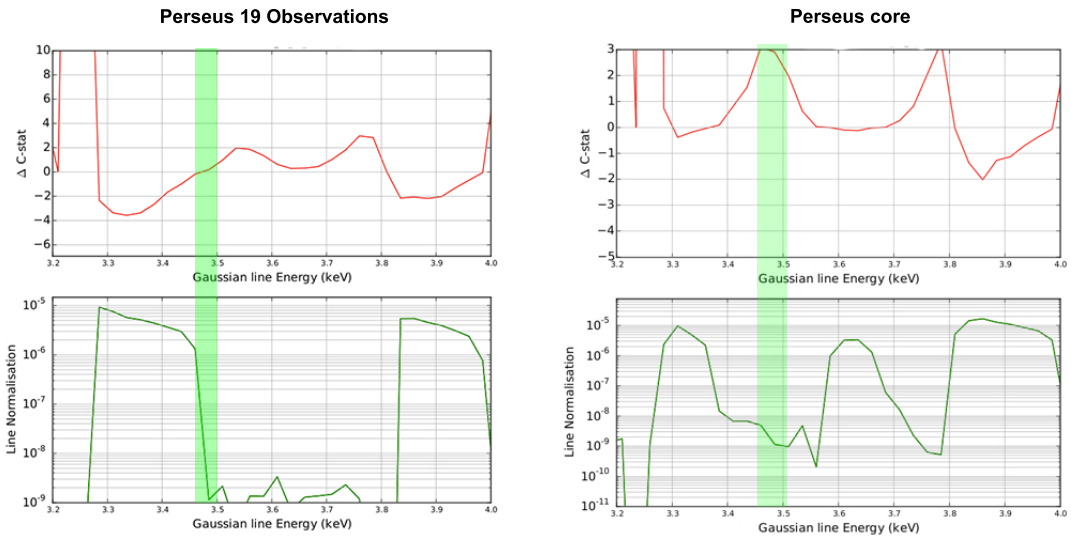

Figure 6.19: Figure shows how adding a Gaussian emission line to a `wabs` × `vapec` model improves (or not) the fit to 19 stacked Perseus (left) and 2 core region only (right) spectra when adding a Gaussian emission line at energy between 3 keV and 5 keV. The top panel in each shows the change in C-statistic when an Gaussian emission line is added at that energy, and bottom panel shows the best-fit normalisation of the line in units of photons $\mathrm{cm}^{-2}\mathrm{s}^{-1}$. The green bar highlights the area of where authors have claimed an unknown emission line at around 3.5 keV in the cluster frame (3.55 keV in local frame).

Our results (i.e. a non detection of a 3.55 keV line) differ from those of Urban et al. (2015) as shown in Figure 6.7. Whereas the authors find that adding a Gaussian line improves the fit (3.525 keV and 3.575 keV in the core and confining region respectively) this is not true for our method. However, our current approach is not sufficiently robust (e.g. we have not carried out a full background subtraction) to draw firm conclusions with regard to possible errors in the Urban et al. (2015) analysis (which is based on data from Suzaku). In § 6.10 we suggest other thoughts and further work which may help resolve these differences.

6.9 Application of our Method to a Stacked Sample of XCS Clusters

We now analyze each of the temperature-binned stacked spectra of the samples shown in Table 6.2, using the method described in Section 6.6.5. We also analyze the complete sample of all clusters stacked together. We allow the temperature and the $\mathtt{n_H}$ column to be free, we fix the abundance to 0.3 $Z_\odot$ and the redshift to zero. We freeze the Gaussian line energy and loop in intervals of 25 eV, keeping the normalization of the line free and

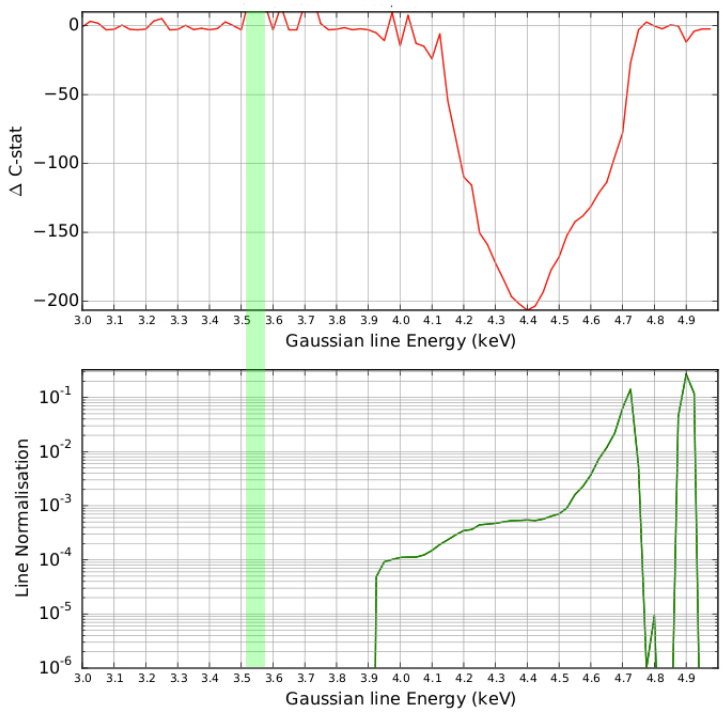

Figure 6.20: Improvement (or not) to the spectral fit to stacked XCS identified clusters. In this plot the whole cluster sample has been blueshifted and stacked. The red curve (top) shows the change to the fitting statistic when a adding a Gaussian line is added to an `wabs(apec)` model, compared to the case where no line has been added. The line is added to the model between energies of 3 keV and 5 keV at intervals of 25 eV. The green curve (bottom) shows how the best fit nomalisation of the added line changes with energy. The light green bar highlights the location of a dark matter line ∼3.55 keV proposed by other authors.

fixing the line width to zero as before and we note the best fit C-stat results and how that compares to the fit without the added Gaussian line.

6.9.1 Results

The changes to the fit when we add a Gaussian emission line to the spectral model are shown in Figures 6.20 to 6.23. We see no evidence of an improvement in the fit at ≃3.5 keV when we apply our method to the stacked spectrum of all the clusters (Figure 6.20). We note that the significant improvement in the fit at ≃3.9 keV is due to the fact that there are several plasma emission lines in that energy region: Ca XIX (at 3.9 keV) and Ca XX (at 4.1 keV). The results are similar for the three lowest temperature bin stacks ($T < 2$ keV,

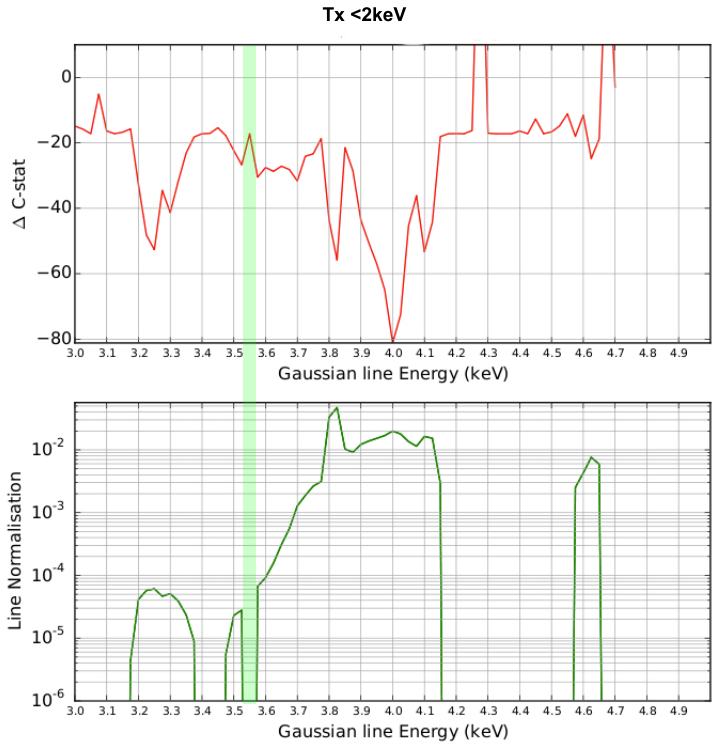

Figure 6.21: As Figure 6.20, but for cluster stacks in the temperature bins $T_{\rm X}$ <2 keV.

$2 < T < 3$ keV and $3 < T < 4$ keV, Figures 6.21, 6.22).

We do see a hint of improvement in the two highest temperature bin stacks at $\simeq$3.5 keV (the improvement due to plasma lines at $\simeq$3.9 keV is also evident). In the $4 < T < 6$ keV bin, there is evidence for a line at $\simeq$3.6 keV, where the improvement in Cash-statistic is 233 compared to the model without an emission line. In the $T > 6$ keV bin, there is evidence for a line at $\simeq$3.5 keV (Figure 6.23) where the improvement in Cash-statistic is 729 compared to the model without an emission line.

Although this suggests support of a dark matter (DM) explanation i.e. we would expect DM lines to get stronger with mass (and $T_{\rm X}$) opposite to what is expected from plasma lines, the results rely on the best-fit model and parameters being valid. When we inspect the goodness-of-fit we find a very poor fit as shown in Figure 6.24 (showing the spectrum of the $>$ 6 keV bin stack when fit with `wabs(apec + gussian)` model and Gaussian at 3.5 keV) where the reduced χ^2 statistic is 16.12 for 281 degrees of freedom, even though it is a 'better' fit than the model that doesn't include the Gaussian line. The temperature associated with this best-fit model is $\sim$2 keV which is in tension with the clusters being

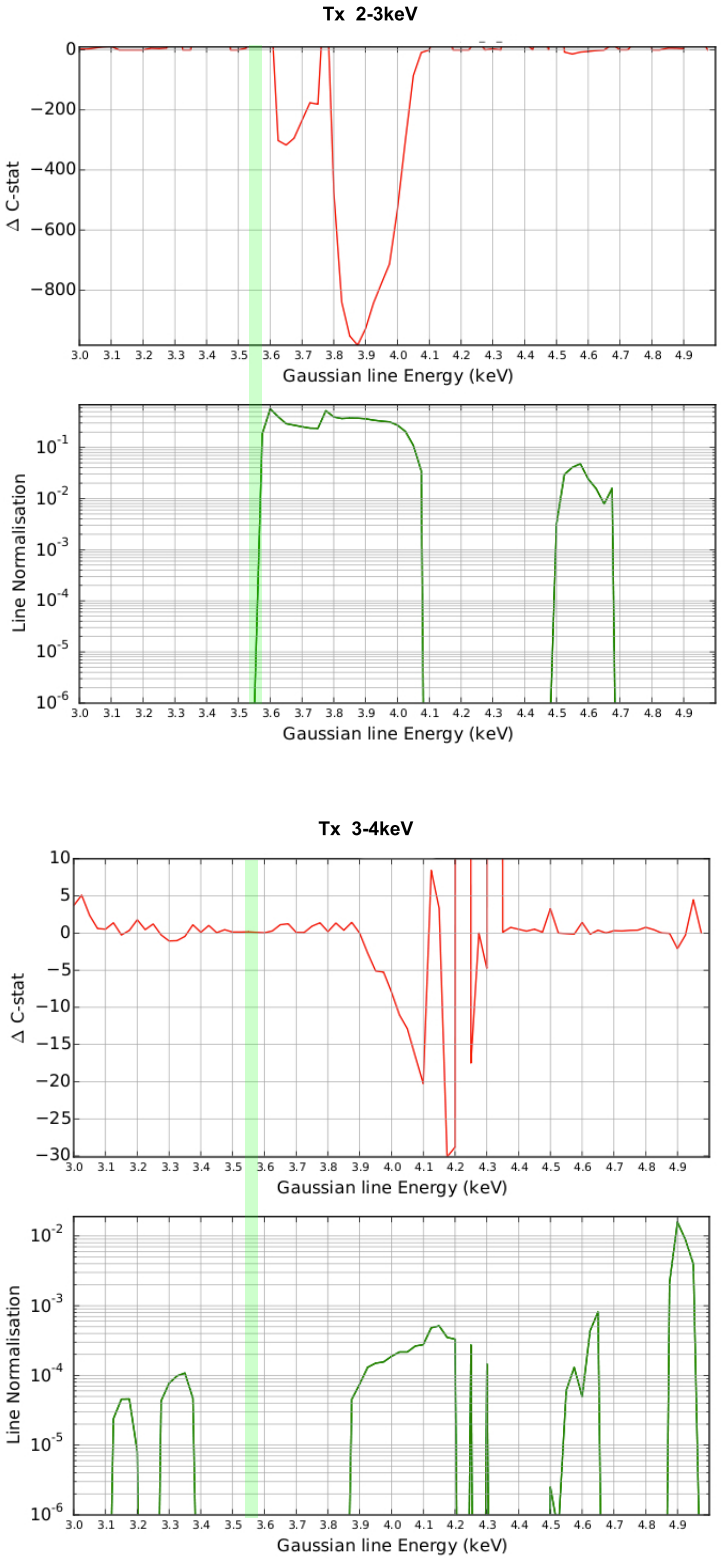

Figure 6.22: As Figure 6.20, but for cluster stacks in two temperature bins, 2 keV< T_X <3 keV (top), and 3 keV< T_X <4 keV(bottom).

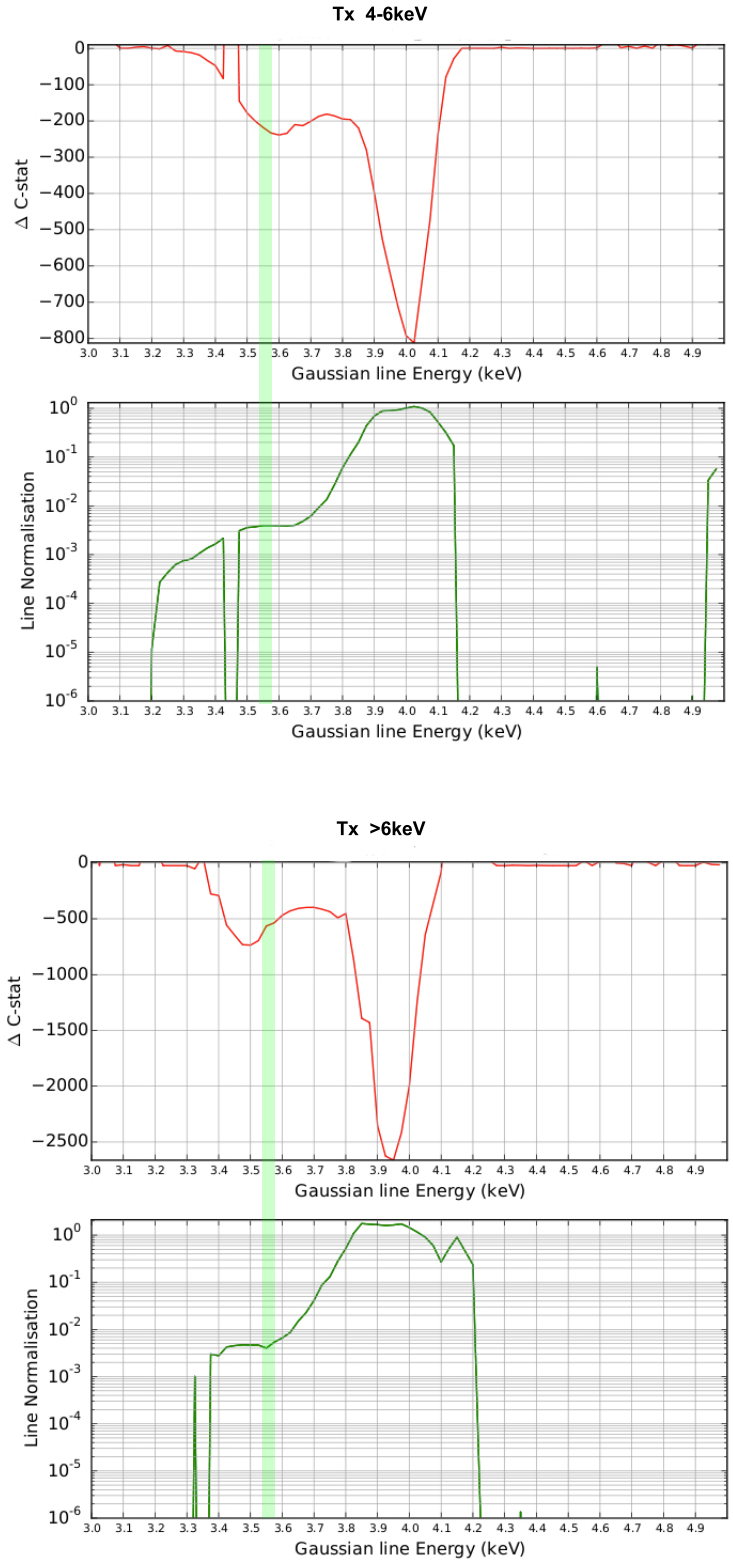

Figure 6.23: As Figure 6.20, but for cluster stacks in two temperature bins, 4 keV< T_X <6 keV (bottom), and T_X > 6 keV (top).

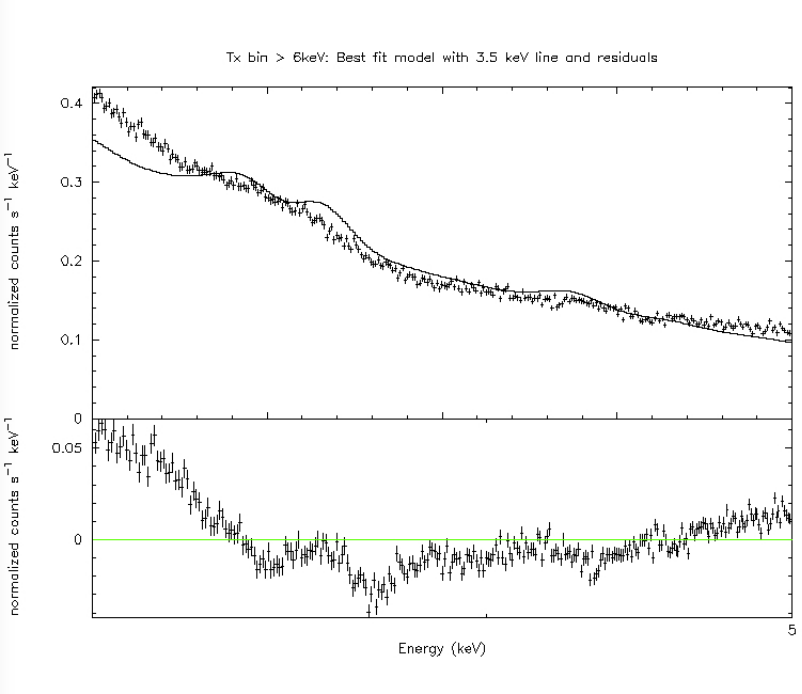

Figure 6.24: Plot from XSPEC showing the stacked spectrum of $T_{\rm X}$ ($> 6\,$keV) clusters and best fit `wabs`(`apec` + `gussian`) model (with the added Gaussian line at 3.5 keV). The residuals are in the lower panel. This shows that the best fit model is clearly a poor fit to the data.

binned in the >6 keV range. (For these reasons we do not include the level of significance of the very tentative detections in the hotter cluster bins as they are somewhat meaningless). Similar results and conclusions are reached with the tentative detection in the $4 < T < 6\,$keV bin when a 3.6 keV Gaussian line is included in the model.
Therefore these results require further investigation as we set out in the following Section 6.10 before we can publish a paper.

6.10 Checks, Anomalies and Further work

Each of the three processes that are central to the project pipeline (blueshifting, stacking and detecting unknown lines) have been tested individually and successfully. We see, however, that when combined and applied to actual data, there are puzzling results and behaviour as highlighted in; Figures 6.20 with reference to stacking the spectra, Figure 6.19 with reference to the non-detection in Perseus and Figure 6.24 with reference to the 'poor' best-fit results.

Therefore, further work is required to investigate the nature of these. Specifically we will

check the following:

Source Selection

In our work, the source spectra had been previously generated from observation data that had been previously reduced (Bermeo 2017) with the associated cluster temperature taken from the XCS-DR2 catalogue. We propose to re-examine, and where necessary re-make, spectra from individual observations to ensure that they all meet minimum quality standards. This includes:

- **Source Spectra**. When we extract a cluster region from the observation's clean event file in order to create a spectrum, it is important that we do not include unrelated point or extended sources within this region. This is especially important for clusters at lower redshift which take up more of the field of view and thus more likely to include unrelated point sources. Our cluster source spectra assumed that unwanted sources had been cleanly excluded. A visual inspection of each observation will confirm this or if necessary allow us to manually exclude further sources and remake spectra.

- **Background subtraction** Background spectra had been created using the in-field method described in §6.6.1. As with the source spectra these were generated and supplied from previous work. Again we should visually inspect these regions for point sources that had not been excluded.

  Where the cluster takes up most or all of the field of view, (e.g in the case of Perseus cluster) we cannot use this method. In this case we modeled the background in the `XSPEC` fitting process with an extra `powerlaw` term. This is a fast yet simplistic approach which could be modified by a more sophisticated modeling such as that used by Bulbul et al. (2014). They model a superposition of four main background components specific to the location of each cluster, these being: cosmic X-ray background emission (including Galactic halo, local hot bubble, and unresolved extragalactic sources), quiescent particle background, solar wind CX as well as residual contamination from soft protons.

- **Robustness of cluster temperature**. The source catalogue provided us with a list of clusters with associated temperatures. Each cluster may have multiple observations and we used all these when stacking the spectra together. However, there is an assumption that the temperature yielded (from fitting in `XSPEC`) for an

individual observation is consistent with the overall cluster temperature. This may not be the case. Therefore we should check that a) this temperature is consistent with that of the combined observations of the cluster and that b) that the temperature uncertainty for an individual observation is less than 15%. Where this is not met, we will reject the observation from the stack.

- **Observation duration**. We have been excluding observations of less than 500 sec from our source sample. However, in doing so, we have been rejecting observations with a high signal to noise ratio that pass the previous criteria. Therefore we will include these extra cluster observations in our analysis.

Blueshifting Process

Blueshifting a source or background spectrum to the local frame is no easy task. There is, as yet, no script within the `XSPEC` environment that does this. Although we are confident that our method (§6.6.4) is valid, having been tested as described in §6.7, we note that Bulbul et al. (2014) use a different method in their paper. Rather than blueshifting the spectrum, they re-scale the energies of each source and background X-ray photon (i.e. the `PI` values in the clean events file) to the local frame using the best-fit redshifts, and then they also blueshift the bounds of the `rmf` and `arf` files by the same ($1+z$ scaling factor).

Intuitively, this method sounds like it should work and was an approach that we initially undertook. However when we stacked the blue-shifted spectra generated in this way, there was an anomalous and physically meaningless divergence in the output spectrum (for example as shown in Figure 6.25).

After correspondence with `XMM SAS`, we were made aware that the `rmf` could not be changed in this way to take account of the re-scaled energy of the photon. For example, a spectral line at 3.5 keV has a very different shape in `PI` space to a line at 4 keV. For this reason we rejected this method and devised the new method as described.

An analogy would be to assume that the shape of a point source, made by photons of a particular energy at the centre of a detector, remains the same if we simply change the `DETX/Y` in the clean events file to near the edge of the detector i.e. taking no account of the change in `PSF` across the detector.

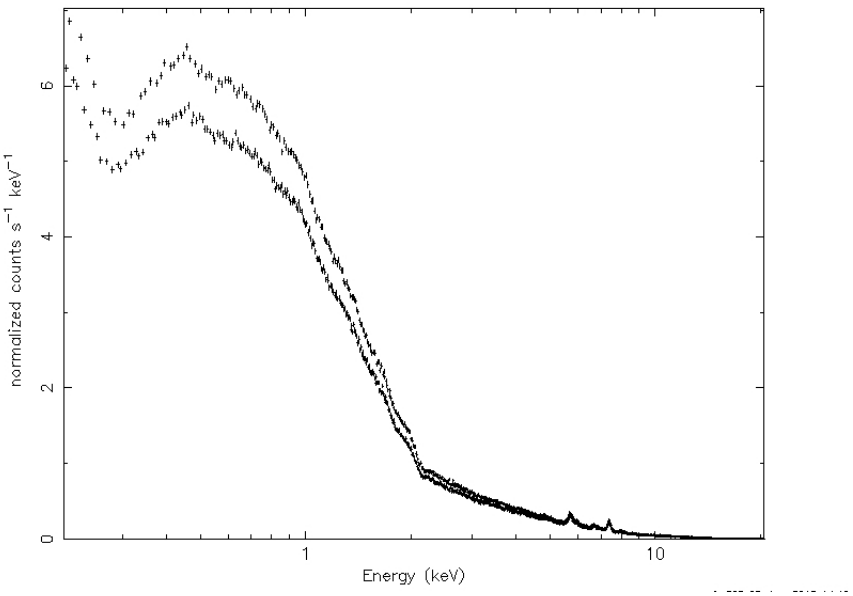

Figure 6.25: Spectrum produced from 40 PN observations of clusters, where each individual spectrum is first blueshifted by the rejected approach as described in the text and then stacked. An anomalous divergence is clearly seen in the spectrum.

A further investigation would be the robustness of how we create the individual **background-subtracted** spectrum. Although XSPEC automatically combines a source with its associated background (as well as rmf and arf files) when it plots data, there is no way of outputting this background-subtracted spectrum as a file in its own right (e.g. as a .fits) file which we would stack with others). Therefore the method we employed, described in §6.6.4, makes background-subtracted files outside of the XSPEC environment. We compare the two methods in Figure 6.26. This shows the respective background-subtracted spectra made from the PN detector of observation 0700180201 in the 3 - 4 keV range. Although both methods generate the same spectral shape, our method has a spectral energy bin size smaller than that generated inside XSPEC. Because of this, we see more data points in the spectrum from our method and with greater error bars. We should re-write our method to match the energy bin size for all our cluster spectra, and therefore check whether it has an effect on the accuracy of our blueshifting process.

Stacking process

We feel that our stacking process is fairly robust; in that, adding source (or background) spectra together can be done easily using the mathpha routine. Making the associated rmf and arf stacked files is also fairly straight-forward, using the ADDRMF/ADDARF routines. These files were made by adding weighted values of the individual rmf/arf, with the

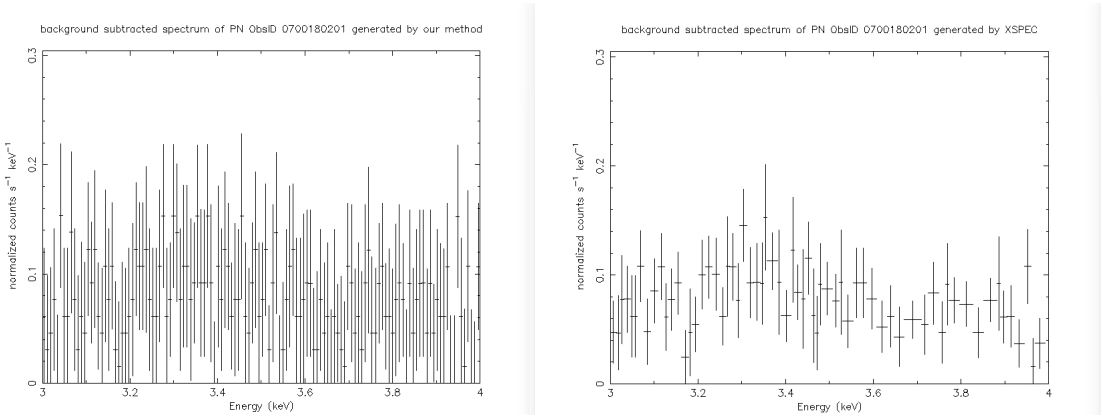

Figure 6.26: Background-subtracted spectra from the `PN` detector of observation 0700180201 in the 3 - 4 keV range. Left, as generated by our method and right, as automatically generated inside `XSPEC`

weights based on the exposure time of the associated observation. It is also possible to weight values based on the number count in the associated source. This should make little difference, but as a sanity check could be included in our tests of the methodology.

Detection Process

In the detection part of the pipeline, as described in §6.6.5, we used an `apec` model in the fitting to the temperature binned stacked clusters. This is a single temperature plasma model with the metalicity fixed to $Z_{\odot} = 0.3$. We note that Bulbul et al. (2014) fit theirs with a slightly more complex version. Their model is a line-free multi-temperature `apec`, where individual Gaussian lines at known emission line energies are added so long as they improved the fit.

Although this method increases the number of free parameters in the model, we could update our detection script to include this multi-temperature aspect of the stacked clusters. We could then re-analyse the stacked clusters and compare our results.

Other further work

- In §6.7 we tested our method by inserting fake photons into the clean event file of a observation with a cluster. The result was shown in Figure 6.18. It would be possible to predict the limit of detection using this process by reducing the number of fake photons and repeating with clusters with a range of temperatures - and hence estimate a minimum flux detection.

- We should like to test whether stacking the central cores of the clusters, i.e. where the dark matter content is greatest, leads to a stronger signal of an unknown emission line at 3.55 keV. In order to do so, we should need to adapt the original XCS spectrum-making pipeline such that we generate a core-only spectrum from an observation. We would define the core as the region $< 0.1R_{500}$ (this is temperature dependent as shown in Equation 7.1). Fortunately, this work had previously been done in the early part of the PhD for an unrelated project. In §7.2.2 we describe how we used an iterative approach to estimate the temperature and R_{500} of a cluster. In §7.2.3 we describe how we adapted the XCS pipeline in order to excise the core-region from cluster spectra (the reverse of what we need for this modification).

6.11 Chapter Summary

In this chapter we have described a method to search for unknown emission lines in cluster spectra. If such lines are found, they may be explained by a sterile neutrino interpretation for dark matter. They could also be explained by an inadequate description of plasma emission in existing XSPEC models. Given that other authors have claimed the existence of an unknown line at $\simeq$3.55 keV, we have focused our attention on that energy.

Our method involves blueshifting the individual spectra of clusters to the local frame, stacking these spectra and then searching for any unknown line.
We have demonstrated that the code associated with each of three processes work; that we can blueshift a spectrum successfully, that we can stack multiple clusters to improve the signal-to-noise, and that our method to search unknown emission lines, by adding dummy 3.5 eV photons into an observation's clean events file, does correctly identify the fake line.

We applied our method to stacked spectra of Perseus cluster, first to to the core region, and then outer region. We found no evidence for an unknown emission line at around 3.55 keV as claimed by some authors. We do not draw any firm conclusions from this non-detection because our approach does not fully currently take into account the background.

We have also applied our method to 322 cluster spectra that were stacked in five temperature bins and into a single combined spectrum. We find no evidence of an emission line at 3.55 keV in the combined spectrum nor in the three lower temperature bins. We find tentative evidence for a line at $\simeq$3.55 keV in the two hotter bins - this line seems to

get stronger with $T_{\rm X}$, as would be expected of a dark matter feature, but as the model best-fits are poor and best-fit temperature dubious, we require further work to clean and re-analyse the input data as well as further tests on our methodology.

We are planning to write up the work in this chapter for a journal article because our temperature binning approach is genuinely new to the literature. However, significant work remains before we can claim to have made either a detection or a non-detection. We have suggested reasons as to why our results are inconclusive at this stage and provided ways improve the quality of our cluster input sources as well as other checks of the method. Once these are resolved, bootstrapping would then be used to ensure that the results are not sensitive to the cluster sample being tested. We will also add more clusters, to improve signal to noise, by exploiting our access to redMaPPer clusters in the Dark Energy Survey. This will also give us a redshift lever arm to test for instrument effects (if the unknown line does not change energy with cluster redshift, then it must be associated with the instrument, rather than with the dark matter halo).

Chapter 7

Contributions to published articles

In this Chapter, we summarise the journal articles that the candidate has co-authored (Section 7.1), and review the contributions to XCS infrastructure that the authorships reflect (Section 7.2). For context, we note that those infrastructure contributions were made during the first years of the (part-time) PhD, i.e. before an intermission was taken in 2014.

7.1 Publication Summaries

The following sections review journal articles that benefit from the adaptations to the XCS cluster temperature pipeline described in Section 7.2. The candidate is a co-author on a further three papers. *The XMM Cluster Survey: optical analysis methodology and the first data release*, Mehrtens et al. (2016). *The XMM Cluster Survey: predicted overlap with the Planck Cluster Catalogue*, Viana et al. (2012). *The XMM Cluster Survey: Evidence for energy injection at high redshift from evolution of the X-ray luminosity temperature relation*, Hilton et al. (2012). These three publications benefit from contributions made before the start of the PhD programme and so are not discussed further herein.

7.1.1 The XMM Cluster Survey: The Halo Occupation Number of BOSS galaxies in X-ray clusters

Mehrtens et al. (2016) describes a direct measurement of the mean halo occupation distribution (HOD) of galaxies taken from the eleventh data release (DR11) of the Sloan Digital Sky Survey-III Baryon Oscillation Spectroscopic Survey (BOSS). The HOD of BOSS low-redshift (LOWZ: $0.2 < z < 0.4$) and Constant-Mass (CMASS: $0.43 < z < 0.7$) galaxies was inferred via association with the dark-matter halos of 174 X-ray-selected

galaxy clusters drawn from the *XMM* Cluster Survey (XCS). Halo masses were determined for each galaxy cluster based on X-ray temperature measurements, and range between $\log_{10}(M_{180}/M_{\odot}) = 13 - 15$. The directly measured HODs (Figure 7.1) were found to be consistent with the HOD-model fits inferred via the galaxy-clustering analyses of Parejko et al. (2008) for the BOSS LOWZ sample and White et al. (2011). for the BOSS CMASS sample. The best-fit alpha-index was measured to be 0.91 ± 0.08 and $1.27^{+0.03}_{-0.04}$ for the CMASS and LOWZ HOD, respectively. These alpha-index values are consistent with those measured by Parejko et al. (2008) and White et al. (2011). In summary, this study provides independent support for the HOD models assumed during the development of the BOSS mock-galaxy catalogues. This is important because those assumed models were subsequently used to derive BOSS cosmological constraints.

7.1.2 The XMM Cluster Survey: Evolution of the Velocity Dispersion-Temperature Relation Over Half a Hubble Time

Wilson et al. (2016) describes the evolution of the velocity dispersion–temperature ($\sigma_{\rm v}$–$T_{\rm X}$) relation up to $z = 1$ using a sample of 38 galaxy clusters drawn from the *XMM* Cluster Survey (Figure 7.2). This work improves upon previous studies by the use of a homogeneous cluster sample and in terms of the number of high redshift clusters included. It presents new redshift and velocity dispersion measurements for 12 $z > 0.5$ clusters observed with the GMOS instruments on the Gemini telescopes. Using an orthogonal regression method, the slope of the relation is found to be steeper than that expected if clusters were self-similar. The evolution of the normalisation is slightly negative, but not significantly different from zero ($\sigma_{\rm v} \propto T^{0.86 \pm 0.14} E(z)^{-0.37 \pm 0.33}$). The results have been verified using cosmological hydrodynamical simulations. The lack of evolution seen in the data is consistent with simulations that include both feedback and radiative cooling.

7.1.3 The `redMaPPer` Galaxy Cluster Catalog From DES Science Verification Data

Rykoff et al. (2016) describes updates to the redMaPPer algorithm, a photometric red-sequence cluster finder specifically designed for large photometric surveys. The updated algorithm was applied to 150 deg^2 of Science Verification (SV) data from the Dark Energy Survey (DES), and to the Sloan Digital Sky Survey (SDSS) DR8 photometric data set. The DES SV catalog is locally volume limited, and contains 786 clusters with richness $\lambda > 20$ (roughly equivalent to $M_{500c} \gtrsim 10^{14}\, h_{70}^{-1}\, M_{\odot}$) and $0.2 < z < 0.9$. The DR8

catalog consists of 26311 clusters with $0.08 < z < 0.6$, with a sharply increasing richness threshold as a function of redshift for $z \gtrsim 0.35$. The photometric redshift performance of both catalogs is shown to be excellent, with photometric redshift uncertainties controlled at the $\sigma_z/(1+z) \sim 0.01$ level for $z \lesssim 0.7$, rising to ~ 0.02 at $z \sim 0.9$ in DES SV. The study makes use of *Chandra* and XCS X-ray and South Pole Telescope Sunyaev-Zeldovich data to show that the centering performance and mass–richness scatter (Figure 7.3) were consistent with expectations.

7.1.4 The XMM Cluster Survey: Testing Chameleon Gravity Using the Profiles of Clusters

Wilcox et al. (2015) describes the application of a technique to place constraints on a 'fifth force'[1] using the stacked profiles of 58 clusters at higher redshifts ($0.1 < z < 1.2$), including 12 new to the literature, using X-ray data from the XMM Cluster Survey (XCS) and weak lensing data from the Canada France Hawaii Telescope Lensing Survey (CFHTLenS). If it exists, the fifth force would influence the hot X-ray emitting gas filling the potential wells of the galaxy clusters, but would not influence the clusters' weak lensing signal. Using a multi-parameter MCMC analysis, the two chameleon gravity parameters (β and ϕ_∞) were constrained by the data. The fits proved to be fully consistent with general relativity, i.e. not providing evidence for a fifth force. In the special case of $f(R)$ gravity (where $\beta = \sqrt{1/6}$), the upper limit on the current background field amplitude was measured to be $|f_{\rm R0}| < 6 \times 10^{-5}$ (95% CL): one of the strongest constraints to date on $|f_{\rm R0}|$ on cosmological scales.

7.2 Adaptation of the XCS Cluster Temperature Pipeline

The publications described above (Section 7.1) all rely on the measurement of reliable X-ray temperatures ($T_{\rm X}$) for XCS clusters. Even though there was a working $T_{\rm X}$ pipeline in place before the first XCS data release (Mehrtens et al. (2012)), this version of the pipeline (i.e. that described in LD11) was not ideal and required a series of improvements, as described in the sections below.

These improvements had been incorporated into the XCS pipelines before the candidate took intermission in 2014. By that time, a draft of a paper describing the X-ray properties of redMaPPer SDSS and DES-SV clusters was in preparation. An early version of the

[1] The chameleon gravity model postulates the existence of a scalar field that couples with matter to mediate a fifth force.

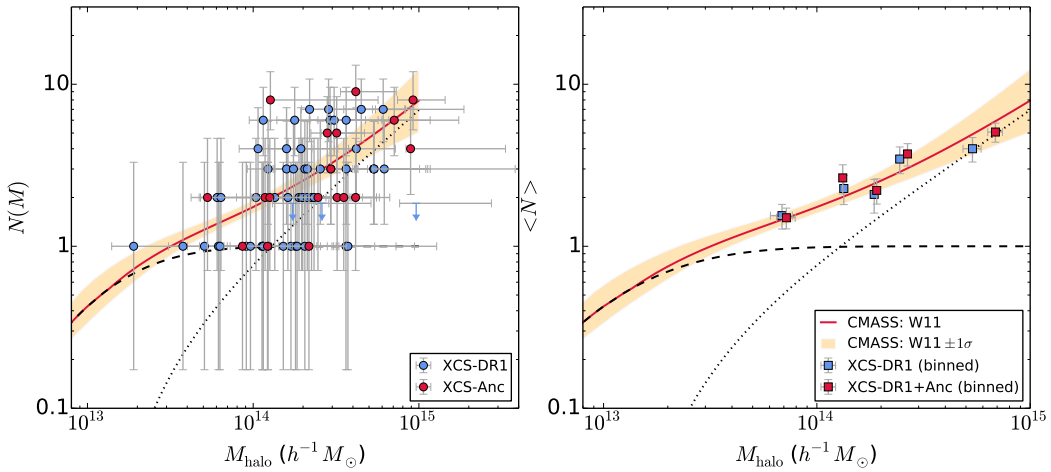

Figure 7.1: [Image and caption taken from Mehrtens et al. (2016) (Figure 4).] LEFT: The Halo Occupation Distribution of CMASS-galaxies ($0.43 < z < 0.7$) as a function of halo mass within X-ray selected clusters (XCS-DR1: blue circles; XCS-Ancillary: red circles). Uncertainties (including those for clusters HON value of 0) are Poisson. For presentation purposes, points with a HON value of 0 are shown as upper limits due to the log-scale of the y-axis. RIGHT: The mean Halo Occupation Distribution of CMASS-galaxies for clusters in mass bins containing approximately equal numbers of clusters (XCS-DR1: blue squares; XCS-DR1 plus XCS-Ancillary: red squares). Uncertainties on the binned points are given by the error on the mean. BOTH: The mean HOD prediction (and the 1-σ uncertainty range) for the combined central and satellite population of W11 is indicated by the solid red line (and the yellow shaded region). The mean HOD predictions for the separate central galaxy and satellite galaxy populations are shown by the black dashed and dotted lines, respectively. Note that the W11 results did not extend beyond $10^{15} M_\odot$. While the halo occupation numbers of CMASS-galaxies measured for individual clusters show a broad distribution of values, the binned values are consistent with the CMASS HOD-model fit of W11.

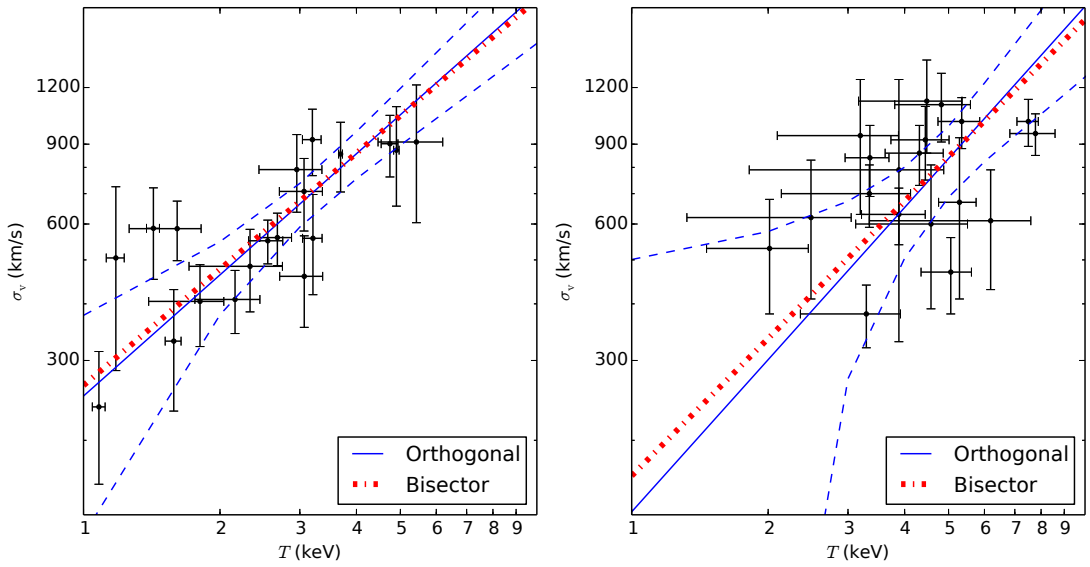

Figure 7.2: [Image and caption taken from Wilson et al. (2016) (Figure 3).] The σ_v–T relation assuming no evolution, i.e., $C = 0$ in Equation 3, for low (left - $0.0 < z < 0.5$) and high (right- $0.5 < z < 0.9$) redshift samples. The solid blue line shows an orthogonal regression fit to the data with the dashed line representing the 95 % confidence interval. The dot-dashed line shows a bisector regression fit to the data. A model of the form seen in Equation 3 was used in the Metropolis algorithm to determine a line of best-fit. It is interesting to note that the two best-measured systems (XMMXCS J105659.5-033728.0 and XMMXCS J114023.0+660819.0) in the high-redshift subsample are relatively far off the best-fit relation, with a higher than predicted temperature. Our current observations do not provide good enough spatial resolution or deep enough multi-colour photometry to determine the exact reason for this and require further study and re-observations.

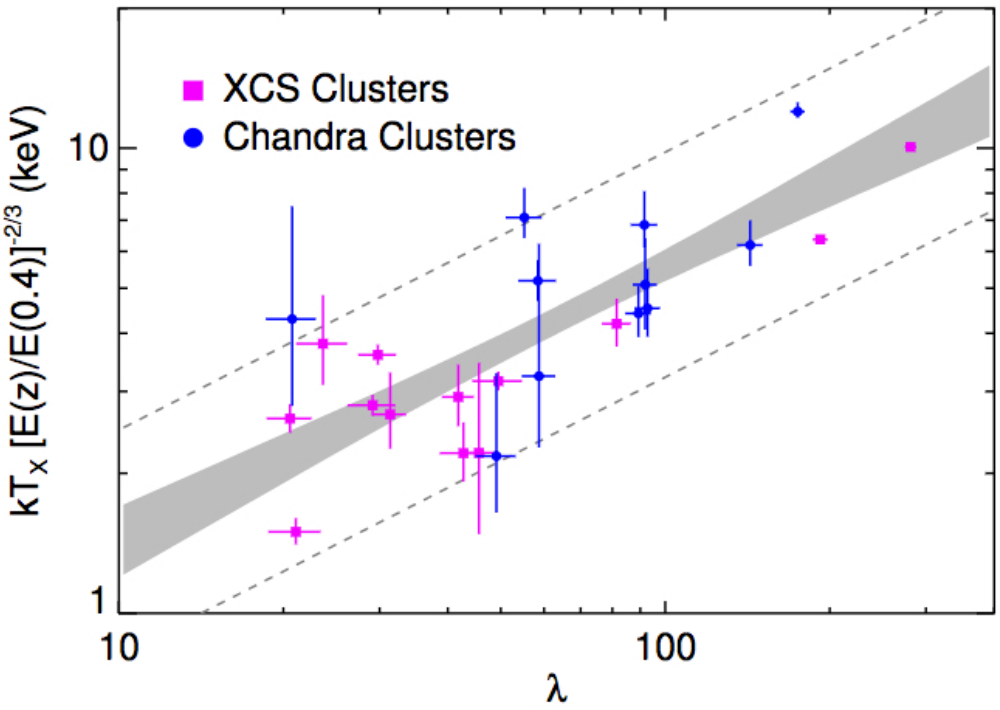

Figure 7.3: [Image and caption taken from Rykoff et al. (2016) (Figure 10).] T_X–λ scaling relation derived from XCS (magneta squares) and *Chandra* (blue circles) clusters. All *Chandra* temperatures have been corrected according to Eqn. 5. The gray band shows the best fit ($\pm 1\sigma$) scaling relation, and the dashed gray lines show $2\sigma_{\rm int}$ intrinsic scatter constraints.

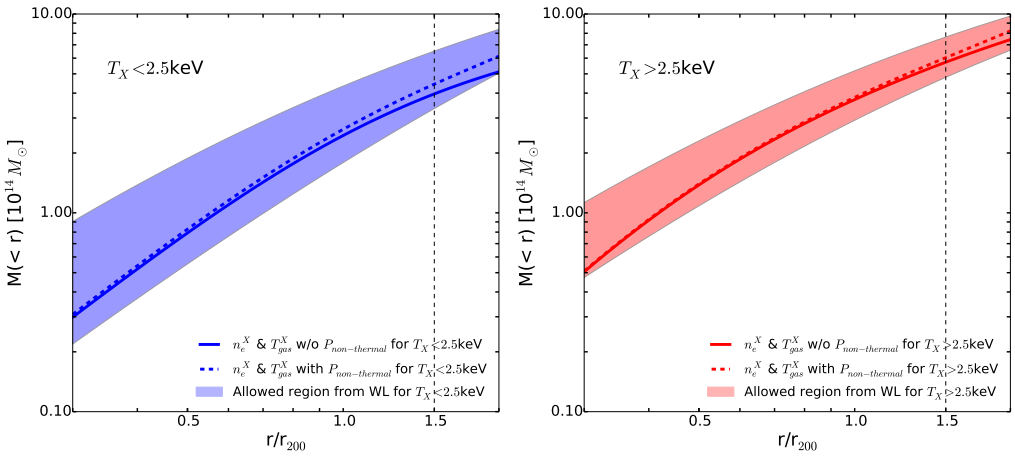

Figure 7.4: [Image and caption taken from Wilcox et al. (2015) (Figure 5).] Mass profile from the $T < 2.5\,\mathrm{keV}$ ($T > 2.5\,\mathrm{keV}$) cluster bin in blue (red). The shaded area is the one-sigma allowed region from the weak lensing measurement and the solid line is the thermal mass reconstructed from the X-rays. The dashed line shows the thermal mass with an additional non-thermal component as discussed in the text. The vertical line is the upper extent of our X-ray data; to its right we have extrapolated the X-ray data.

redMaPPer richness-T_{X} relation, generated by the candidate in December 2013, is shown in Figure 7.5 (top). This work was subsequently developed by another PhD student at Sussex (Alberto Bermeo, Figure 7.5, bottom), although the candidate continued to play a significant supporting role after returning from intermission.

7.2.1 Correction to R-500 Calculation

The XCS team was contacted in October 2012 by cluster expert Monique Arnaud. She altered us to a arithmetic error in our calculation of R_{500}, i.e. the radius where the density is at 500 times the critical density. The calculation is based on an expression in one of her papers, Arnaud et al. (2005b):

$$E(z)R_{500} = 1.104((T_{\mathrm{X}}/5.0))^{0.57} \tag{7.1}$$

where R_{500} is in units of h^{-1} Mpcs and $E(z) = \sqrt{0.27(1+z)^3 + 0.73}$

Arnaud alerted us to the fact that she was only able to recreate that relation if she multiplied the R_{500} values in Mehrtens et al. (2012) by $h(z)^2$ (Figure 7.6). The cause of this error was tracked down by the candidate to a mistake by former XCS postdoc (Ed Lloyd-Davies), who had used the expression `**(1/2)` rather than `**(0.5)` in the $E(z)$

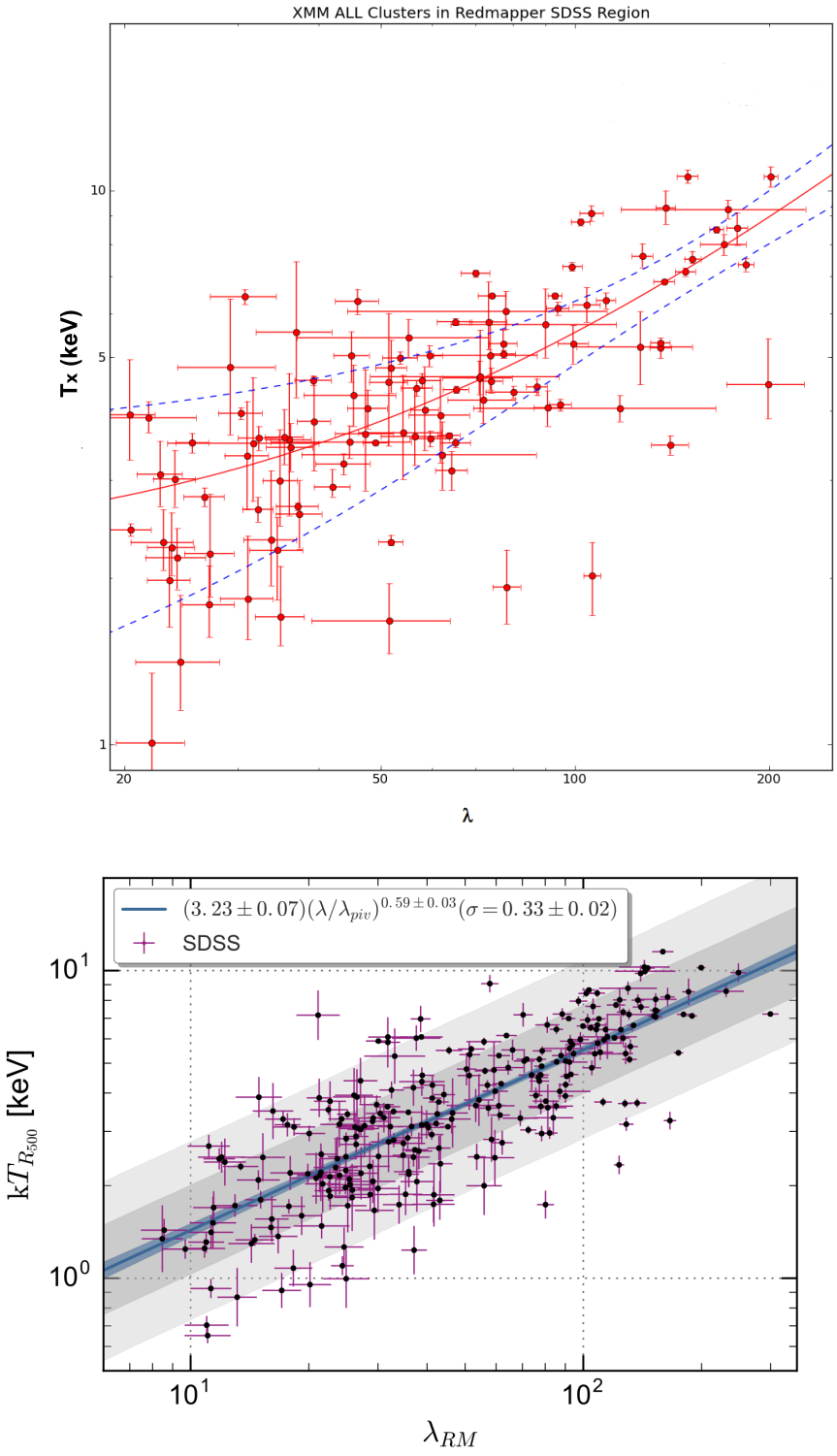

Figure 7.5: Top: An early version of the richness-T_X relation derived by the candidate for redMaPPer clusters in the SDSS region. The dashed lines show the 2σ limits on the scatter. Bottom: The latest (September 2017) version of this relation derived by the XCS team. Plot courtesy of Alberto Bermeo.

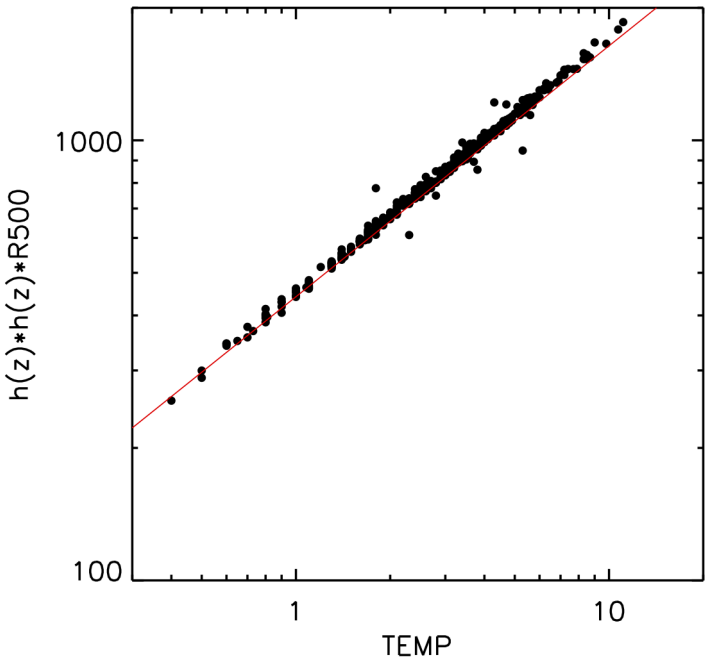

Figure 7.6: Comparison of the R_{500} and $T_{\rm X}$ values in Mehrtens et al. (2012): the values only line up on the predicted (red) relation when a factor of $h(z)^2$ is included. Plot courtesy of Monique Arnaud.

calculation. (In the PYTHON language `(1/2)=1`, because integer calculations have integer answers.) The XCS $T_{\rm X}$ pipeline was subsequently corrected.

7.2.2 Addition of an iterative approach to $L_{\rm X}$ and $T_{\rm X}$ calculations

In the LD11 version of $T_{\rm X}$ pipeline a fixed aperture, based on the size of an XAPA determined source ellipse, was used to extract the cluster spectrum. The $T_{\rm X}$ pipeline was upgraded by the candidate so that it adjusted the aperture used to extract the cluster spectrum in an iterative manner. The XAPA aperture was used to measure an intitial temperature, $T_{{\rm X}initial}$. From $T_{{\rm X}initial}$, an R_{500} value was calculated (using Equation 7.1). This became the radius of a new spectral aperture, and $T_{\rm X}$ was recalculated. The priocess was repeared until the value converged, i.e. until the ratio to the previous value of R_{500} was less than 10%. When there was no convergence after three iterations, XCS records that a $T_{\rm X}$ value cannot be determined. Another advantage of deriving the R_{500} value in this iterative way, is that an estimate for bolometric luminosity at this consistent radius $L_{\rm X}$ can be output from `XSPEC` at the same times as the $T_{\rm X}$. This method to estimate $L_{\rm X}$ represents a significant simplification over that used in LD11 (which involved complex

β-model fits to the 2D surface brightness distribution). A schematic of the new approach is shown in Figure 7.7.

7.2.3 Addition of 'core-excised' analyses

In the LD11 version of the T_X pipeline, all the flux from the cluster was used during the spectral fitting. However, there are strong motivations to exclude the core region before measuring either T_X or L_X: cluster populations can be divided into two distinct groups, *cool-core* (CC) and *non-cool-core* (NCC). The CC clusters show characteristic surface brightness peaks and temperature drops in their cores. If we are interested in estimating the mass of a cluster from its T_X (e.g. via Equation 7.1), then the inclusion of the cluster's core region may be skewing our results. Arnaud et al (2005) Arnaud et al. (2005a) show that by excising the data from the $< 0.1R_{500}$ region and from $> 0.5R_{500}$, we can resolve this problem (Figure 7.2.3). They propose that within these radii gravitational heating dominates the properties of the ICM, and hence the virial theory holds. (See aslo Maughan et al. (2012).) Therefore, the XCS T_X code was adapted so that it would run either with or without the central regions ($r < 0.15R_{500}$) excised (Figure 7.9).

7.2.4 Application to target clusters

The first XCS data release (Mehrtens et al. 2012) deliberately excluded any clusters that had been the intended target of their respective XMM observation. However, going forward, it was clear that XCS would need to measure X-ray parameters for all clusters in the XMM archive, i.e. including targets. This was because XCS was, by then, providing X-ray support to the Dark Energy Survey (DES): many clusters in the DES footprint, especially those also detected (via the SZ effect) by the SPT telescope, had been the subject of targeted XMM observations. For this, several additions to the T_X were required. For example, most target clusters had been masked before the source detection (XAPA) pipeline had been run. They, therefore, did not appear in the XCS master source list (MSL). Previous to the update, the T_X pipeline could not process sources that were not in MSL. After the pipeline had been adjusted so that it would work on cluster targets, we tested its efficacy by comparing XCS determined values to those measured by other authors. Initially this suggested that our measurements were systematically overestimated (Figure 7.10, left). However, further investigation showed that this was due to the difference between using Cash-statistic rather than χ-squared errors during XSPEC fits (Figure 7.10, right).

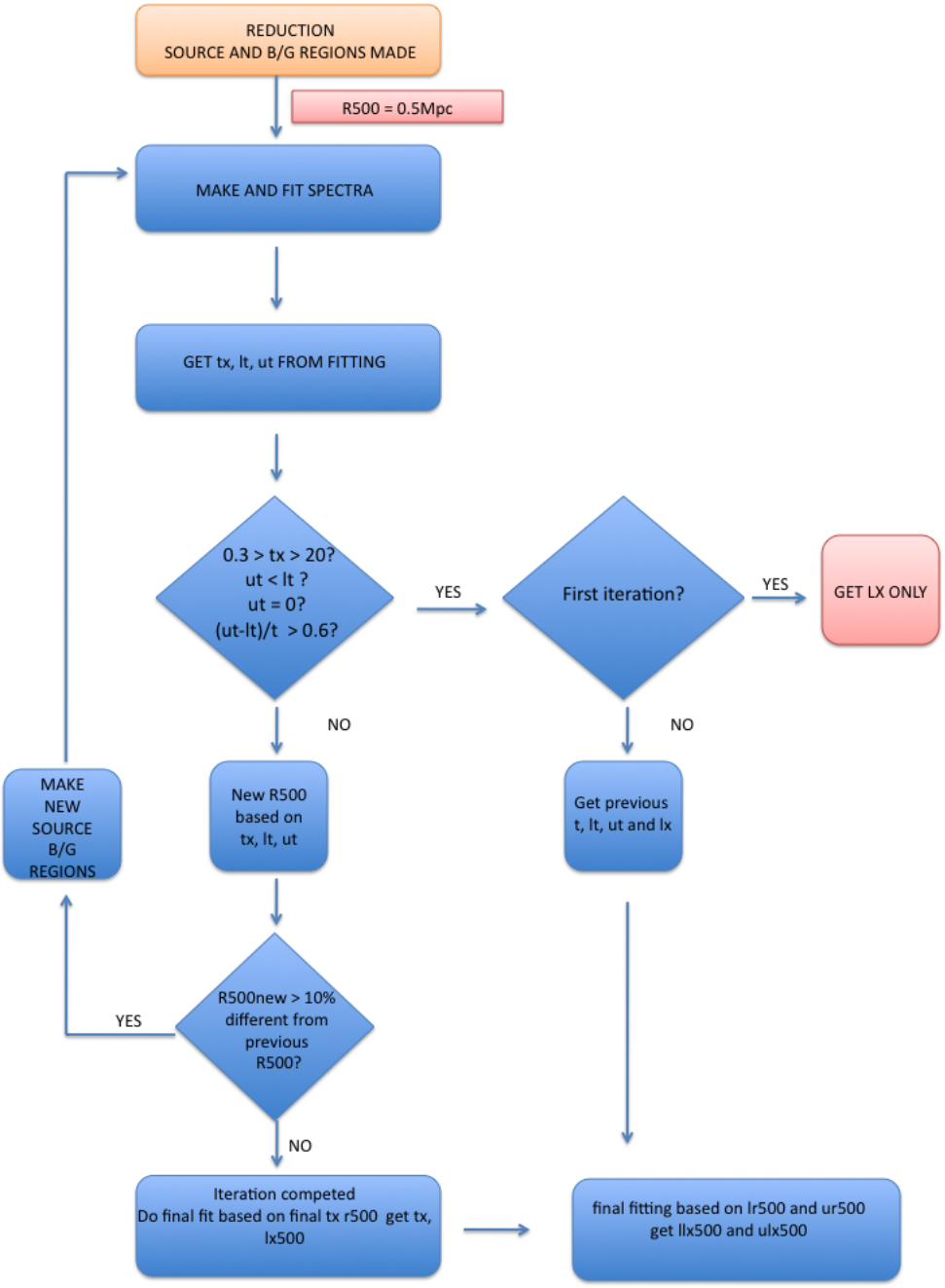

Figure 7.7: Schematic of the iterative approach to $T_{\rm X}$ and $L_{\rm X}$ calculations that was established by the candidate for XCS

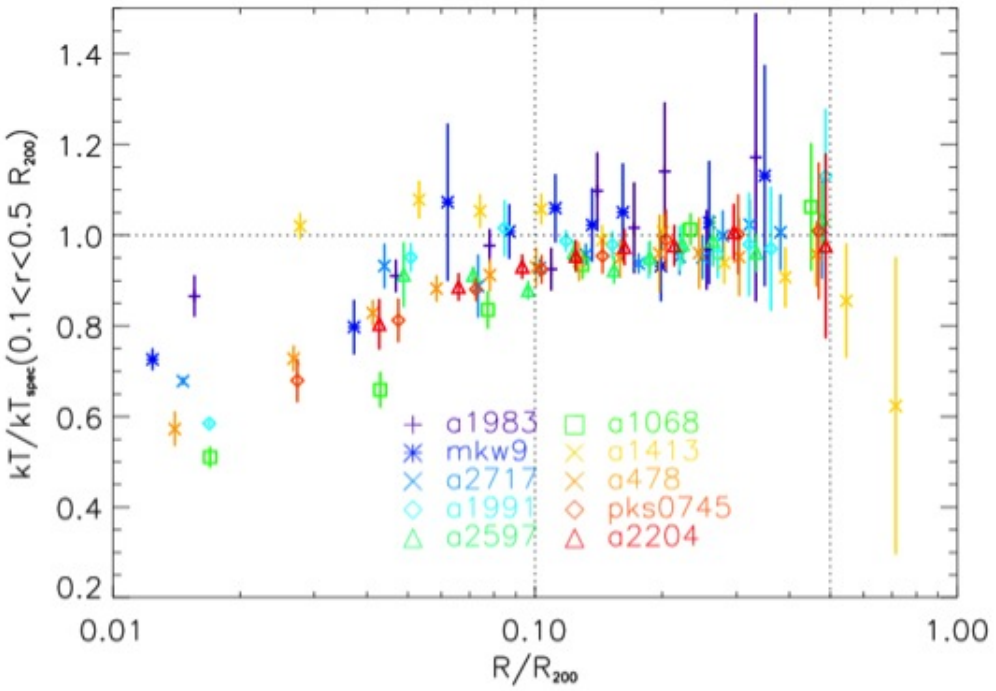

Figure 7.8: Normalised temperature profiles of ten low-z clusters from Arnaud et al. (2005a).

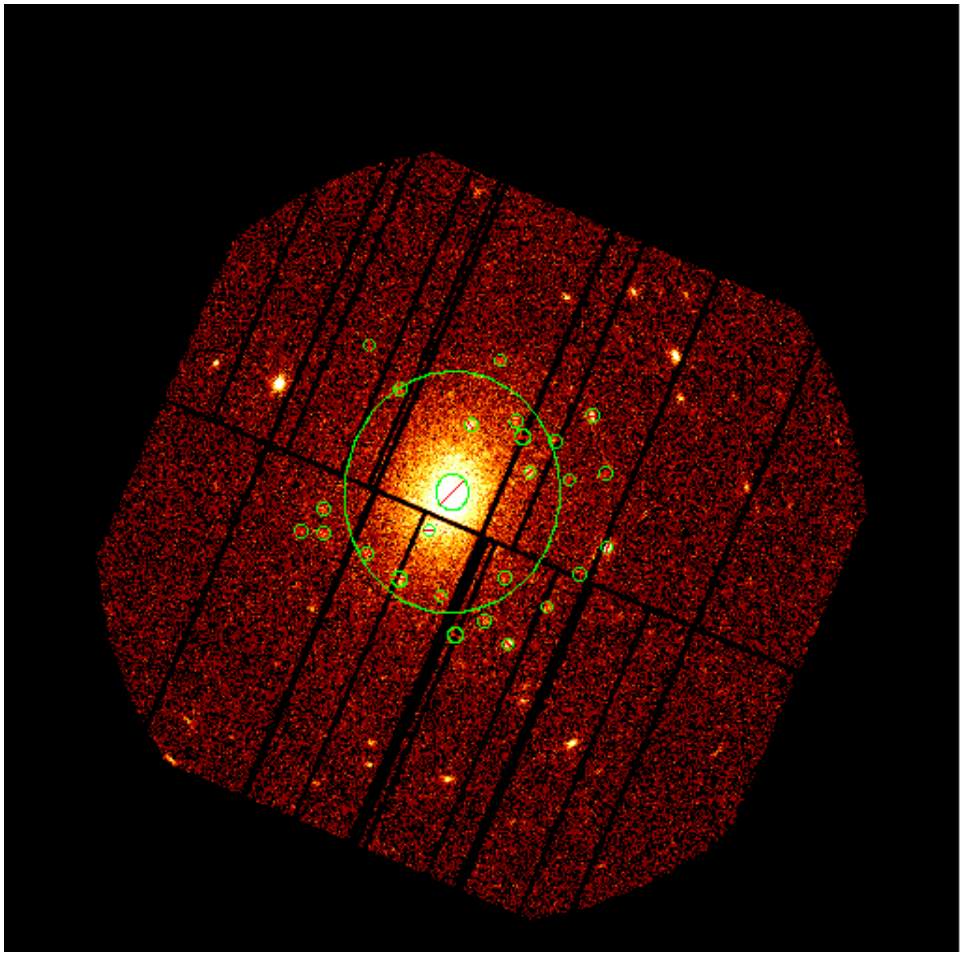

Figure 7.9: An XMM image of a cluster showing the how the core region is excised from the spectral aperture.

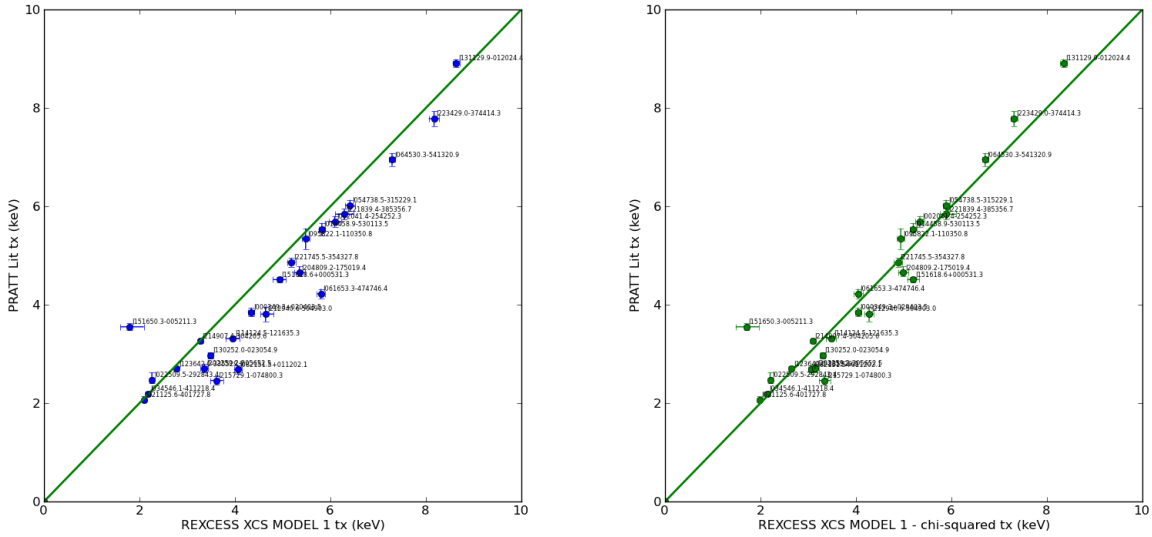

Figure 7.10: Comparison of XCS determined $T_{\rm X}$ values to those measured by Arnaud et al. (2010). Before (left) and after (right) changing from Cash (Cash 1979) to χ^2 statistics in `XSPEC`.

Chapter 8

Conclusions

In this work, we have described our use of the source catalogue and analysis pipelines adapted from the XMM-Newton Cluster Survey in three projects that investigate exotic X-ray phenomena. Each project widens the scope of XCS beyond purely cluster cosmology.

In Chapter 4, we described how we used AGN associated with XCS point sources to confirm the existence of scaling relations between $M_{\rm BH}$, $L_{\rm X}$ and with $\sigma^2_{\rm NXS}$. With our sample, we have found no significant redshift evolution of these scaling relations, thus improving the accuracy of the $L_{\rm X}$-$M_{\rm BH}$ relation.

We have estimated that our sample of AGN with both XCS derived $L_{\rm X}$ values, and $M_{\rm BH}$ estimates, can be doubled once the OzDES survey starts providing new reverberation mapped data of AGN.

We have also described a method to estimate the $L_{\rm X}$ of an AGN from count-rates of short duration observations where the $\sigma^2_{\rm NXS}$ cannot be measured. We have shown that though the uncertainties on the count-rate derived $L_{\rm X}$ are larger than spectrally derived $L_{\rm X}$, the scaling relation with $M_{\rm BH}$ is statistically similar. This will be particularly relevant to future X-ray missions such as eROSITA where short observations allow us to estimate potentially millions of $M_{\rm BH}$ from this scaling relation.

The work in presented in this chapter is being prepared for submission to MNRAS.

In Chapter 5 we described a new method to detect XRFs, some of the rarest X-ray transient events, by a serendipitous search of the XCS point source catalogue. From the 21

candidates we have detected to $> 5\sigma$ level in the PN and $> 3.9\sigma$ in the MOS cameras we categorized them into confirmed (presumably flaring) stars, likely stars (and definitely not XRFs), and one strong XRF candidate. We looked in detail at this candidate and speculated on its nature by comparing its spectrum and light-curve with that a Type-I X-ray burst. We cannot be certain that this candidate is an XRF rather than a Type 1 X-ray burst (or other source). For future work we would like to obtain a deep optical/IR image this source to ascertain if there is a faint external galaxy or Milky Way star at that location. It would also be useful to obtain another targeted XMM or Chandra observation of this location, as it only appears in the FOV of one unique ObsID to date. The second XMM or Chandra observation would demonstrate if there is faint X-ray source at that location.

We defined a method to derive a selection function of percentage of XRF detection to observation exposure time which we made by injecting dummy XRF events in to existing XMM observations. We used this to estimate an upper-limit of number of XRFs of a fluence per sky per year based on our best candidate XRF.

Looking forward, for this work to be suitable for journal publication, more work would need to be done on the selection function used to estimate the fluence. For example, by taking into account vignetting, chip gaps, and n_H column as well as scaling the dummy counts to take account of the exposure map. Further, we assumed that all our fake XRF sources would have been detected as point sources by our XAPA detection pipeline. We should like to test whether this is a fair assumption. This is a non-trivial and time consuming effort, as it involves re-running thousands of ObsIDS in each of the three EPIC camera through the XCS source detection pipeline.

Using our pipeline we would also like to investigate variable X-ray sources candidates within Galactic Plane (our current analysis is restricted to $|b| > 20^\circ$. The methodology we have developed could be adapted be able to uncover *all* flaring and transient sources in the XMM archive. We would then be able to predict the expected detection rate of such sources in eRASS.

In Chapter 6 we described a method to search for unknown emission lines in cluster spectra. If such lines are found, they may be explained by a sterile neutrino interpretation

for dark matter. They could also be explained by an inadequate description of plasma emission in existing XSPEC models. Given that other authors have claimed the existence of an unknown line at $\simeq$3.55 keV, we have focused our attention on that energy.

Our method involves stacking individual cluster observations after blueshifting to a common rest frame. We have demonstrated how this approach improves signal-to-noise. We have also demonstrated our method to search unknown emission lines by adding fake lines to cluster spectra.

When we applied our method to stacked spectra of Perseus cluster, and found no evidence for an unknown emission line at around 3.55 keV as claimed by some authors. We do not draw any firm conclusions from this non-detection because our approach does not fully currently take into account the background.

We have also applied our method to 322 cluster spectra, that were stacked in five temperature bins, and into a single combined spectrum. We find no evidence of an emission line at 3.55 keV in the combined spectrum nor in the three lower temperature bins. However, we do find tentative evidence for a line at $\simeq$3.55 keV in the two hotter bins. Importantly, this line seems to get stronger with $T_{\rm X}$, as would be expected of a dark matter feature.

We are planning to write up the work in this chapter for a journal article because our temperature binning approach is genuinely new to the literature. However, significant work remains before we can claim to have made either a detection or a non-detection.

Thank you for reading this thesis.

Bibliography

Abbott, B. P., Abbott, R., Abbott, T. D., Abernathy, M. R., Acernese, F., Ackley, K., Adams, C., Adams, T., Addesso, P., Adhikari, R. X., and et al. (2016). Observation of Gravitational Waves from a Binary Black Hole Merger. *Physical Review Letters*, 116(6):061102. 20

Abbott, B. P., Abbott, R., Abbott, T. D., Acernese, F., Ackley, K., Adams, C., Adams, T., Addesso, P., Adhikari, R. X., Adya, V. B., and et al. (2017). Multi-messenger Observations of a Binary Neutron Star Merger. *The Astrophysical Journal Letters*, 848:L12. 20

Abolfathi, B., Aguado, D. S., Aguilar, G., Allende Prieto, C., Almeida, A., Tasnim Ananna, T., Anders, F., Anderson, S. F., Andrews, B. H., Anguiano, B., and et al. (2017). The Fourteenth Data Release of the Sloan Digital Sky Survey: First Spectroscopic Data from the extended Baryon Oscillation Sky Survey and from the second phase of the Apache Point Observatory Galactic Evolution Experiment. *ArXiv e-prints*. 133

Ageron, M., Aguilar, J. A., Al Samarai, I., Albert, A., Ameli, F., André, M., Anghinolfi, M., Anton, G., Anvar, S., Ardid, M., and et al. (2011). ANTARES: The first undersea neutrino telescope. *Nuclear Instruments and Methods in Physics Research A*, 656:11–38. 22

Aharonian, F. A., Akamatsu, H., Akimoto, F., Allen, S. W., Angelini, L., Arnaud, K. A., Audard, M., Awaki, H., Axelsson, M., Bamba, A., and et al. (2017). Hitomi Constraints on the 3.5 keV Line in the Perseus Galaxy Cluster. *The Astrophysical Journal Letters*, 837:L15. xxvi, 156, 157

Allen, S. W., Evrard, A. E., and Mantz, A. B. (2011). Cosmological Parameters from Observations of Galaxy Clusters. *Annual review of astronomy and astrophysics*, 49:409–470. xv, 17, 19

Amati, L., Frontera, F., in't Zand, J. J. M., Capalbi, M., Landi, R., Soffitta, P., Vetere, L., Antonelli, L. A., Costa, E., Del Sordo, S., Feroci, M., Guidorzi, C., Heise, J., Masetti, N., Montanari, E., Nicastro, L., Palazzi, E., and Piro, L. (2004). Prompt and afterglow X-ray emission from the X-Ray Flash of 2002 April 27. *Astronomy and Astrophysics*, 426:415–423. 116

Antonucci, M., Vagnetti, F., and Trevese, D. (2014). On the cosmological bias of the excess variance as a variability estimator. In *The X-ray Universe 2014*, page 222. 69

Antonucci, R. (1993). Unified models for active galactic nuclei and quasars. *Annual review of astronomy and astrophysics*, 31:473–521. 14

Arnaud, M., Pointecouteau, E., and Pratt, G. W. (2005a). The structural and scaling properties of nearby galaxy clusters. II. The M-T relation. *Astronomy and Astrophysics*, 441:893–903. xxx, 192, 194

Arnaud, M., Pointecouteau, E., and Pratt, G. W. (2005b). The structural and scaling properties of nearby galaxy clusters. II. The M-T relation. *Astronomy and Astrophysics*, 441:893–903. 189

Arnaud, M., Pratt, G. W., Piffaretti, R., Böhringer, H., Croston, J. H., and Pointecouteau, E. (2010). The universal galaxy cluster pressure profile from a representative sample of nearby systems (REXCESS) and the Y_{SZ} - M_{500} relation. *Astronomy and Astrophysics*, 517:A92. xxx, 196

Baade, W. and Minkowski, R. (1954). Identification of the Radio Sources in Cassiopeia, Cygnus A, and Puppis A. *The Astrophysical Journal*, 119:206. 55

Barcons, X., Barret, D., Decourchelle, A., den Herder, J.-W., Dotani, T., Fabian, A. C., Fraga-Encinas, R., Kunieda, H., Lumb, D., Matt, G., Nandra, K., Piro, L., Rando, N., Sciortino, S., Smith, R. K., Strüder, L., Watson, M. G., White, N. E., and Willingale, R. (2012). Athena (Advanced Telescope for High ENergy Astrophysics) Assessment Study Report for ESA Cosmic Vision 2015-2025. *ArXiv e-prints*. 35

Barr, P. and Mushotzky, R. F. (1986). Limits of X-ray variability in active galactic nuclei. *Nature*, 320:421–423. 94

Barraud, C., Daigne, F., Mochkovitch, R., and Atteia, J. L. (2005). On the nature of X-ray flashes. *Astronomy and Astrophysics*, 440:809–817. 116

Barraud, C., Olive, J.-F., Lestrade, J. P., Atteia, J.-L., Hurley, K., Ricker, G., Lamb, D. Q., Kawai, N., Boer, M., Dezalay, J.-P., Pizzichini, G., Vanderspek, R., Crew, G., Doty, J., Monnelly, G., Villasenor, J., Butler, N., Levine, A., Yoshida, A., Shirasaki, Y., Sakamoto, T., Tamagawa, T., Torii, K., Matsuoka, M., Fenimore, E. E., Galassi, M., Tavenner, T., Donaghy, T. Q., Graziani, C., and Jernigan, J. G. (2003). Spectral analysis of 35 GRBs/XRFs observed with HETE-2/FREGATE. *Astronomy and Astrophysics*, 400:1021–1030. 119

Bauer, F. E., Treister, E., Schawinski, K., Schulze, S., Luo, B., Alexander, D. M., Brandt, W. N., Comastri, A., Forster, F., Gilli, R., Kann, D. A., Maeda, K., Nomoto, K., Paolillo, M., Ranalli, P., Schneider, D. P., Shemmer, O., Tanaka, M., Tolstov, A., Tominaga, N., Tozzi, P., Vignali, C., Wang, J., Xue, Y., and Yang, G. (2017). A new, faint population of X-ray transients. *Monthly Notices of the Royal Astronomical Society*, 467:4841–4857. 116, 119

Begelman, M. C. and Rees, M. J. (1978). The fate of dense stellar systems. *Monthly Notices of the Royal Astronomical Society*, 185:847–860. 56

Begelman, M. C., Volonteri, M., and Rees, M. J. (2006). Formation of supermassive black holes by direct collapse in pre-galactic haloes. *Monthly Notices of the Royal Astronomical Society*, 370:289–298. 56

Begeman, K. G., Broeils, A. H., and Sanders, R. H. (1991). Extended rotation curves of spiral galaxies - Dark haloes and modified dynamics. *Monthly Notices of the Royal Astronomical Society*, 249:523–537. xxv, 147, 148

Bennett, C. L., Larson, D., Weiland, J. L., Jarosik, N., Hinshaw, G., Odegard, N., Smith, K. M., Hill, R. S., Gold, B., Halpern, M., Komatsu, E., Nolta, M. R., Page, L., Spergel, D. N., Wollack, E., Dunkley, J., Kogut, A., Limon, M., Meyer, S. S., Tucker, G. S., and Wright, E. L. (2013). Nine-year Wilkinson Microwave Anisotropy Probe (WMAP) Observations: Final Maps and Results. *The Astrophysical Journal Supplement*, 208:20. 7

Bentz, M. C. and Katz, S. (2015). The AGN Black Hole Mass Database. *Publications of the Astronomical Society of the Pacific*, 127:67–73. xii, xiv, xxi, xxii, 92, 94, 96, 97, 111, 236

Bentz, M. C., Peterson, B. M., Pogge, R. W., and Vestergaard, M. (2009a). The Black Hole Mass-Bulge Luminosity Relationship for Active Galactic Nuclei From Reverberation

Mapping and Hubble Space Telescope Imaging. *The Astrophysical Journal Letters*, 694:L166–L170. xviii, 63

Bentz, M. C., Walsh, J. L., Barth, A. J., Baliber, N., Bennert, V. N., Canalizo, G., Filippenko, A. V., Ganeshalingam, M., Gates, E. L., Greene, J. E., Hidas, M. G., Hiner, K. D., Lee, N., Li, W., Malkan, M. A., Minezaki, T., Sakata, Y., Serduke, F. J. D., Silverman, J. M., Steele, T. N., Stern, D., Street, R. A., Thornton, C. E., Treu, T., Wang, X., Woo, J.-H., and Yoshii, Y. (2009b). The Lick AGN Monitoring Project: Broad-line Region Radii and Black Hole Masses from Reverberation Mapping of Hβ. *The Astrophysical Journal*, 705:199–217. 62

Bermeo, A. (2017). *XCS, Optical to X-ray Scaling Relations*. PhD thesis, Univsersity of Sussex. 43, 160, 177

Bianchi, S., Bonilla, N. F., Guainazzi, M., Matt, G., and Ponti, G. (2009a). CAIXA: a catalogue of AGN in the XMM-Newton archive. II. Multiwavelength correlations. *Astronomy and Astrophysics*, 501:915–924. xxi, 98

Bianchi, S., Guainazzi, M., Matt, G., Fonseca Bonilla, N., and Ponti, G. (2009b). CAIXA: a catalogue of AGN in the XMM-Newton archive. I. Spectral analysis. *Astronomy and Astrophysics*, 495:421–430. xiii, 98

Blandford, R. D. and McKee, C. F. (1982). Reverberation mapping of the emission line regions of Seyfert galaxies and quasars. *The Astrophysical Journal*, 255:419–439. 60

Bloom, J. S., Fox, D., van Dokkum, P. G., Kulkarni, S. R., Berger, E., Djorgovski, S. G., and Frail, D. A. (2003). The First Two Host Galaxies of X-Ray Flashes: XRF 011030 and XRF 020427. *The Astrophysical Journal*, 599:957–963. 119

Blumenthal, G. R., Faber, S. M., Primack, J. R., and Rees, M. J. (1984). Formation of galaxies and large-scale structure with cold dark matter. *Nature*, 311:517–525. 151

Boehm, F. and P., V. (1987). *Physics of Massive Neutrinos*. Cambridge University Press. 153

Boyarsky, A., Ruchayskiy, O., Iakubovskyi, D., and Franse, J. (2014). Unidentified Line in X-Ray Spectra of the Andromeda Galaxy and Perseus Galaxy Cluster. *Physical Review Letters*, 113(25):251301. 154, 168

Brandt, W. N. and Hasinger, G. (2005). Deep Extragalactic X-Ray Surveys. *Annual review of astronomy and astrophysics*, 43:827–859. 13

Brightman, M., Baloković, M., Ballantyne, D. R., Bauer, F. E., Boorman, P., Buchner, J., Brandt, W. N., Comastri, A., Del Moro, A., Farrah, D., Gandhi, P., Harrison, F. A., Koss, M., Lanz, L., Masini, A., Ricci, C., Stern, D., Vasudevan, R., and Walton, D. J. (2017). X-ray bolometric corrections for Compton-thick active galactic nuclei. *ArXiv e-prints*. 15

Bromm, V. and Loeb, A. (2003). Formation of the First Supermassive Black Holes. *The Astrophysical Journal*, 596:34–46. 56

Bulbul, E., Markevitch, M., Foster, A., Smith, R. K., Loewenstein, M., and Randall, S. W. (2014). Detection of an Unidentified Emission Line in the Stacked X-Ray Spectrum of Galaxy Clusters. *The Astrophysical Journal*, 789:13. xxv, 154, 155, 156, 159, 168, 177, 178, 180

Butler, N., Dullighan, A., Ford, P., Ricker, G., Vanderspek, R., Hurley, K., Jernigan, J., Lamb, D., and Graziani, C. (2004). Optical and X-ray Observations of the Afterglow to XRF 030723. In Fenimore, E. and Galassi, M., editors, *Gamma-Ray Bursts: 30 Years of Discovery*, volume 727 of *American Institute of Physics Conference Series*, pages 111–114. 116

Cappelluti, N., Bulbul, E., Foster, A., Natarajan, P., Urry, M. C., Bautz, M. W., Civano, F., Miller, E., and Smith, R. K. (2017). Searching for the 3.5 keV Line in the Deep Fields with Chandra: the 10 Ms observations. *ArXiv e-prints*. xxvi, 157, 159

Carroll, S. M., Press, W. H., and Turner, E. L. (1992). The cosmological constant. *Annual review of astronomy and astrophysics*, 30:499–542. 5

Cash, W. (1979). Parameter estimation in astronomy through application of the likelihood ratio. *The Astrophysical Journal*, 228:939–947. xxx, 196

Chandrasekhar, S. (1935). The highly collapsed configurations of a stellar mass (Second paper). *Monthly Notices of the Royal Astronomical Society*, 95:207–225. 55

Chincarini, G. (2005). Witnessing the Flash from a Black Hole's Cannibal Act. In *European Southern Observatory Press Release*. 119

Cline, J. M. and Frey, A. R. (2014). Consistency of dark matter interpretations of the 3.5 keV x-ray line. *Physical Review D*, 90(12):123537. 155

Clowe, D., Bradač, M., Gonzalez, A. H., Markevitch, M., Randall, S. W., Jones, C., and Zaritsky, D. (2006). A Direct Empirical Proof of the Existence of Dark Matter. *The Astrophysical Journal Letters*, 648:L109–L113. 149

Colgate, S. A., Cen, R., Li, H., Currier, N., and Warren, M. S. (2003). Cosmological Mestel Disks and the Rossby Vortex Instability: The Origin of Supermassive Black Holes. *The Astrophysical Journal Letters*, 598:L7–L10. 56

Conlon, J. P., Day, F., Jennings, N., Krippendorf, S., and Rummel, M. (2016). Consistency of Hitomi, XMM-Newton and Chandra 3.5 keV data from Perseus. *ArXiv e-prints*. xxvi, 156, 158

Connolly, S. D., McHardy, I. M., Skipper, C. J., and Emmanoulopoulos, D. (2016). Long-term X-ray spectral variability in AGN from the Palomar sample observed by Swift. *Monthly Notices of the Royal Astronomical Society*, 459:3963–3985. 88

Corral, A., Della Ceca, R., Caccianiga, A., Severgnini, P., Brunner, H., Carrera, F. J., Page, M. J., and Schwope, A. D. (2011). The X-ray spectral properties of the AGN population in the XMM-Newton bright serendipitous survey. *Astronomy and Astrophysics*, 530:A42. xxii, 88, 103

Cravens, T. E. (2000). Heliospheric X-ray Emission Associated with Charge Transfer of the Solar Wind with Interstellar Neutrals. *The Astrophysical Journal Letters*, 532:L153–L156. 13

Davies, R. I., Thomas, J., Genzel, R., Müller Sánchez, F., Tacconi, L. J., Sternberg, A., Eisenhauer, F., Abuter, R., Saglia, R., and Bender, R. (2006). The Star-forming Torus and Stellar Dynamical Black Hole Mass in the Seyfert 1 Nucleus of NGC 3227. *The Astrophysical Journal*, 646:754–773. 62

DeGraf, C., Di Matteo, T., Khandai, N., and Croft, R. (2012). Growth of Early Supermassive Black Holes and the High-redshift Eddington Ratio Distribution. *The Astrophysical Journal Letters*, 755:L8. xx, 75, 77

Dewdney, P. E., Hall, P. J., Schilizzi, R. T., and Lazio, T. J. L. W. (2009). The Square Kilometre Array. *IEEE Proceedings*, 97:1482–1496. 20

Di Matteo, T., Colberg, J., Springel, V., Hernquist, L., and Sijacki, D. (2008). Direct Cosmological Simulations of the Growth of Black Holes and Galaxies. *The Astrophysical Journal*, 676:33–53. 75

Dickey, J. M. and Lockman, F. J. (1990a). H I in the Galaxy. *Annual review of astronomy and astrophysics*, 28:215–261. 47, 161, 168

Dickey, J. M. and Lockman, F. J. (1990b). H I in the Galaxy. *Annual review of astronomy and astrophysics*, 28:215–261. 87, 109, 170

Djorgovski, S. G., Gal, R. R., Odewahn, S. C., de Carvalho, R. R., Brunner, R., Longo, G., and Scaramella, R. (1998). The Palomar Digital Sky Survey (DPOSS). In Colombi, S., Mellier, Y., and Raban, B., editors, *Wide Field Surveys in Cosmology*, page 89. 133

Dolgov, A. D. and Hansen, S. H. (2002). Massive sterile neutrinos as warm dark matter. *Astroparticle Physics*, 16:339–344. 154

Düchting, N. (2004). Supermassive black holes from primordial black hole seeds. *Physical Review D*, 70(6):064015. 57

Elvis, M., Maccacaro, T., Wilson, A. S., Ward, M. J., Penston, M. V., Fosbury, R. A. E., and Perola, G. C. (1978). Seyfert galaxies as X-ray sources. *Monthly Notices of the Royal Astronomical Society*, 183:129–157. 16

Evans, I. N., Primini, F. A., Glotfelty, K. J., Anderson, C. S., Bonaventura, N. R., Chen, J. C., Davis, J. E., Doe, S. M., Evans, J. D., Fabbiano, G., Galle, E. C., Gibbs, II, D. G., Grier, J. D., Hain, R. M., Hall, D. M., Harbo, P. N., (Helen He, X., Houck, J. C., Karovska, M., Kashyap, V. L., Lauer, J., McCollough, M. L., McDowell, J. C., Miller, J. B., Mitschang, A. W., Morgan, D. L., Mossman, A. E., Nichols, J. S., Nowak, M. A., Plummer, D. A., Refsdal, B. L., Rots, A. H., Siemiginowska, A., Sundheim, B. A., Tibbetts, M. S., Van Stone, D. W., Winkelman, S. L., and Zografou, P. (2010). The Chandra Source Catalog. *The Astrophysical Journal Supplement*, 189:37–82. 133, 243

Ferrarese, L. (2002). Beyond the Bulge: A Fundamental Relation between Supermassive Black Holes and Dark Matter Halos. *The Astrophysical Journal*, 578:90–97. 74

Ferrarese, L. and Merritt, D. (2000). A Fundamental Relation between Supermassive Black Holes and Their Host Galaxies. *The Astrophysical Journal Letters*, 539:L9–L12. 74

Ford, H. C., Harms, R. J., Tsvetanov, Z. I., Hartig, G. F., Dressel, L. L., Kriss, G. A., Bohlin, R. C., Davidsen, A. F., Margon, B., and Kochhar, A. K. (1994). Narrowband

HST images of M87: Evidence for a disk of ionized gas around a massive black hole. *The Astrophysical Journal Letters*, 435:L27–L30. 55

Frampton, P. H., Kawasaki, M., Takahashi, F., and Yanagida, T. T. (2010). Primordial black holes as all dark matter. *Journal of Cosmology and Astro-Particle Physics*, 4:023. 151

Freedman, W. L., Madore, B. F., Gibson, B. K., Ferrarese, L., Kelson, D. D., Sakai, S., Mould, J. R., Kennicutt, Jr., R. C., Ford, H. C., Graham, J. A., Huchra, J. P., Hughes, S. M. G., Illingworth, G. D., Macri, L. M., and Stetson, P. B. (2001). Final Results from the Hubble Space Telescope Key Project to Measure the Hubble Constant. *The Astrophysical Journal*, 553:47–72. 3

Frieman, J. A., Turner, M. S., and Huterer, D. (2008). Dark Energy and the Accelerating Universe. *Annual review of astronomy and astrophysics*, 46:385–432. xv, 6

Gaia Collaboration, Prusti, T., de Bruijne, J. H. J., Brown, A. G. A., Vallenari, A., Babusiaux, C., Bailer-Jones, C. A. L., Bastian, U., Biermann, M., Evans, D. W., and et al. (2016). The Gaia mission. *Astronomy and Astrophysics*, 595:A1. 19

Gebhardt, K., Bender, R., Bower, G., Dressler, A., Faber, S. M., Filippenko, A. V., Green, R., Grillmair, C., Ho, L. C., Kormendy, J., Lauer, T. R., Magorrian, J., Pinkney, J., Richstone, D., and Tremaine, S. (2000). A Relationship between Nuclear Black Hole Mass and Galaxy Velocity Dispersion. *The Astrophysical Journal Letters*, 539:L13–L16. xx, 73, 75

Gehrels, N., Chincarini, G., Giommi, P., Mason, K. O., Nousek, J. A., Wells, A. A., White, N. E., Barthelmy, S. D., Burrows, D. N., Cominsky, L. R., Hurley, K. C., Marshall, F. E., Mészáros, P., Roming, P. W. A., Angelini, L., Barbier, L. M., Belloni, T., Campana, S., Caraveo, P. A., Chester, M. M., Citterio, O., Cline, T. L., Cropper, M. S., Cummings, J. R., Dean, A. J., Feigelson, E. D., Fenimore, E. E., Frail, D. A., Fruchter, A. S., Garmire, G. P., Gendreau, K., Ghisellini, G., Greiner, J., Hill, J. E., Hunsberger, S. D., Krimm, H. A., Kulkarni, S. R., Kumar, P., Lebrun, F., Lloyd-Ronning, N. M., Markwardt, C. B., Mattson, B. J., Mushotzky, R. F., Norris, J. P., Osborne, J., Paczynski, B., Palmer, D. M., Park, H.-S., Parsons, A. M., Paul, J., Rees, M. J., Reynolds, C. S., Rhoads, J. E., Sasseen, T. P., Schaefer, B. E., Short, A. T., Smale, A. P., Smith, I. A., Stella, L., Tagliaferri, G., Takahashi, T., Tashiro, M., Townsley, L. K., Tueller, J., Turner, M. J. L., Vietri, M., Voges, W., Ward, M. J.,

Willingale, R., Zerbi, F. M., and Zhang, W. W. (2004). The Swift Gamma-Ray Burst Mission. *The Astrophysical Journal*, 611:1005–1020. 19

George, I. M., Turner, T. J., Yaqoob, T., Netzer, H., Laor, A., Mushotzky, R. F., Nandra, K., and Takahashi, T. (2000). X-Ray Observations of Optically Selected, Radio-quiet Quasars. I. The ASCA Results. *The Astrophysical Journal*, 531:52–80. 16

Ghez, A. M., Duchêne, G., Matthews, K., Hornstein, S. D., Tanner, A., Larkin, J., Morris, M., Becklin, E. E., Salim, S., Kremenek, T., Thompson, D., Soifer, B. T., Neugebauer, G., and McLean, I. (2003). The First Measurement of Spectral Lines in a Short-Period Star Bound to the Galaxy's Central Black Hole: A Paradox of Youth. *The Astrophysical Journal Letters*, 586:L127–L131. 59

Gilli, R. (2013). The cosmic X-ray background: abundance and evolution of hidden black holes. *Memorie della Societa Astronomica Italiana*, 84:647. xv, 13

González-Martín, O. and Vaughan, S. (2012). X-ray variability of 104 active galactic nuclei. XMM-Newton power-spectrum density profiles. *Astronomy and Astrophysics*, 544:A80. xix, 65, 67

Goobar, A., Hannestad, S., Mörtsell, E., and Tu, H. (2006). The neutrino mass bound from WMAP 3 year data, the baryon acoustic peak, the SNLS supernovae and the Lyman-α forest. *Journal of Cosmology and Astro-Particle Physics*, 6:019. 153

Graham, A. W., Erwin, P., Caon, N., and Trujillo, I. (2001). A Correlation between Galaxy Light Concentration and Supermassive Black Hole Mass. *The Astrophysical Journal Letters*, 563:L11–L14. xx, 74, 76

Grupe, D., Nousek, J. A., Veres, P., Zhang, B.-B., and Gehrels, N. (2013). Evidence for New Relations between Gamma-Ray Burst Prompt and X-Ray Afterglow Emission from 9 Years of Swift. *The Astrophysical Journal Supplement*, 209:20. 131

Haardt, F. and Maraschi, L. (1993). X-ray spectra from two-phase accretion disks. *The Astrophysical Journal*, 413:507–517. 58

Haehnelt, M. G. and Rees, M. J. (1993). The formation of nuclei in newly formed galaxies and the evolution of the quasar population. *Monthly Notices of the Royal Astronomical Society*, 263:168–178. 56

Häring, N. and Rix, H.-W. (2004). On the Black Hole Mass-Bulge Mass Relation. *The Astrophysical Journal Letters*, 604:L89–L92. xix, 73, 74

Harms, R. J., Ford, H. C., Tsvetanov, Z. I., Hartig, G. F., Dressel, L. L., Kriss, G. A., Bohlin, R., Davidsen, A. F., Margon, B., and Kochhar, A. K. (1994). HST FOS spectroscopy of M87: Evidence for a disk of ionized gas around a massive black hole. *The Astrophysical Journal Letters*, 435:L35–L38. 55

Heise, J., Zand, J. I., Kippen, R. M., and Woods, P. M. (2001). X-Ray Flashes and X-Ray Rich Gamma Ray Bursts. In Costa, E., Frontera, F., and Hjorth, J., editors, *Gamma-ray Bursts in the Afterglow Era*, page 16. xxiii, 115, 116, 117, 118, 119, 121, 138

Helou, G., Madore, B. F., Schmitz, M., Bicay, M. D., Wu, X., and Bennett, J. (1991). The NASA/IPAC extragalactic database. In Albrecht, M. A. and Egret, D., editors, *Databases and On-line Data in Astronomy*, volume 171 of *Astrophysics and Space Science Library*, pages 89–106. 133, 168

Hilton, M., Romer, A. K., Kay, S. T., Mehrtens, N., Lloyd-Davies, E. J., Thomas, P. A., Short, C. J., Mayers, J. A., Rooney, P. J., Stott, J. P., Collins, C. A., Harrison, C. D., Hoyle, B., Liddle, A. R., Mann, R. G., Miller, C. J., Sahlén, M., Viana, P. T. P., Davidson, M., Hosmer, M., Nichol, R. C., Sabirli, K., Stanford, S. A., and West, M. J. (2012). The XMM Cluster Survey: evidence for energy injection at high redshift from evolution of the X-ray luminosity-temperature relation. *Monthly Notices of the Royal Astronomical Society*, 424:2086–2096. 183

Hofmann, F., Sanders, J. S., Nandra, K., Clerc, N., and Gaspari, M. (2016). 7.1 keV sterile neutrino constraints from X-ray observations of 33 clusters of galaxies with Chandra ACIS. *Astronomy and Astrophysics*, 592:A112. 156

Hubble, E. (1929). A Relation between Distance and Radial Velocity among Extra-Galactic Nebulae. *Proceedings of the National Academy of Science*, 15:168–173. 3

IceCube Collaboration, Achterberg, A., Ackermann, M., Adams, J., Ahrens, J., Andeen, K., Atlee, D. W., Baccus, J., Bahcall, J. N., Bai, X., and et al. (2006). First year performance of the IceCube neutrino telescope. *Astroparticle Physics*, 26:155–173. 22

Irwin, J. A., Maksym, W. P., Sivakoff, G. R., Romanowsky, A. J., Lin, D., Speegle, T., Prado, I., Mildebrath, D., Strader, J., Liu, J., and Miller, J. M. (2016). Ultraluminous X-ray bursts in two ultracompact companions to nearby elliptical galaxies. *Nature*, 538:356–358. 130

Jeltema, T. and Profumo, S. (2015). Discovery of a 3.5 keV line in the Galactic Centre and a critical look at the origin of the line across astronomical targets. *Monthly Notices of the Royal Astronomical Society*, 450:2143–2152. 155

Kamizasa, N., Terashima, Y., and Awaki, H. (2012). A New Sample of Candidate Intermediate-mass Black Holes Selected by X-Ray Variability. *The Astrophysical Journal*, 751:39. 83, 87

Kaspi, S., Smith, P. S., Netzer, H., Maoz, D., Jannuzi, B. T., and Giveon, U. (2000). Reverberation Measurements for 17 Quasars and the Size-Mass-Luminosity Relations in Active Galactic Nuclei. *The Astrophysical Journal*, 533:631–649. 62

Kelly, B. C. (2007). Some Aspects of Measurement Error in Linear Regression of Astronomical Data. *The Astrophysical Journal*, 665:1489–1506. 92

Kelly, B. C., Sobolewska, M., and Siemiginowska, A. (2011). A Stochastic Model for the Luminosity Fluctuations of Accreting Black Holes. *The Astrophysical Journal*, 730:52. 64

Kelly, B. C., Treu, T., Malkan, M., Pancoast, A., and Woo, J.-H. (2013). Active Galactic Nucleus Black Hole Mass Estimates in the Era of Time Domain Astronomy. *The Astrophysical Journal*, 779:187. xix, 68, 69, 71

Klypin, A., Kravtsov, A. V., Valenzuela, O., and Prada, F. (1999). Where Are the Missing Galactic Satellites? *The Astrophysical Journal*, 522:82–92. 153

Körding, E. G., Migliari, S., Fender, R., Belloni, T., Knigge, C., and McHardy, I. (2007). The variability plane of accreting compact objects. *Monthly Notices of the Royal Astronomical Society*, 380:301–310. 65

Kormendy, J. and Ho, L. C. (2013). Coevolution (Or Not) of Supermassive Black Holes and Host Galaxies. *Annual review of astronomy and astrophysics*, 51:511–653. 71, 74, 76

Kozłowski, S. (2016). Virial Black Hole Mass Estimates for 280,000 AGNs from the SDSS Broad-Band Photometry and Single Epoch Spectra. *ArXiv e-prints*. 81

Kuntz, K. D. and Snowden, S. L. (2008). The EPIC-MOS particle-induced background spectra. *Astronomy and Astrophysics*, 478:575–596. xvii, 45

Kuo, C. Y., Braatz, J. A., Condon, J. J., Impellizzeri, C. M. V., Lo, K. Y., Zaw, I., Schenker, M., Henkel, C., Reid, M. J., and Greene, J. E. (2011). The Megamaser Cosmology Project. III. Accurate Masses of Seven Supermassive Black Holes in Active Galaxies with Circumnuclear Megamaser Disks. *The Astrophysical Journal*, 727:20. 60

Law, N. M., Rutledge, R. E., and Kulkarni, S. R. (2004). A search for X-ray flashes with XMM-Newton. *Monthly Notices of the Royal Astronomical Society*, 350:1079–1086. xxiii, xxiv, xxv, 119, 120, 130, 132, 144

Lawrence, A. (1991). The relative frequency of broad-lined and narrow-lined active galactic nuclei - Implications for unified schemes. *Monthly Notices of the Royal Astronomical Society*, 252:586–592. 15

Lawrence, A. and Papadakis, I. (1993). X-ray variability of active galactic nuclei - A universal power spectrum with luminosity-dependent amplitude. *The Astrophysical Journal Letters*, 414:L85–L88. 65, 94

Lemson, G. and Virgo Consortium, t. (2006). Halo and Galaxy Formation Histories from the Millennium Simulation: Public release of a VO-oriented and SQL-queryable database for studying the evolution of galaxies in the LambdaCDM cosmogony. *ArXiv Astrophysics e-prints*. 150

Lewin, W. H. G., van Paradijs, J., and Taam, R. E. (1995). X-ray bursts. *X-ray Binaries*, pages 175–232. 116

Lingam, M. and Loeb, A. (2017). Fast Radio Bursts from Extragalactic Light Sails. *The Astrophysical Journal Letters*, 837:L23. 22

Lloyd-Davies, E. J., Romer, A. K., Mehrtens, N., Hosmer, M., Davidson, M., Sabirli, K., Mann, R. G., Hilton, M., Liddle, A. R., Viana, P. T. P., Campbell, H. C., Collins, C. A., Dubois, E. N., Freeman, P., Harrison, C. D., Hoyle, B., Kay, S. T., Kuwertz, E., Miller, C. J., Nichol, R. C., Sahlén, M., Stanford, S. A., and Stott, J. P. (2011). The XMM Cluster Survey: X-ray analysis methodology. *Monthly Notices of the Royal Astronomical Society*, 418:14–53. 36, 43

Lo, K. K., Farrell, S., Murphy, T., and Gaensler, B. M. (2014). Automatic Classification of Time-variable X-Ray Sources. *The Astrophysical Journal*, 786:20. xv, xxiii, 17, 123

Lorimer, D. R., Bailes, M., McLaughlin, M. A., Narkevic, D. J., and Crawford, F. (2007). A Bright Millisecond Radio Burst of Extragalactic Origin. *Science*, 318:777. 22

Ludlam, R. M., Cackett, E. M., Gültekin, K., Fabian, A. C., Gallo, L., and Miniutti, G. (2015). X-ray spectral and variability properties of low-mass active galactic nuclei. *Monthly Notices of the Royal Astronomical Society*, 447:2112–2122. xix, 72

Lumb, D. H., Warwick, R. S., Page, M., and De Luca, A. (2002). X-ray background measurements with XMM-Newton EPIC. *Astronomy and Astrophysics*, 389:93–105. 13

Magorrian, J., Tremaine, S., Richstone, D., Bender, R., Bower, G., Dressler, A., Faber, S. M., Gebhardt, K., Green, R., Grillmair, C., Kormendy, J., and Lauer, T. (1998). The Demography of Massive Dark Objects in Galaxy Centers. *The Astronomical Journal*, 115:2285–2305. 73

Malyshev, D., Neronov, A., and Eckert, D. (2014). Constraints on 3.55 keV line emission from stacked observations of dwarf spheroidal galaxies. *Physical Review D*, 90(10):103506. 155

Manne-Nicholas, E., Batiste, M., Valluri, M., Bentz, M. C., Onken, C. A., and Ferrarese, L. (2016). A Stellar Dynamical Black Hole Mass for Broad-Lined Seyfert Galaxy NGC 6814 and Comparison to Results from Reverberation Mapping. In *American Astronomical Society Meeting Abstracts*, volume 227 of *American Astronomical Society Meeting Abstracts*, page 104.08. 62

Mantz, A., Allen, S. W., Ebeling, H., Rapetti, D., and Drlica-Wagner, A. (2010). The observed growth of massive galaxy clusters - II. X-ray scaling relations. *Monthly Notices of the Royal Astronomical Society*, 406:1773–1795. 18

Mantz, A. B., Allen, S. W., Morris, R. G., von der Linden, A., Applegate, D. E., Kelly, P. L., Burke, D. L., Donovan, D., and Ebeling, H. (2016). Weighing the giants- V. Galaxy cluster scaling relations. *Monthly Notices of the Royal Astronomical Society*, 463:3582–3603. 18

Marconi, A. and Hunt, L. K. (2003). The Relation between Black Hole Mass, Bulge Mass, and Near-Infrared Luminosity. *The Astrophysical Journal Letters*, 589:L21–L24. xix, 73, 74

Marin, F. (2016). Are there reliable methods to estimate the nuclear orientation of Seyfert galaxies? *Monthly Notices of the Royal Astronomical Society*, 460:3679–3705. 15

Markevitch, M., Randall, S., Clowe, D., Gonzalez, A., and Bradac, M. (2006). Dark matter

and the bullet cluster. In *36th COSPAR Scientific Assembly*, volume 36 of *COSPAR Meeting*. 147

Markowitz, A., Edelson, R., Vaughan, S., Uttley, P., George, I. M., Griffiths, R. E., Kaspi, S., Lawrence, A., McHardy, I., Nandra, K., Pounds, K., Reeves, J., Schurch, N., and Warwick, R. (2003). X-Ray Fluctuation Power Spectral Densities of Seyfert 1 Galaxies. *The Astrophysical Journal*, 593:96–114. xviii, 65, 66

Marziani, P. and Sulentic, J. W. (2012). Estimating black hole masses in quasars using broad optical and UV emission lines. *New Astronomy Reviews*, 56:49–63. xviii, 63

Mathur, S., Wilkes, B., and Elvis, M. (1998). Discovery of Associated Absorption LInes in an X-Ray Warm Absorber: Hubble Space Telescope Observations of PG 1114+445. *The Astrophysical Journal Letters*, 503:L23–L26. 15

Matsuoka, M., Kawasaki, K., Ueno, S., Tomida, H., Kohama, M., Suzuki, M., Adachi, Y., Ishikawa, M., Mihara, T., Sugizaki, M., Isobe, N., Nakagawa, Y., Tsunemi, H., Miyata, E., Kawai, N., Kataoka, J., Morii, M., Yoshida, A., Negoro, H., Nakajima, M., Ueda, Y., Chujo, H., Yamaoka, K., Yamazaki, O., Nakahira, S., You, T., Ishiwata, R., Miyoshi, S., Eguchi, S., Hiroi, K., Katayama, H., and Ebisawa, K. (2009). The MAXI Mission on the ISS: Science and Instruments for Monitoring All-Sky X-Ray Images. *Publications of the Astronomical Society of Japan*, 61:999–1010. 19

Maughan, B. J., Giles, P. A., Randall, S. W., Jones, C., and Forman, W. R. (2012). Self-similar scaling and evolution in the galaxy cluster X-ray luminosity-temperature relation. *Monthly Notices of the Royal Astronomical Society*, 421:1583–1602. 192

Mayers, J. A., Romer, K., Fahari, A., Stott, J. P., Giles, P., Rooney, P. J., Bermeo-Hernandez, A., Collins, C. A., Hilton, M., Hoyle, B., Liddle, A. R., Mann, R. G., Miller, C. J., Nichol, R. C., Sahlén, M., Vergara-Cervantes, C., and Viana, P. T. P. (2018). Correlations between X-ray properties and Black Hole Mass in AGN: towards a new method to estimate black hole mass from short exposure X-ray observations. *ArXiv e-prints*. 79

McConnell, N. J. and Ma, C.-P. (2013). Revisiting the Scaling Relations of Black Hole Masses and Host Galaxy Properties. *The Astrophysical Journal*, 764:184. 59

McHardy, I. M., Koerding, E., Knigge, C., Uttley, P., and Fender, R. P. (2006). Active galactic nuclei as scaled-up Galactic black holes. *Nature*, 444:730–732. 65

McLure, R. J. and Dunlop, J. S. (2002). On the black hole-bulge mass relation in active and inactive galaxies. *Monthly Notices of the Royal Astronomical Society*, 331:795–804. 74

Mehrtens, N., Romer, A. K., Hilton, M., Lloyd-Davies, E. J., Miller, C. J., Stanford, S. A., Hosmer, M., Hoyle, B., Collins, C. A., Liddle, A. R., Viana, P. T. P., Nichol, R. C., Stott, J. P., Dubois, E. N., Kay, S. T., Sahlén, M., Young, O., Short, C. J., Christodoulou, L., Watson, W. A., Davidson, M., Harrison, C. D., Baruah, L., Smith, M., Burke, C., Mayers, J. A., Deadman, P.-J., Rooney, P. J., Edmondson, E. M., West, M., Campbell, H. C., Edge, A. C., Mann, R. G., Sabirli, K., Wake, D., Benoist, C., da Costa, L., Maia, M. A. G., and Ogando, R. (2012). The XMM Cluster Survey: optical analysis methodology and the first data release. *Monthly Notices of the Royal Astronomical Society*, 423:1024–1052. xxx, 185, 189, 191, 192

Mehrtens, N., Romer, A. K., Lloyd-Davies, E. J., Hilton, M., Miller, C. J., Stanford, S. A., Hosmer, M., Hoyle, B., Collins, C. A., Liddle, A. R., Viana, P. T. P., Nichol, R. C., Stott, J. P., Dubois, E. N., Kay, S. T., Sahlen, M., Young, O., Short, C. J., Christodoulou, L., Watson, W. A., Davidson, M., Harrison, C. D., Baruah, L., Smith, M., Burke, C., Deadman, P.-J., Rooney, P. J., Edmondson, E. M., West, M., Campbell, H. C., Edge, A. C., Mann, R. G., Wake, D., Benoist, C., da Costa, L., Maia, M. A. G., and Ogando, R. (2011). The XMM Cluster Survey: Optical analysis methodology and the first data release. *ArXiv e-prints*. 47

Mehrtens, N., Romer, A. K., Nichol, R. C., Collins, C. A., Sahlén, M., Rooney, P. J., Mayers, J. A., Bermeo-Hernandez, A., Bristow, M., Capozzi, D., Christodoulou, L., Comparat, J., Hilton, M., Hoyle, B., Kay, S. T., Liddle, A. R., Mann, R. G., Masters, K., Miller, C. J., Parejko, J. K., Prada, F., Ross, A. J., Schneider, D. P., Stott, J. P., Streblyanska, A., Viana, P. T. P., White, M., Wilcox, H., and Zehavi, I. (2016). The XMM Cluster Survey: the halo occupation number of BOSS galaxies in X-ray clusters. *Monthly Notices of the Royal Astronomical Society*, 463:1929–1943. xxix, 183, 186

Merloni, A., Predehl, P., Becker, W., Böhringer, H., Boller, T., Brunner, H., Brusa, M., Dennerl, K., Freyberg, M., Friedrich, P., Georgakakis, A., Haberl, F., Hasinger, G., Meidinger, N., Mohr, J., Nandra, K., Rau, A., Reiprich, T. H., Robrade, J., Salvato, M., Santangelo, A., Sasaki, M., Schwope, A., Wilms, J., and German eROSITA Consortium, t. (2012). eROSITA Science Book: Mapping the Structure of the Energetic Universe. *ArXiv e-prints*. 107

Merritt, D. and Ferrarese, L. (2001). The M-σ Relation for Supermassive Black Holes. *The Astrophysical Journal*, 547:140–145. 74

Middei, R., Vagnetti, F., Antonucci, M., and Serafinelli, R. (2016). A new approach to the variability characterization of active galactic nuclei. *Journal of Physics Conference Series*, 689(1):012006. 69

Milgrom, M. (2008). Marriage à-la-MOND: Baryonic dark matter in galaxy clusters and the cooling flow puzzle. *New Astronomy Reviews*, 51:906–915. 149

Miller, M. C. and Hamilton, D. P. (2002). Production of intermediate-mass black holes in globular clusters. *Monthly Notices of the Royal Astronomical Society*, 330:232–240. 56

Mushotzky, R. F., Done, C., and Pounds, K. A. (1993). X-ray spectra and time variability of active galactic nuclei. *Annual review of astronomy and astrophysics*, 31:717–761. 47

Nandra, K. (2011). ATHENA: The Advanced Telescope for High Energy Astrophysics. In Ness, J.-U. and Ehle, M., editors, *The X-ray Universe 2011*, page 022. 35

Nandra, K., George, I. M., Mushotzky, R. F., Turner, T. J., and Yaqoob, T. (1997). ASCA Observations of Seyfert 1 Galaxies. I. Data Analysis, Imaging, and Timing. *The Astrophysical Journal*, 476:70–82. 67

Nandra, K. and Pounds, K. A. (1994). GINGA Observations of the X-Ray Spectra of Seyfert Galaxies. *Monthly Notices of the Royal Astronomical Society*, 268:405. 16, 88

Neronov, A., Malyshev, D., and Eckert, D. (2016). Decaying dark matter search with NuSTAR deep sky observations. *Physical Review D*, 94(12):123504. 157

O'Brien, P. T. and Smartt, S. J. (2013). Interpreting signals from astrophysical transient experiments. *Philosophical Transactions of the Royal Society of London Series A*, 371:20120498–20120498. xvi, 21

O'Neill, P. M., Nandra, K., Papadakis, I. E., and Turner, T. J. (2005). The relationship between X-ray variability amplitude and black hole mass in active galactic nuclei. *Monthly Notices of the Royal Astronomical Society*, 358:1405–1416. 69, 82, 89, 94, 99

Onken, C. A., Valluri, M., Peterson, B. M., Pogge, R. W., Bentz, M. C., Ferrarese, L., Vestergaard, M., Crenshaw, D. M., Sergeev, S. G., McHardy, I. M., Merritt, D., Bower, G. A., Heckman, T. M., and Wandel, A. (2007). The Black Hole Mass of NGC

4151: Comparison of Reverberation Mapping and Stellar Dynamical Measurements. *The Astrophysical Journal*, 670:105–115. 62

Oppenheimer, J. R. and Serber, R. (1938). On the Stability of Stellar Neutron Cores. *Physical Review*, 54:540–540. 55

Osterbrock, D. E. (1974). *Astrophysics of gaseous nebulae*. 9

Padovani, P. (1989). The evolution of the Eddington ratio for active galactic nuclei. *Astronomy and Astrophysics*, 209:27–45. 64

Padovani, P. and Rafanelli, P. (1988). Mass-luminosity relationships and accretion rates for Seyfert 1 galaxies and quasars. *Astronomy and Astrophysics*, 205:53–70. 64

Pan, H., Yuan, W., Zhou, X.-L., Dong, X., and Liu, B. (2016). On the relationship between black hole mass and X-ray variability amplitude in the low-mass regime of active galactic nuclei. In Meiron, Y., Li, S., Liu, F.-K., and Spurzem, R., editors, *Star Clusters and Black Holes in Galaxies across Cosmic Time*, volume 312 of *IAU Symposium*, pages 73–74. xix, 71, 72

Papadakis, I. E. (2004). The scaling of the X-ray variability with black hole mass in active galactic nuclei. *Monthly Notices of the Royal Astronomical Society*, 348:207–213. 69

Parejko, J. K., Constantin, A., Vogeley, M. S., and Hoyle, F. (2008). Source Matching in the SDSS and Rass: which Galaxies are Really X-Ray Sources? *The Astronomical Journal*, 135:10–19. 184

Peebles, P. J. and Ratra, B. (2003). The cosmological constant and dark energy. *Reviews of Modern Physics*, 75:559–606. 5

Perlmutter, S., Aldering, G., Goldhaber, G., Knop, R. A., Nugent, P., Castro, P. G., Deustua, S., Fabbro, S., Goobar, A., Groom, D. E., Hook, I. M., Kim, A. G., Kim, M. Y., Lee, J. C., Nunes, N. J., Pain, R., Pennypacker, C. R., Quimby, R., Lidman, C., Ellis, R. S., Irwin, M., McMahon, R. G., Ruiz-Lapuente, P., Walton, N., Schaefer, B., Boyle, B. J., Filippenko, A. V., Matheson, T., Fruchter, A. S., Panagia, N., Newberg, H. J. M., Couch, W. J., and Project, T. S. C. (1999). Measurements of Ω and Λ from 42 High-Redshift Supernovae. *The Astrophysical Journal*, 517:565–586. 4

Peterson, B. M. (2003). Masses of Supermassive Black Holes in Active Galactic Nuclei. In Collin, S., Combes, F., and Shlosman, I., editors, *Active Galactic Nuclei: From Central*

Engine to Host Galaxy, volume 290 of *Astronomical Society of the Pacific Conference Series*, page 43. xviii, 61

Peterson, B. M., Ferrarese, L., Gilbert, K. M., Kaspi, S., Malkan, M. A., Maoz, D., Merritt, D., Netzer, H., Onken, C. A., Pogge, R. W., Vestergaard, M., and Wandel, A. (2004). Central Masses and Broad-Line Region Sizes of Active Galactic Nuclei. II. A Homogeneous Analysis of a Large Reverberation-Mapping Database. *The Astrophysical Journal*, 613:682–699. 60

Planck Collaboration, Ade, P. A. R., Aghanim, N., Armitage-Caplan, C., Arnaud, M., Ashdown, M., Atrio-Barandela, F., Aumont, J., Baccigalupi, C., Banday, A. J., and et al. (2014). Planck 2013 results. XVI. Cosmological parameters. *Astronomy and Astrophysics*, 571:A16. 150

Planck Collaboration, Ade, P. A. R., Aghanim, N., Arnaud, M., Ashdown, M., Aumont, J., Baccigalupi, C., Banday, A. J., Barreiro, R. B., Bartlett, J. G., and et al. (2016). Planck 2015 results. XIII. Cosmological parameters. *Astronomy and Astrophysics*, 594:A13. 7

Ponti, G., Papadakis, I., Bianchi, S., Guainazzi, M., Matt, G., Uttley, P., and Bonilla, N. F. (2012). CAIXA: a catalogue of AGN in the XMM-Newton archive. III. Excess variance analysis. *Astronomy and Astrophysics*, 542:A83. xix, xxi, 64, 69, 70, 72, 82, 89, 94, 98, 103, 104

Popov, S. B. and Postnov, K. A. (2010). Hyperflares of SGRs as an engine for millisecond extragalactic radio bursts. In Harutyunian, H. A., Mickaelian, A. M., and Terzian, Y., editors, *Evolution of Cosmic Objects through their Physical Activity*, pages 129–132. 22

Predehl, P., Andritschke, R., Böhringer, H., Bornemann, W., Bräuninger, H., Brunner, H., Brusa, M., Burkert, W., Burwitz, V., Cappelluti, N., Churazov, E., Dennerl, K., Eder, J., Elbs, J., Freyberg, M., Friedrich, P., Fürmetz, M., Gaida, R., Hälker, O., Hartner, G., Hasinger, G., Hermann, S., Huber, H., Kendziorra, E., von Kienlin, A., Kink, W., Kreykenbohm, I., Lamer, G., Lapchov, I., Lehmann, K., Meidinger, N., Mican, B., Mohr, J., Mühlegger, M., Müller, S., Nandra, K., Pavlinsky, M., Pfeffermann, E., Reiprich, T., Robrade, J., Rohé, C., Santangelo, A., Schächner, G., Schanz, T., Schmid, C., Schmitt, J., Schreib, R., Schrey, F., Schwope, A., Steinmetz, M., Strüder, L., Sunyaev, R., Tenzer, C., Tiedemann, L., Vongehr, M., and Wilms, J. (2010). eROSITA on SRG. In *Space Telescopes and Instrumentation 2010: Ultraviolet to Gamma Ray*, volume 7732 of *Proceedings of the SPIE*, page 77320U. 20, 35

Rees, M. J. (1984). Black Hole Models for Active Galactic Nuclei. *Annual review of astronomy and astrophysics*, 22:471–506. 16

Ricci, C. (2011). *Active Galactic Nuclei at hard X-ray energies: Absorbption, Reflection and the Unified Model*. PhD thesis, Univsersity of Geneva. xviii, 59

Riess, A. G., Macri, L. M., Hoffmann, S. L., Scolnic, D., Casertano, S., Filippenko, A. V., Tucker, B. E., Reid, M. J., Jones, D. O., Silverman, J. M., Chornock, R., Challis, P., Yuan, W., Brown, P. J., and Foley, R. J. (2016). A 2.4% Determination of the Local Value of the Hubble Constant. *The Astrophysical Journal*, 826:56. 7

Romer, A. K., Viana, P. T. P., Liddle, A. R., and Mann, R. G. (2001). A Serendipitous Galaxy Cluster Survey with XMM: Expected Catalog Properties and Scientific Applications. *The Astrophysical Journal*, 547:594–608. 2, 41, 159

Rooney, P. (2016). *XCS, A New Catalogue and Applications*. PhD thesis, Univsersity of Sussex. xvi, xvii, 42, 43, 47, 49

Rosen, S. R., Webb, N. A., Watson, M. G., Ballet, J., Barret, D., Braito, V., Carrera, F. J., Ceballos, M. T., Coriat, M., Della Ceca, R., Denkinson, G., Esquej, P., Farrell, S. A., Freyberg, M., Grisé, F., Guillout, P., Heil, L., Koliopanos, F., Law-Green, D., Lamer, G., Lin, D., Martino, R., Michel, L., Motch, C., Nebot Gomez-Moran, A., Page, C. G., Page, K., Page, M., Pakull, M. W., Pye, J., Read, A., Rodriguez, P., Sakano, M., Saxton, R., Schwope, A., Scott, A. E., Sturm, R., Traulsen, I., Yershov, V., and Zolotukhin, I. (2016). The XMM-Newton serendipitous survey. VII. The third XMM-Newton serendipitous source catalogue. *Astronomy and Astrophysics*, 590:A1. 138

Rykoff, E. S., Rozo, E., Busha, M. T., Cunha, C. E., Finoguenov, A., Evrard, A., Hao, J., Koester, B. P., Leauthaud, A., Nord, B., Pierre, M., Reddick, R., Sadibekova, T., Sheldon, E. S., and Wechsler, R. H. (2014). redMaPPer. I. Algorithm and SDSS DR8 Catalog. *The Astrophysical Journal*, 785:104. xxvi, 105, 160

Rykoff, E. S., Rozo, E., Hollowood, D., Bermeo-Hernandez, A., Jeltema, T., Mayers, J., Romer, A. K., Rooney, P., Saro, A., Vergara Cervantes, C., Wechsler, R. H., Wilcox, H., Abbott, T. M. C., Abdalla, F. B., Allam, S., Annis, J., Benoit-Lévy, A., Bernstein, G. M., Bertin, E., Brooks, D., Burke, D. L., Capozzi, D., Carnero Rosell, A., Carrasco Kind, M., Castander, F. J., Childress, M., Collins, C. A., Cunha, C. E., D'Andrea, C. B., da Costa, L. N., Davis, T. M., Desai, S., Diehl, H. T., Dietrich, J. P., Doel, P., Evrard, A. E., Finley, D. A., Flaugher, B., Fosalba, P., Frieman, J., Glazebrook, K., Goldstein,

D. A., Gruen, D., Gruendl, R. A., Gutierrez, G., Hilton, M., Honscheid, K., Hoyle, B., James, D. J., Kay, S. T., Kuehn, K., Kuropatkin, N., Lahav, O., Lewis, G. F., Lidman, C., Lima, M., Maia, M. A. G., Mann, R. G., Marshall, J. L., Martini, P., Melchior, P., Miller, C. J., Miquel, R., Mohr, J. J., Nichol, R. C., Nord, B., Ogando, R., Plazas, A. A., Reil, K., Sahlén, M., Sanchez, E., Santiago, B., Scarpine, V., Schubnell, M., Sevilla-Noarbe, I., Smith, R. C., Soares-Santos, M., Sobreira, F., Stott, J. P., Suchyta, E., Swanson, M. E. C., Tarle, G., Thomas, D., Tucker, D., Uddin, S., Viana, P. T. P., Vikram, V., Walker, A. R., Zhang, Y., and DES Collaboration (2016). The RedMaPPer Galaxy Cluster Catalog From DES Science Verification Data. *The Astrophysical Journal Supplement*, 224:1. xxx, 184, 188

Sakamoto, T., Lamb, D. Q., Graziani, C., Donaghy, T. Q., Suzuki, M., Ricker, G., Atteia, J.-L., Kawai, N., Yoshida, A., Shirasaki, Y., Tamagawa, T., Torii, K., Matsuoka, M., Fenimore, E. E., Galassi, M., Tavenner, T., Doty, J., Vanderspek, R., Crew, G. B., Villasenor, J., Butler, N., Prigozhin, G., Jernigan, J. G., Barraud, C., Boer, M., Dezalay, J.-P., Olive, J.-F., Hurley, K., Levine, A., Monnelly, G., Martel, F., Morgan, E., Woosley, S. E., Cline, T., Braga, J., Manchanda, R., Pizzichini, G., Takagishi, K., and Yamauchi, M. (2004). High Energy Transient Explorer 2 Observations of the Extremely Soft X-Ray Flash XRF 020903. *The Astrophysical Journal*, 602:875–885. 116

Sambruna, R. M., Eracleous, M., and Mushotzky, R. F. (1999). An X-Ray Spectral Survey of Radio-loud Active Galactic Nuclei with ASCA. *The Astrophysical Journal*, 526:60–96. 17

Sanders, W. T., Kraushaar, W. L., Nousek, J. A., and Fried, P. M. (1977). Soft diffuse X-rays in the southern galactic hemisphere. *The Astrophysical Journal Letters*, 217:L87–L91. 13

Schmidt, B. P., Suntzeff, N. B., Phillips, M. M., Schommer, R. A., Clocchiatti, A., Kirshner, R. P., Garnavich, P., Challis, P., Leibundgut, B., Spyromilio, J., Riess, A. G., Filippenko, A. V., Hamuy, M., Smith, R. C., Hogan, C., Stubbs, C., Diercks, A., Reiss, D., Gilliland, R., Tonry, J., Maza, J., Dressler, A., Walsh, J., and Ciardullo, R. (1998). The High-Z Supernova Search: Measuring Cosmic Deceleration and Global Curvature of the Universe Using Type IA Supernovae. *The Astrophysical Journal*, 507:46–63. 4

Schwartz, D. A. (2014). Invited Review Article: The Chandra X-ray Observatory. *Review of Scientific Instruments*, 85(6):061101. 32

Schwarzschild, K. (1916). Über das Gravitationsfeld einer Kugel aus inkompressibler Flüssigkeit nach der Einsteinschen Theorie. In *Sitzungsberichte der Königlich Preussischen Akademie der Wissenschaften zu Berlin, Phys.-Math. Klasse, 424-434 (1916)*. 54

Seyfert, C. K. (1943). Nuclear Emission in Spiral Nebulae. *The Astrophysical Journal*, 97:28. 55

Shen, Y., Greene, J. E., Strauss, M. A., Richards, G. T., and Schneider, D. P. (2008). Biases in Virial Black Hole Masses: An SDSS Perspective. *The Astrophysical Journal*, 680:169–190. 112

Shlosman, I., Frank, J., and Begelman, M. C. (1989). Bars within bars - A mechanism for fuelling active galactic nuclei. *Nature*, 338:45–47. 56

Silk, J. and Rees, M. J. (1998). Quasars and galaxy formation. *Astronomy and Astrophysics*, 331:L1–L4. 56

Simm, T., Salvato, M., Saglia, R., Ponti, G., Lanzuisi, G., Trakhtenbrot, B., Nandra, K., and Bender, R. (2016). Pan-STARRS1 variability of XMM-COSMOS AGN. II. Physical correlations and power spectrum analysis. *Astronomy and Astrophysics*, 585:A129. xix, 67, 68, 69

Skrutskie, M. F., Cutri, R. M., Stiening, R., Weinberg, M. D., Schneider, S., Carpenter, J. M., Beichman, C., Capps, R., Chester, T., Elias, J., Huchra, J., Liebert, J., Lonsdale, C., Monet, D. G., Price, S., Seitzer, P., Jarrett, T., Kirkpatrick, J. D., Gizis, J. E., Howard, E., Evans, T., Fowler, J., Fullmer, L., Hurt, R., Light, R., Kopan, E. L., Marsh, K. A., McCallon, H. L., Tam, R., Van Dyk, S., and Wheelock, S. (2006). The Two Micron All Sky Survey (2MASS). *The Astronomical Journal*, 131:1163–1183. 133

Soderberg, A. M., Kulkarni, S. R., Berger, E., Fox, D. B., Price, P. A., Yost, S. A., Hunt, M. P., Frail, D. A., Walker, R. C., Hamuy, M., Shectman, S. A., Halpern, J. P., and Mirabal, N. (2004). A Redshift Determination for XRF 020903: First Spectroscopic Observations of an X-Ray Flash. *The Astrophysical Journal*, 606:994–999. 119

Spitler, L. G., Cordes, J. M., Hessels, J. W. T., Lorimer, D. R., McLaughlin, M. A., Chatterjee, S., Crawford, F., Deneva, J. S., Kaspi, V. M., Wharton, R. S., Allen, B., Bogdanov, S., Brazier, A., Camilo, F., Freire, P. C. C., Jenet, F. A., Karako-Argaman, C., Knispel, B., Lazarus, P., Lee, K. J., van Leeuwen, J., Lynch, R., Ransom, S. M.,

Scholz, P., Siemens, X., Stairs, I. H., Stovall, K., Swiggum, J. K., Venkataraman, A., Zhu, W. W., Aulbert, C., and Fehrmann, H. (2014). Fast Radio Burst Discovered in the Arecibo Pulsar ALFA Survey. *The Astrophysical Journal*, 790:101. 22

Strigari, L. E. (2013). Galactic searches for dark matter. *Physics Reports*, 531:1–88. 153

Terada, Y. and Dotani, T. (2010). The International X-ray Observatory and other X-ray missions, expectations for pulsar physics. *ArXiv e-prints*. xvi, 33

The Dark Energy Survey Collaboration (2005). The Dark Energy Survey. *ArXiv Astrophysics e-prints*. 133

Tie, S. S., Martini, P., Mudd, D., Ostrovski, F., Reed, S. L., Lidman, C., Kochanek, C., Davis, T. M., Sharp, R., Uddin, S., King, A., Wester, W., Tucker, B. E., Tucker, D. L., Buckley-Geer, E., Carollo, D., Childress, M., Glazebrook, K., Hinton, S. R., Lewis, G., Macaulay, E., O'Neill, C. R., Abbott, T. M. C., Abdalla, F. B., Annis, J., Benoit-L'evy, A., Bertin, E., Brooks, D., Carnero Rosell, A., Carrasco Kind, M., Carretero, J., Cunha, C. E., da Costa, L. N., DePoy, D. L., Desai, S., Doel, P., Eifler, T. F., Evrard, A. E., Finley, D. A., Flaugher, B., Fosalba, P., Frieman, J., Garcia-Bellido, J., Gaztanaga, E., Gerdes, D. W., Goldstein, D. A., Gruen, D., Gruendl, R. A., Gutierrez, G., Honscheid, K., James, D. J., Kuehn, K., Kuropatkin, N., Lima, M., Maia, M. A. G., Marshall, J. L., Menanteau, F., Miller, C. J., Miquel, R., Nichol, R. C., Nord, B., Ogando, R., Plazas, A. A., Romer, A. K., Sanchez, E., Santiago, B., Scarpine, V., Schubnell, M., Sevilla-Noarbe, I., Smith, R. C., Soares-Santos, M., Sobreira, F., Suchyta, E., Swanson, M. E. C., Tarle, G., Thomas, D., Walker, A. R., and The DES Collaboration (2016). A Study of Quasar Selection in the Dark Energy Survey Supernova fields. *ArXiv e-prints*. 112

Tremaine, S., Gebhardt, K., Bender, R., Bower, G., Dressler, A., Faber, S. M., Filippenko, A. V., Green, R., Grillmair, C., Ho, L. C., Kormendy, J., Lauer, T. R., Magorrian, J., Pinkney, J., and Richstone, D. (2002). The Slope of the Black Hole Mass versus Velocity Dispersion Correlation. *The Astrophysical Journal*, 574:740–753. 64, 74

Trujillo, I., Graham, A. W., and Caon, N. (2001). On the estimation of galaxy structural parameters: the Sérsic model. *Monthly Notices of the Royal Astronomical Society*, 326:869–876. 74

Turner, T. J., George, I. M., Nandra, K., and Turcan, D. (1999). On X-Ray Variability in Seyfert Galaxies. *The Astrophysical Journal*, 524:667–673. 67

Tyson, J. A. (2002). Large Synoptic Survey Telescope: Overview. In Tyson, J. A. and Wolff, S., editors, *Survey and Other Telescope Technologies and Discoveries*, volume 4836 of *Proceedings of the SPIE*, pages 10–20. 20

Umemura, M., Loeb, A., and Turner, E. L. (1993). Early Cosmic Formation of Massive Black Holes. *The Astrophysical Journal*, 419:459. 56

Urban, O., Werner, N., Allen, S. W., Simionescu, A., Kaastra, J. S., and Strigari, L. E. (2015). A Suzaku search for dark matter emission lines in the X-ray brightest galaxy clusters. *Monthly Notices of the Royal Astronomical Society*, 451:2447–2461. xxvi, 154, 156, 159, 168, 170, 171

Uttley, P., McHardy, I. M., and Papadakis, I. E. (2002). Measuring the broad-band power spectra of active galactic nuclei with RXTE. *Monthly Notices of the Royal Astronomical Society*, 332:231–250. xviii, 65, 66

Vagnetti, F., Turriziani, S., and Trevese, D. (2011). Ensemble X-ray variability of active galactic nuclei from serendipitous source catalogues. *Astronomy and Astrophysics*, 536:A84. 69

van der Klis, M. (1989). Fourier techniques in X-ray timing. In Ögelman, H. and van den Heuvel, E. P. J., editors, *NATO Advanced Science Institutes (ASI) Series C*, volume 262 of *NATO Advanced Science Institutes (ASI) Series C*, page 27. 67

van Haarlem, M. P., Wise, M. W., Gunst, A. W., Heald, G., McKean, J. P., Hessels, J. W. T., de Bruyn, A. G., Nijboer, R., Swinbank, J., Fallows, R., Brentjens, M., Nelles, A., Beck, R., Falcke, H., Fender, R., Hörandel, J., Koopmans, L. V. E., Mann, G., Miley, G., Röttgering, H., Stappers, B. W., Wijers, R. A. M. J., Zaroubi, S., van den Akker, M., Alexov, A., Anderson, J., Anderson, K., van Ardenne, A., Arts, M., Asgekar, A., Avruch, I. M., Batejat, F., Bähren, L., Bell, M. E., Bell, M. R., van Bemmel, I., Bennema, P., Bentum, M. J., Bernardi, G., Best, P., Bîrzan, L., Bonafede, A., Boonstra, A.-J., Braun, R., Bregman, J., Breitling, F., van de Brink, R. H., Broderick, J., Broekema, P. C., Brouw, W. N., Brüggen, M., Butcher, H. R., van Cappellen, W., Ciardi, B., Coenen, T., Conway, J., Coolen, A., Corstanje, A., Damstra, S., Davies, O., Deller, A. T., Dettmar, R.-J., van Diepen, G., Dijkstra, K., Donker, P., Doorduin, A., Dromer, J., Drost, M., van Duin, A., Eislöffel, J., van Enst, J., Ferrari, C., Frieswijk, W., Gankema, H., Garrett, M. A., de Gasperin, F., Gerbers, M., de Geus, E., Grießmeier, J.-M., Grit, T., Gruppen, P., Hamaker, J. P., Hassall, T., Hoeft, M., Holties, H. A.,

Horneffer, A., van der Horst, A., van Houwelingen, A., Huijgen, A., Iacobelli, M., Intema, H., Jackson, N., Jelic, V., de Jong, A., Juette, E., Kant, D., Karastergiou, A., Koers, A., Kollen, H., Kondratiev, V. I., Kooistra, E., Koopman, Y., Koster, A., Kuniyoshi, M., Kramer, M., Kuper, G., Lambropoulos, P., Law, C., van Leeuwen, J., Lemaitre, J., Loose, M., Maat, P., Macario, G., Markoff, S., Masters, J., McFadden, R. A., McKay-Bukowski, D., Meijering, H., Meulman, H., Mevius, M., Middelberg, E., Millenaar, R., Miller-Jones, J. C. A., Mohan, R. N., Mol, J. D., Morawietz, J., Morganti, R., Mulcahy, D. D., Mulder, E., Munk, H., Nieuwenhuis, L., van Nieuwpoort, R., Noordam, J. E., Norden, M., Noutsos, A., Offringa, A. R., Olofsson, H., Omar, A., Orrú, E., Overeem, R., Paas, H., Pandey-Pommier, M., Pandey, V. N., Pizzo, R., Polatidis, A., Rafferty, D., Rawlings, S., Reich, W., de Reijer, J.-P., Reitsma, J., Renting, G. A., Riemers, P., Rol, E., Romein, J. W., Roosjen, J., Ruiter, M., Scaife, A., van der Schaaf, K., Scheers, B., Schellart, P., Schoenmakers, A., Schoonderbeek, G., Serylak, M., Shulevski, A., Sluman, J., Smirnov, O., Sobey, C., Spreeuw, H., Steinmetz, M., Sterks, C. G. M., Stiepel, H.-J., Stuurwold, K., Tagger, M., Tang, Y., Tasse, C., Thomas, I., Thoudam, S., Toribio, M. C., van der Tol, B., Usov, O., van Veelen, M., van der Veen, A.-J., ter Veen, S., Verbiest, J. P. W., Vermeulen, R., Vermaas, N., Vocks, C., Vogt, C., de Vos, M., van der Wal, E., van Weeren, R., Weggemans, H., Weltevrede, P., White, S., Wijnholds, S. J., Wilhelmsson, T., Wucknitz, O., Yatawatta, S., Zarka, P., Zensus, A., and van Zwieten, J. (2013). LOFAR: The LOw-Frequency ARray. *Astronomy and Astrophysics*, 556:A2. 19

Vaughan, S., Edelson, R., Warwick, R. S., and Uttley, P. (2003a). On characterizing the variability properties of X-ray light curves from active galaxies. *Monthly Notices of the Royal Astronomical Society*, 345:1271–1284. 90

Vaughan, S., Fabian, A. C., and Nandra, K. (2003b). X-ray continuum variability of MCG-6-30-15. *Monthly Notices of the Royal Astronomical Society*, 339:1237–1255. 67, 90

Veron-Cetty, M. P. and Veron, P. (2010). VizieR Online Data Catalog: Quasars and Active Galactic Nuclei (13th Ed.) (Veron+ 2010). *VizieR Online Data Catalog*, 7258. 65, 80

Viana, P. T. P., da Silva, A., Ramos, E. P. R. G., Liddle, A. R., Lloyd-Davies, E. J., Romer, A. K., Kay, S. T., Collins, C. A., Hilton, M., Hosmer, M., Hoyle, B., Mayers, J. A., Mehrtens, N., Miller, C. J., Sahlén, M., Stanford, S. A., and Stott, J. P. (2012). The

XMM Cluster Survey: predicted overlap with the Planck Cluster Catalogue. *Monthly Notices of the Royal Astronomical Society*, 422:1007–1013. 183

Vikhlinin, A. (1998). A Search for X-Ray Counterparts of Gamma-Ray Bursts with the ROSAT PSPC. *The Astrophysical Journal Letters*, 505:L123–L126. xxiii, 119, 120, 144

Vikhlinin, A., Kravtsov, A., Forman, W., Jones, C., Markevitch, M., Murray, S. S., and Van Speybroeck, L. (2006). Chandra Sample of Nearby Relaxed Galaxy Clusters: Mass, Gas Fraction, and Mass-Temperature Relation. *The Astrophysical Journal*, 640:691–709. 18

Volonteri, M. (2010). Formation of supermassive black holes. *The Astronomy and Astrophysics Review*, 18:279–315. 55

Volonteri, M., Haardt, F., and Madau, P. (2003). The Assembly and Merging History of Supermassive Black Holes in Hierarchical Models of Galaxy Formation. *The Astrophysical Journal*, 582:559–573. 56

Wandel, A., Peterson, B. M., and Malkan, M. A. (1999). Central Masses and Broad-Line Region Sizes of Active Galactic Nuclei. I. Comparing the Photoionization and Reverberation Techniques. *The Astrophysical Journal*, 526:579–591. 62

Wang, J.-G., Dong, X.-B., Wang, T.-G., Ho, L. C., Yuan, W., Wang, H., Zhang, K., Zhang, S., and Zhou, H. (2009). Estimating Black Hole Masses in Active Galactic Nuclei Using the Mg II λ2800 Emission Line. *The Astrophysical Journal*, 707:1334–1346. 62

Watson, M. G., Schröder, A. C., Fyfe, D., Page, C. G., Lamer, G., Mateos, S., Pye, J., Sakano, M., Rosen, S., Ballet, J., Barcons, X., Barret, D., Boller, T., Brunner, H., Brusa, M., Caccianiga, A., Carrera, F. J., Ceballos, M., Della Ceca, R., Denby, M., Denkinson, G., Dupuy, S., Farrell, S., Fraschetti, F., Freyberg, M. J., Guillout, P., Hambaryan, V., Maccacaro, T., Mathiesen, B., McMahon, R., Michel, L., Motch, C., Osborne, J. P., Page, M., Pakull, M. W., Pietsch, W., Saxton, R., Schwope, A., Severgnini, P., Simpson, M., Sironi, G., Stewart, G., Stewart, I. M., Stobbart, A.-M., Tedds, J., Warwick, R., Webb, N., West, R., Worrall, D., and Yuan, W. (2009). The XMM-Newton serendipitous survey. V. The Second XMM-Newton serendipitous source catalogue. *Astronomy and Astrophysics*, 493:339–373. 65

Webb, N. and XMM-Newton Survey Science Centre, o. (2017). The 3XMM catalogue. In Ness, J.-U. and Migliari, S., editors, *The X-ray Universe 2017*, page 236. 129

Weinberg, S. (1977). *The First Three Minutes, A Modern View of the Origin of the Universe*. Basic Books. 1

Wenger, M., Ochsenbein, F., Egret, D., Dubois, P., Bonnarel, F., Borde, S., Genova, F., Jasniewicz, G., Laloë, S., Lesteven, S., and Monier, R. (2000). The SIMBAD astronomical database. The CDS reference database for astronomical objects. *Astronomy and Astrophysics Supplement Series*, 143:9–22. 92, 133

White, M., Blanton, M., Bolton, A., Schlegel, D., Tinker, J., Berlind, A., da Costa, L., Kazin, E., Lin, Y.-T., Maia, M., McBride, C. K., Padmanabhan, N., Parejko, J., Percival, W., Prada, F., Ramos, B., Sheldon, E., de Simoni, F., Skibba, R., Thomas, D., Wake, D., Zehavi, I., Zheng, Z., Nichol, R., Schneider, D. P., Strauss, M. A., Weaver, B. A., and Weinberg, D. H. (2011). The Clustering of Massive Galaxies at z ˜ 0.5 from the First Semester of BOSS Data. *The Astrophysical Journal*, 728:126. 184

Wilcox, H., Bacon, D., Nichol, R. C., Rooney, P. J., Terukina, A., Romer, A. K., Koyama, K., Zhao, G.-B., Hood, R., Mann, R. G., Hilton, M., Manolopoulou, M., Sahlén, M., Collins, C. A., Liddle, A. R., Mayers, J. A., Mehrtens, N., Miller, C. J., Stott, J. P., and Viana, P. T. P. (2015). The XMM Cluster Survey: testing chameleon gravity using the profiles of clusters. *Monthly Notices of the Royal Astronomical Society*, 452:1171–1183. xxx, 185, 189

Wilson, S., Hilton, M., Rooney, P. J., Caldwell, C., Kay, S. T., Collins, C. A., McCarthy, I. G., Romer, A. K., Bermeo, A., Bernstein, R., da Costa, L., Gifford, D., Hollowood, D., Hoyle, B., Jeltema, T., Liddle, A. R., Maia, M. A. G., Mann, R. G., Mayers, J. A., Mehrtens, N., Miller, C. J., Nichol, R. C., Ogando, R., Sahlén, M., Stahl, B., Stott, J. P., Thomas, P. A., Viana, P. T. P., and Wilcox, H. (2016). The XMM Cluster Survey: evolution of the velocity dispersion-temperature relation over half a Hubble time. *Monthly Notices of the Royal Astronomical Society*, 463:413–428. xxix, 184, 187

Wolter, H. (1952). Spiegelsysteme streifenden Einfalls als abbildende Optiken für Röntgenstrahlen. *Annalen der Physik*, 445:94–114. 28

Zhou, X.-L., Zhang, S.-N., Wang, D.-X., and Zhu, L. (2010). Calibrating the Correlation Between Black Hole Mass and X-ray Variability Amplitude: X-ray Only Black Hole Mass Estimates for Active Galactic Nuclei and Ultra-luminous X-ray Sources. *The Astrophysical Journal*, 710:16–23. xviii, 64, 65, 69, 82

Zwicky, F. (1933). Die Rotverschiebung von extragalaktischen Nebeln. *Helvetica Physica Acta*, 6:110–127. 17, 147

Appendix A

Metrics and Measuring Distances

A.1 Robertson-Walker Metric

Since the appearance of objects at cosmological distances depends on the curvature of spacetime, we must define a metric that describes how light propagates within our expanding isotropic and homogeneous Universe. This is the Roberston-Walker metric

$$ds^2 = -c^2dt^2 + a(t)^2\left(\frac{dr^2}{\sqrt{1-kr^2}}\right) + a(t)^2r^2\left(d\theta^2 + \sin^2\theta d\varphi^2\right) \tag{A.1}$$

where spherical polar co-ordinates have been used. The following distance measurements use this metric.

A.2 Measuring Distances

Central to any cosmological survey is the challenge of measuring distances to extra-Galactic objects. Not only does the vast size of the Universe makes accurate measurement difficult, but it is necessary to take into account an expanding universe where the expansion rate has been evolving. Assuming a flat model of the Universe simplifies the need to incorporate any curvature. As a result, we can define not one, but several distance scales each of which has their own use. A proper distance, a luminosity distance and an angular-diameter distance.

A.2.1 Proper distance

The proper distance to a galaxy is the actual distance if we could stop time and measure it with a ruler today. If the universe were static, it might seem that it would be much easier

to measure the distances between galaxies. However, the significant advantage that this expansion brings is to stamp a redshift onto the photons that we observe and from which we can make a first estimate at a distance. A naive approach would be to use Equations 1.2 and 1.3 to define the proper distance:

$$d_p = r = \frac{cz}{H_0} \tag{A.2}$$

However, this assumes a constant value for H rather than one that we know from the Friedman equation is time-dependent. At low redshift this approximation might not be a problem, but becomes more so at greater redshifts. Although the redshift cannot, therefore, tell us the proper distance to galaxies, it can give us the value of the scale factor a at the time that the light was emitted from that galaxy. From the definition of redshift in Equation 1.1 and general relativity (i.e. that light travels along null geodesics) we can express redshift of light from distant objects in terms of the scale factor as:

$$1 + z = \frac{a(t_0)}{a(t_e)} = \frac{1}{a(t_e)} \tag{A.3}$$

where t_0 and t_e are the current and time of emission.
From Equation A.1, assuming a flat Universe and setting $ds = 0$, gives:

$$\frac{cdt}{a(t)} = dr \tag{A.4}$$

and so the proper distance is the integral of this over the time taken for a photon to reach us i.e.:

$$\int_{t_e}^{t^r} \frac{cdt}{a(t)} \tag{A.5}$$

which, in a spatially flat universe, can be expressed in terms of the H and z:

$$\frac{c}{H_0} \int_0^x \frac{dz}{\sqrt{\Omega_M (1+z)^3 + \Omega_\Lambda}} \tag{A.6}$$

A.2.2 Luminosity distance

Since the proper distance for large redshifts is not something that is readily measurable, we look to measuring distances from an object's observable properties. The most obvious of these is its luminosity, from which we can define a **luminosity distance**, which is an indication of how far away an object appears based on its brightness. In a static universe,

using the inverse square law, the flux S, received by us at a distance d_L is related to the luminosity of the object L by the simple relation:

$$d_L^2 = \frac{L}{4\pi S} \tag{A.7}$$

In an expanding universe, however, we also have to take into account two effects on the photons as they propagate towards us which decrease the flux by a factor of $(1+z)^2$. First the expansion causes the energy of each photon to fall by $(1+z)$, and second, the time between photon detection also drops off by another factor of $(1+z)$. And so the overall flux received in a flat universe is

$$S = \frac{L}{r^2(1+z)^2} \tag{A.8}$$

hence the luminosity distance is approximated by

$$d_L = d_p\,(1+z) \tag{A.9}$$

Therefore, for nearby objects, where $z \ll 1$, d_L approaches the physical distance d_P, whereas more distant objects appear further than they are. Using Equation 1.16, we can also express the luminosity distance purely in terms of redshift, deceleration parameter and Hubble constant.

$$d_L \approx \frac{c}{H_0} z \left(1 + \frac{1-q_0}{2} z\right), (k=0) \tag{A.10}$$

A.2.3 Angular diameter distance

As well as a luminosity distance, we can also define an **angular diameter distance** which can be thought of as the proper distance at the time of emission. Looking at a standard yardstick of length l whose ends subtend an angle $d\theta$, the distance to the yardstick, angular diameter distance dA in a static universe is simply derived from basic trigonometry, taking the small angle approximation:

$$d_A \approx \frac{l}{d\theta} \tag{A.11}$$

In an expanding universe the length of the yardstick is

$$l = r_0 a(t_e) d\theta \tag{A.12}$$

where r_0 is the radial coordinate of the object from the observer. Similarly, we can also express this distance in terms of redshift, deceleration parameter and Hubble constant as

$$d_A \approx \frac{c}{H_0} z \left(1 - \frac{3 + q_o}{2} z\right) \tag{A.13}$$

We can now relate these cosmological distances:

$$d_A = \frac{d_L}{(1+z)^2} = \frac{d_P}{(1+z)} \tag{A.14}$$

Appendix B

Table of AGNs in Combined Sample S10, S20, S40

XCS Name	AGN Name	Type	z	$\log(L_{\rm X})$	Γ	$\sigma^2_{\rm NXS\,10ks}$	$N_{\rm 10ks}$	$\sigma^2_{\rm NXS\,20ks}$	$N_{\rm 20ks}$	$\sigma^2_{\rm NXS\,40ks}$	$N_{\rm 40ks}$	$\log(M_{\rm BH})$
				$\rm erg\,s^{-1}$							$\rm M_\odot$	
(1)	(2)	(3)	(4)	(5)	(6)	(7)	(8)	(9)	(10)	(11)	(12)	(13)
J000619.5+201210.3	MARK 335	1	0.026	$42.84\pm^{0.003}_{0.002}$	1.52	0.01±0.005	34	0.013±0.007	11	0.031±0.017	5	$7.23\pm^{0.042}_{0.044}$
J001030.9+105829.6	MARK 1501	1	0.089	$44.13\pm^{0.026}_{0.019}$	1.2							$8.067\pm^{0.119}_{0.165}$
J004153.3+402116.1	MARK 957	1	0.073	$42.84\pm^{0.031}_{0.015}$	1.84	0.015±0.006	5					
J005452.3+252538.1	2E 217	1.2	0.155	$44.58\pm^{0.007}_{0.006}$	2.03							$8.462\pm^{0.083}_{0.094}$
J010516.7-582615.8	ESO 113-G10	1.8	0.026	$42.68\pm^{0.003}_{0.003}$	2.34	0.01±0.005	9	0.019±0.01	5			
J012345.6-584822.5	F 9	1	0.046	$43.82\pm^{0.003}_{0.003}$	2.25	0±0.001	12					$8.299\pm^{0.078}_{0.116}$
J021433.4-004601.4	NGC 863	1	0.027	$42.89\pm^{0.014}_{0.012}$	1.35							$7.57\pm^{0.062}_{0.074}$
J023005.5-085953.4	MARK 1044	1	0.017	$42.81\pm^{0.002}_{0.002}$	1.83	0.026±0.008	13	0.032±0.012	6			
J023437.9-084715.2	NGC 985	1.5	0.043	$43.59\pm^{0.004}_{0.004}$	1.47			0.001±0.001	5			
J032240.5-371637.2	IXO 10	2	0.515	$43.85\pm^{0.035}_{0.016}$	1.95	0.011±0.064	5	0.012±0.035	5			
J033301.7-275819.2	ECDF-S 441	1	1.842	$44.84\pm^{0.084}_{0.012}$	2.25			0.445±0.856	6			
J033312.0-361947.9	MS 03313-3629	BL	0.308	$44.43\pm^{0.009}_{0.008}$	1.92			0±0.008	29			
J033336.4-360826.1	NGC 1365	1.8	0.0060	$41.2\pm^{0.036}_{0.034}$	0.07	0.011±0.004	41	0.012±0.003	25	0.017±0.007	12	
J033841.3-353132.8	CXOMP J03386-3531	1	0.36	$43.95\pm^{0.043}_{0.012}$	2.17	0.002±0.018	12	-0.093±0.134	7			
J043311.0+052116.1	MARK 1506	1.5	0.033	$44.92\pm^{0.003}_{0.003}$	1.64							$7.745\pm^{0.038}_{0.04}$
J051045.4+162956.7	2E 1228	1.5	0.017	$43.2\pm^{0.003}_{0.003}$	1.41							$6.876\pm^{0.074}_{0.424}$
J051611.4-000859.5	AKN 120	1	0.033	$44.57\pm^{0.001}_{0.001}$	1.66	0±0	17	0±0	13	0±0	8	$8.068\pm^{0.048}_{0.063}$
J051621.1-103342.3	MCG -02.14.009	1	0.028	$43.27\pm^{0.003}_{0.003}$	1.58	0.001±0.002	11	0.007±0.006	5			
J053159.9-691951.4	1WGA J0531.9-6919	1	0.149	$43.03\pm^{0.05}_{0.027}$	1.83	0.004±0.02	5					
J055802.0-382002.9	H 0557-385	1.2	0.034	$42.85\pm^{0.017}_{0.016}$	0.46	0.028±0.011	5	0.011±0.011	5			
J055947.3-502652.2	PKS 0558-504	1	0.137	$45.57\pm^{0.002}_{0.002}$	2.3	0.006±0.002	33	0.012±0.004	18	0.024±0.013	9	
J074232.7+494833.3	MARK 79	1.2	0.022	$42.92\pm^{0.006}_{0.006}$	1.99	0.001±0.001	5				$7.612\pm^{0.107}_{0.136}$	

XCS Name	AGN Name	Type	z	$\log(L_{\rm X})$	Γ	$\sigma^2_{\rm NXS\,10ks}$	$N_{\rm 10ks}$	$\sigma^2_{\rm NXS\,20ks}$	$N_{\rm 20ks}$	$\sigma^2_{\rm NXS\,40ks}$	$N_{\rm 40ks}$	$\log(M_{\rm BH})$
				$\rm erg\,s^{-1}$							$\rm M_\odot$	
(1)	(2)	(3)	(4)	(5)	(6)	(7)	(8)	(9)	(10)	(11)	(12)	(13)
J081058.6+760243.0	2E 1919	1	0.1	$44.17\pm^{0.006}_{0.005}$	2.29							$8.735\pm^{0.048}_{0.053}$
J083538.8-040517.0	NGC 2617	1.8	0.014	$43\pm^{0.002}_{0.002}$	1.42	0±0	5					
J084742.5+344504.0	Ton 951	1	0.064	$42.98\pm^{0.016}_{0.016}$	0.91							$7.858\pm^{0.154}_{0.23}$
J091826.0+161822.6	MARK 704	1.2	0.029	$43.31\pm^{0.004}_{0.004}$	2.11	0.004±0.002	6	0.003±0.002	5			
J092512.7+521711.7	MARK 110	1	0.035	$43.87\pm^{0.004}_{0.003}$	1.68							$7.292\pm^{0.101}_{0.097}$
J094233.2+093836.3	MS 09398+0952	1	0.205	$43.12\pm^{0.038}_{0.024}$	2.29	0.044±0.04	5					
J095651.9+411519.7	2XMM J095652.4+411522	1	0.239	$44.69\pm^{0.009}_{0.007}$	2.08							$8.333\pm^{0.082}_{0.108}$
J095847.4+653353.9	S4 0954+65	BL	0.367	$44.89\pm^{0.006}_{0.005}$	1.31	0.001±0.007	5					
JJ100200.1-080945.0	IRAS 09595-0755	1	0.055	$43.3\pm^{0.011}_{0.008}$	1.97	0.003±0.002	6					
J102348.6+040553.7	ACIS J10212+0421	1	0.099	$42.17\pm^{0.135}_{0.009}$	3.85	0.044±0.016	14	0.02±0.033	9			
J103118.3+505333.9	1ES 1028+511	BL	0.361	$45.42\pm^{0.002}_{0.002}$	2.32			0±0.001	8			
J103438.6+393825.8	KUG 1031+398	1	0.042	$42.12\pm^{0.011}_{0.012}$	2.48	0.011±0.005	23	0.01±0.005	13	0.012±0.005	5	
J103935.5+533037.2	1AXG J103934+5330	1	0.229	$43.7\pm^{0.028}_{0.015}$	1.74	0.012±0.014	7	0.015±0.008	5			
J105421.1+572544.1	RX J10543+5725	1	0.205	$44.03\pm^{0.014}_{0.011}$	1.51	0.003±0.006	12					
J110647.4+723407.0	NGC 3516	1.5	0.0090	$42.45\pm^{0.003}_{0.003}$	0.85	0.004±0.002	24	0.006±0.003	12	0.008±0.005	6	$7.395\pm^{0.037}_{0.061}$
J112916.6-042407.6	MARK 1298	1	0.06	$42.59\pm^{0.022}_{0.023}$		0.041±0.036	5					
J114008.7+030711.1	SDSS J11401+0307	1	0.081	$42.56\pm^{0.014}_{0.015}$	2.41	0.038±0.01	10	0.044±0.023	5			
J115851.2+435046.3	SDSS J11588+4350	1	0.287	$44.11\pm^{0.391}_{0.062}$	5.07	0.043±0.036	5					
J115941.0-195923.3	CTS J08.06	1	0.456	$45.31\pm^{0.002}_{0.002}$	1.65	0.002±0	5					
J120114.3-034039.6	MARK 1310	1	0.019	$41.85\pm^{0.615}_{0.464}$	1.73							$6.212\pm^{0.071}_{0.089}$
J120256.9-205602.9	POX 52	1.8	0.022	$42.06\pm^{0.015}_{0.016}$	0.64	0.073±0.016	7					
J120309.5+443153.0	NGC 4051	1	0.0020	$41.16\pm^{0.003}_{0.003}$	1.53	0.061±0.012	39	0.068±0.013	23	0.08±0.019	7	$6.13\pm^{0.121}_{0.155}$

XCS Name	AGN Name	Type	z	$\log(L_{\rm X})$	Γ	$\sigma^2_{\rm NXS\,10ks}$	$N_{\rm 10ks}$	$\sigma^2_{\rm NXS\,20ks}$	$N_{\rm 20ks}$	$\sigma^2_{\rm NXS\,40ks}$	$N_{\rm 40ks}$	$\log(M_{\rm BH})$
				$\rm erg\,s^{-1}$							$\rm M_\odot$	
(1)	(2)	(3)	(4)	(5)	(6)	(7)	(8)	(9)	(10)	(11)	(12)	(13)
J121417.6+140313.9	PG 1211+143	1	0.082	$43.72\pm^{0.003}_{0.003}$	1.78	0.005±0.001	31	0.009±0.003	16	0.01±0.003	8	
J121651.9+375436.1	MS 12143+3811	1	0.063	$42.53\pm^{0.026}_{0.016}$	2.13	0.021±0.006	9					
J121826.5+294847.1	MARK 766	1	0.013	$42.62\pm^{0.003}_{0.003}$	1.77	0.021±0.009	46	0.023±0.006	27	0.056±0.034	13	$6.822\pm^{0.05}_{0.057}$
J122206.7+752616.3	XMM J12221+7526	2	0.238	$43.81\pm^{0.02}_{0.017}$	1.56	0.002±0.017	5					
J122324.2+024044.9	MARK 50	1.2	0.023	$43.01\pm^{0.005}_{0.004}$	1.94							$7.422\pm^{0.057}_{0.068}$
J122548.8+333249.0	NGC 4395	1.8	0.0010	$40.84\pm^{0.01}_{0.009}$	0.86	0.195±0.066	11	0.246±0.032	5			$5.449\pm^{0.13}_{0.145}$
J122906.6+020309.0	3C 273.0	1	0.158	$46\pm^{0.001}_{0.001}$	1.57	0±0	14	0±0	5			$8.839\pm^{0.077}_{0.113}$
J123147.1+123836.7	SDSS J12317+1238	1	0.292	$43.51\pm^{0.092}_{0.027}$	2.41	0.001±0.006	5					
J123203.7+200928.1	MARK 771	1	0.064	$43.45\pm^{0.016}_{0.013}$	2.2							$7.758\pm^{0.175}_{0.219}$
J123800.8+621337.1	Q 1235+6230	1	0.44	$43.47\pm^{0.096}_{0.016}$	3.99	0.015±0.081	11					
J123939.4-052043.3	NGC 4593	1	0.0090	$42.81\pm^{0.004}_{0.003}$	2.35							$6.882\pm^{0.084}_{0.104}$
J124210.5+331701.9	WAS 61	1	0.045	$43.37\pm^{0.003}_{0.003}$	2.1	0.006±0.002	7					
J124635.1+022210.2	PG 1244+026	1	0.048	$43.14\pm^{0.005}_{0.005}$	2.42	0.017±0.005	12	0.027±0.009	6			
J124938.4+050925.5	SDSS J12496+0509	1	0.991	$44.92\pm^{0.025}_{0.01}$	2.07	0.023±0.061	6					
J124955.3+051629.0	SDSS J12499+0516	1	0.212	$43.05\pm^{0.041}_{0.023}$	1.28	0.02±0.026	5					
J125611.1-054720.7	3C 279	Q	0.538	$45.92\pm^{0.002}_{0.002}$	1.58			0±0.001	6			
J130022.1+282402.8	X COM	1.5	0.092	$43.57\pm^{0.005}_{0.004}$	2.33	0.003±0.001	8	0.002±0.002	10	0.003±0.002	7	
J130028.7+283008.7	5C 4.105	1.2	0.645	$44.97\pm^{0.008}_{0.006}$	1.71	0.006±0.006	19					
J132519.2-382455.2	IRAS 13224-3809	1	0.065	$42.66\pm^{0.009}_{0.008}$	2.53	0.117±0.03	42	0.157±0.03	25	0.217±0.049	13	
J133553.7-341745.5	MCG -06.30.015	1.5	0.0080	$42.55\pm^{0.004}_{0.004}$	1.6	0.022±0.008	27	0.032±0.015	16	0.048±0.014	8	
J133718.9+242303.2	IRAS 13349+2438	1	0.107	$44\pm^{0.008}_{0.008}$	1.69	0.005±0.003	5	0.008±0.003	6			
J134208.4+353916.1	NGC 5273	1.9	0.0030	$41.13\pm^{0.008}_{0.007}$	1.21							$6.66\pm^{0.125}_{0.19}$

XCS Name	AGN Name	Type	z	$\log(L_{\rm X})$	Γ	$\sigma^2_{\rm NXS\,10ks}$	$N_{\rm 10ks}$	$\sigma^2_{\rm NXS\,20ks}$	$N_{\rm 20ks}$	$\sigma^2_{\rm NXS\,40ks}$	$N_{\rm 40ks}$	$\log(M_{\rm BH})$
				$\rm erg\,s^{-1}$							$\rm M_\odot$	
(1)	(2)	(3)	(4)	(5)	(6)	(7)	(8)	(9)	(10)	(11)	(12)	(13)
J135303.7+691828.9	MARK 279	1	0.031	$43.51\pm^{0.003}_{0.003}$	1.83							$7.435\pm^{0.099}_{0.133}$
J141759.5+250812.2	NGC 5548	1.5	0.017	$43.4\pm^{0.003}_{0.002}$	1.8	0.002±0.001	41	0.001±0.001	23	0.002±0.001	13	$7.718\pm^{0.016}_{0.016}$
J141922.4-263841.1	ESO 511-G030	1	0.022	$44.03\pm^{0.002}_{0.002}$	2.05	0±0	10	0.001±0	5			
J142832.6+424021.4	H 1426+428	1	0.129	$44.91\pm^{0.005}_{0.005}$	1.94	0±0	17	0±0	11	0±0	6	
J150401.1+102616.4	MARK 841	1.5	0.036	$43.45\pm^{0.004}_{0.004}$	1.27	0.002±0.001	5					
J153552.2+575411.7	MARK 290	1.5	0.03	$43.23\pm^{0.006}_{0.006}$	1.47	0.004±0.001	6					$7.277\pm^{0.061}_{0.061}$
J155543.0+111125.4	PG 1553+11	BL	0.36	$45.42\pm^{0.001}_{0.001}$	2.28	0±0	22	0.001±0	17	0±0	12	
J163323.7+471857.6	RXS J16333+4718	1	0.116	$43.66\pm^{0.017}_{0.008}$	1.64	0.023±0.006	6					
J164823.2+350324.4	SDSS J16483+3503	1	0.178	$43.5\pm^{0.044}_{0.031}$	1.45	0.016±0.022	6					
J165640.6+275257.7	SDSS J16566+2752	1	0.195	$43.72\pm^{0.058}_{0.021}$	1.14	0.007±0.013	5					
J172819.6-141555.7	PDS 456	Q	0.184	$44.45\pm^{0.003}_{0.002}$	2.26	0.002±0.001	37	0.004±0.001	32	0.007±0.003	15	
J190525.8+422739.8	Z 229-15	1	0.027	$42.8\pm^{0.006}_{0.005}$	1.62							$6.913\pm^{0.075}_{0.119}$
J194240.5-101924.5	NGC 6814	1.5	0.0050	$42.09\pm^{0.003}_{0.003}$	1.49							$7.038\pm^{0.056}_{0.058}$
J204409.7-104325.8	MARK 509	1.5	0.035	$44.03\pm^{0.002}_{0.002}$	2.13	0±0	30	0±0	28	0.001±0.001	11	$8.049\pm^{0.035}_{0.035}$
J213227.8+100819.6	MARK 1513	1.5	0.061	$43.47\pm^{0.02}_{0.016}$	1.69							$7.433\pm^{0.055}_{0.063}$
J213631.6+003153.1	MS 21340+0018	Q	0.805	$44.63\pm^{0.023}_{0.01}$	1.73			0.02±0.075	6			
J215852.0-301332.4	PKS 2155-304	BL	0.116	$44.75\pm^{0.003}_{0.002}$	2.65	0.001±0	40	0.001±0	22	0.003±0.001	7	
J220916.1-470959.2	NGC 7213	1	0.0060	$41.96\pm^{0.003}_{0.003}$	1.93			-0.001±0	6			
J221918.4+120754.4	II Zw 177	1	0.082	$42.94\pm^{0.009}_{0.009}$	2.41	0.021±0.016	12	0.034±0.023	6			
J224239.3+294331.9	AKN 564	2	0.025	$43.89\pm^{0.002}_{0.002}$	2.55	0.025±0.008	29	0.036±0.011	13	0.044±0.011	6	
J225405.9-173459.3	MR 2251-178	1.5	0.064	$44.3\pm^{0.002}_{0.002}$	1.39	0±0	9	0±0	7	0±0	6	
J225739.1-365605.1	MS 22549-3712	1	0.039	$42.9\pm^{0.004}_{0.003}$	2.33	0.006±0.003	7					

XCS Name	AGN Name	Type	z	$\log(L_{\rm X})$	Γ	$\sigma^2_{\rm NXS\,10ks}$	$N_{\rm 10ks}$	$\sigma^2_{\rm NXS\,20ks}$	$N_{\rm 20ks}$	$\sigma^2_{\rm NXS\,40ks}$	$N_{\rm 40ks}$	$\log(M_{\rm BH})$
				erg s^{-1}							$M_\odot$	
(1)	(2)	(3)	(4)	(5)	(6)	(7)	(8)	(9)	(10)	(11)	(12)	(13)
J230315.6+085223.9	NGC 7469	1.5	0.017	$43.25\pm^{0.002}_{0.003}$	1.95	0.001±0	7	0.002±0	5			$6.956\pm^{0.048}_{0.05}$

Table B.1: Parameters derived or from literature for combined S10, S20 and S40 samples (1) XCS point source name, (2) AGN name if given from literature (3) AGN Type if given from VC13 or SIMBAD, 1, 2 and intermediate, Q-Quasar, BL-BL Lac (4) redshift (5) log hard-band luminosity erg s^{-1} (6) hard-band photon spectral index (7) 10 ks light-curve $\sigma^2_{\rm NXS}$ value (8) number of AGN with five or more good 10 ks light-curve segments,(9) - (12) as (7) and (8)for 20 ks and 40 ks light-curve segments. (13) Black hole mass $M_\odot$ from Bentz and Katz (2015)

Appendix C

XRF Candidates Category B

C.1 XMMXCSJ102809.3-434628.7

X-ray and optical images and light-curves for the candidate XMMXCSJ102809.3-434628.7 are shown in Figure C.2.The source position is in the FOV of one other observation (0112810201), but no detection of point source is made by XAPA nor XRF detected by our method. The nearest IR source is less than 1″ separation from the position, .

C.2 XMMXCSJ205958.4-425647.8

X-ray and optical images and light-curves for the candidate XMMXCSJ205958.4-425647.8 are shown in Figure C.3. The source position is in the FOV of one other observation (0603500901), where no point source is detected at that position, nor an XRF detected.

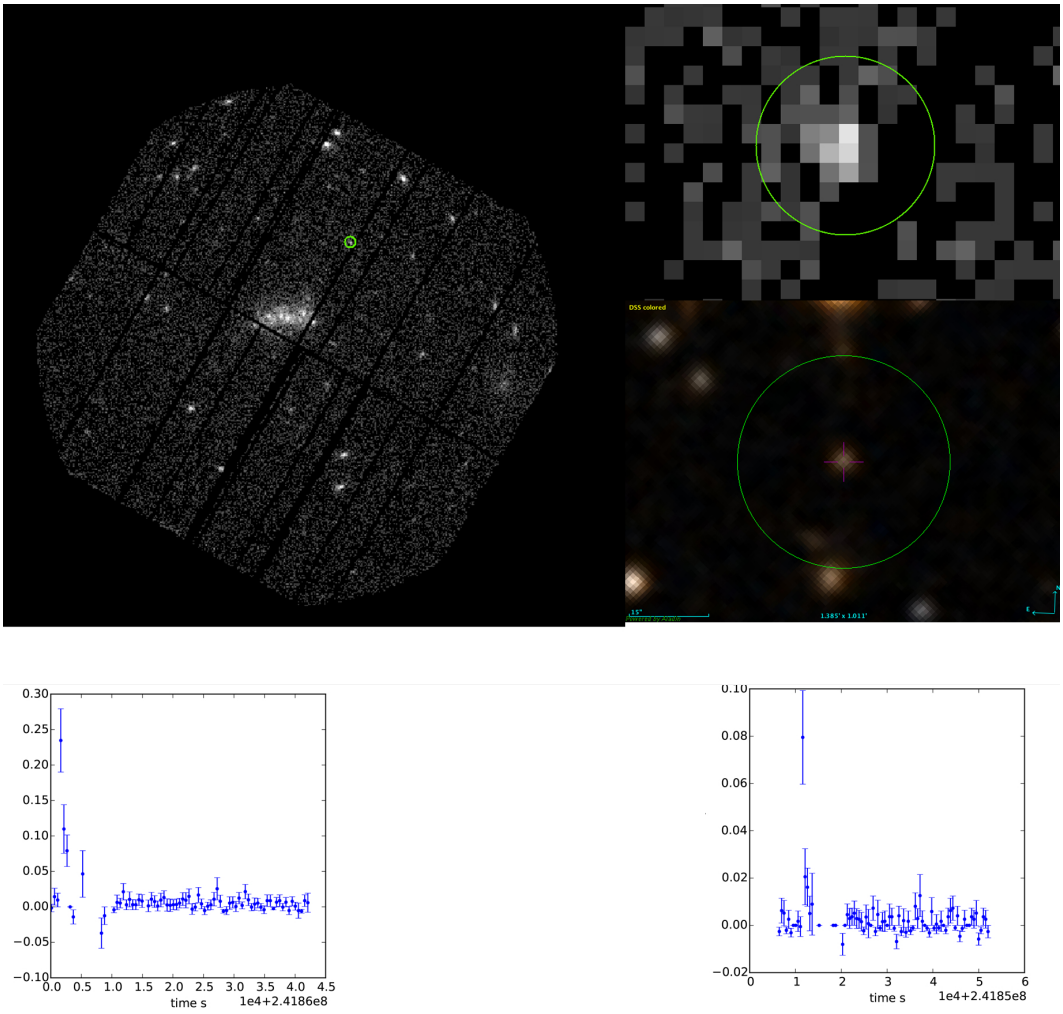

Figure C.1: XMMXCSJ061606.4-211801.4. Top. X-ray image in PN observation 0300800101 with 32xzoom 0.5-2.0 keV and optical DSS image, each with green 20″ region. Bottom. PN and MOS2 light curves (no MOS1 light-curve was made due to source falling on missing MOS1 chip).

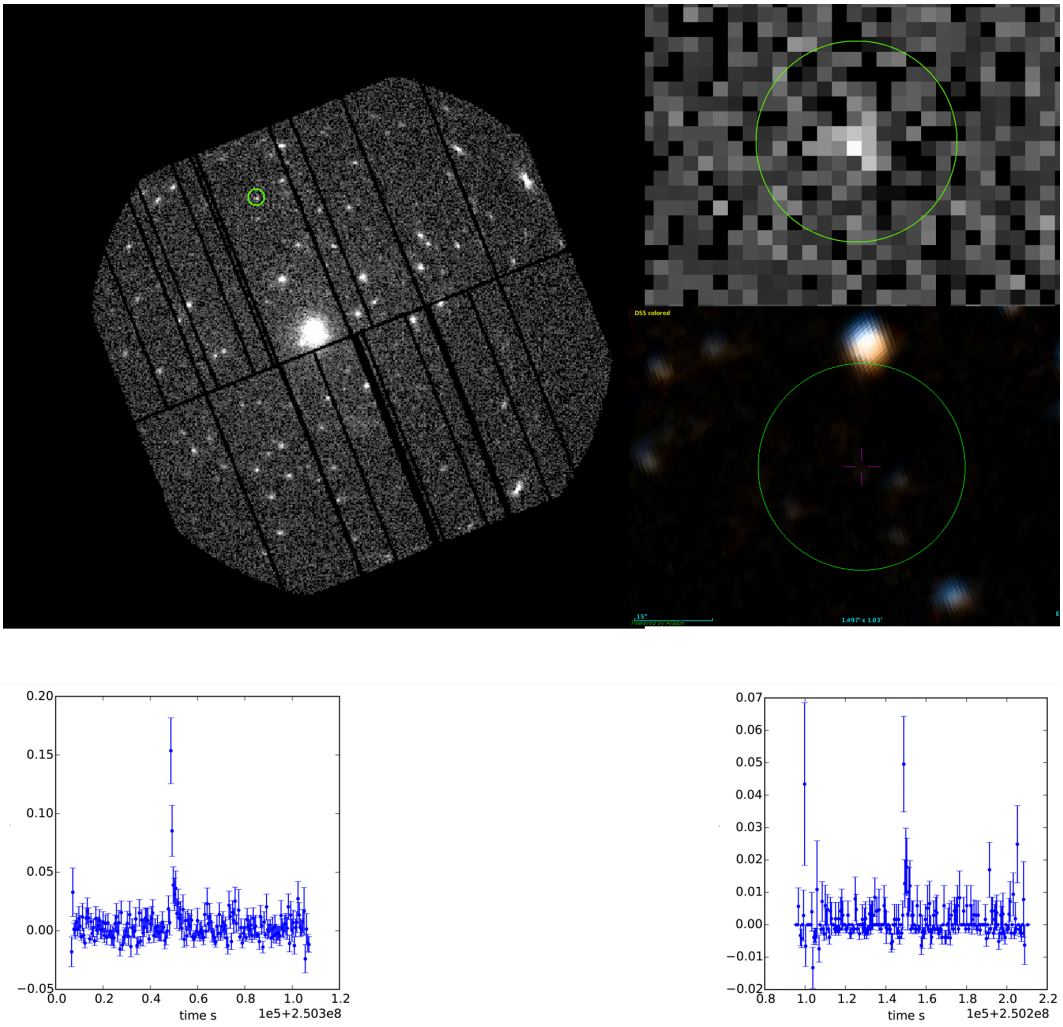

Figure C.2: XMMXCSJ102809.3-434628.7. Top. X-ray image in PN observation 0300430101 with 32xzoom 0.5-2.0 keV and optical DSS image, each with green 20″ region. Bottom. PN and MOS2 light curves (no MOS1 light-curve was made due to source falling on missing MOS1 chip).

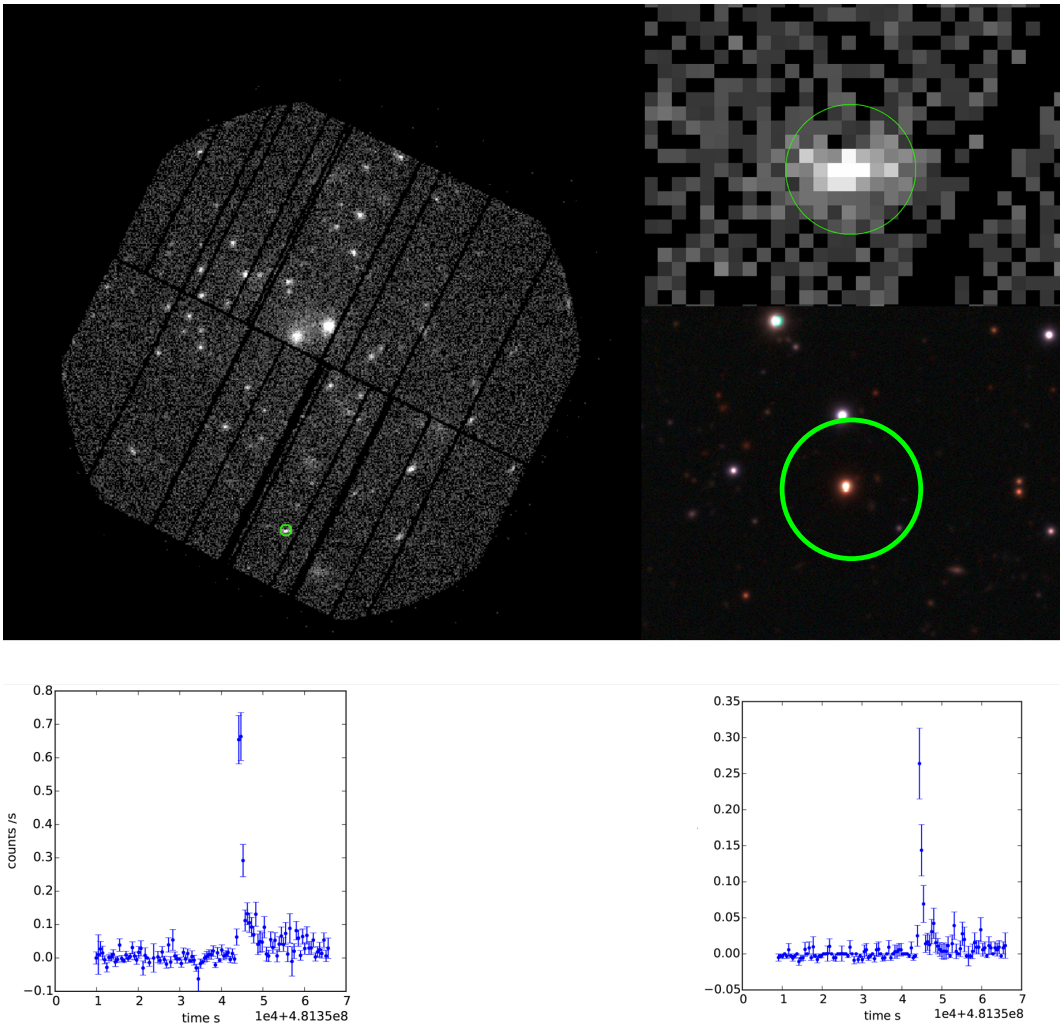

Figure C.3: XMMXCSJ205958.4-425647.8. Top. X-ray image in PN observation 0691670101 with 32xzoom 0.5-2.0 keV and optical DES image, each with green 20″ region. Bottom. PN and MOS2 light curves (no MOS1 light-curve was made due to source falling on missing MOS1 chip).

Appendix D

XRF Candidates Category C

D.1 XMMXCS001527.9-390508.8

X-ray and optical images and light-curves for the candidate XMMXCS001527.9-390508.8 are shown in Figure D.2. A flare event was detected at 5.42σ above the median level (as defined above). The source position is also in the FOV in two other observations (0028740101 and 0028740201) where is it detected as a point source by XAPA. The point source is also detected in an observation by Chandra at $1''$ separation.

D.2 XMMXCSJ004336.3+405336.1

X-ray and optical images and light-curves for the candidate XMMXCSJ004336.3+405336.1 are shown in Figure D.3. The source position is also in the FOV of two other obserations 0511380201 and 0672130501. However no source is detected by XAPA at this position in either. The nearest source is an star $0.6''$ separation.

D.3 XMMXCSJ011057.3-730515.2

X-ray and optical images and light-curves for the candidate XMMXCSJ011057.3-730515.2 are shown in Figure D.4. The position of the source also falls in the FOV of observation 0601212701, where a point source is also detected by XAPA. A star UCAC3 34-10833 in SIMBAD is *lt* $2.5''$ separation can be seen in the optical image.

D.4 XMMXCSJ025412.5+414303.0

X-ray and optical images and light-curves for the candidate XMMXCSJ025412.5+414303.0 are shown in Figure D.5. The detection in the PN detector was at 5.61σ, in and 5.1 in MOS2. There is no detection in MOS1 due to the dead chip at the time of observation. A flare event was detected at 4.3σ above the median level (as defined above). The source position falls in the FOV of one other observation (0135950301) but a point source is not detected by XAPA nor XRF detected by our method. A star (02541245+4143028 in 2MASS catalogue) is the nearest object in SIMBAD. This is not probably not a an XRF but a flaring star.

D.5 XMMXCSJ033241.9-275704.0

X-ray and optical images and light-curves for the candidate XMMXCSJ033241.9-275704.0 are shown in Figure D.6. The source position falls in the FOV of seven other observations, and is detected by XAPA as a point source in three of these (0108060401, 0108061801, 0604960201) - although not detected as an XRF event by our method. The star CDFS-H 4540 is at 1.6″ separation from this location in SIMBAD. A flare event was detected at 4.52σ above the median level

D.6 XMMXCSJ042815.1+155410.6

X-ray and optical images and light-curves for the candidate XMMXCSJ042815.1+155410.6 are shown in Figure D.7. The source falls in the FOV of only one observation. A star 04281499+1554025 is the closest optical object at 8″ separation. The light-curves indicate a flaring star.

D.7 XMMXCSJ050749.0-373823.9

X-ray and optical images and light-curves for the candidate XMMXCSJ050749.0-373823.9 are shown in Figure D.8. he source falls in the FOV of only one observation. The star HD 33352 is at 2.9″ separation from this location in SIMBAD. The point source is also detected in an observation by Chandra at 5″ separation.

D.8 XMMXCSJ053547.0-062911.8

X-ray and optical images and light-curves for the candidate XMMXCSJ053547.0-062911.8 are shown in Figure D.9. The source falls in the FOV of only one observation. The flaring star V* V988 Ori is seen in the image at 2.7 ″ separation in SIMBAD. An X-ray point source, J053547.1-062910, is also detected in Evans et al. (2010) at 2.9″ separation.

D.9 XMMXCSJ065423.9-240056.5

X-ray and optical images and light-curves for the candidate XMMXCSJ065423.9-240056.5 are shown in Figure D.10. A flare event was detected at 4.55σ above the median level. The source position fall in the FOV of three other observations (0204850401, 0204850501 and 0092790101) and detected as a point source in two of these by XAPA, but in none of these is an XRF detection made by our method. The 2MASS source 06542393-2400567 is ″ separation from the point source in SIMBAD.

D.10 XMMXCSJ074410.3+393507.2

X-ray and optical images and light-curves for the candidate XMMXCSJ074410.3+393507.2 are shown in Figure D.11. The source position fall in the FOV of one other observation (0551850101) but no point source detected by XAPA at this position nor XRF detection made by our method. A star is at 1.7″ separation from the source position.

D.11 XMMXCSJ083841.2+195946.2

X-ray and optical images and light-curves for the candidate XMMXCSJ083841.2+195946.2 are shown in Figure D.12. The source was in the FOV of only one observation. The star 2MASS J08384128+1959471 is at 2 ″ separation in SIMBAD.

D.12 XMMXCSJ095802.0+685710.3

X-ray and optical images and light-curves for the candidate XMMXCSJ095802.0+685710.3 are shown in Figure D.13. The source position is in the FOV of nine other observations, the longest exposure being 0657802201, where it is also detected as a point source by XAPA. However, a transient XRF-like event is not detected in any other observations. The infrared source 09580235+6857096 is found in the 2MASS catalogue at 2.1″ separtion.

D.13 XMMXCSJ191527.4-241826.5

X-ray and optical images and light-curves for the candidate XMMXCSJ191527.4-241826.5 are shown in Figure D.14. The source position is in the FOV of six other observations and detected as a source in each. In none of the other exposures is an XRF detected by our method. The point source is also detected in an observation by Chandra at 1.0″ separation.

D.14 XMMXCSJ215906.1-201602.3

X-ray and optical images and light-curves for the candidate XMMXCSJ215906.1-201602.3 are shown in Figure D.15. The source position is in the FOV of only one observation. A source 2MASS 21590602-2016037 is seen at less than 2″s separation. The nature of the light-curves suggest that this is not an XRF by our definition.

D.15 XMMXCSJ220310.7-344406.5

X-ray and optical images and light-curves for the candidate XMMXCSJ220310.7-344406.5 are shown in Figure D.16. The detection in the `PN` detector was at 6.73σ and 6.32σ in `MOS2` (the source falls on a dead chip `MOS1`). The source position is in the FOV of one other observation (503480601) where no point source nor XRF event is detected at this position, however the exposure time is less than 1 ks and therefore too short to make any meaningful conclusions from this observation. A source 2MASS 22031047-3444067 is seen at less than 2″ separation and classified as a star in The Guide Star Catalog, Version 2.3.2 (GSC2.3) (STScI, 2006). The nature of the light-curves also suggest that this is a flaring star.

D.16 XMMXCSJ235138.2-261304.0

X-ray and optical images and light-curves for the candidate XMMXCSJ235138.2-261304.0 are shown in Figure D.17. The detection in the `PN` detector was at 5.12σ, 5.31σ in `MOS1` and 4.64σ in `MOS2`. The source was in the FOV of only one observation. The infra-red source 23513820-2613044 is at 0.6 ″ separation in the 2MASS catalogue.

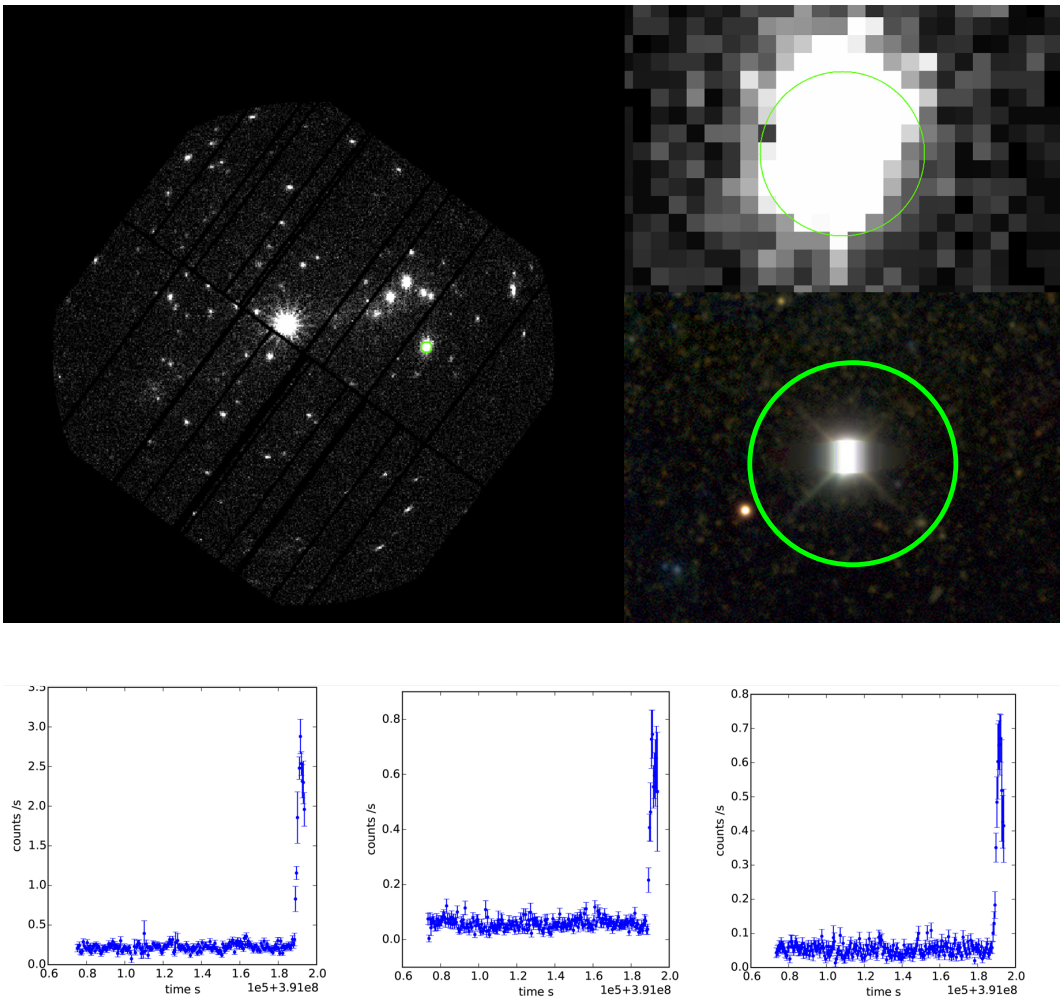

Figure D.1: XMMXCSJ001445.7-391440.9. Top. X-ray image in PN observation 0655050101 with 32xzoom 0.5-2.0 keV and optical DES image, each with green 20″ region. Bottom. PN, MOS1 and MOS2 light curves.

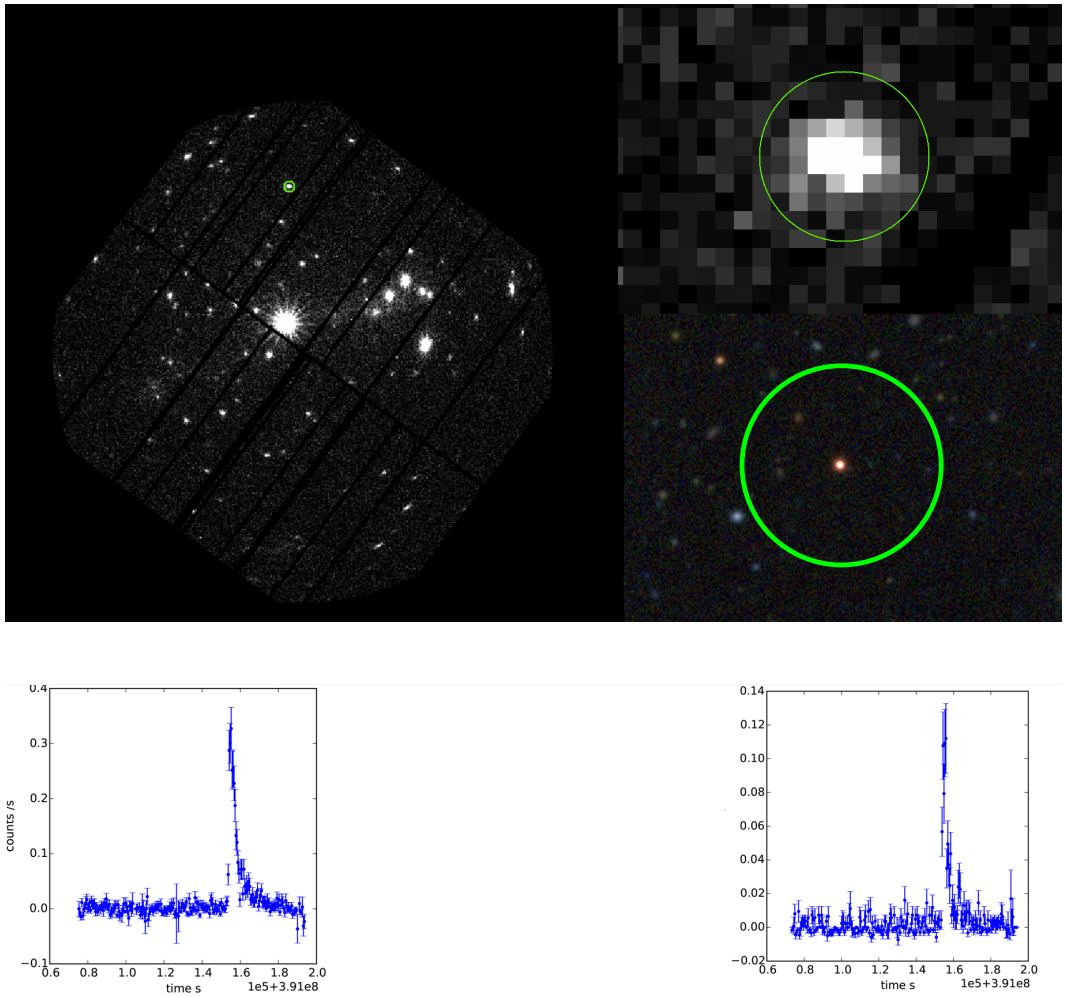

Figure D.2: XMMXCSJ001527.9-390508.8. Top. X-ray image in PN observation 0149780101 with 32xzoom 0.5-2.0 keV and optical DES image, each with green 20″ region. Bottom. PN and MOS2 light curves (no MOS1 light-curve was made due to source falling on missing MOS1 chip).

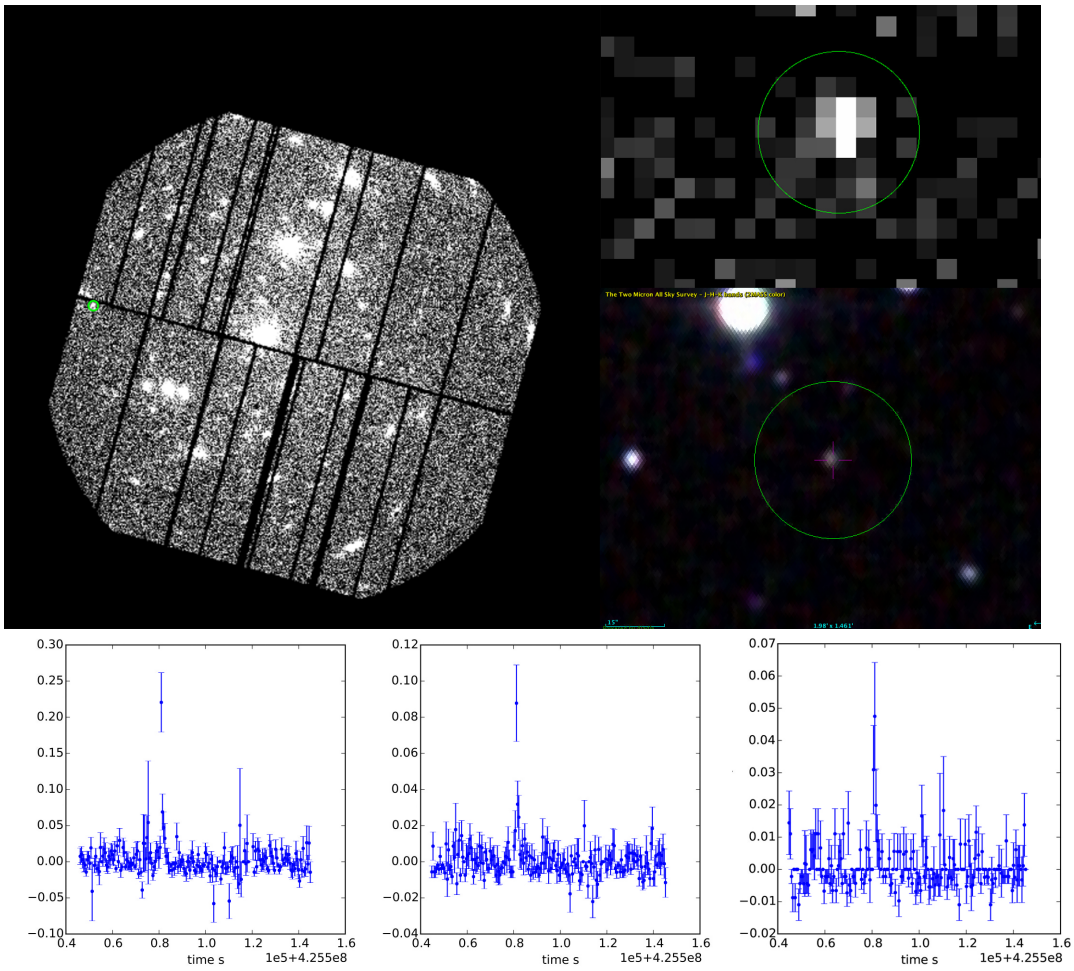

Figure D.3: XMMXCSJ004336.3+405336.1. Top. X-ray image in PN observation 0672130101 with 32xzoom 0.5-2.0 keV and Infra-red 2MASS image each with green 20″ region. Bottom. PN, MOS1 and MOS2 light curves.

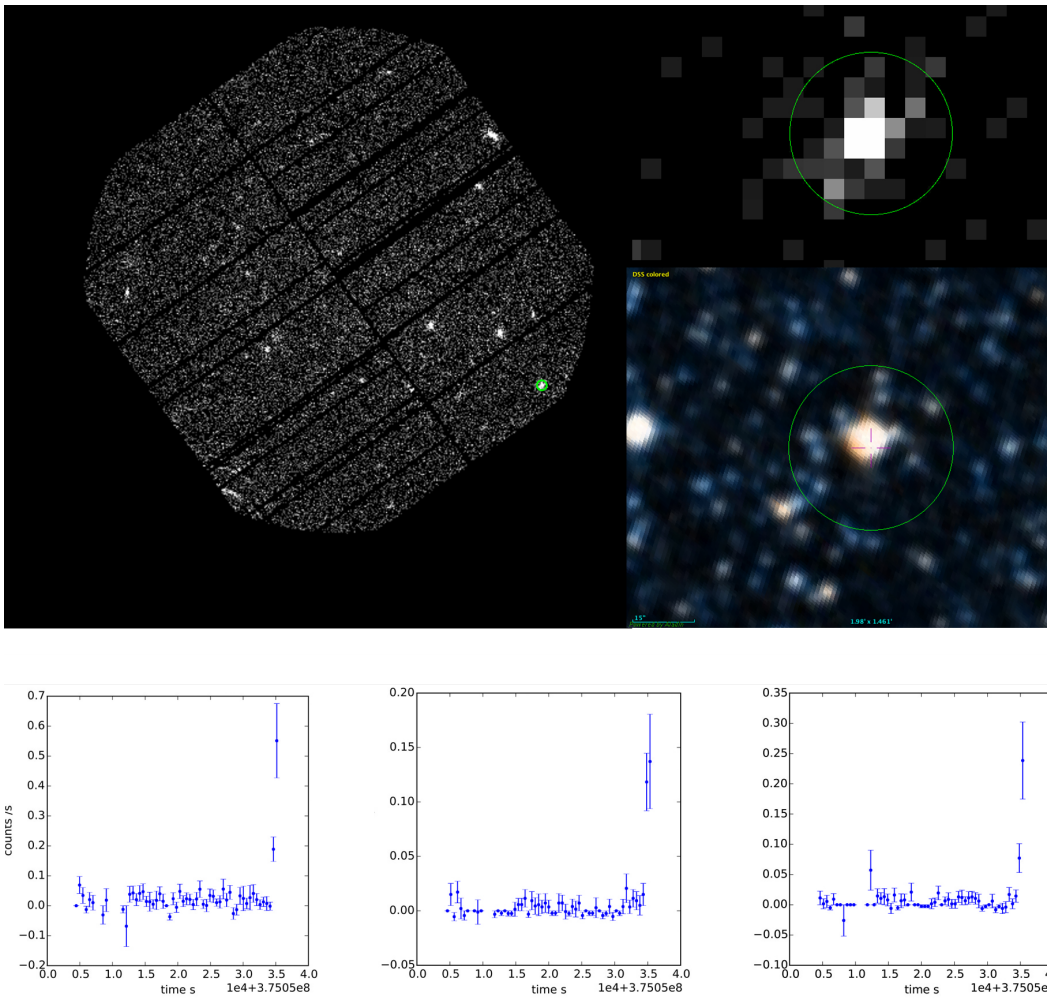

Figure D.4: XMMXCSJ011057.3-730515.2. Top. X-ray image in PN observation 0601212201 with 32xzoom 0.5-2.0 keV and optical DSS image, each with green 20″ region. Bottom. PN, MOS1 and MOS2 light curves.

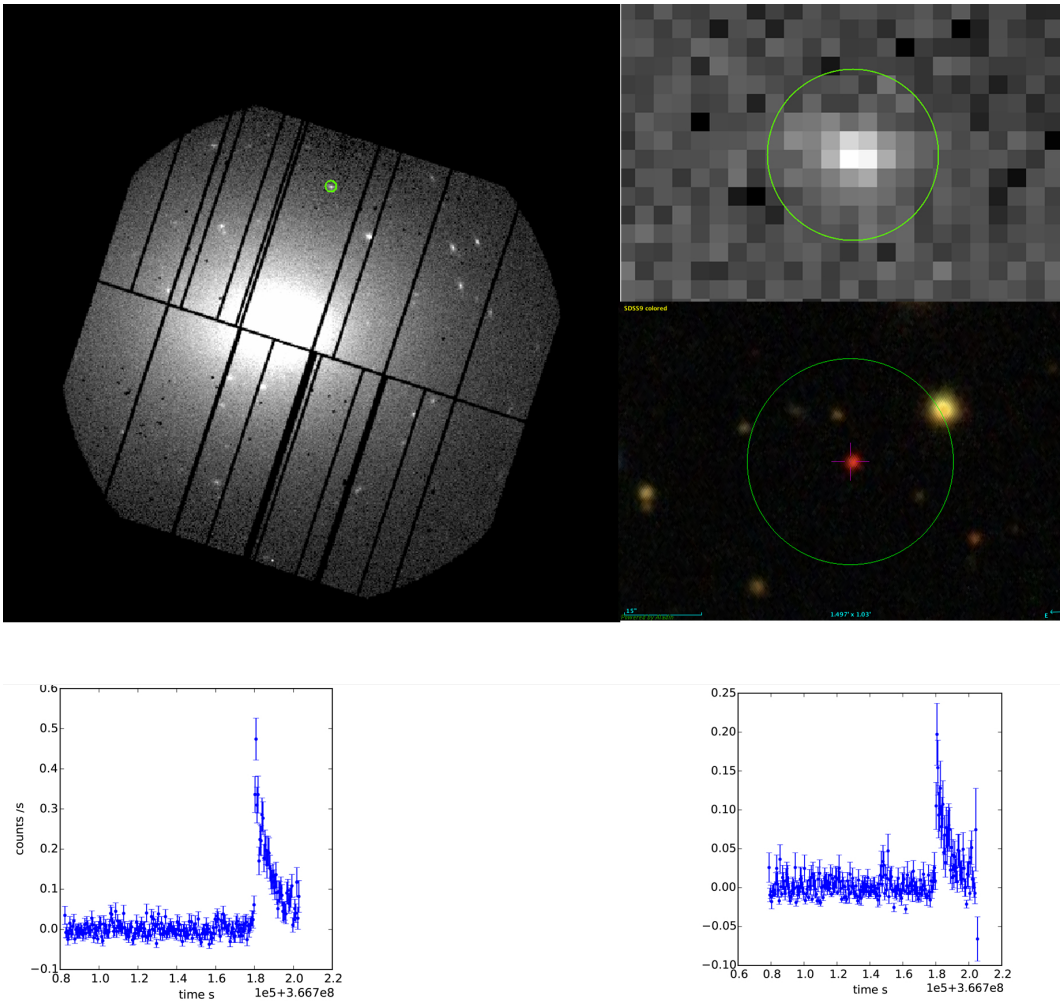

Figure D.5: XMMXCSJ025412.5+414303.0. Top. X-ray image in PN observation 0605540101 with 32xzoom 0.5-2.0 keV and optical SDSS image, each with green 20″ region. Bottom. PN and MOS2 light curves (no MOS1 light-curve was made due to source falling on missing MOS1 chip).

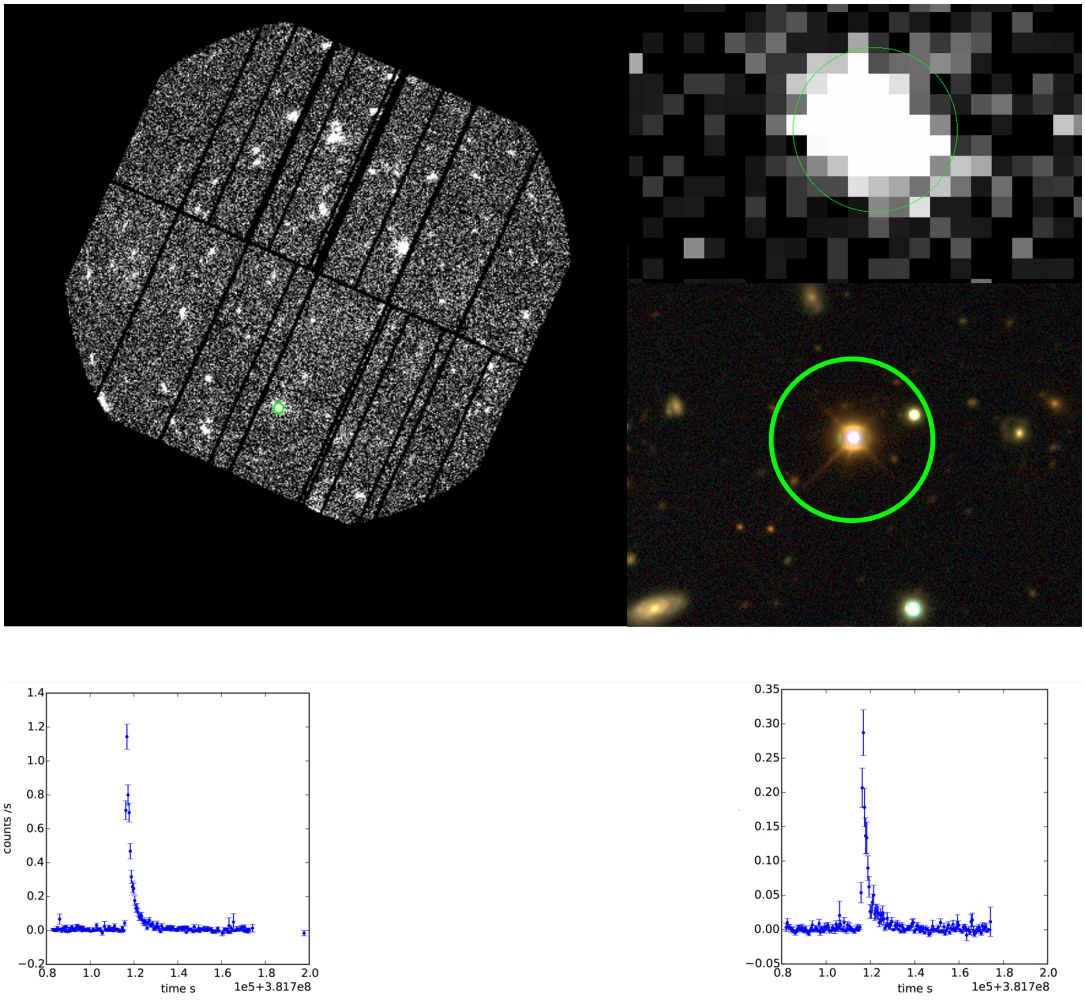

Figure D.6: XMMXCSJ033241.9-275704.0. Top. X-ray image in PN observation 0604960801 with 32xzoom 0.5-2.0 keV and optical DES image, each with green 20″ region. Bottom. PN and MOS2 light curves (no MOS1 light-curve was made due to source falling on missing MOS1 chip).

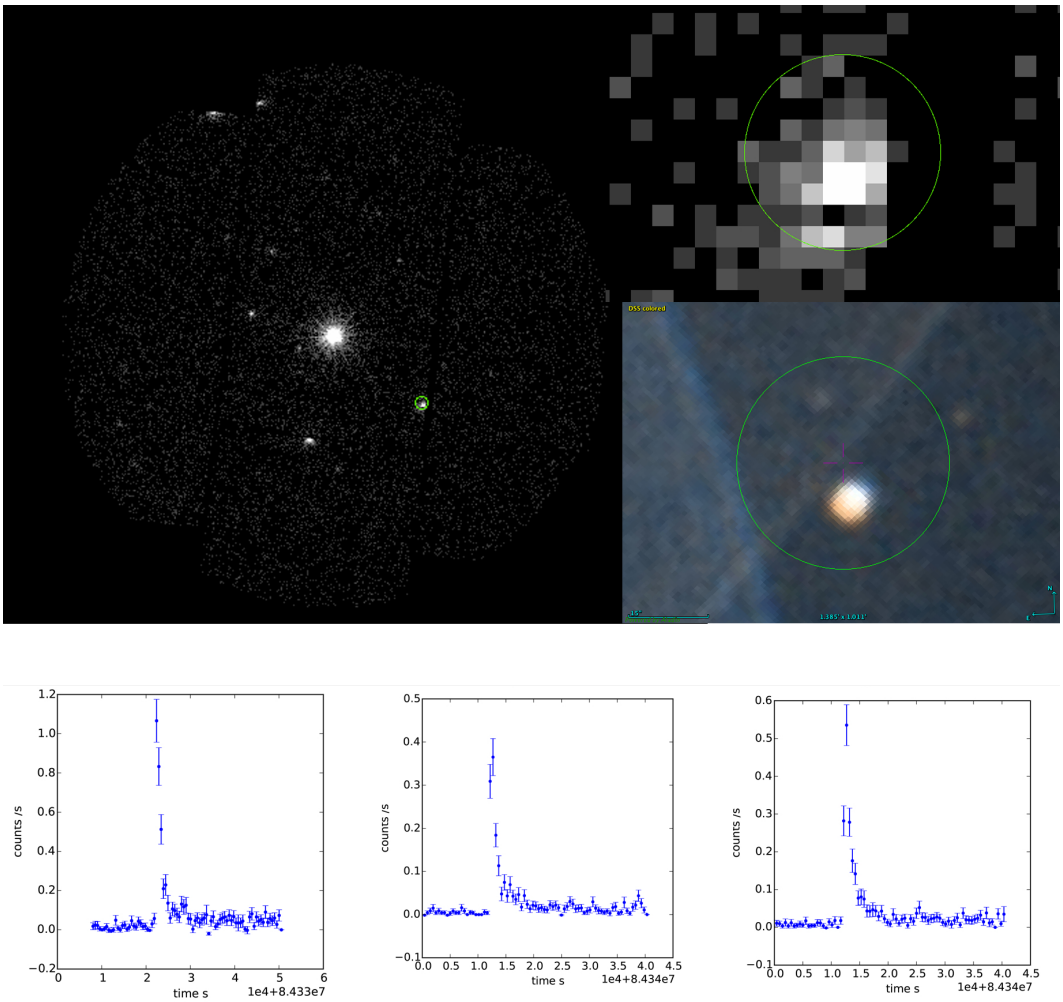

Figure D.7: XMMXCSJ042815.1+155410.6. Top. X-ray image in `MOS1` observation 0101440501 with 32xzoom 0.5-2.0 keV and optical DSS image, each with green 20″ region. Bottom. `PN`, `MOS1` and `MOS2` light curves.

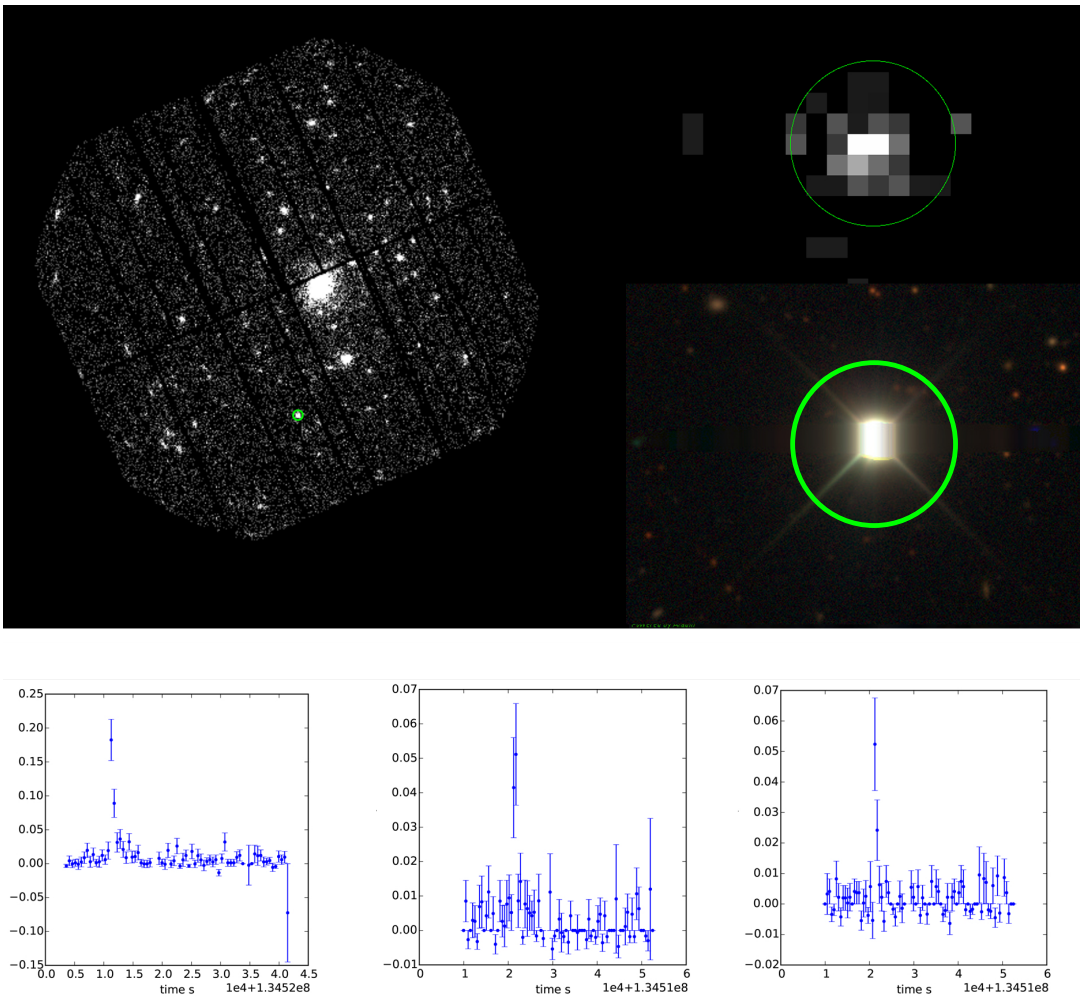

Figure D.8: XMMXCSJ050749.0-373823.9. Top. X-ray image in PN observation 0110980801 with 32xzoom 0.5-2.0 keV and optical DES image, each with green 20″ region. Bottom. PN, MOS1 and MOS2 light curves.

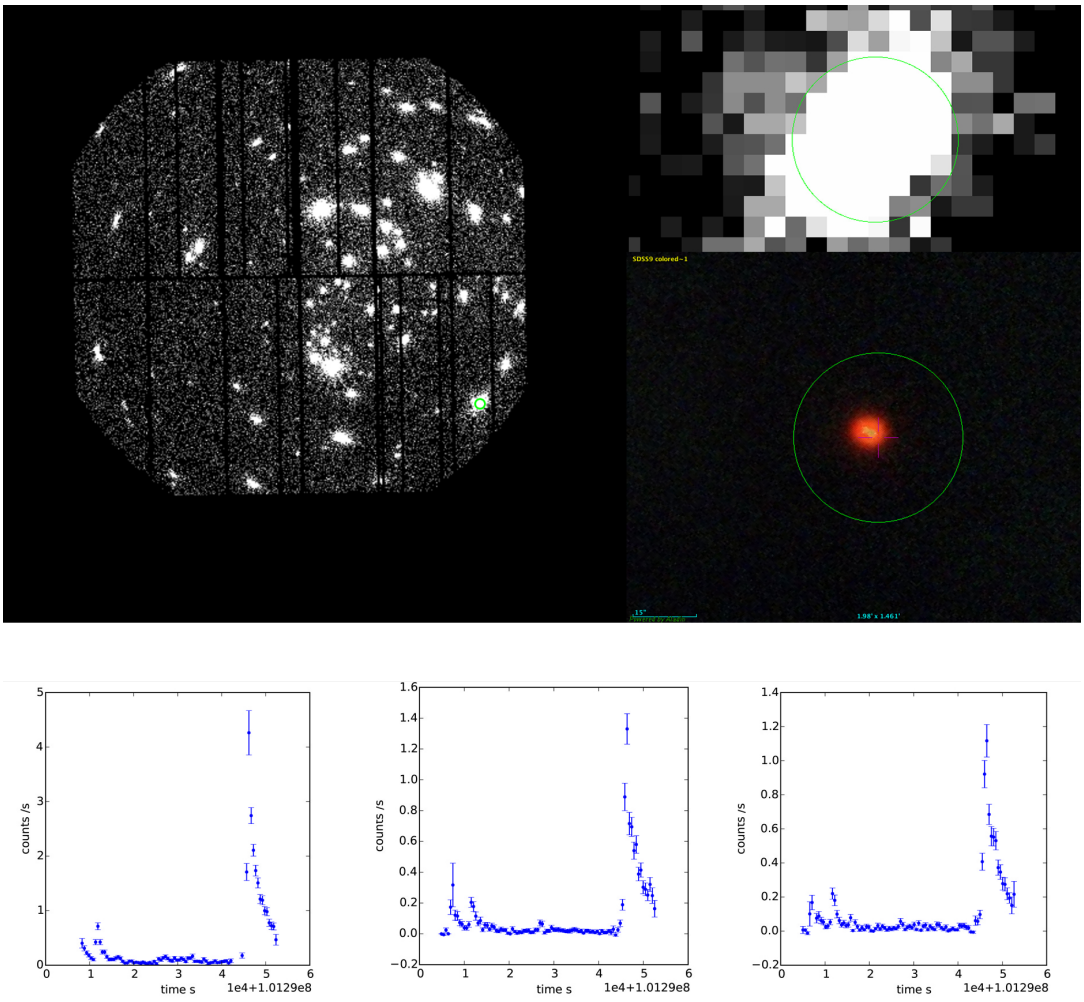

Figure D.9: XMMXCSJ053547.0-062911.8. Top. X-ray image in PN observation 0089940301 with 32xzoom 0.5-2.0 keV and optical DSS image, each with green 20″ region. Bottom. PN, MOS1 and MOS2 light curves.

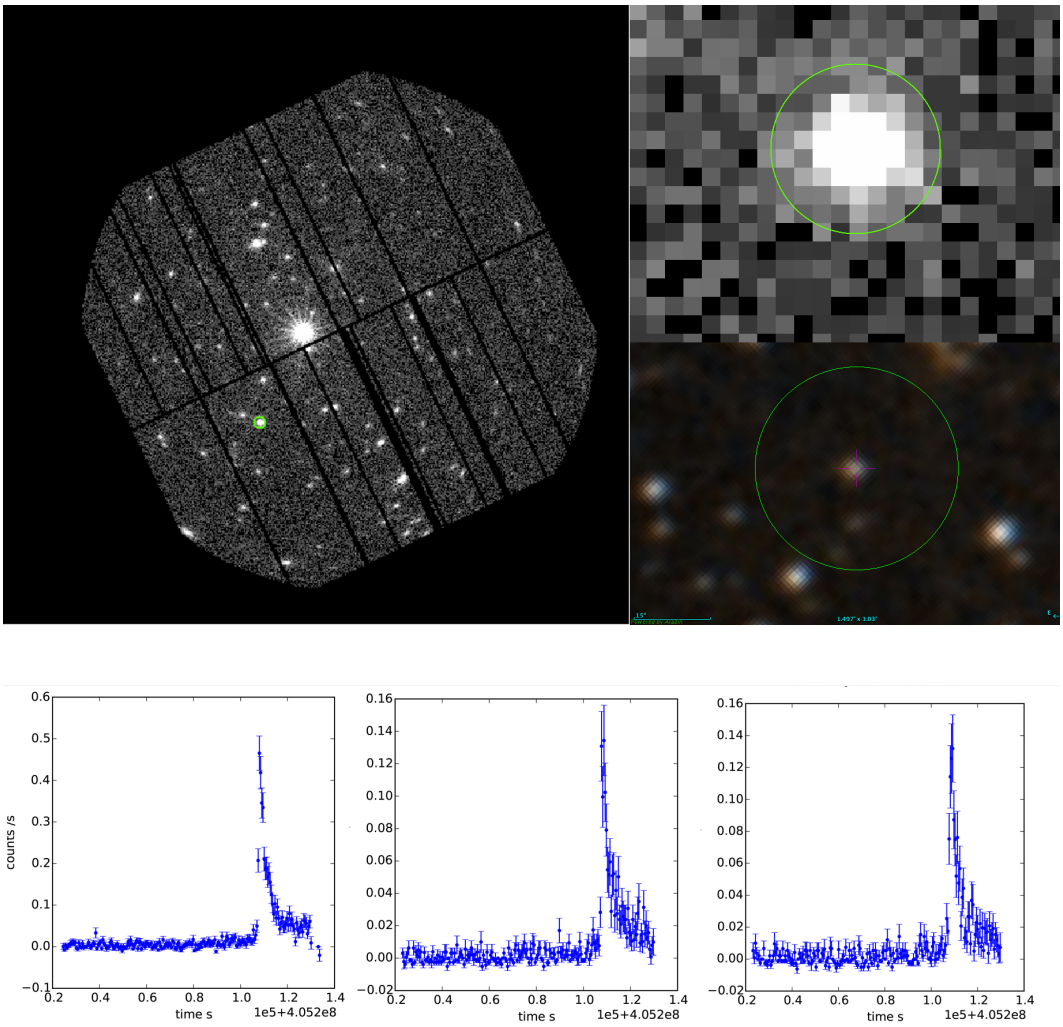

Figure D.10: XMMXCSJ065423.9-240056.5. Top. X-ray image in PN observation 0652250701 with 32xzoom 0.5-2.0 keV and optical DSS image, each with green 20″ region. Bottom. PN, MOS1 and MOS2 light curves.

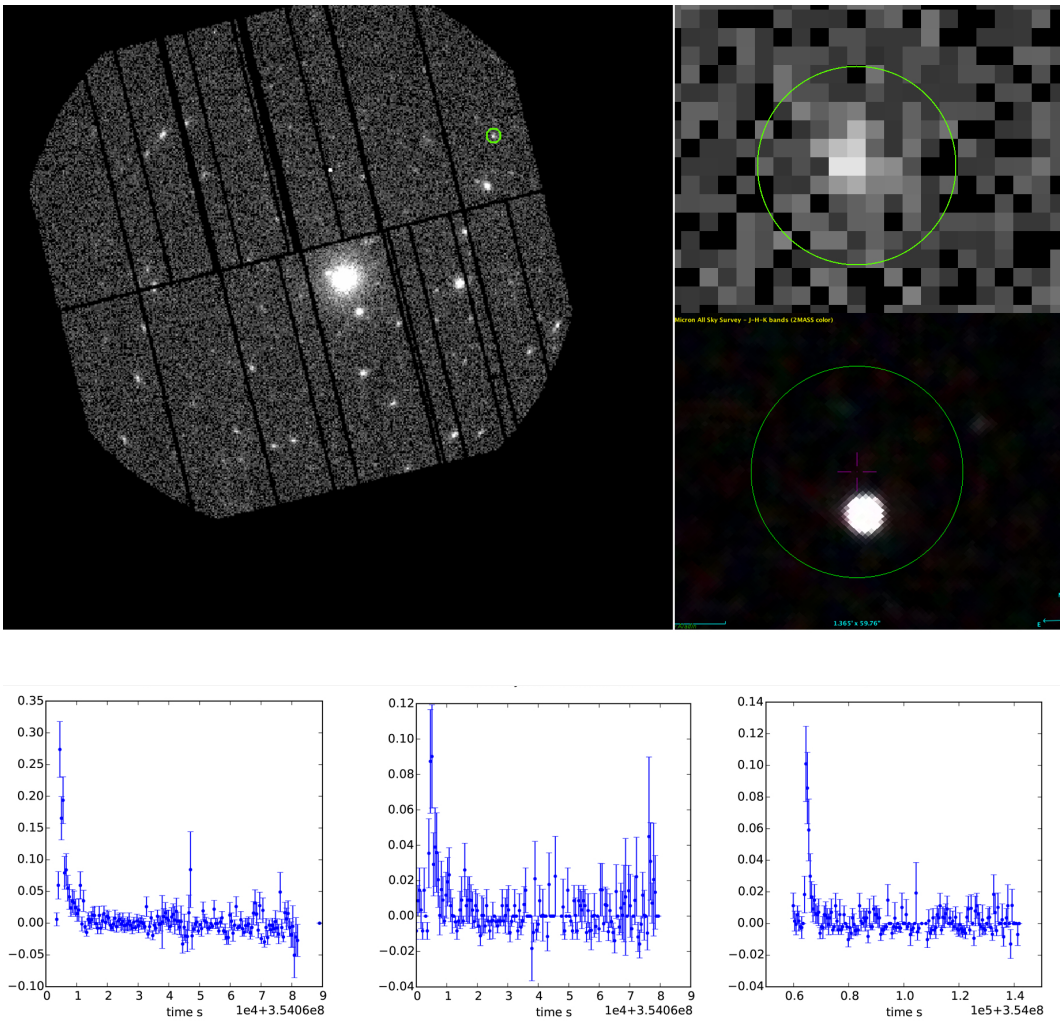

Figure D.11: XMMXCSJ074410.3+393507.2. Top. X-ray image in PN Observation 0551851201 with 32xzoom 0.5-2.0 keV and optical 2MASS image, each with green 20″ region. Bottom. PN, MOS1 and MOS2 light curves.

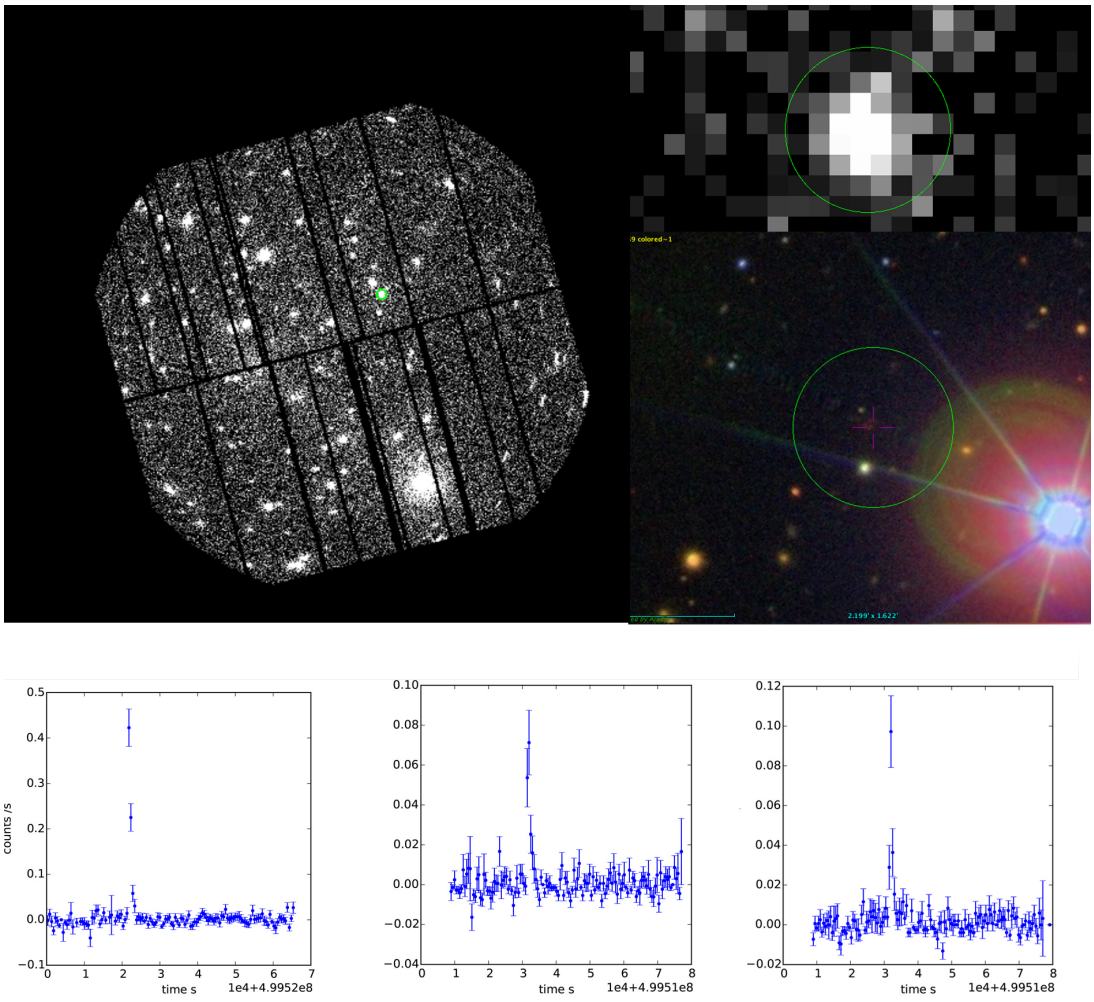

Figure D.12: XMMXCSJ083841.2+195946.2 Top. X-ray image in PN observation 0721620101 with 32xzoom 0.5-2.0 keV and optical SDSS DS9 image, each with green 20″ region. Bottom. PN, MOS1 and MOS2 light curves.

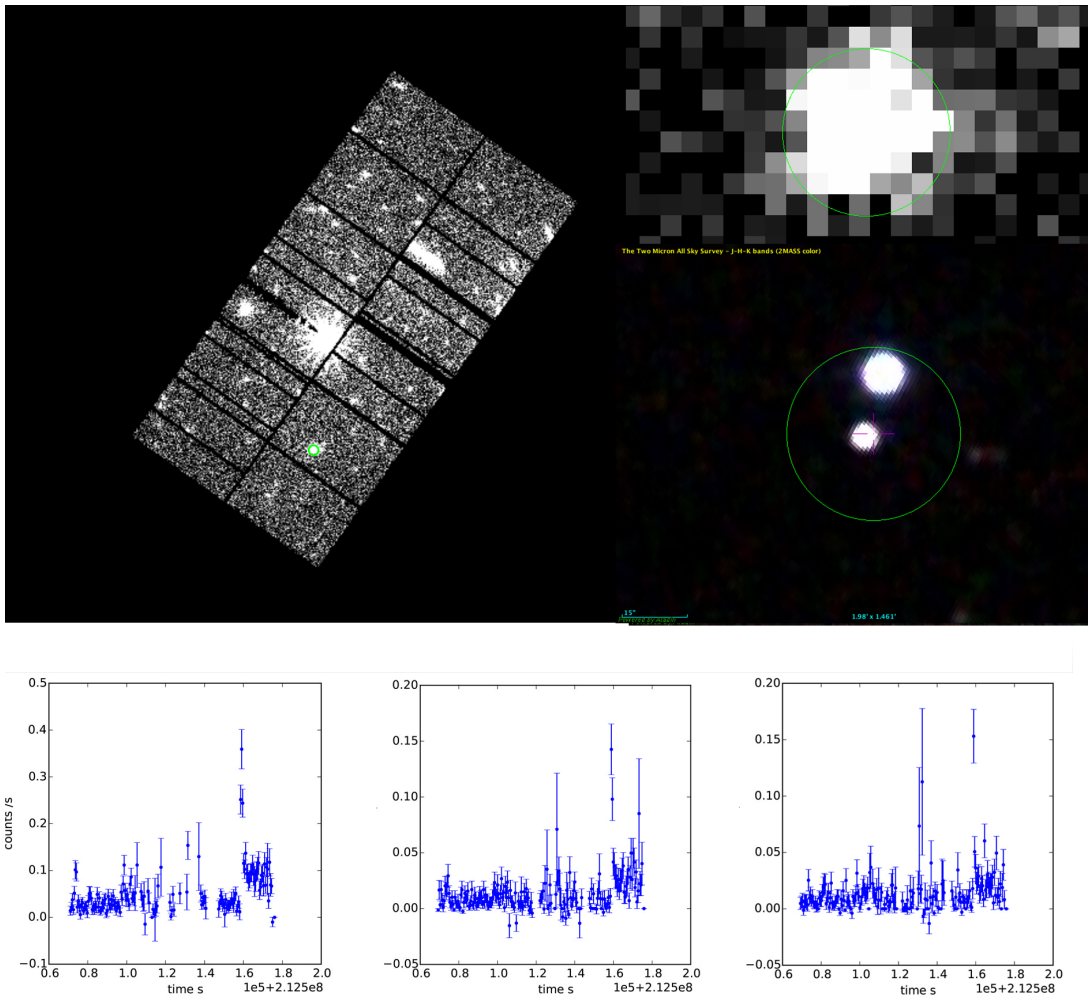

Figure D.13: XMMXCSJ095802.0+685710.3 Top. X-ray image in PN observation 0200980101 with 32xzoom 0.5-2.0 keV and infra-red 2MASS image, each with green 20″ region. Bottom. PN, MOS1 and MOS2 light curves.

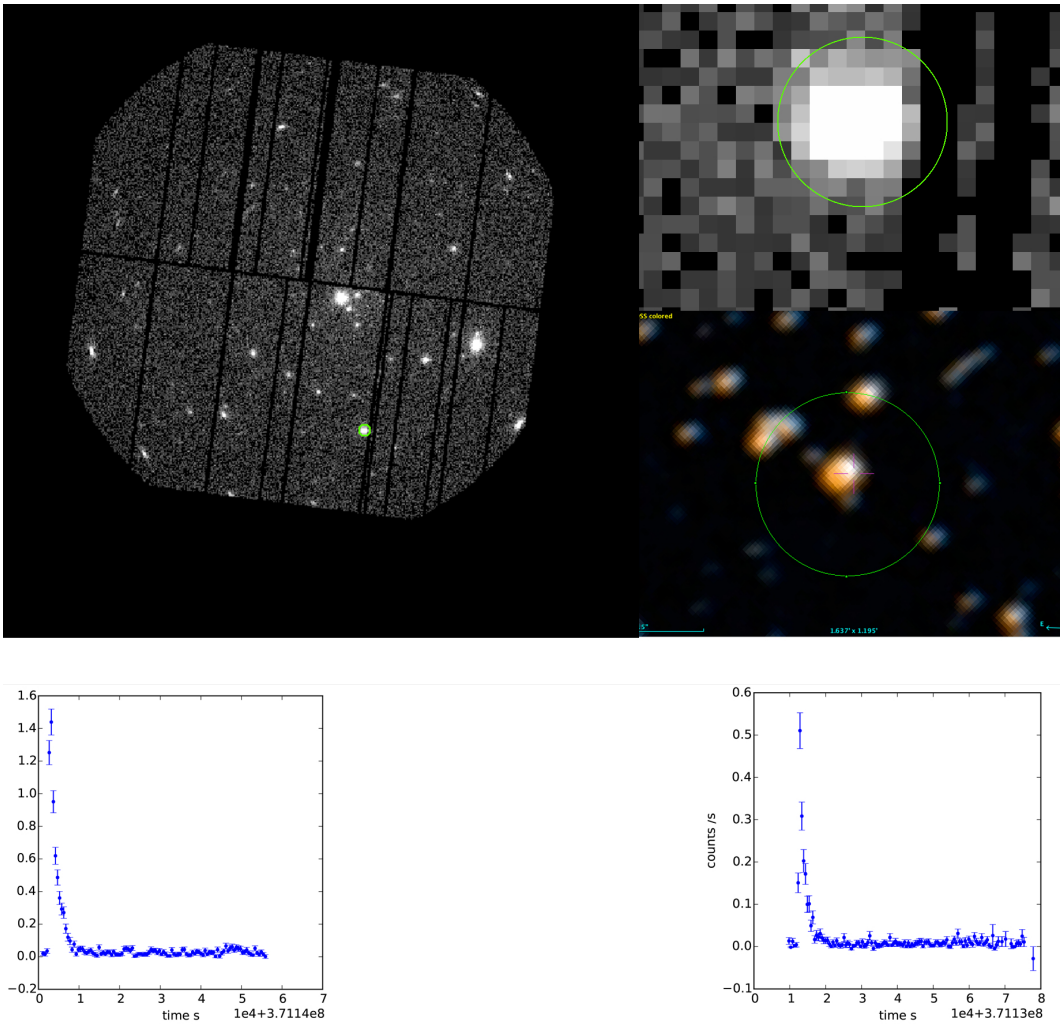

Figure D.14: XMMXCSJ191527.4-241826.5. Top. X-ray image in PN observation 0605580901 with 32xzoom 0.5-2.0 keV and optical DSS image, each with green 20″ region. Bottom. PN and MOS2 light curves (no MOS1 light-curve was made due to source falling on missing MOS1 chip).

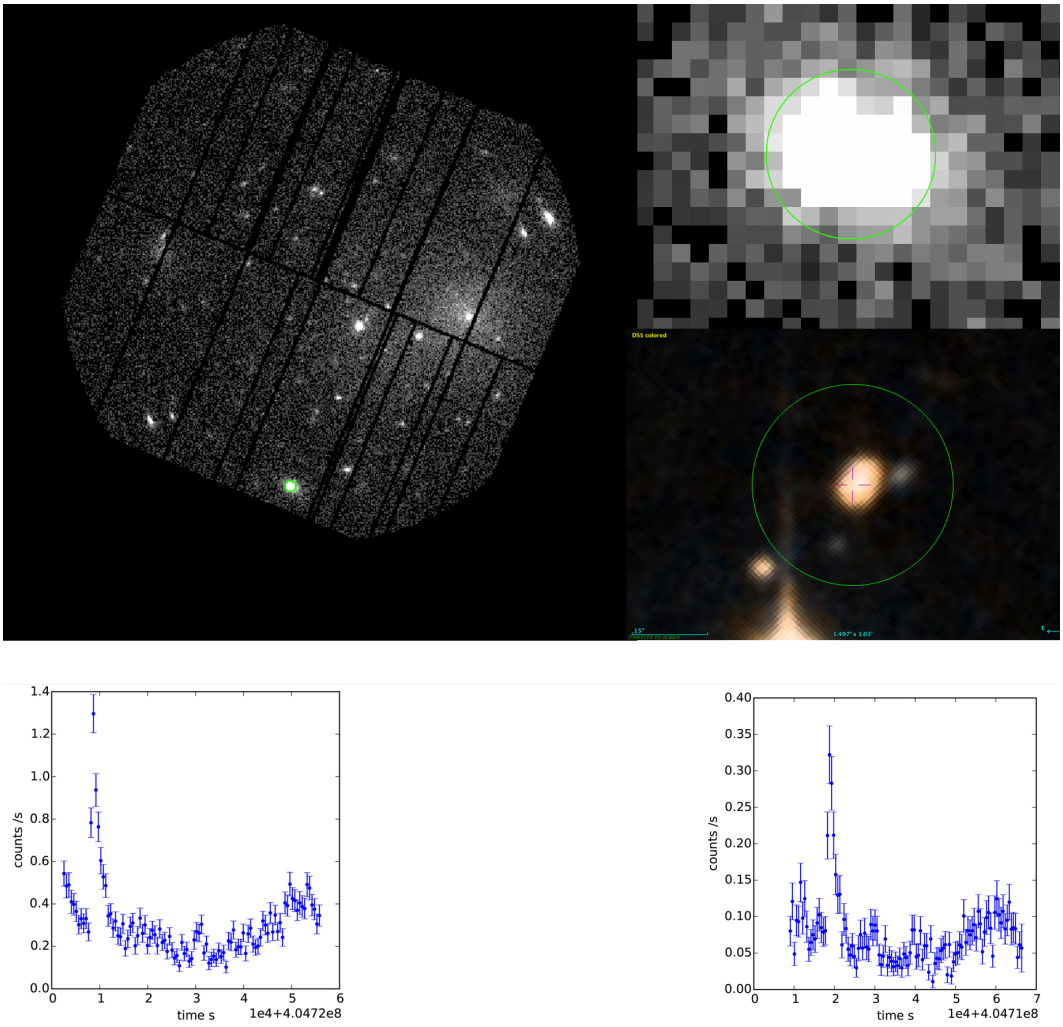

Figure D.15: XMMXCSJ215906.1-201602.3. Top. X-ray image in PN observation 0555220101 with 32xzoom 0.5-2.0 keV and optical DSS image, each with green 20″ region. Bottom. PN and MOS2 light curves (no MOS1 light-curve was made due to source falling on missing MOS1 chip).

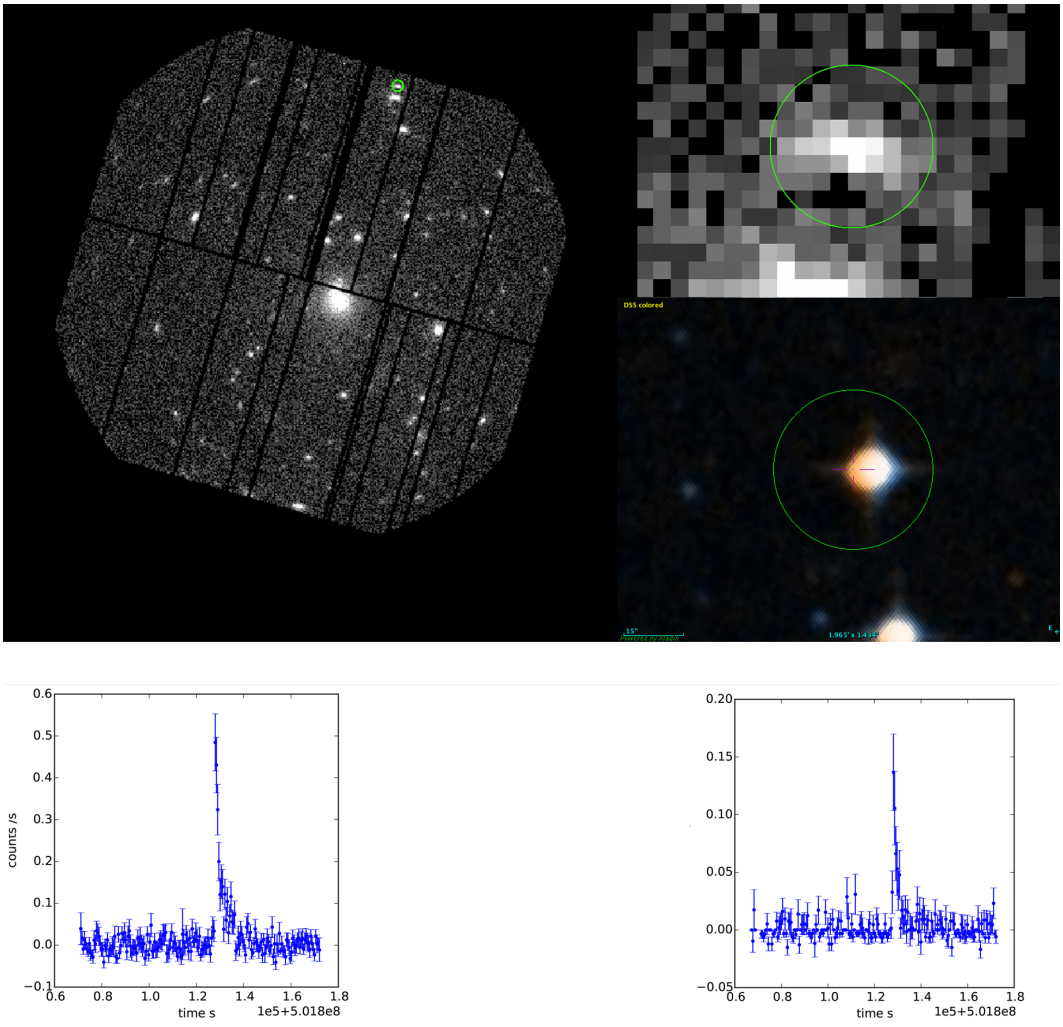

Figure D.16: XMMXCSJ220310.7-344406.5. Top. X-ray image in PN observation 0722360301 with 32xzoom 0.5-2.0 keV and optical DSS image, each with green 20″ region. Bottom. PN and MOS2 light curves (no MOS1 light-curve was made due to source falling on missing MOS1 chip).

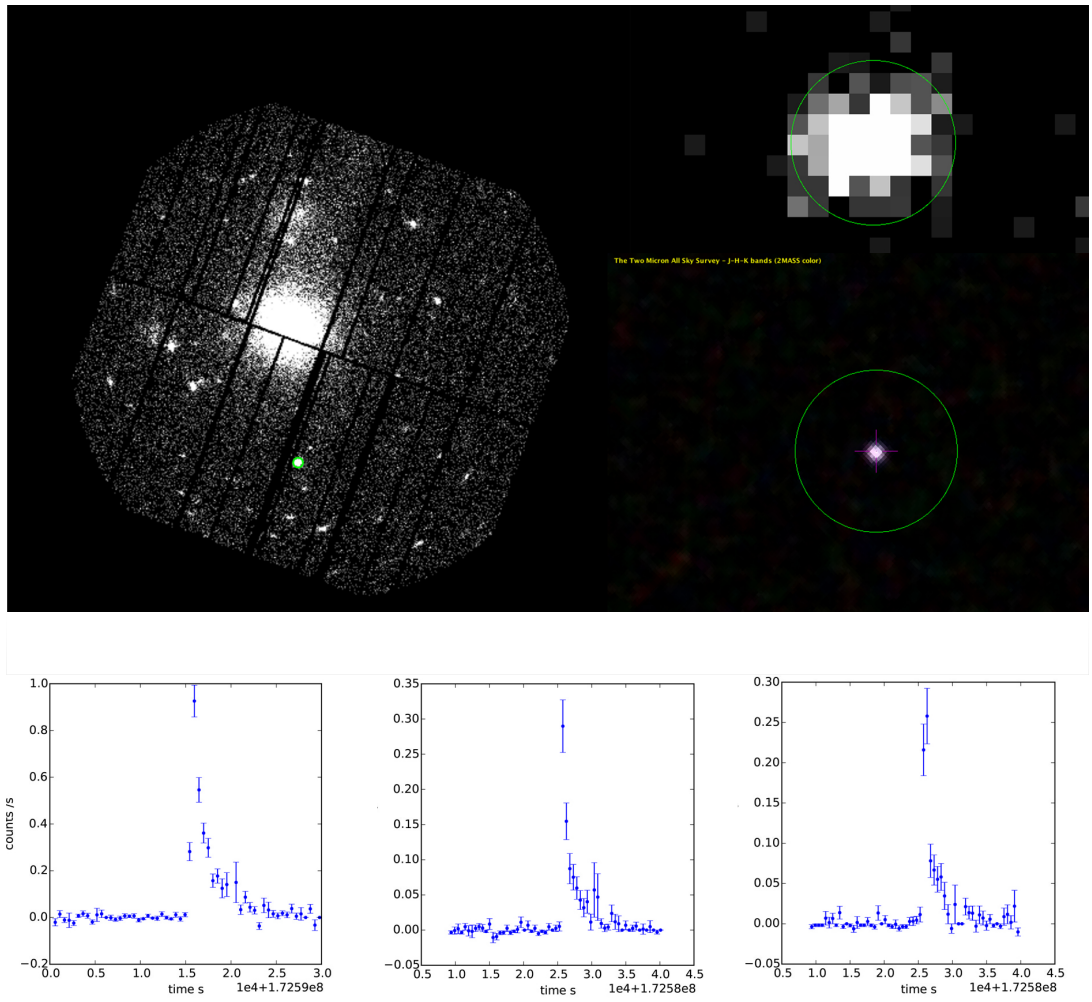

Figure D.17: XMMXCSJ235138.2-261304.0 Top. X-ray image in PN observation 0148990101 with 32xzoom 0.5-2.0 keV and infra-red 2MASS image, each with green 20″ region. Bottom. PN, MOS1 and MOS2 light curves.